

Technische Universität München
Institut für Energietechnik

Professur für Thermofluidynamik

Analysis and Low-Order Modeling of Interactions between Acoustics, Hydrodynamics and Premixed Flames

Thomas Steinbacher

Vollständiger Abdruck der von der Fakultät für Maschinenwesen der
Technischen Universität München zur Erlangung des akademischen Grades
eines

DOKTOR – INGENIEURS

genehmigten Dissertation.

Vorsitzender:

Prof. Dr.-Ing. Hartmut Spliethoff

Prüfer der Dissertation:

Prof. Wolfgang Polifke, Ph.D.

Prof. Matthew Juniper, Ph.D., University of Cambridge, UK

Die Dissertation wurde am 29.04.2019 bei der Technischen Universität München
eingereicht und durch die Fakultät für Maschinenwesen am 24.07.2019
angenommen.

Kurzfassung

Die vorliegende Dissertationsschrift untersucht die Wechselwirkung zwischen Akustik und mager vorgemischten Flammen. Im Fokus stehen hierbei die thermoakustischen Eigenschaften von Brennerflammen, welche gemeinhin durch die Flammen-Transfer-Funktion (FTF), also die lineare Antwort der globalen Wärme-freisetzungsrates auf akustische Störungen, beschrieben werden. Ausgangspunkt aller Untersuchungen ist die Feststellung, dass das in der Literatur vorherrschende physikalische Verständnis des vorliegenden Problems von den etablierten Erkenntnissen zur Dynamik dünner Flammen abweicht. Während letztere hauptsächlich auf flammenintrinsic hydrodynamischen und thermodynamischen Prozessen beruhen, dreht sich die Theorie akustisch angeregter Flammen hauptsächlich um experimentell beobachtete konvektiv transportierte Geschwindigkeitsstörungen, welche mit der Flamme wechselwirken. Das Ziel der vorliegenden Arbeit ist es daher, beide Betrachtungsweisen zu vereinen und dabei die wichtigsten Mechanismen der Akustik-Flammen-Interaktion herauszuarbeiten. Zu diesem Zweck wird ein neues Konzept zur niedrigdimensionalen Modellierung entwickelt, mit dessen Hilfe bestimmte, klar definierte Aspekte der zugrunde liegenden Dynamik getrennt untersucht werden können. Detaillierte numerische Rechnungen dienen zu dessen Validierung und bieten zudem aufschlussreiche Einblicke in die physikalischen Vorgänge. Die damit durchgeführte Analyse beschränkt sich auf Schachtflammen. Zwei Arten der Akustik-Flammen-Strömungsinteraktion konnten identifiziert werden: (i) Primäre Wechselwirkungen, welche ausschließlich unmittelbare Auswirkungen akustischer Störungen einschließen, und (ii) sekundäre Wechselwirkungen, welche flammenintrinsic Prozesse umfassen, die im Wesentlichen auf einer Kopplung zwischen Hydrodynamik und Flammendynamik beruhen. Ein Ergebnis der durchgeführten Untersuchungen ist es, dass das rotationsfreie akustische Feld in erster Linie die Region am Flammenfuß beeinflusst, während von der Akustik erzeugte abgelöste Wirbel so gut wie nicht mit der Flamme interagieren. Die daraus resultierenden primären Auslenkungen der stationären Flammenfront sind anschließend hydrodynamischen Mechanismen ausgesetzt, welche aufgrund des verbrennungsinduzierten Dichtesprungs zu deren Anwachsen führen. Zusätzlich dazu bilden sich in der Umgebung primärer Störungen weitere, sekundäre aus. Beide Phänomene zusammen führen zu einer Amplitudenverstärkung der zugehörigen FTF, die Werte von Eins deutlich übersteigen kann. In Übereinstimmung mit der Literatur, konnte das Auftreten der genannten konvektiv transportierten Geschwindigkeitsstörungen auf eine Kopplung zwischen Hydrodynamik und Flammendynamik zurückgeführt werden. Basierend auf theoretischen Untersuchungen zur Auswirkung der Flammengeometrie auf die lineare Flammenantwort, wird abschließend eine Methode vorgeschlagen, die es ermöglicht, die für Schachtflammen gewonnenen Erkenntnisse auch auf andere Flammgeometrien wie Bunsen- oder Keilflammen, zu übertragen.

Abstract

This doctoral thesis analyses interactions between acoustics and lean premixed flames from a thermoacoustic point of view. Special focus is put on the linear response of the global heat release rate of burner-stabilized laminar flames to acoustic perturbations, commonly expressed by the flame transfer function (FTF). The starting point of all investigations is the inconsistency between (i) the prevailing notion of the underlying physical mechanisms of the problem at hand and (ii) first principle-based descriptions of the dynamics of thin flames. While the latter are essentially based on hydrodynamic and thermal-diffusive modes of flame propagation, the former revolve around the empirical concept of acoustically triggered convected velocity perturbations interacting with the flame. This work strives to bring together both perceptions and, in doing so, aims to identify the skeletal processes governing acoustics-flame interactions. To this end, a first principle-based low order modeling framework is developed, which allows to separately investigate well-defined aspects of the underlying dynamics. High fidelity numerical simulations provide instructive validation data. Focusing on Slit flames, two types of acoustics-flame-flow interactions are identified: (i) Primary interactions, which involve only immediate effects of acoustic perturbations on the flame, and (ii) secondary interactions, which cover flame intrinsic processes essentially depending on a hydrodynamic flame-flow feedback. It is found that the irrotational acoustic field predominantly interacts with the flame base region, while vortex shedding has almost no impact. The acoustically triggered primary flame displacements are subject to mechanisms of flame-flow feedback provoked by the change in density across the flame sheets. These mechanisms lead to their convective growth as well as to the formation of secondary displacements, which altogether results in FTF peak gain values significantly exceeding unity. Furthermore, in agreement with the literature, flame-flow feedback is found to be responsible for the mentioned convected velocity perturbations. By analyzing consequences of flame geometry for the acoustic response, a simple way is suggested how to transfer the results found for Slit flames to the more widespread Bunsen and Wedge flame configurations.

Acknowledgements

The research project, which finally led to the completion of the thesis at hand, would not have been successful without the support and encouragement of so many helpful and great people. There is, of course, Prof. Polifke who gave me the unique opportunity to do scientific research without imposing too many obligations to predefined research projects — that has been a great chance, but also kind of a challenge. Then there is this remarkable research group of which I could be part of. Everyone has been so helpful and, many times, instructive and fruitful discussion sparked. Furthermore, I have to thank all of the students I supervised, I learned more from them and their work than they might be aware of. And — last but not least — I am deeply indebted to my wife Sofi, my parents and my two sisters.

Thank you!

Wesentliche Teile der vorliegenden Dissertationsschrift wurden vom Autor bereits auf Konferenzen vorgetragen oder als Konferenz und Zeitschriftenbeiträge veröffentlicht [1, 2]. Alle Vorveröffentlichungen sind entsprechend der gültigen Promotionsordnung ordnungsgemäß gemeldet. Sie sind deshalb nicht zwangsläufig im Detail einzeln referenziert. Vielmehr wurde bei der Referenzierung eigener Vorveröffentlichungen Wert auf Verständlichkeit und inhaltlichen Bezug gelegt.

Major parts of the present thesis have been presented by the author at conferences, and published in conference proceedings or journal papers [1, 2]. All of the author's prior publications are registered according to the valid doctoral regulations. In the interest of clarity and comprehensibility of presentation, not all of the prior publications are explicitly cited throughout the present work.

Contents

Contents	xi
Nomenclature	xvii
Introduction	1
I Literature Review on Acoustics-Flame Interactions	9
1 Dynamics of Thin Flame Sheets	11
1.1 Scope	12
1.1.1 Definition of the Term “Thin Flame”	12
1.1.2 Historical Background	15
1.2 Mechanisms Governing Flame Propagation	21
1.2.1 Propagation Normal to Itself	22
1.2.2 Thermal-Diffusive	24
1.2.3 Hydrodynamic	27
1.2.4 Advection of Perturbations at Inclined Flames	31
1.3 Low-Order Models	33
1.3.1 Level-Set or G-Equation Approach	34
1.3.2 1D Linearized Flame Dynamics	35
1.4 Summary	38
2 Acoustic Response of Burner-Stabilized Flames	41
2.1 Problem Definition	42
2.2 Acoustics-Flame Interactions	43
2.2.1 Freely Propagating Flame Sheet	43
2.2.2 Burner-Stabilized Flame	44
2.2.3 Global Heat Release Rate Dynamics	49
2.3 Low-Order Models	52
2.4 Summary	55

II	Analysis of Acoustics-Flame Interactions of Slit Flames	57
3	Flow-Decomposition Based Modeling Framework	59
3.1	Helmholtz Decomposition	60
3.2	Problem Formulation and Governing Equations	62
3.3	Conformal Mapping Technique	66
3.3.1	Schwarz-Christoffel Mapping	66
3.3.2	Flow-Field Singularities	67
3.3.3	Kutta Condition	69
3.4	Summary	76
4	Primary Interactions	77
4.1	Test Case Setups	78
4.2	Irrotational and Vortical Response Analysis	79
4.2.1	Harmonic Forcing	80
4.2.2	Impulse Forcing	81
4.2.3	Discussion	84
4.3	Summary and Conclusions	86
5	Secondary Interactions	89
5.1	Flame Response Revisited in the Light of Flame-Flow Feedback	91
5.1.1	High Fidelity CFD/SI Data	91
5.1.2	Convective Velocity Model	94
5.2	Modeling of Flame-Flow Feedback	96
5.2.1	Jump Conditions Across a Flame Sheet	97
5.2.2	Modeling of Flame Generated Vorticity	99
5.2.3	Modeling of Geometrical Focusing	102
5.3	Analysis of the Impact of Flame-Flow Feedback	106
5.3.1	Flame Generated Vorticity	108
5.3.2	Irrotational Flame-Flow Feedback	112
5.4	Summary and Conclusions	116
III	Generalization to Other Burner Configurations	119
6	Consequences of Flame Geometry	121
6.1	Test Case Setups	123
6.2	Integral Heat-Release	125
6.3	Physics Based Illustration of the Heat Release Dynamics	133
6.4	Incompressible-Convective FTF Models	137
6.5	Geometry-Dependent Analysis of the Incompressible-Convective Model	141
6.6	Validation of Flame Response Models	145
6.7	Summary and Conclusions	153

Summary and Conclusions	155
Appendix A Numerical Response Analysis	161
A.1 Test Case Setups	161
A.2 CFD/SI Method	162
A.2.1 Incompressible Numerical Simulations	162
A.2.2 System Identification	163
A.2.3 Goodness of the Identified Model	167
A.3 Time vs. Frequency Domain Based Response Analysis	173
A.4 Computation of Flame Normal Displacements	175
Appendix B Impact of the Anchoring Wall Temperature	177
Appendix C Flame Transfer Functions	181
C.1 Convective Incompressible FTFs with Gaussian Kernel	181
C.2 Flame Base Velocity Forcing	183
Appendices	
List of Figures	191
List of Tables	193
Bibliography	215

Nomenclature

Acronyms

BIBO Bounded-Input Bounded Output

CFD Computational Fluid Dynamics

DIC Incompressible-Convective Velocity Model with Dirac Kernel, see Sec. 6.4

FBD Flame Base Displacement Model, see Eq. 4.2

FIR Finite Impulse Response, see Sec. A.2.2

FR Frequency Response

FTF Flame Transfer Function

GIC Incompressible-Convective Velocity Model with Gaussian Kernel, see Sec. 6.4

IC Incompressible-Convective Velocity Model, see Sec. 2.3

IR Impulse Response

LOM Low-Order Model

LTI Linear Time Invariant

MS equation Michelson-Sivashinsky equation

PA system Public address system comprising microphones, amplifiers and loudspeakers

SI System Identification

SNR Signal-to-Noise Ratio

Modifiers

(.)' Fluctuating quantity

- (.)^{*} Non-dimensional quantity
- (.)^F Quantity in flame aligned coordinates
- (.)^L Quantity in laboratory coordinates
- (.)_{con} Quantity concerning a conical configuration (Wedge or Bunsen)
- (.)_{ref} Quantity at a reference position
- (.)_{slit} Quantity concerning a slit configuration
- (.)_{||} Component parallel to the mean flame front
- (.)_⊥ Component perpendicular to the mean flame front
- (.)_b Quantity of the burned flow
- (.)_i Component of a vector quantity in the i -th direction
- (.)_u Quantity of the unburned flow
- (.)_Λ Quantity concerning a (Conical) Bunsen configuration
- (.)_V Quantity Concerning a (Conical) Wedge configuration
- [*]_u^b Change of a quantity across the flame: $*_b - *_u$, see Eq. (1.7)
- $\overline{(\cdot)}$ Mean flow quantity
- $\tilde{(\cdot)}$ Complex conjugate

Non-Dimensional Numbers

- α^* Non-dimensional flame angle $\alpha^* = \sin(\alpha) = s_L^0 / \bar{u}_1$, see Sec. 1.2.4.
- α_M Reduced Markstein number, see Sec. 1.1.2
- C_r Confinement ratio $C_r = R_i / R_a$
- \hat{e} Inverse expansion ratio $e = \rho_b / \rho_u$
- E Non-dimensional increase of specific volume $E = \rho_u / \rho_b - 1$
- e Expansion ratio $e = \rho_u / \rho_b$
- f^* Strouhal number (non-dimensional frequency) with $f^* = f \tau_r$
- He Helmholtz number, see Eq. (3.3)
- Ka Karlovitz number, see Eq. (1.12)
- Le Lewis number, see Eq. (1.5)

M_a	Markstein number, see Eqs. (1.9) and (1.11)
Pe	Péclet number, see Eq. (1.4)
\tilde{r}	Non-dimensional rod radius $\tilde{r} = R_r / R_a$
Re	Reynolds number
Ze	Zeldovich number, see Eq. (1.6)

Symbols

A_f	Flame surface area	[m ²]
α	Flame angle, see Fig. 1.13	[rad]
$\beta_{x/\xi}$	Angle defining a vortex panel in the physical/image domain, see Fig. 3.6	
c_p	Specific heat capacity for constant pressure	[J kg ⁻¹ K ⁻¹]
δ_D	Thickness of the preheat zone, see Sec. 1.1.1	[m]
$\delta(.)$	Dirac Delta function	
δ_R	Thickness of the reaction sheet, see Sec. 1.1.1	[m]
δ_{th}	Thermal diffusivity	[m ² s ⁻¹]
δ_Y	Mass diffusivity of species Y	[m ² s ⁻¹]
E_a	Activation energy of a chemical reaction	[J]
ϵ	A small number $\epsilon \ll 1$	
η	Flame front displacement in laboratory coordinates, see Fig. 1.13	[m]
f	Temporal frequency	[s ⁻¹]
$F(\omega)$	Frequency response function, see Eqs. (2.1) or (A.2)	
f_g	Geometrical factor, $f_g = 1$ (Slit) and $f_g = 1/2$ (Conical)	
f_O^*	Strouhal number of the oscillatory feature of the IR, see Eq. (6.23)	
G	G-field of the Level-Set method, see Sec. 1.3	
$G(.)$	General kernel function of the convective flow perturbation: 1st antiderivative	
$g(.)$	General kernel function of the convective flow perturbation	
Γ	Circulation, see Eq. (5.18)	[m ² s ⁻¹]

$\Gamma(\cdot)$	General kernel function of the convective flow perturbation: 2nd antiderivative	
$\gamma_{x/\xi}$	Vortex sheet strength in the physical/image domain, see Eqs. (3.27) and (3.28)	$[\text{m s}^{-1}]$
$h(t)$	Impulse response function, see Eq. (2.3)	
H_f	Axial length (height) of the mean flame front, see Fig. 6.4	$[\text{m}]$
h_i	Impulse response coefficients, see Eq. (A.1)	
i	Complex unit or (summation) index	
K	Flow perturbation convection speed relative to the mean flow speed $K = u_c/\bar{u}_1$, see Eqs. (6.17) and (6.18)	
κ_f	Local flame front mean curvature, see Eqs. (1.8) or (1.25)	$[\text{m}^{-1}]$
κ_s	Flame stretch, see Eq. (1.10)	$[\text{m}^{-1}]$
λ	Wave length $[\text{m}]$ or thermal conductivity	$[\text{W m}^{-1} \text{K}^{-1}]$
L_f	Length of the mean flame front, see Fig. 1.13	$[\text{m}]$
$l_f(t)$	Length of the perturbed flame front with ref. to Fig. 6.4	$[\text{m}]$
l_M	Markstein length, see Eq. (1.8)	$[\text{m}]$
\mathbf{n}_f	Vector normal to the flame front, see Eqs. (5.2) or (1.21)	$[\text{m}]$
ν	Kinematic viscosity	$[\text{m}^2 \text{s}^{-1}]$
ω	Angular frequency $[\text{rad s}^{-1}]$ or vorticity $[\text{s}^{-1}]$	
Ω_0	Darrieus-Landau parameter, see Eq. (1.18)	
p	Pressure	$[\text{Pa}]$
ϕ	Equivalence ratio [-] or flow potential $\text{m}^2 \text{s}^{-1}$, see Eq. (3.1)	
ψ	Flow vector potential $\text{m}^2 \text{s}^{-1}$, see Eq. (3.2)	
\dot{Q}	Heat-release rate	$[\text{W}]$
R_a	Outlet half-diameter, see Fig. 6.1	$[\text{m}]$
r_f	Local flame front radius, see Fig. 6.4	$[\text{s}]$
R_g	Gas constant	$[\text{JK}^{-1}]$
ρ	Density	$[\text{kg m}^{-3}]$

R_i	Inlet half-diameter, see Fig. 6.1	[m]
R_r	Rod radius, see Fig. 6.1	[m]
s	Parametrization of the (perturbed) flame front, see Fig. 6.4	[m]
σ	Standard deviation of the gaussian kernel function [s] or temporal growth rate [rads ⁻¹]	
s_L	Flame speed	[ms ⁻¹]
s_L^0	Unstretched flame speed	[ms ⁻¹]
T	Temperature	[K]
t	Time	[s]
τ	Time delay	[s]
τ_c	Characteristic flame time scale of convection in the convective velocity FTF models, see Eq. (6.22)	[s]
τ_r	Characteristic flame time scale of restoration, see Eq. (6.21)	[s]
τ_t	Flame transition time $t_f = \delta_D / s_L$ used to non-dimensionalize growth rates, see Sec. (5.1.1)	[s]
T_{BP}	Temperature of the combustion chamber back plate, see Fig. 6.1	[K]
\mathbf{t}_f	Vector parallel to the flame front, see Eq. (5.2)	[m]
$\theta(\cdot)$	Heaviside Step function	
u	Flow velocity	[ms ⁻¹]
u_c	Flow perturbation convection speed along the mean flame front $u_c = K\bar{u}_1 / \cos(\alpha)$, see Tab. 6.1	[ms ⁻¹]
U_{edge}	Velocity evaluated right at the edge of separation including a Kutta condition	[ms ⁻¹]
k	Wave number	[rad m ⁻¹]
x	Coordinate	[m]
ξ	Flame front displacement in flame coordinates, see Fig. 1.13 [m] or coordinate in the complex plane, see Sec. 3.3.1	
y_Y	Mass fraction of species Y	

Introduction

Simplicity is a great virtue but it requires hard work to achieve it and education to appreciate it. And to make matters worse: complexity sells better.

– Edsger Wybe Dijkstra

Turbulent combustion is complex and of high technical relevance and, as a consequence, increasingly attracts the attention of scientific research. Laminar combustion, on the other hand, is apparently simple and of less technical relevance; accordingly, the number of fundamental studies published in this field is receding, particularly in industry-funded research projects. Yet, most of the low-order modeling concepts used to capture the dynamics of turbulent flames are derived from laminar theory. This means, blind spots in laminar theory propagate to gaps of knowledge in turbulent combustion and hence might hinder a more fundamental understanding as well as the development of new modeling frameworks. Ultimately, the development of highly relevant technical innovations might be delayed by just some missing insights at the very foundations of knowledge. As will be shown in the course of this thesis, there are indeed significant blind spots concerning the specific topic of laminar acoustic-flame interactions in a thermoacoustic context. Motivated by this realization, this work is devoted to contribute to their illumination.

The Thermoacoustic Problem

Why are interactions between acoustics and lean premixed flames important at all? This question will be answered in the following relying on three examples: (i) Lord Rayleigh's early and fundamental studies of a Rijke tube, (ii) the extravagant Saturn V program and (iii) modern gas turbine combustors. A common feature of these three examples is that they are all prone to instabilities driven by thermoacoustic effects, which may lead to high amplitude oscillations. Due to the fact that these oscillations manifest themselves as pressure fluctuations that may lead to severe sound emissions or even to system failure, they are usually undesired. Consequently, this section speaks of the *thermoacoustic problem* when referring to these kind of instabilities.

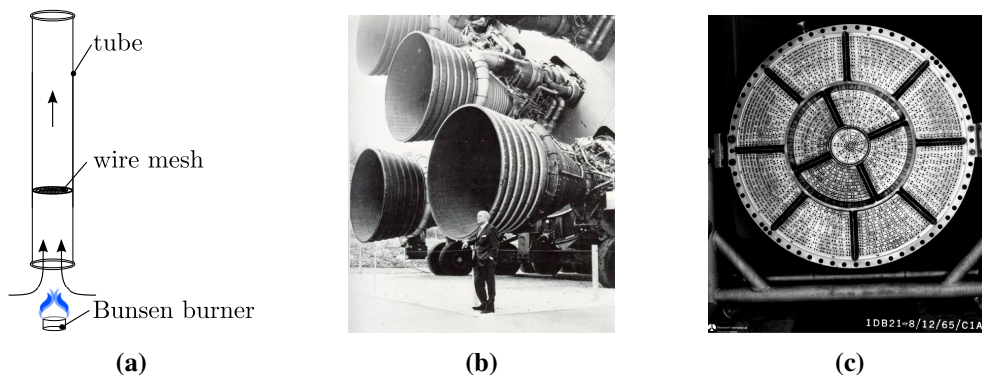


Figure 1: (a): Sketch of a Rijke tube. (b): Rocketdyne F-1 engines of the Saturn V rocket with Wernher von Braun standing in front of it (taken from [9], Chap. 3.2). (c): Injector plate of the Rocketdyne F-1 engine (taken from [10]).

A literal definition of the field of thermoacoustics would include all acoustic phenomena in a gaseous medium that rely either on diffusive effects or entropy variations [3]. Following Rott [3], however, a more restrictive definition shall be adopted here that emphasizes one essential thermoacoustic phenomenon, namely the maintenance of aerial vibrations by heat, as put by Rayleigh [4]. This definition shall be clarified in the following by use of one of the most famous thermoacoustic experimental setups, the Rijke tube [5–7].

A sketch of such a device is provided in Fig. 1a. It consists of a vertical tube, where a metallic wire mesh (or wire gauze) is mounted somewhere in its lower half. By placing a Bunsen burner right beneath its lower end, the wire mesh is heated. Removing the burner, astonishingly, an enervating high-pitched sound appears, which slowly decays over time. Lord Rayleigh was the first to provide an adequate explanation of this phenomenon. According to him, the key ingredient responsible for the sound generation is the right phasing between pressure fluctuations and heat transfer from the wire to the flow: Only if heat is added to the fluid at the moment of greatest condensation or taken from it at the moment of greatest rarefaction, a self-sustained oscillation can develop, which manifest itself as a clearly audible sound [8]. The phasing is essentially defined by the acoustic properties of the tube and by the dynamics as well as the location of the heat source.

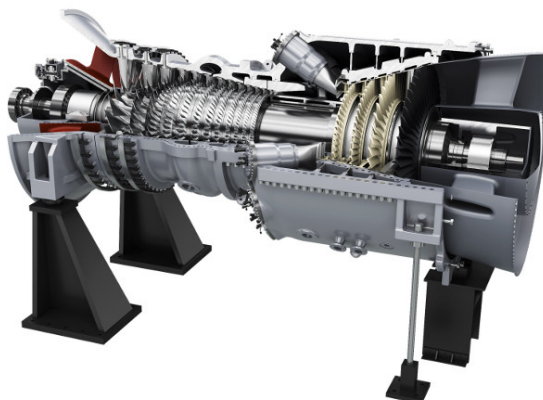
One of the most illustrative examples of the drastic consequences and difficulties related to thermoacoustic phenomena is taken from the endeavor of the USA to bring a man to the moon. Such a mission requires the possibility to cope with high payloads, since a lot of equipment has to be brought into earth orbit. For that reason, the NASA developed the Saturn V rocket. Its first stage was equipped with five Rocketdyne F-1 engines, each providing a thrust of at least 6672 kN [11], whose impressive dimensions are illustrated in Fig. 1b. One important problem encountered during their

development were combustion instabilities caused by thermoacoustic effects, which caused three total engine losses and several emergency shutdowns during the testing phase [12]. In order to solve this problem and to develop a dynamically stable system, the *Project First* program was initiated in 1962 [11]. The desired performance specifications required certain combustion chamber and nozzle geometry designs and, hence, those parameters could not be changed. The principal leverage of the engineers to improve system stability was the design of the injector as well as the thereon attached baffles, see Fig. 1c. During the course of this project, about 2000 full scale test of 14 basic injector patterns and 15 baffle configurations were conducted [11]. Knowing that the two turbopumps used delivered nominal flow rates of 984 l/s of fuel and 1577 l/s of oxidizer [11], one can imagine the costs and logistical requirements of this series of tests. This emphasizes the severity of the (thermoacoustic) combustion instabilities they had to cope with. Ultimately, an injector design was found that enabled stable operation as well as safe 165 first seconds on the long journey to the moon.

With the increasing significance of gas turbines for the generation of electrical power or for the propulsion of airplanes during the second half of the previous century, a variety of thermoacoustic combustion instabilities, which limit the operational ranges of these devices or require advanced damping strategies, have been detected. Furthermore, thermoacoustic effects enhance acoustic emissions of gas turbine combustors, commonly termed as combustion noise, whose reduction increasingly shifts into the focus of current research [13–15]. Depending on the area of application, different challenges have to be met. In the following, the focus is put on stationary gas turbines.

Fig. 2a shows a modern low-emission stationary gas turbine as used for the generation of electrical power. In the design of such devices, engineers have to manage a balancing act between thermodynamics, emission regulations and component loads. Thermodynamics requires combustion at high temperatures in order to reach high efficiencies, which is compulsory to minimize fuel consumption and CO₂ emissions. On the other hand, high temperatures promote the formation of harmful nitrogen oxides, shortly NO_x, and require advanced cooling concepts for all parts of the machine that are in contact with the hot gases. It was found that these requirements are best met relying on lean premixed combustion, which allows for a well controllable and homogeneous combustion process at high power densities. Gas turbine manufacturers, however, have to pay dearly for these beneficial properties since it turned out that such devices are prone to thermoacoustic oscillations. Keeping them under control is still one of the major challenges gas turbine industry has to face today.

In doing so, several strategies have been followed. On the one hand, damping devices were developed, which, ideally, can calm already existing noisy combustors without having to redesign big parts of them. One example for such a device is depicted in Fig. 2b. Here, the back plate of an annular combustion chamber is shown, where the big black holes represent the burners through which the fresh mixture is injected into



(a)



(b)

Figure 2: (a): Modern gas turbine as used for the generation of electrical power (taken from [16]). (b): Back plate of a annular combustion chamber with burners (big black holes). The smaller black holes next to the burners are Helmholtz dampers (taken from [17]).

the chamber. Additionally, smaller black holes are visible, which are the entrances to connected cavities placed behind the plate. Each hole/cavity assembly forms a damping device denoted as Helmholtz damper, which significantly reduce pulsation amplitudes occurring during engine operation [18, 19]. On the other hand, instead of improving existing designs, it is desirable to include thermoacoustic considerations already in early stages of the design process of a new machine. To this end, a fundamental understanding of all processes involved has to be generated and, based on the insights gained, tools need to be developed that allow for reliable low-order based thermoacoustic stability analyses. In the best case, this helps to avoid expensive test series as they were, for example, conducted for the F-1 engine.

The Role of the Flame in Thermoacoustic Stability Analysis

Many harmful combustion instabilities are low-frequency phenomena. For gas turbines, the associated frequency range can roughly be specified to 100 – 500 Hz [19].

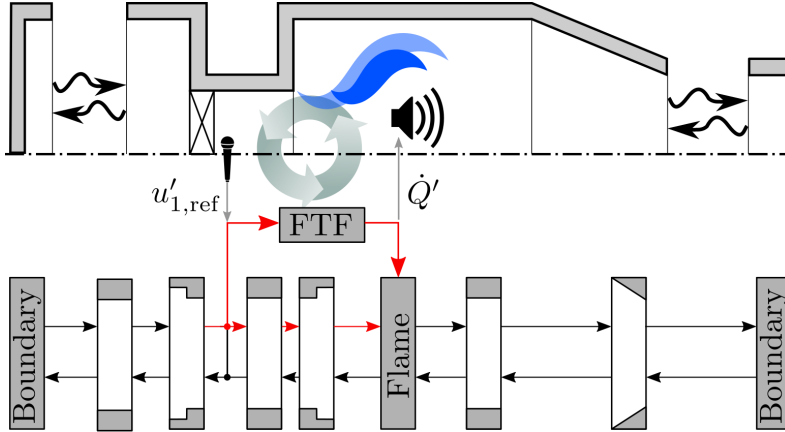


Figure 3: Sketch of a gas turbine combustor (top) and its associated network model (bottom). Marked in red is the intrinsic feedback loop.

At these frequencies, the acoustic field inside the combustor can in good approximation be assumed to be one-dimensional. Therefore, such systems exhibit essentially longitudinal modes resulting from planar acoustic waves [20]. Note that annular combustion chambers may also show azimuthal acoustic modes in this frequency range, which shall not be discussed here. Low-order modeling concepts developed to analyze such longitudinal modes are referred to as network models and are usually structured as depicted in Fig. 3. In the top of this figure, a typical gas turbine combustor is sketched: fresh mixture is supplied through a plenum, which feeds the premixed gases through a swirler (crossed box) into the combustion chamber where they are burned. The hot products are then emitted to the environment (or the turbine) through a converging nozzle. The lower half of the figure shows a network model representing the 1D-acoustics of the model combustor mentioned before. Each element represents a specific part of the real device, such as a plain duct, a change in cross-sectional area, a boundary condition or the flame. The dynamics of the flame are hereby described by the flame transfer function (FTF) which connects acoustic velocity fluctuations upstream of the flame to variations of the global heat release rate. This again is fed into the network model as an acoustic source.

Following Fig. 3, a flame can be viewed as a PA system: It captures sound at a specific position, similar to what a microphone does, amplifies and phase changes the recorded signals and emits them at a different location, just like a speaker¹. What becomes clear from this analogy is that the heat source establishes a feedback cycle, which may become unstable and lead to a self-oscillatory state. One possible cycle, the so-called intrinsic thermoacoustic feedback cycle [21–23], is marked in red in Fig. 3. In the case of a PA system — or a Rijke tube as mentioned above — such a state manifests itself as a loud screech. If that happens, usually either the position

¹Note that premixed flames “listen” to velocity fluctuations while most microphones capture pressure fluctuations. The analogy presented here should hence not be taken literally!

of the microphone is changed or the gain of the amplifier is reduced in order to get rid of this perturbing sound. In the case of a gas turbine combustor, consequences of a developed self-oscillatory state are more severe and might — in the worst case — even lead to system failure, similar to what has been shown above for the F-1 rocket engine. The main leverage for counteracting such a state is the FTF, which can, for example, be modified by changing the mass flux or the air-to-fuel ratio.

Since the flame is the driving force of a combustion instability, understanding its dynamics is crucial. Having powerful low-order models at hand that allow adequate predictions of the flame dynamics would significantly enhance stability predictions, particularly in early stages of the design process of a full combustor or a damping system. To this end, a profound understanding of interactions between acoustics and a flame needs to be established. This is not an easy task, considering that even a Rijke tube, where a heated mesh instead of a flame acts as a heat source, exhibits non trivial behavior [24, 25]. Although there are many studies that have already dealt with this topic, the flame response to acoustic perturbations is not yet adequately understood - even for the simple case of a Bunsen flame and low forcing amplitudes (linear regime). Thus, it seems to be a good idea to focus on these setups first before advancing to even more complex, turbulent flames, as used in gas turbine combustors.

Objective and Outline of the Thesis

The ultimate goal of this work is to advance the understanding and modeling of the response of burner-stabilized laminar flames to acoustic perturbations. The behavior of the global heat release rate is of particular interest, since its fluctuations are proportional to the sound generated by a flame, which is an important quantity in thermoacoustic analysis. To this end, instructive low-order models shall be developed and extended, which allow to bring order into the analysis of acoustics-flame interactions.

In the field of thermoacoustics, there is a lack of first principle-based, low-order modeling concepts for the linear flame response expressed by the flame transfer function (FTF), see Fig. 3. As will be detailed in the course of this work, the most widespread models all rely on the assumption of convective velocity perturbations, which is based on experimental observations instead of a rigorous derivation starting from first principles. Although they allow for reasonable FTF predictions relying on empirical parameters (*they are useful ...*), they are not suitable for the analysis of the underlying physical mechanisms (*... but not instructive*).

Based on this realization, this thesis starts with a review of the literature on the dynamics of laminar flames. A lot has been achieved in this field, however, only a rather small fraction of the gathered knowledge has made its way to the field of thermoacoustics. A similar statement can be made concerning the field of aero-acoustics, which deals with the generation and attenuation of acoustic energy in flows without

chemical reactions. Elaborate models for the transient acoustic field inside a confinement or the process of vortex shedding have been developed here, which would qualify as candidates for low-order descriptions of the velocity field in the vicinity of an acoustically perturbed anchored flame. Again, rather few concepts made it to the field of thermoacoustics. This thesis tries to account for the inherently interdisciplinary nature of thermoacoustics and strives to bring together knowledge and methods from the fields of laminar premixed combustion and aero-acoustics.

The work is split into three parts:

- Part I** provides a review of the literature on the dynamics of acoustically perturbed laminar premixed flames. Chap. 1 deals with the fundamental mechanisms governing the dynamics of thin flame sheets far away from any boundary. Correspondingly, the wide-spread G-equation modeling concept is introduced. Based on these results, Chap. 2 extends the scope and focuses on the dynamics and low-order modeling strategies of acoustically perturbed burner-stabilized flames.
- Part II** analyzes interactions between acoustic perturbations with burner-stabilized flames relying on a new first principle-based low-order modeling concept. The analysis is split into primary and secondary interactions, motivated by the characteristics of the flame response to an impulsively acoustic forcing: At the very moment the impulse hits the flame, its behavior is well described neglecting flame-flow feedback (primary interactions). At later times, the flame dynamics are no longer directly governed by acoustics but by the dynamics of the individual flame sheets, which particularly includes flame-flow feedback (secondary interactions). These secondary mechanisms have severe consequences for the FTF leading to gains significantly exceeding unity and are hence important.
- Part III** analyzes the implications the choice of a specific burner configuration has for the linear acoustic flame response. While the literature mostly reports on Bunsen flames, Part II analyzed the dynamics of Slit flame configurations due to their simpler analytical treatment. Hence, the questions arises how the results obtained in Part II could be generalized. Chap. 6 seeks to provide an answer by investigating consequences of flame geometry for the linear acoustic flame response. In the course of this study, an extension to the convective velocity model is proposed relying on Gaussian kernel functions, which particularly improves response predictions of Slit flames.

The contents of the work are summarized in Fig. 4, which contains a collection of the key ideas of each chapter. This overview is not meant to be self-explanatory, but rather to assist the reading process of this thesis.

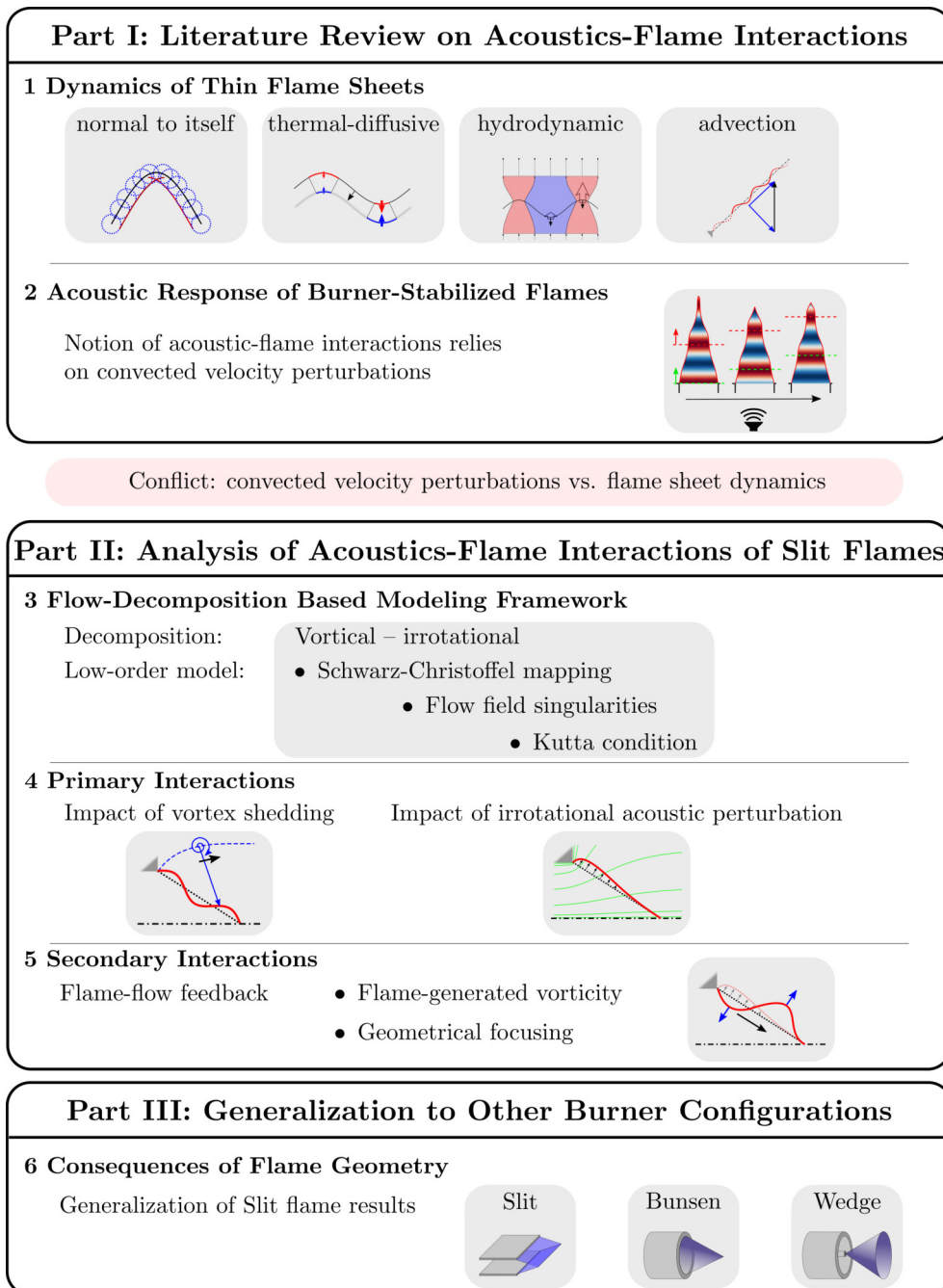


Figure 4: Contents of the thesis in a nutshell.

Part I

Literature Review on Acoustics-Flame Interactions

This thesis seeks to analyze and model interactions between acoustics and laminar lean premixed flames. A well-established method to efficiently assess the dynamics of such flames avoiding the need to deal with chemical reactions relies on a kinematic description: the usually thin flame sheets are viewed as gasdynamic discontinuities that propagate normal to themselves with a characteristic speed. Their dynamics are hereby governed by consequences of density changes across the flame sheets as well as by dependencies of the flame speed on various geometrical and mixture properties. This approach became state-of-the-art and, thus, the literature review provided in this Part of the thesis revolves around this key concept.

Chap. 1 introduces the fundamental dynamics of freely propagating flame sheets. Four canonical mechanisms are identified and explicated that govern flame propagation. Most low-order modeling concepts are based on the so-called G-equation approach, which is subsequently discussed. Relying on these ideas, Chap. 2 then moves on to the more realistic setups of burner-stabilized flames. Here, driven by the thermoacoustics focus of this work, their interactions with acoustic perturbations are emphasized. The phenomenological convective velocity model is introduced, which is, combined with the G-equation framework, the state-of-the-art low-order model of such systems.

1 Dynamics of Thin Flame Sheets

A literature review on the dynamics of thin flame sheets far away from any boundary is provided, ranging from (i) a discussion on the internal flame structure, over (ii) an outline of four important canonical mechanisms of flame propagation to (iii) associated low-order modeling concepts.

Premixed laminar flame fronts are often assumed to be thin with respect to a characteristic length of the considered problem, such as the overall flame length or a perturbation wave length. This approximation allows for a purely kinematic treatment of their spatio-temporal behavior avoiding detailed considerations of flame-internal chemical and transport processes that govern the combustion process. A description of the complete dynamics boils down to an expression for the flame propagation velocity as well as jump conditions, connecting macroscopic properties of the fluid up- and downstream of the flame. This simplified treatment enables analytical studies on the dynamics of planar flame sheets and allows to identify the physical key mechanisms. Hence, it constitutes one of the central concepts when dealing with the dynamics of premixed flame fronts.

Accordingly, this chapter introduces the relevant findings and observations required to understand the key motivations and theoretical concepts associated to this idea. For the sake of clearness, this chapter is limited to the study of freely propagating thin flame sheets far away from any boundary. Burner-stabilized flames are only introduced in the subsequent chapter as an extension to the theory introduced here.

Sec. 1.1 specifies the term “thin” in the context of a lean methane-air flame and provides a historical review of important experiments and theoretical achievements in the field. Subsequently, the four main governing mechanisms for the dynamics of lean methane-air flame sheets are summarized in Sec 1.2. Finally, Sec 1.3 introduces the G-equation or level-set method as well as a 1D linearized advection-diffusion equation, which are both widely used modeling approach in order to efficiently capture the dynamics of flame sheets.

1.1 Scope

The overview presented in the following clarifies when a flame front is considered to be “thin” and how the analysis of such flames evolved, starting from the early works of Darrieus [26] and Landau [27]. This section is not strictly limited to findings directly related to the main topic of this thesis, but rather seeks to provide a more comprehensive view. Readers who are only interested in the main mechanisms governing the dynamics of flame sheets, may skip this section for now and directly continue with Sec 1.2.

1.1.1 Definition of the Term “Thin Flame”

The overall combustion process of lean methane-oxygen mixtures to carbon dioxide and water involves tens of chemical sub-reactions and the formation of hundreds of intermediate species. Peters and Williams [28] systematically reduced these for sufficiently high pressures and temperatures to only three global reactions that involve six species:



Fig. 1.1 illustrates the inner structure of such an adiabatic, lean methane-air flame of equivalence ratio $\phi = 0.8$ ¹. Three characteristic layers are identified [28, 31]: (i) An inert convective-diffusive layer of thickness δ_D where the fresh mixture is preheated and methane molecules are transported towards the reaction zone. (ii) A thin reaction layer of extension δ_R where methane CH_4 and oxygen O_2 react to carbon monoxide CO , hydrogen H_2 and water H_2O , as expressed by Reaction (1.1). (iii) A second reaction layer of thickness δ_O where hydrogen and carbon monoxide are oxidized to carbon dioxide and water, see Reactions (1.2) and (1.3).

The reaction zone can be visualized by the heat release rate \dot{q} , which is a consequence of the transformation of chemically stored enthalpy of the products to sensible enthalpy via the three global exothermic oxidation reactions. The heat release rate is plotted in Fig. 1.1 and it is apparent that the reaction layer associated with the global Reaction (1.1) has a much thinner spatial extension than the one of the secondary oxidation zone associated with the global Reactions (1.2) and (1.3). This is reflected by different activation energies, which are significantly higher for the global Reaction (1.1) than for the Reaction (1.2). The latter is also known as the moderately exothermic water-gas shift reaction [32] and, compared to Reaction (1.1), only adds a secondary contribution to the total heat release rate. It, however, leads to the formation of hydrogen that is finally oxidized by Reaction (1.3). All in all, due to the

¹Computed with Cantera [29] using the GRI-Mech 3.0 reaction mechanism [30]

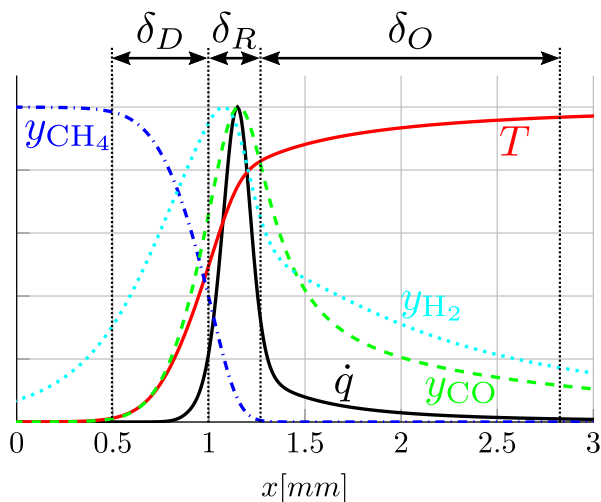


Figure 1.1: Internal structure of a lean methane-air flame of equivalence ratio $\phi = 0.8$. All curves are normalized by their maximum value.

dominance of Reaction (1.1), the combustion of methane-air mixtures is essentially a very localized process.

Based on the insight that this also holds for a variety of mixtures, where the combustion process is confined to a layer that is thin compared to a global length scale — such as the burner mouth diameter — flames are often approximated as gas dynamic discontinuities, i. e. surfaces separating cold reactants from hot products [26, 27, 33–35]. Far away from this discontinuity, fluid composition, temperature and density are essentially constant. The dynamics of the flame sheet is governed by a local consumption speed, which defines a propagation velocity of the flame normal to itself and relative to the fresh mixture, quantified by the flame speed. This speed is a manifestation of chemical reactions and transport processes in the reaction and the convective-diffusive layer, respectively [34–37].

Models that regard a flame as a discontinuity are specifically designed to capture the spatio-temporal dynamics of a reacting flow, while the formation of pollutants or any other chemical property of the combustion process are neglected. In order to retrieve a closed formulation of such flow problems, a flame speed and jump conditions, connecting up- and downstream flow quantities, need to be specified at the surface representing the flame. They were derived from first principles by use of matched asymptotic expansion methods, which exploit the fact that flames exhibit length scales of different order. Each scale has its own characteristic properties, which allows to drop specific terms from the full set of governing equations. By asymptotically matching the results of the individual length scales, a macroscopic description of the internal processes could be derived, which essentially boils down to an expression for the desired flame speed and the jump conditions, see e. g. [28, 34, 35, 37–41].

In order to apply these matched asymptotic expansion methods, characteristic length scales associated with the available internal layers need to be found. Based on them, non-dimensional parameters are defined that are used to derive the respective governing equation for each layer. In the case of premixed combustion, the relative thickness of the convective-diffusive boundary layer δ_D , see Fig. 1.1, is quantified by a Péclet number

$$\text{Pe} = \frac{L}{\delta_D}, \quad (1.4)$$

which relates a typical length scale of the macroscopic (or *outer*) flow problem L , to a length scale of the microscopic (or *inner*) advection-diffusion problem. Here, the outer problem may be characterized by the burner diameter or the perturbation wave length of interest and the inner problem by a diffusion length $\delta_D = D/s_L$, where s_L is the flame speed and D either the thermal diffusivity D_{th} or the mass diffusivity of the deficient species relative to the fresh mixture D_Y [37, 41, 42]. Both diffusivities are related by the Lewis number

$$\text{Le} = \frac{D_{th}}{D_Y}, \quad (1.5)$$

where the thermal diffusivity is defined by $D_{th} = \lambda/(\rho c_p)$ with the thermal conductivity λ , the density ρ and the specific heat capacity for constant pressure c_p , all evaluated for the fresh mixture. If $D_{th} = D_Y$ and thus $\text{Le} = 1$ holds, the thermal and the species boundary layer are identical. Otherwise, one of them outweighs the other. Lean methane-air flames, as considered in this thesis, typically have Lewis numbers very close unity, which is also reflected in the similar boundary layer thicknesses of CH_4 and temperature ahead of the reaction zone shown in Fig. 1.1. Hence, the Lewis number quantifies the coupling of species transport and energy equation, similarly as the Prandtl number does it for momentum and energy. For the $\text{Le} \approx 1$ case, typically the thermal, instead of the mass, diffusion length scale $\delta_D = D_{th}/s_L$ is used in order to quantify the extension of the preheat layer.

The thickness of the reaction layer δ_R is related to the Zeldovich number

$$\text{Ze} = \frac{E_a}{R_g T_b} \frac{T_b - T_u}{T_b} \quad (1.6)$$

with the activation energy of the global chemical reaction E_a , the gas constant R_g and the temperatures of the unburned and burned fluid T_u and T_b , respectively [43]. High activation energies, and hence $\text{Ze} \gg 1$, lead to thin reaction layers [35].

Using these definitions, the spatial extension of the convective-diffusive layer is of order $\delta_D = \mathcal{O}(\text{Pe}^{-1})$ and the one of the two reaction zones of order $\delta_{R/O} = \mathcal{O}(\text{Pe}^{-1}\text{Ze}^{-1})$ [35, 37]. For the flame configurations considered in this thesis (lean methane-air mixtures at $\phi \approx 0.8$ and burner inlet radii of $R_i = 5$ mm), we retrieve a Péclet number of the order $\mathcal{O}(100)$. Hence, all flames can safely be considered as thin flame sheets.

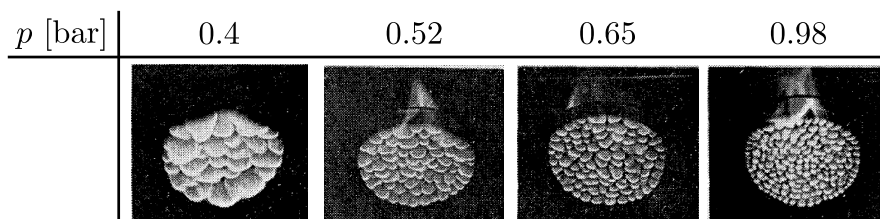


Figure 1.2: Cellular structure of a flat flame for n-butane-air-nitrogen mixtures at four different ambient pressures (photos taken from [44]).

1.1.2 Historical Background

Approximating thin flames as discontinuities separating two flow domains of constant chemical composition and density made an efficient analysis of combustion problems possible. Numerical investigations became affordable and, particularly, the way to analytical studies was paved. Of specific interest was the analysis of freely propagating planar flames in order to retrieve closed analytical expressions for the flame propagation speed, which then allowed for a detailed analysis of flame front dynamics and, particularly, their stability.

The works of Darrieus [26] and Landau [27] were among the first to analytically study the stability of thin planar flame fronts. They regarded the flame as a discontinuity propagating at a constant flame speed s_L with respect to the fresh flow and imposed continuous mass and momentum fluxes through the flame sheet leading to a set of jump conditions

$$\left[\rho \left(u_{\perp} - \frac{\partial \xi}{\partial t} \right) \right]_u^b = 0, \quad \left[p + \rho \left(u_{\perp} - \frac{\partial \xi}{\partial t} \right) u_{\perp} \right]_u^b = 0, \quad [u_{\parallel}]_u^b = 0 \quad (1.7)$$

that connect quantities of the unburned (“u”) to those of the burned (“b”) side of the flame, see also [33, 35]. The squared brackets denote the change of a quantity across the flame front: $[*]_u^b = *_b - *_u$. The first equation results from the conservation of mass, the second and third from the conservation of flame normal (index “ \perp ”) and tangential (index “ \parallel ”) momentum, respectively. Velocities are denoted by the letter u , the density by ρ and the pressure by p . The displacement of the flame from its steady state is given by $\xi = \xi(x, t)$, where x denotes a direction parallel to the flame front and t the time. For a given flame normal flow velocity $u_{\perp} = u_{\perp}(x, t)$, the flame front moves according to $\frac{\partial \xi}{\partial t} = u_{\perp} - s_L$.

Solving a system of linearized Euler equations up- and downstream the flame that are coupled via the jump conditions (1.7), Landau [27] obtained a dispersion relation stating that the growth rate of a flame perturbation increases linearly with wavenumber. That means that flat flames were unconditionally unstable to perturbations of any wave length caused by the density jump imposed at the flame front.

This result, however, is inconsistent with experimental observations reporting that it

is indeed possible to stabilize flat planar flames, see e. g. [44–47]. Further, it is in conflict with observations made by Markstein [44], who showed that a flat flame develops cellular structures whose averaged cell size decreases with rising ambient pressure, see Fig. 1.2. While the theory of Landau [27] predicts a linear increase of growth rate with the wave number, the experimental results of Markstein [44] reported a pressure dependent uniform cell size, which suggests the existence of a pressure dependent maximum growth rate at a wave number approximately corresponding to the observed cell sizes (approximately since the observed cellular structures are already affected by non-linear processes, see [48]).

Noticing that the theory of Landau [27] was restricted to disturbances whose wave length is large compared to the thickness of the flame and that the thickness of a flame decreases with pressure (lower pressure \rightarrow thicker flame \rightarrow larger average size of the cellular structures), Markstein [44] introduced the ad hoc hypotheses of a flame speed that depends on the local flame front mean curvature κ_f :

$$s_L = s_L^0(1 - l_M \kappa_f). \quad (1.8)$$

Here, the Markstein length l_M is computed from the characteristic length of the convective-diffusive layer $\delta_D = \lambda_u / (s_L \rho_u c_{p,u})$ and the Markstein number Ma , which typically is of order unity: $l_M = \delta_D Ma$. Following the ideas of Karlovitz *et al.* [49] and Eckhaus [50], Markstein [33] extended his phenomenological theory by including flow strain as a second source of flame stretch $\kappa_s = 1/A(dA/dt)$ and related it to the Markstein number, as well:

$$s_L = s_L^0 \left[1 - Ma \left(l_c \kappa_f + \frac{1}{s_L} \mathbf{n}_f \cdot \nabla \mathbf{u} \cdot \mathbf{n}_f \right) \right], \quad (1.9)$$

where \mathbf{n}_f is a vector normal to the flame front and $\nabla \mathbf{u}$ the strain rate tensor of the upstream flow.

According to Markstein [44], the lack of knowledge concerning combustion reactions and the reaction-kinetic terms prevented a rigorous derivation of the flame speed relations from first principles. Subsequent studies were able to close this gap and could derive the phenomenological flame stretch terms from first principles, see e. g. [34, 35, 37, 39–41, 51]. These studies are based on the aforementioned matched asymptotic methods exploiting the fact that hydrodynamic length scales are much larger than the length scales of the convective-diffusive boundary layer and the reaction zone. This approach is briefly sketched in the following.

Studies relying on matched asymptotic expansions are based on the consideration of two coupled flow domains of different length scales. The large scale *outer* hydrodynamic model, on the one hand, consists of two incompressible fluid domains coupled via jump conditions at a flow discontinuity representing the flame. The small scale *inner* reaction model, on the other hand, is represented by a low Mach number flow where density depends on temperature only and chemical reactions are usually dominated by a single deficient component (1-step chemistry). Later studies such as the

one by Matalon *et al.* [41] included a 2-step mechanism allowing for consideration of mixtures whose composition varies from rich to lean conditions. The outer and the inner models are matched by assuming that their solutions have to coincide far away from the flame, which results in expressions for the flame speed and the jump conditions. Flame speed relations, as well as the definition of the Markstein number, generally depend on the exact location of the discontinuity with respect to the inner flame structure [37, 41, 52–54]. By constraining the mass flux of the outer solution to be continuous at the discontinuity, Class *et al.* [37] naturally fixed the position of the flame and, thus, the expressions for the flame speed as well as the Markstein number.

All those studies derived jump conditions similar to the one shown in Eq. (1.7), but they extended the analysis by considering higher order terms of the respective expansion parameters. Furthermore, they also obtained expressions for the flame speed that solely rely on macroscopic or combustion intrinsic/thermophysical parameters. For example, Matalon *et al.* [41] specified

$$s_L = s_L^0 \left(1 - \frac{1}{\text{Pe}} Ma \kappa_s \right) \quad (1.10)$$

with a Markstein number

$$Ma = \frac{1}{1 - \hat{\epsilon}} \int_1^{1/\hat{\epsilon}} \frac{\lambda^*(x)}{x} dx + \frac{\text{Ze}(\text{Le}_{eff} - 1) \hat{\epsilon}}{2(1 - \hat{\epsilon})} \int_1^{1/\hat{\epsilon}} \frac{\lambda^*(x)}{x} \ln \left(\frac{1 - \hat{\epsilon}}{\hat{\epsilon}(x - 1)} \right) dx, \quad (1.11)$$

where $\hat{\epsilon} = \rho_b / \rho_u$ denotes the burned to the unburned density ratio, $\lambda^* = \lambda / \lambda_u$ and Le_{eff} the normalized thermal conductivity and the effective Lewis number of the mixture, respectively. The flame speed is hence related to flame stretch κ_s , which is composed of flame curvature and flow strain, via a Markstein number. Therefore, the aforementioned ad hoc hypothesis of Markstein [44] that the flame speed depends on flame curvature could indeed be confirmed by rigorous first-principle-based analyses of the flame internal structure. Once the jump conditions and the flame speed relation is known, a stability analysis of flame sheets can be performed, which results in a dispersion relation. This topic is discussed in more detail in Sec. 1.2.

Various types of flame configurations have been investigated in the literature trying to validate the theoretically retrieved flame speed relations, stability predictions and/or determine flame parameters such as the Markstein length. Most theoretical studies were performed for 2D planar or flat flames since the analysis simplifies for such configurations. Experimental investigations of such flames, however, are not straight forward since stabilization requires an active stabilization loop [47, 55] and/or elaborate ignition methods [44]. Heat losses to nearby walls further complicate the analysis of the results [42].

Hence, many experimental studies focused on different configurations such as spherical bombs. Here, a mixture of fuel and oxidizer is ignited by a spark that causes a radially expanding deflagration front. In order to ensure a negligible increases of the pressure in the combustor during the combustion process, the volume of the combustion chamber of the test rig has to be large compared to the one of the burned

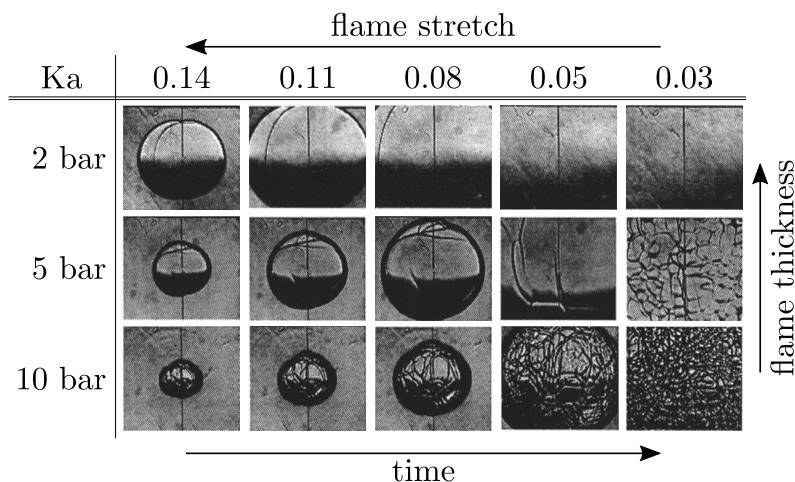


Figure 1.3: Snapshots of spherically expanding stoichiometric propane/air flames (spherical bombs) for three different ambient pressures at a Lewis number close to unity. The snapshots compare instants in time of the same non-dimensional stretch rate, defined by the Karlovitz number Ka (snapshots are taken from [62]).

mixture. Advantages of such test rigs are the relatively simple adjustment of experimental parameters such as pressure and temperature of the mixture, the absence of initial turbulence in the unburned fluid and a well defined and uniformly distributed flame stretch [56, 57]. In particular, the latter property qualifies these configurations for measurements of Markstein numbers and laminar flame speeds [58–61], as well as for the assessment of flame front instabilities.

Fig. 1.3, for example, shows experimental results of Kwon *et al.* [62]. They investigated the development of spherically expanding stoichiometric propane/air flame at three ambient pressures. By variation of pressure, they changed the flame thickness (higher pressure \rightarrow thinner flames), while all other parameters influencing flame stability were kept approximately constant. The higher the ambient pressure and, thus, the thinner the flame, the less stable the expanding flame front becomes: Similarly to the experimental results of Markstein [44] shown in Fig. 1.2, a lower pressure increases stability and successively less “cracks” – indicating the formation of growing cellular structures – are visible in Fig. 1.3 comparing the 10 bar, 5 bar and the 2 bar series of snapshots.

Finally, aerodynamically anchored flames such as Bunsen or Slit flames constitute another important flame configuration of high technical relevance. Since for such flames local displacements are convected downstream, flame instabilities cause spatially growing displacements, as depicted in experiments carried out by Searby *et al.* [63] and reproduced in Fig 1.4. Several studies have analyzed such configurations and found that, besides the advection of flame front displacements and the existence of

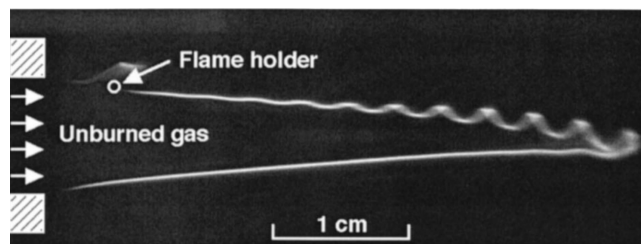


Figure 1.4: Snapshot of an aerodynamically anchored and inclined rich propane/air/oxygen flame whose base is displaced by a vibrating flame holder (taken from [63]).

a flame anchoring and tip, the dynamics of anchored and inclined flames essentially corresponds to the one of the planar counterpart, i. e. the same instability mechanisms are present [45, 64–66]. Such type of flames are investigated within the scope of this thesis. Formally, they will only be introduced in the following chapter.

Having solved the linear stability problem of planar flames for many canonical configurations, the next step was to assess the process of non-linear saturation. For this purpose, on the one hand, Navier-Stokes based simulations treating the flame as a gas dynamic discontinuity [67–70] have been performed. On the other, a low-order weakly non-linear flame model, known as the Michelson-Sivashinsky (MS) equation, has been introduced [38, 48, 71]. It has been proven to be a valuable tool for the prediction of the onset of hydrodynamic instabilities and their fully non-linear development [67]. The dynamics of the MS equation on a finite domain of width L is controlled by a reduced Markstein number $\alpha_M = l_M / (\rho_u / \rho_b - 1)L$. For sufficiently small values of this parameter, short wave length flame front displacements perpetually coalesce forming bigger and bigger structures until, eventually, a stable single peak solution is reached [72]. This process is illustrated in Fig. 1.5 where a randomly perturbed flame sheet (top line) develops into a stable cusp (bottom line), which continues to propagate at a constant speed [67].

Instabilities, such as the ones described above, are responsible for many crucial and practically relevant flow phenomena and often result in characteristic large-scale coherent structures. There are, for example, the widely known Kelvin-Helmholtz instability or the Tollmien–Schlichting waves. Both lead to the formation of flow features that have several important consequences for technical applications, such as pipe flows or the flow around airplane wings. Accordingly, stability considerations have made their way to the analysis of flames in a thermoacoustic context, as well. Here, technically relevant setups often rely on swirl-stabilized turbulent flames. One important feature of these flames is a precessing vortex core that responds to acoustics and significantly interacts with the combustion process [73–75], another the occurrence of a so-called vortex breakdown [76–78]. Both mechanisms are related to flow field instabilities and essentially determine the flame response to acoustic perturbations. Exploiting this principal finding, Oberleithner *et al.* [79] and Oberleithner

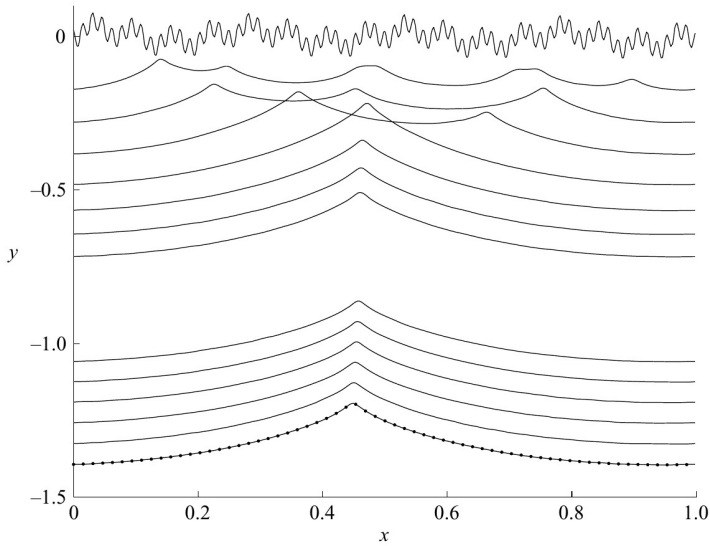


Figure 1.5: Temporal evolution of a randomly perturbed flame sheet according to the MS equation for $\alpha_M = 0.005$. Several snapshots of the same flame front at different times are shown, where time progresses from the top to the bottom line (taken from [67]).

and Paschereit [80] developed a method that is capable to adequately predict the frequency and amplitude dependent flame response based on a linear stability analysis of the underlying mean flow. It can hence be concluded that the understanding and consideration of the relevant instability mechanisms constitutes one important prerequisite in order to correctly interpret and model the complex flow behavior of both laminar and turbulent flames.

The dynamics and stability of thin flame fronts has historically been classified according to a variety of non-dimensional numbers. The Markstein number has already been mentioned above and quantifies the effect of stretch (curvature and flow strain) onto the flame speed. It usually is of order $\mathcal{O}(1)$, and large positive Markstein numbers indicate stable flames. Note that its definition depends on the assumed location of the gas dynamic discontinuity representing the flame with respect to the inner flame structure. Often it is assumed that it coincides with the reaction layer, see e. g. [52]. A second important number is the Lewis number Le , which relates the thermal to the mass diffusivity of the deficient species relative to the mixture [81]. The experimental data shown in Fig. 1.3 was obtained at unity Lewis number. The fact that thermal and mass diffusion are approximately equal prevents the occurrence of thermo-diffusive and pulsating instabilities. The former will be discussed in Sec. 1.2.2. Another important non-dimensional number is the Karlovitz number, which quantifies flame stretch:

$$Ka = \frac{2\delta_f}{s_L^0 R_f} \frac{dR}{dt}, \quad (1.12)$$

where R_f is the flame radius, t the time, δ_f the flame thickness and s_L^0 the unstretched flame speed. The snapshots of the spherical bombs shown in Fig. 1.3 are taken at distinct Karlovitz numbers for all three pressure levels. As mentioned above, stretched flames are less prone to develop instabilities than unstretched ones. An expanding spherical flame increases its radius and, hence, the flame front is exposed to successively decreasing stretch. By comparing snapshots of constant Ka, the effect of different pressure dependent stretch levels on stability can be eliminated.

Finally, flames usually propagate in the gravitational field of the earth. For flames whose associated flow direction points upwards (heavy unburned mixture below light burned products), gravity tends to stabilize perturbations of long wave lengths [82, 83]. The impact of gravity relative to the flame speed is given by a Froude number $Fr = s_L^2 / (g\delta_f)$ with the gravitational acceleration g . As pointed out by Searby and Clavin [82], for a given mixture there exists a critical value of the Froude number Fr_c below which planar flames are unconditionally stable. The wave length of the perturbations that become unstable at Fr_c is large compared to the flame thickness [82]. The effect of gravity together with the effect of flame curvature explains why it is possible to experimentally implement stable planar flame fronts [44, 82]. Flames with a flow streaming downwards (light burned products below heavy unburned mixture) are destabilized by the Rayleigh-Taylor instability [84].

1.2 Mechanisms Governing Flame Propagation

In the previous section it was shown that the representation of a flame as a propagating discontinuity connecting the unburned with the burned flow domain by means of jump conditions provides an efficient tool for understanding and modeling the dynamics of thin flame sheets. First principle-based expressions for the propagation speed as well as jump conditions could be derived by means of matched asymptotic expansion techniques. While the latter ensure the conservation of mass, normal and tangential momentum across the flame, the former emerges as a consequence of chemical kinetics combined with the energy and species transport. One important outcome of this kind of analysis is that the local flame speed depends on flame stretch, i. e. flame curvature and flow strain.

Coupling two incompressible flow domains of different densities using aforementioned jump conditions and flame speed relations results in an powerful framework for the analysis of the dynamics of thin flame sheets. Its main advantage consists in the fact that the chemical details of the combustion process need no longer to be considered and, thus, the focus is shifted to macroscopic quantities, such as the flame speed or the flame shape. This method consequently brings order into the complex field of flame propagation and allows to differentiate between well-defined intuitively accessible governing mechanisms.

The within the scope of this thesis four most important mechanisms are discussed in

the following. Each one is in a first step formally introduced and subsequently its implications are illustrated by analyzing how it affects the dynamics of a perturbed flame sheet. Section 1.2.1 deals with the most elementary mechanism of flame propagation, namely the fact that flame sheets propagate normal to themselves. Section 1.2.2 analyzes thermal-diffusive mechanisms that address implications of the flame speed relation onto flame sheet propagation. This is followed by an analysis of hydrodynamic mechanisms, which arise as soon as two flow domains of different densities are coupled via jump conditions. Finally, Sec. 1.2.4 deals with flame sheets that are inclined with respect to the mean flow field, e. g. by anchoring them. Here, in addition to the former mechanisms, the advection of flame front perturbations becomes important.

1.2.1 Propagation Normal to Itself

1D simulations, as the one shown in Fig. 1.1, reveal that a (thin) reaction zone propagates into the domain of the fresh mixture at a certain speed. The velocity of the mean flow field far upstream of the flame that is required to maintain the flame front at a fixed position is referred to as the flame speed s_L in the following. Note that, theoretically, also other definitions of s_L are possible, such as the flow speed far downstream of the reaction zone. Since the properties of the fresh mixture are the ones that are set by an experimentalist or at a numerical simulation, it is convenient to define s_L with respect to them.

Knowing how a 1D flame propagates, we are now interested in the transient behavior of a flame sheet, where each point on this sheet propagates at a constant speed s_L . Without loss of generality, we approach this problem by assuming a 2D sheet that has at a time t_0 the shape as depicted by the black line in Fig. 1.6a. Since a point of that line propagates at a speed s_L , its position at a time $t_0 + \Delta t$ has to be somewhere on a circle of radius $\Delta t s_L$ drawn around the current position. This has to hold for each point on the black line and, therefore, the flame front position at $t_0 + \Delta t$ can only be given by the upstream envelope of all circles, depicted by the red line in Fig. 1.6a. From this consideration, which is also known as Huygens's principle, it naturally evolves that a flame propagates normal to itself.

One important consequence of this mechanism is the formation of cusps, which are perturbations of the flame front of discontinuous slope. Following Huygens's principle, it can be shown that such non-smooth flame shapes develop from an initially smooth flame front, which is concavely bent towards the fresh fuel mixture [85]. Since flame fronts propagate normal to themselves, the position of the flame sheet at later times can be estimated by rays drawn normal to the current flame front position, see Fig. 1.6a (---). These rays will eventually intersect and, hence, one side of the initially smooth flame wrinkle propagates into the opposing front, which leads to the generation of cusps and to a propagation of the tip of the wrinkle in the direction of the unburned gases with a speed faster than the flame speed [86]. This process is

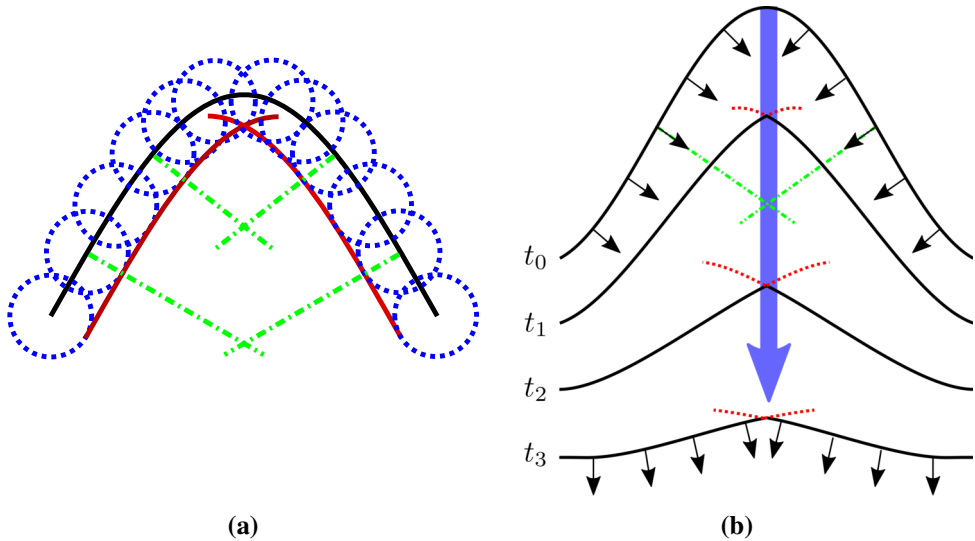


Figure 1.6: Illustration of Huygens's Principle (1.6a), which explains the formation of cusps from an initially smooth flame front (1.6b).

illustrated for four instants in time in Fig. 1.6b (blue arrow). On the contrary, convex parts of a flame sheet will expand and heal themselves from eventual cusps [86].

It is interesting to note that the formation of cusps constitutes a non-linear mechanism that leads to saturation of high amplitude perturbations, particularly for high wave numbers. Further, it is not symmetric since convex displacements are smoothed out, while concave ones form sharp edges. Hence, as pointed out by Sivashinsky [38], Landau [27] eliminated a major stabilizing mechanism by linearizing all of the equations. This argument partly resolves Landau's paradoxical prediction of unconditionally unstable flame fronts. This becomes more clear when considering the fact that Clanet and Searby [55] were the first to experimentally measure and visualize the growth of planar flame front perturbations due to the Darrieus-Landau instability as late as 1998. All previous studies on planar flames only measured cellular structures that were already non-linearly saturated and, hence, subjected to the mechanism described above.

This thesis is devoted to the study of the linear response of acoustically perturbed flames. The non-linear mechanism described above leads to the formation of very characteristic flame shapes that exhibit sharp edges at concave and smooth fronts at convex parts of a flame sheet. Hence, it provides a simple tool to estimate if the response of a flame is still in the linear regime or if non-linear processes have already started to become significant.

1.2.2 Thermal-Diffusive

So far it was assumed that all points of a flame sheet propagate at a constant speed. Theory, however, predicts that this speed depends on the local flame stretch $\kappa_s = 1/A(dA/dt)$, i. e. the normalized rate of change of the local flame surface area. Flame stretch has its origin in flame curvature and flow strain. Since the related processes are governed by thermal as well as mass diffusion of a deficient species, their consequences for the flame dynamics are attributed to the so-called thermal-diffusive (or also thermodiffusive) mechanism.

The decisive parameter for this mechanism is the Lewis number, which relates the thermal to the mass diffusivity of the deficient species¹. It allows to distinguish between several distinct regimes of flame propagation: The first consists of mixtures whose mass diffusivity of the deficient component with respect to the mixture is significantly higher than the thermal one. Those flame fronts exhibit thermal-diffusive instabilities that cause strongly corrugated flame surfaces. One example for such mixtures are lean hydrogen-air flames, e. g., $Le \approx 0.4$ for $\phi = 0.6$ [87]. The second regime is defined by mixtures with a Lewis number close to one, such as lean methane-air flames ($Le \approx 1$ [88]), as considered in this work. Conditions with $Le > 1$ are usually observed in lean mixtures of heavy fuels (e. g. propane/air [88]) or rich mixtures of light fuels, as well as for combustion in porous media (blocked mass and enhanced thermal diffusion) or for solid propellants [89]. These high Lewis number flames show a third type of instability not considered in this work, the so-called pulsating instability. It is expected to occur for $Ze(Le - 1) \gtrsim 10$ and is — since it results from a thermal-diffusive mechanism — affected (enhanced) by flame stretch [48, 90–93].

In order to suppress hydrodynamic mechanisms, which will only be discussed in the next section, it is assumed that the density of the flow does not change across the flame. That way consequences of thermal-diffusive mechanisms can efficiently be studied. In order to maintain chemical reactions inside a flame, on the one hand, heat has to diffuse from the reaction zone into the fresh mixture and, in doing so, preheat it to a temperature where the (fast) combustion processes can take place. On the other hand, the deficient component is diffusively transported from the unburned mixture to the reaction zone — i. e. methane molecules in the case of a lean methane-air flame. Both diffusive processes together with the kinetics of the reaction define a laminar unstretched flame speed, which depends on temperature, pressure and equivalence ratio of the fresh gases, see e. g. [94].

If now the flame front is perturbed as illustrated in Fig. 1.7, from a geometrical point of view, the heat released at regions that are convex towards the fresh mixture has to heat up more cool reactants than in concave ones. Hence, more heat is carried away

¹Later studies relying on a matched asymptotic expansion technique analyzed a two-step instead of a one-step chemical scheme, see Matalon *et al.* [41]. They introduced an effective Lewis number, which is a weighted sum of the Lewis numbers of the individual species. This extension of the theory shall not be considered here.

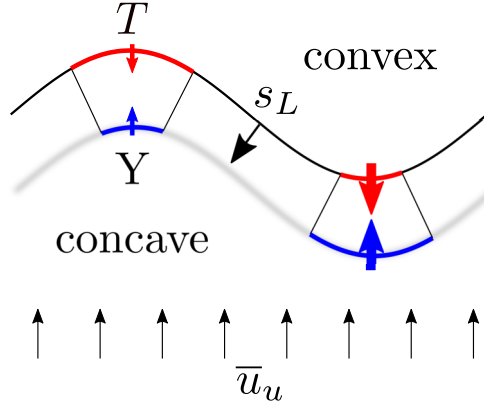


Figure 1.7: Illustration of the thermal-diffusive flame instability mechanism. Temperature fluxes are marked in red, mass fluxes of the deficient species in blue.

from the reaction zone in convex regions, which therefore cool down and propagate at lower speeds than the unperturbed flame. On the contrary, heat accumulates in concave regions, an effect that increases the local flame speed. Since the flow speed is constant everywhere (we presently assume constant density across the flame front!), perturbations of the flame sheet will be damped by this mechanism. At the same time, however, mass diffusion of the deficient component is enhanced in convex and attenuated in concave regions for analogous reasons as explicated above for temperature. This increases the flame speed in convex and decreases it in concave regions and, therefore, has exactly the reverse effect of temperature diffusion: flame sheet perturbations are further amplified. Depending on the Lewis number either one or the other mechanism dominates. At a critical Lewis number $Le_{c,TD}^0$ both effects cancel each other and the flame sheet is marginally stable, that is (small) perturbations neither grow (unstable) nor do they asymptotically decay (stable). An increase of mass — or decrease in heat — diffusivity leads to $Le < Le_{c,TD}^0$ and, therefore, to an unstable flame sheet. Conversely, a reduction of mass — or increase in heat — diffusivity causes $Le > Le_{c,TD}^0$ and, thus, a stable flame sheet.

This phenomenon was analytically analyzed for flows of constant density by Sivashinsky [90]. Assuming an inviscid flow up- and downstream the flame sheet, a dispersion relation

$$\sigma = \underbrace{D_{th} \left[\frac{Ze}{2} (1 - Le) - 1 \right] k^2}_{\text{long-wave disturbances}} - \underbrace{4D_{th}\delta_D^2 k^4}_{\text{short-wave correction}} \quad (1.13)$$

was derived relating a growth rate σ to a wave vector k . Harmonic perturbations of the flame sheet develop in time according to $\exp(\sigma t + i k x_1)$. Thus, positive growth rates correspond to unstable, negative ones to asymptotically stable regimes. A growth rate of zero corresponds to a marginally stable flame sheet. Neglecting the correction term

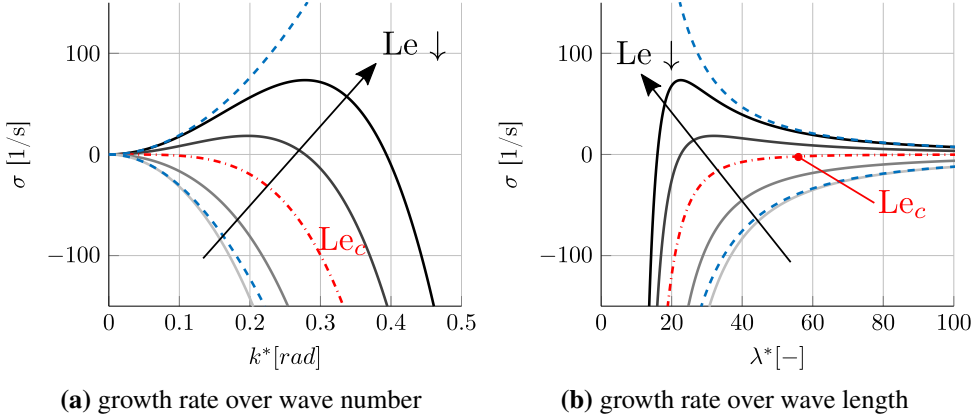


Figure 1.8: Dispersion relation of Eq. (1.13) for the thermal-diffusive instability mechanism plotted over non-dimensional wave number (1.8a) and wave length (1.8b) for several Lewis numbers $Le \in [0.5, 1]$. The one for $Le_{c,TD}^0 \approx 0.7$ is highlighted in red (-.-.-). Additionally, for the two shown extreme Lewis numbers dispersion relations neglecting the short-wave number correction term are plotted (-.-.-).

in Eq. (1.13), one can compute a critical Lewis number $Le_{c,TD}^0 = 1 - 2Ze^{-1}$ for which the growth rate is at maximum zero, i. e. $\sigma \leq 0, \forall k$. The short-wave correction in Eq. (1.13) accounts for the fact that perturbations with a wave length that is of the order of the preheat zone thickness δ_D are damped by diffusion since boundary layers of two adjacent flame wrinkles overlap and merge.

Using Eq. (1.13), dispersion relations such as the one shown in Fig. 1.8 are retrieved. Fig. 1.8a shows the growth rate over the non-dimensional wave number $k^* = k\delta_D$ and Fig. 1.8b the one over the non-dimensional wave length $\lambda^* = \lambda/\delta_D$. By using the flame thickness δ_D as reference length, it is recognized that wave lengths of the order $\mathcal{O}(\delta_D)$ are damped (i. e. the growth rate is negative) for all Lewis numbers shown. The dispersion relation corresponding to the critical Lewis number $Le_{c,TD}^0$ is highlighted in red (-.-.-). Dispersion relations of higher and lower Lewis number, respectively, are shown by the gray lines (darker shades correspond to lower Le). The blue dashed line (-.-.-) corresponds to the two extreme Le cases neglecting the short-wave correction term.

The critical Lewis number evaluates to $Le_{c,TD}^0 \lesssim 0.8$ for lean methane-air mixtures. Since such flames have Lewis numbers of approximately unity, thermal-diffusive mechanisms do not lead to a growth of flame front perturbations, but rather dampen existing ones. Hence, they stabilize a flame front by damping existing disturbances, which is especially important when considering that hydrodynamic mechanisms resulting from a change of density across the flame always have a destabilizing effect. They counteract each other, as will be shown in the following section.

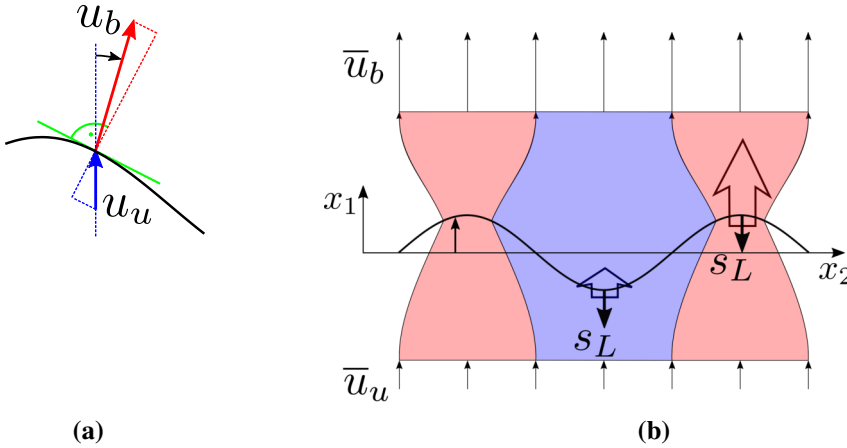


Figure 1.9: (a): Since the flow across the flame front is accelerated in flame normal direction, velocity vectors are bend towards the flame normal direction downstream a flame. (b): Illustration of contracting (red) and expanding (blue) flow tubes due to a displaced flame front, which explain the occurrence of the Darrieus-Landau instability.

1.2.3 Hydrodynamic

As discussed in Sec. 1.1, according to the seminal work of Darrieus [26] and Landau [27], a change in density across the flame sheet destabilizes planar flames for perturbation wave lengths that are much longer than the flame thickness. In honor of its two discoverers, this instability is referred to as the Darrieus-Landau (DL) instability in the literature. The intensity of this mechanism is proportional to the prevailing density change across the flame sheet, which is quantified by the non-dimensional increase of specific volume

$$E = \frac{\rho_u}{\rho_b} - 1. \quad (1.14)$$

The first term in this expression is also referred to as the expansion ratio $e = \rho_u/\rho_b$. Since all flames covered in this thesis produce a significant change in density of $E \approx 5.7$, it can be expected that the DL mechanism plays an important role for their dynamics.

Before assessing the problem analytically, a qualitative description shall be provided. A planar, perturbed flame front stabilized in a uniform flow, as shown in Fig. 1.9b is assumed. Due to the density jump across the flame front, the upstream flow u_u is accelerated in flame normal direction, as illustrated in Fig. 1.9a. The tangential component stays constant. This leads to a bending of the flow vector towards the local flame normal direction. Consequently, in regions where the flame front is concave towards the fresh mixture, the flow tubes are contracted, while they expand in con-

vex ones. This is illustrated in Fig. 1.9b by red (contraction) and blue (expansion) flow tubes. Assuming that the flame speed is not affected by stretch, in red regions, the local flow speed will outweigh the flame speed and the flame front is transported further downstream. This will lead to an increase in amplitude of the flame displacement. In blue regions, the reduced flow speed will lead to an upstream propagation of the flame front, which also increases the displacement amplitude. Hence, flames sheets imposing a density jump are prone to a hydrodynamic kind of instability. This mechanism will be assessed analytically in the following.

Assuming inviscid Eulerian flow equations up- and downstream of the flame

$$\frac{\partial u_j}{\partial x_j} = 0 \quad (1.15)$$

$$\frac{\partial u_i}{\partial t} + u_j \frac{\partial u_i}{\partial x_j} = -\frac{1}{\rho} \frac{\partial p}{\partial x_i}, \quad (1.16)$$

inserting harmonic perturbations of the form $\exp(\sigma t + i k x_1 \pm k_x 2)$ for all flow states and coupling both domains by use of the jump conditions of Eq. (1.7), one retrieves a dispersion relation

$$\sigma = \Omega_0 s_L k \quad (1.17)$$

with the Darrieus-Landau parameter

$$\Omega_0 = \frac{\sqrt{e^3 + e^2 - e - e}}{e + 1}. \quad (1.18)$$

This is the classical result obtained by Landau [27] and Darrieus [26] and predicts that flame sheets are unconditionally unstable to perturbations of all wave lengths, since $\Omega_0 \geq 0$. In particular, the growth rate linearly increases with k and, thus, shorter wave lengths are more amplified than longer ones. Based on this result, one would expect that planar flames always develop high frequency oscillations that rapidly grow in amplitude until non-linear effects lead to saturation [42].

It was already mentioned in Sec. 1.1.2 that such a behavior could not be observed experimentally. Instead, planar flames form a cellular structure of a certain wave-length, which suggests the existence of a maximum growth rate at this wave length (or close to it, since the amplitude of the observed cellular flame structure is finite and, therefore, non-linear effects have already lead to a saturation). Markstein suggested a phenomenological correction by relating the flame speed to the local flame sheet curvature multiplied by a factor l_M , see Eq. (1.8). This factor is called the Markstein length and is of the order of the thickness of the convective-diffusive layer of a flame. It lumps the effects of various transport processes inside the flame as well as those concerning the kinetics of the chemical reaction into one single parameter. Physically, flame stretching effects result from interactions of the external hydrodynamic field and the inner flame structure, which leads to convective fluxes along the flame redistributing heat and species. This affects the local reaction rates and thus the

flame speed [42]. According to Zeldovich *et al.* [42], introduction of a curvature dependent flame speed is analogous to the introduction of a stabilizing surface tension at the flame front.

The solution of Darrieus and Landau is asymptotically valid for Péclet number $Pe = L/\delta_D$ approaching infinity. Hence, the Darrieus-Landau model is a proper approximation in the limit of very long wave lengths. Stated differently, expanding all state variables using the small parameter $1/Pe$, it is the zeroth order approximation of the flow problem. The extension of Markstein is then a first order correction of that model in the limiting case of high activation energies of the global reaction [42]. It is interesting to note that this first order correction only affects the flame speed and not the jump conditions of Eq. (1.7). This can be explained by the strong dependency of the flame speed to temperature for high activation energy global reactions [42].

Later studies could derive expressions for the flame speed from first principles using matched asymptotic expansion methods. They included also effects of terms that are of first or higher order in $1/Pe$ and considered different Lewis and Zeldovich numbers. Since these theories capture effects of diffusive and convective fluxes along the flame front and, hence, flame stretch related effects, those studies do not strictly separate thermal-diffusive and hydrodynamic mechanisms. Indeed, they capture the net effect of both mechanisms. Particularly, Frankel and Sivashinsky [95] and Pelce and Clavin [40] derived a dispersion relation accounting for hydrodynamic effects as well as for heat conduction and mass diffusion:

$$\sigma = \Omega_0 s_L k - \Omega_1 D_{th} k^2 \quad (1.19)$$

with

$$\Omega_1 = \frac{\hat{e}(1 - \hat{e})^2 - \hat{e} \ln(\hat{e}) (2\Omega_0 + 1 + \hat{e}) - \hat{e}(1 + \Omega_0)(\hat{e} + \Omega_0) \text{Ze}(1 - \text{Le}) \int_0^E \frac{\ln(1+\tilde{x})}{\tilde{x}} d\tilde{x}}{2(1 - \hat{e}) [\hat{e} + (1 + \hat{e})\Omega_0]}, \quad (1.20)$$

where $\hat{e} = \rho_b/\rho_u$ denotes the inverse of the expansion ratio. Viscosity, responsible for diffusion of momentum and quantified by the Prandtl number in the non-dimensional framework, was found to have only a secondary effect on flame stability and, thus does not show up here [48, 95]. This is surprising, since it usually is of the same order of magnitude as thermal and mass diffusivity. And, indeed, the more recent study of Matalon [83] showed that, if viscosity is allowed to vary across the flame sheet, it has an effect on flame stability which is equal to the one imposed by other diffusive processes. Its impact is proportional to the Prandtl number and always has a stabilizing effect.

For $\Omega_1 > 0$ the flame is thermo-diffusively stable and vice versa for $\Omega_1 < 0$. Based on this criterion, one can derive a critical Lewis number for which $\Omega_1 = 0$ holds. For $E = 0$ this coincides with the critical Lewis number $\text{Le}_{c,\text{TD}}^0$ derived in Sec. 1.2.2. It is interesting to note that the critical Lewis number $\text{Le}_{c,\text{TD}}$ computed from Eq. (1.20) decreases for increasing E , see Fig. 1.10 (top). Hence, gas expansion effects extend the

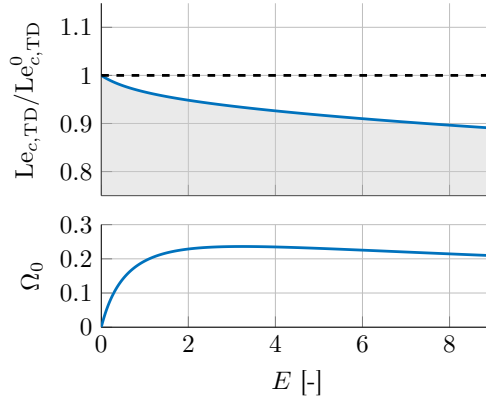


Figure 1.10: Darrius-Landau parameter Ω_0 and critical Lewis number for the onset of thermal-diffusive instability $Le_{c,TD}$ plotted over non-dimensional increase of specific volume. All thermophysical parameters are taken from a lean methane-air mixture.

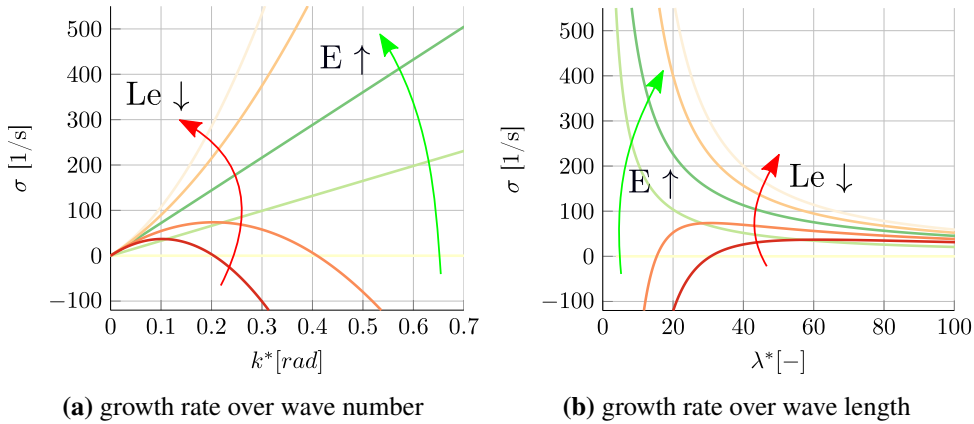


Figure 1.11: Growth rate according to Eq. (1.13) for the hydrodynamic instability mechanism plotted over non-dimensional wave number (1.8a) and wave length (1.8b) for several Lewis numbers and non-dimensional density increases: red lines visualize effect of a varying Lewis number for $E = 6$ and green lines the respective effect of the density jump for $Le = Le_c$

range of stability against thermal-diffusive driving mechanisms. Fig. 1.10 (bottom) shows how Ω_0 behaves for an increasingly strong density jump. A steep increase up to $E \approx 2$ can be observed, which is followed by a saturation and even a slight decrease towards very high E . Hence, one must conclude that the Darrius-Landau mechanism is most dominant for a non-dimensional increase of specific volume of $E \approx 3.2$ and is even slightly reduced towards higher E .

Fig. 1.11a shows the growth rate over non-dimensional wave number as defined by Eq. (1.19). Fig 1.11b shows the same result but this time plotted over wave length.

The green lines visualize the impact of the strength of the density jump alone, since for each E exactly the corresponding critical Lewis number $Le_{c,TD}$ is chosen. A higher non-dimensional increase of specific volume hence leads to a steeper slope of the dispersion relation plotted over k^* , which however saturates around $E \approx 3$ and then slightly decreases. The slope directly follows the trend of Ω_0 shown in Fig. 1.10 (bottom). The red lines visualize how Lewis number affects the dispersion relation for a fixed non-dimensional increase of specific volume of $E = 6$. Lewis numbers larger than the critical one, lead to parabolic dispersion relations, which intersect the zero growth rate line at a critical wave number. Further, they exhibit a certain wave number of maximum growth. Decreasing the Lewis number below its critical value leads to a superposition of thermal-diffusive and hydrodynamic instability mechanisms and, therefore, to a dispersion relation of increasing slope for $k^* \rightarrow \infty$.

Summarizing, all flame fronts are subject to a destabilizing hydrodynamic mechanism since combustion is associated with exothermic reactions, which always lead to an increase in specific volume. Depending on the Lewis number, thermal-diffusive mechanisms may either stabilize a flame front ($Le > Le_{c,TD}^0$) or further destabilize it ($Le < Le_{c,TD}^0$). The stabilizing effect of this mechanism increases with expansion ratio.

1.2.4 Advection of Perturbations at Inclined Flames

So far only freely propagating flame sheets far away from any boundary were analyzed. Such flames are however of no relevance for thermoacoustically driven combustion instabilities, since they allow not for continuous operation. Therefore, the flame sheet has to be anchored such that it stays at a fixed position. One example of such a device is a Bunsen burner, where the flame is anchored at the burner rim. In this chapter, any additional effects of the anchoring shall be excluded from the analysis and only the behavior of the flame sheet far away from this point shall be of interest. It should be noted that the advection of perturbations along an inclined flame sheet is ultimately only a consequence of the fact that flames propagate normal to themselves and the imposed anchoring of the flame. Nevertheless, it constitutes an important mechanism, which is not obvious. Therefore, it is treated as a distinct mechanism here.

Fig. 1.12 shows a sketch of such a flame sheet. The fresh gases stream along the vertical x_1 axis by a mean flow velocity \bar{u}_1 until they eventually reach the flame sheet that burns at a constant speed s_L^0 . From geometrical considerations, the angle between flame the sheet and the velocity \bar{u}_1 is computed as $\alpha^* = \sin(\alpha) = s_L^0 / \bar{u}_1$, with the non-dimensional flame angle α^* . At $\alpha^* = 1$ the flame speed equals the flow velocity and the flame propagates normal to the fresh flow. For $0 < \alpha^* < 1$, the flame sheet propagates slower than the flow field and hence it can only be stabilized at an angle $\alpha < 90^\circ$. One important consequence of such an inclination is that perturbations of the flame front are advected downstream by a velocity $\bar{u}_\parallel = \bar{u}_1 \cos(\alpha)$, which is the to the

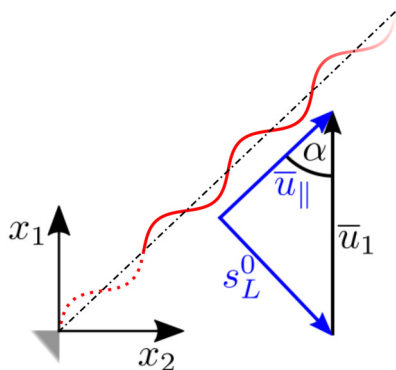


Figure 1.12: Sketch of an anchored and perturbed flame sheet that is inclined by an angle α with respect to the flow velocity of the fresh mixture.

mean flame sheet projected flow velocity \bar{u}_1 [45, 65]. In terms of the non-dimensional flame angle it writes $\bar{u}_\parallel = \bar{u}_1 \sqrt{1 - (\alpha^*)^2}$.

In summary, the main property of inclined flames is that perturbations of the flame sheet are advected along the mean flame front at a velocity \bar{u}_\parallel . How does this interfere with the three other mechanisms explicated in Secs. 1.2.1–1.2.3? Let us for now assume that all of the so far mentioned mechanisms are simply superimposed. Then, flame front displacements of growing amplitude — either driven by a hydrodynamic or a thermal-diffusive mechanism — would be advected downstream along the mean flame front by a velocity \bar{u}_\parallel . Consequently, the originally absolutely unstable flame sheet is now convectively unstable and the growth of flame wrinkles becomes a spatial — instead of a temporal — phenomenon [66, 96].

One might now wonder if the preceding assumption of a perturbation growth rate that is invariant to changes in the flame angle α was too naive. In this regard, Petersen and Emmons [45] experimentally showed that inclined flames indeed exhibit a spatial growth of flame front perturbations that could be associated with the Darrieus-Landau mechanism. They found that, depending on the equivalence ratio, stable or unstable flame sheets could be established. The unstable cases are split into two groups: Those that develop growing flame displacements at a natural frequency without any forcing and those that are stable, but show growing disturbances when the anchoring position is displaced harmonically at a certain frequency. Assuming that the observed natural frequency approximately corresponds to the wave number where the dispersion relation predicts a maximum growth rate, it is possible to compute a corresponding Markstein length, see Fig. 1.11a for a qualitative example of such a dispersion relation. A second method to estimate the Markstein length relies on data gathered from the setup with a forced flame anchoring. By assuming that the lowest forcing frequency, where the flame sheet does not respond, corresponds to the critical wave number (zero growth rate) of the dispersion relation, a Markstein length can be computed. Both methods yielded similar results, which cross-validates the individual

methods.

Therefore, the hydrodynamic and thermal-diffusive mechanism presented in Sec. 1.2.3 are also relevant for anchored flames. This was further confirmed by subsequent studies [63, 64, 66]. Of particular interest is the work of Searby *et al.* [63], who studied the dynamics of stable Bunsen-type flames (no natural oscillations) whose flame anchoring is harmonically displaced by a movable wire. As already reported by Petersen and Emmons [45], this leads to the occurrence of advected flame front perturbations of growing amplitude. For such a situation, Searby *et al.* [63] compared experimental results to predictions of a modified version of the so-called Michelson-Sivashinsky (MS) equation [38, 71]. This kind of equation exhibits a dispersion relation as discussed in Sec. 1.2.3 and, additionally, includes non-linear terms accounting for the mechanisms discussed in Sec. 1.2.1. Searby *et al.* [63] further extended this equation by adding flame parallel advection as described in this section. This new equation now covers all of the four modes of flame propagation introduced above. Very good agreement between this model and the experimental data was found — even for the non-linear saturation process. That means, everything learned by studying downward propagating planar flames should indeed be important to understand the dynamics of inclined flames.

1.3 Low-Order Models

So far an overview of the physical mechanisms governing the dynamics of planar thin flames has been provided. In order to model the propagation of arbitrary flame sheets, several methods were developed — the MS equation, as one example, has already been mentioned.

Another one is the so called level-set or G-equation approach. It is one of the most important and wide-spread methods applied in the field of flame front stability analysis and thermoacoustics. Besides this, it has also found application in many other disciplines such as crystal growth [97], multi-phase flows [98] or reachable set computations [99]. Other than the MS equation, the G-equation approach inherently neglects the hydrodynamic mechanism described in Sec. 1.2.3 and, therefore, does not take into account any flame-flow feedback. In its most basic form, it only fulfills the kinematic relation explicated in Sec. 1.2.1 stating that flame fronts propagate normal to themselves. Often it is supplement by introducing a curvature-dependent flame speed, which then also respects the thermal-diffusive mechanisms for $Le \gtrsim Le_{c,TD}^0$ and no flow strain, as outlined in Sec. 1.2.2. By coupling the G-equation approach additionally with an (incompressible) flow solver using jump conditions or a comparable approach, also the hydrodynamic mechanisms can be captured [100–104].

The basic 2D G-equation approach of an inclined flame sheet can be mapped to a 1D problem, which results — after linearization — in a simple advection-diffusion equation. This equation serves as a basis for most of the available analytically solvable

low-order models of acoustically perturbed flame fronts. Just like the G-equation, it only captures the basic kinematics of a flame sheet, including advection and a curvature-dependent flame speed. It is important to note that it specifically excludes any flame-flow feedback and, hence, the hydrodynamic mechanism of Sec. 1.2.3.

In the following, firstly the level-set or G-equation approach is introduced in Sec. 1.3.1, before the aforementioned 1D advection-diffusion equation is derived from it in Sec. 1.3.2.

1.3.1 Level-Set or G-Equation Approach

Based on the early works of Darrieus [26] and Landau [27], Markstein [33] was the first to introduce a partial differential equation (PDE) in space and time to model the dynamics of a scalar field whose zero iso-line is identified with the gas dynamic discontinuity representing the flame front. The PDE he provided represents the flame as a front that propagates normal to itself at a velocity s_L with respect to a given unburned flow field just ahead of it. To the best knowledge of the author, Williams [105] was the first to use the letter “G” as representation for said scalar field. Presumably since then, the governing PDE is also known as the G-equation. It should be pointed out that the G-field itself has no physical meaning and is just a tool to track the flame front.

As already mentioned, the flame front is represented by the iso-line/-surface $G(x_i, t) = 0$. Regions of $G < 0$ represent the unburned mixture and those of $G > 0$ burned products. The flame normal direction, pointing towards the hot products, is computed from

$$n_{f,i} = \frac{\partial G}{\partial x_i} / \sqrt{\frac{\partial G}{\partial x_j} \frac{\partial G}{\partial x_j}} \quad (1.21)$$

using the Einstein summation convention. The total derivative of the G-field has to satisfy

$$\frac{dG}{dt} = \frac{\partial G}{\partial t} + \frac{\partial G}{\partial x_i} \frac{dx_i}{dt} = 0. \quad (1.22)$$

in order to ensure that G stays zero everywhere at the flame front. Following Sec. 1.2.1, flames propagate normal to themselves and, hence, each point on the flame sheet moves relatively to the cold flow field $u_{u,i}$ ahead of it according to

$$\frac{dx_i}{dt} = u_{u,i} - n_{f,i} s_L. \quad (1.23)$$

Combining Eqs. (1.21)–(1.23) one obtains the final version of the G-equation

$$\frac{\partial G}{\partial t} + u_{u,i} \frac{\partial G}{\partial x_i} = s_L \sqrt{\frac{\partial G}{\partial x_j} \frac{\partial G}{\partial x_j}}. \quad (1.24)$$

The non-linearity in this equation results from the fact that the front propagates normal to itself and that there exist only two distinct states, burned ($G > 0$) and unburned ($G < 0$), see Sec. 1.2.1 for more details.

As discussed in Sec. 1.2.2, the flame speed of thin flames depends on the local curvature of the flame sheet κ_f , which is computed from the G-field by taking the divergence of the normalized gradient (i. e. the flame normal vector)

$$\kappa_f = -\frac{\partial}{\partial x_i} \frac{\frac{\partial G}{\partial x_i}}{\sqrt{\frac{\partial G}{\partial x_j} \frac{\partial G}{\partial x_j}}}, \quad (1.25)$$

see e. g. Smereka [106]. Using the curvature dependent definition of the flame speed of Eq. (1.8) together with Eq. (1.25) and inserting both to the G-equation (1.24) one obtains

$$\frac{\partial G}{\partial t} + u_i \frac{\partial G}{\partial x_i} = s_L^0 (1 - l_M \kappa_f) \sqrt{\frac{\partial G}{\partial x_j} \frac{\partial G}{\partial x_j}}. \quad (1.26)$$

Here, flow strain was neglected and, thus, curvature is assumed to be the only source of flame stretch. It becomes apparent that consideration of a curvature dependent flame speed adds a diffusion term (Laplacian) with diffusion coefficient $s_L^0 l_M$ to the governing equation of a flame sheet. Hence, flame curvature effectively reduces steep gradients of the G-field and, for example, ensures the round tip of a Bunsen flame by increasing the flame speed at this strongly curved flame region.

Concerning the simulation of anchored flames, problems arise at points where flames are aerodynamically anchored and significant heat losses are present, e. g. at Bunsen flames. Those quenching effects change the inner structure of the flame and, on a hydrodynamical scale, the flame speed. This is especially important when a realistic flow solver is coupled with a G-equation approach. Due to friction, flow velocity decreases to zero right at the boundary. If the flame speed is not adjusted in this region, i. e. by considering quenching and/or curvature effects, the flame would flash back in the boundary layer of the flow and, hence, cannot be stabilized. While some studies implemented these quenching effects using empirical correlations [107, 108], others artificially fixed the G-field at the burner mouth using a Dirichlet boundary condition [100–102, 109].

1.3.2 1D Linearized Flame Dynamics

As already mentioned above, practical combustion systems often rely on aerodynamically stabilized flames whose fronts are inclined by an angle α with respect to the bulk flow velocity of the fresh mixture far away from the flame. The dynamics of such flames can be assessed best by mapping the G-equation to a 1D coordinate system by

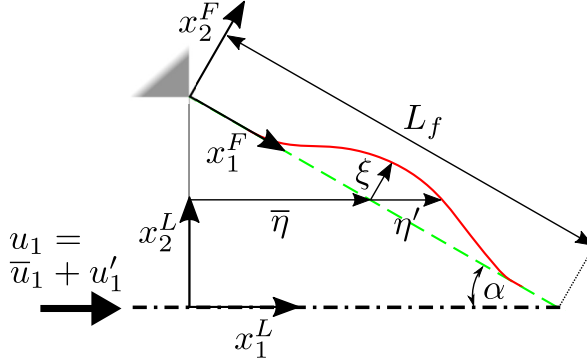


Figure 1.13: Sketch of a perturbed flame front (—) around its mean (- - -). Two coordinate systems are shown: the laboratory (x_1^L, x_2^L) and the flame aligned (x_1^F, x_2^F) one. In the first, the deflected flame front is described by $\bar{\eta} + \eta'$, in the latter by ξ (taken from [2]).

application of one of these transformations [65, 110, 111]:

$$\text{Laboratory coordinates:} \quad G = x_1^L - \eta(x_2^L, t) \quad (1.27)$$

$$\text{Flame coordinates:} \quad G = x_2^F - \xi(x_1^F, t). \quad (1.28)$$

A crucial assumption of this approach is that the 2D flame front is indeed a function of x_1^F (or x_2^L), i. e. there exists a unique value of ξ (or η) for each possible value of x_1^F (or x_2^L). This requirement may be violated at high amplitudes. In this case, the two transformations of Eqs. (1.27) and (1.28) cannot be applied any more. Two new coordinate systems are introduced here, on the one hand, the so called laboratory coordinate system, indicated by a superscript “L” ($x_{1/2}^L$), and, on the other, flame aligned coordinates, indicated by a superscript “F” ($x_{1/2}^F$). The position of the flame front is described by a quantity η in the former, and by ξ in the latter. Both are sketched for a perturbed flame in Fig. 1.13. Fluctuations of the inlet velocity $u_1 = \bar{u}_1 + u_1'$ lead – as indicated in Fig. 1.13 – to displacements η' and ξ in laboratory and flame coordinates, respectively. Throughout the thesis, mean quantities are denoted by an overbar ($\bar{\cdot}$), while a primed quantity (\cdot') indicates a fluctuation around this mean with an amplitude of order $\mathcal{O}(\epsilon)$ with $\epsilon \ll 1$.

Inserting Eq. (1.28) into Eq. (1.26) results in a 1D description of the dynamics of an inclined flame sheet in flame coordinates

$$\frac{\partial \xi}{\partial t} + u_{\parallel} \frac{\partial \xi}{\partial x_1^F} = u_{\perp} - s_L^0 (1 - l_M \kappa_f) \sqrt{1 + \left(\frac{d\xi}{dx_1^F} \right)^2} \quad (1.29)$$

with a flame geometry dependent curvature term κ_f . Assuming a 2D slit geometry of rectangular cross sectional area of the flame (index “slit”), the mean curvature term

writes

$$\kappa_{f,\text{slit}} = \frac{\frac{\partial^2 \xi}{\partial x_1^{F2}}}{\sqrt{1 + \left(\frac{d\xi}{dx_1^F}\right)^2}} - \frac{\left(\frac{\partial \xi}{\partial x_1^F}\right)^2 \frac{\partial^2 \xi}{\partial x_1^{F2}}}{\left(1 + \left(\frac{d\xi}{dx_1^F}\right)^2\right)^{3/2}}, \quad (1.30)$$

[112, 113]. It should be noted that the second term of this equation only adds a $\mathcal{O}(\epsilon^3)$ contribution to Eq. (1.29) and may hence be dropped for small flame front displacements. Similarly, for such conditions, the square root term in the denominator would asymptote to $1 + \mathcal{O}(\epsilon)$ and may be approximated as unity. For conical flames of circular cross sectional flame area, additionally, an azimuthal curvature contribution depending on the local flame radius r_f has to be considered. Neglecting the second as well as the square root term of Eq. (1.30), it writes

$$\kappa_{f,\text{con}} = \frac{1}{2} \left(\frac{1}{r_f} + \frac{\partial^2 \xi}{\partial x_1^{F2}} \right), \quad (1.31)$$

where the index “con” denotes a conical flame [114]. In the following the differences between Slit and Conical flames are neglected and only the curvature relation for Slit flames is considered. Assuming fluctuations of the state variables u_1 and ξ of order $\mathcal{O}(\epsilon)$ and neglecting all second order terms in ϵ , a linear PDE

$$\frac{\partial \xi}{\partial t} + \bar{u}_\parallel \frac{\partial \xi}{\partial x_1^F} = u'_\perp + l_M s_L^0 \frac{\partial^2 \xi}{\partial x_1^{F2}} \quad (1.32)$$

is retrieved. A relation $s_L = \bar{u}_\perp$ was applied, taking into account the fact that, in steady state, the flame normal flow velocity is exactly balanced by the laminar flame speed. Due to its simplicity, this advection-diffusion equation is well suited for analytical treatment [65, 111, 115]. Neglecting flame curvature effects ($l_M \equiv 0$), the resulting non-homogeneous advection equation is solved by integration of the flame-normal velocity perturbations

$$\xi(x_1^F, t) = \frac{1}{\bar{u}_\parallel} \int_0^{x_1^F} u'_\perp \left(\tilde{x}_1^F, t - \frac{x_1^F - \tilde{x}_1^F}{\bar{u}_\parallel} \right) d\tilde{x}_1^F + \xi \left(0, t - \frac{x_1^F}{\bar{u}_\parallel} \right). \quad (1.33)$$

The second term on the right-hand side of this equation considers perturbations at the flame anchoring ($x_1^F = 0$). Hence, perturbations of the flame base would reach the flame tip at a time $\tau_f = L_f / \bar{u}_\parallel$, where L_f denotes the steady state flame length, see Fig. 1.13. This quantity is known as the characteristic time of restoration [116].

Expressing Eq. (1.32) in laboratory coordinates by use of Eq. (1.27) again assuming $l_M \equiv 0$, one obtains

$$\frac{\partial \eta'}{\partial t} - \cos(\alpha) \sin(\alpha) \bar{u}_1 \frac{\partial \eta'}{\partial x_2^L} = \frac{1}{\sin(\alpha)} [\sin(\alpha) u'_1 + \cos(\alpha) u'_2] - \frac{s'_L}{\sin(\alpha)}. \quad (1.34)$$

Inserting the relations $\eta' = \xi / \sin(\alpha)$ and $dx_2^L = -\sin(\alpha) dx_1^F$ (Wedge flames: “+”) into this equation, transforms the equation in flame aligned coordinates, as shown in

Eq. (1.32). Since, for small perturbations, both descriptions are equivalent, it is favorable to use flame aligned coordinates for modeling the flame front dynamics since here the equation becomes more compact. As will be shown in Sec. 6.2, however, the use of a coordinate system other than the flame aligned one can be advantageous for evaluating flame surface integrals, due to a simpler treatment at the boundaries.

Eq. (1.32) holds for slit and conical configurations. It has, however, to be noted that, just like in the aforementioned G-equation approach, flow strain as well as flame-flow-flame feedback resulting from exothermic effects were neglected. Both would act quantitatively different for the two flame geometries. Another consequence of flame geometry concerns flame curvature: Due to their azimuthal curvature, conical flames are generally exposed to higher flame stretch than slit flames, compare Eq. (1.30) for Slit and Eq. (1.31) for conical flames. The maximum stretch due to azimuthal curvature is imposed at the flame tip for Bunsen flames and at the flame anchoring for Wedge flames, since there the respective local flame radius r_f reaches a minimum. It follows that advected flame front perturbations are exposed to increasingly stronger stretch rates for Bunsen flames, which should lead to smoother flame shapes towards the tip compared to Slit flames. This mollifying effect impacts also the generation of flame pockets at the flame tip (pinch off) [104]. For Wedge configurations it is the other way round: flame stretch decreases while a flame perturbation is advected along the flame front, which make it more prone to the formation of cusps.

1.4 Summary

In this chapter, the available literature on the dynamics of thin flame sheets far away from any boundary was reviewed. The general idea concerning the analysis of such flames is based on the fact that these flames can be viewed as propagating discontinuities separating two coupled flow domains of different densities, namely the domain of the fresh mixture and the domain of the burned products. Based on matched asymptotic expansion techniques, a propagation speed of the discontinuity (flame speed) and jump conditions connecting the two flow domains could be derived from first principles. This specific way of describing thin flame sheets shifts the focus away from details of the combustion process to macroscopic properties such as flame speed, flame shape and acceleration/deceleration of the underlying flow field.

Four mechanisms governing the dynamics of thin flame sheets could be identified: (i) the propagation of a flame sheet normal to itself, (ii) thermal-diffusive mechanisms interacting with the propagation speed of a flame front, (iii) hydrodynamic features mainly affecting the surrounding flow field and (iv) the downstream advection of flame perturbations along the flame sheet for inclined flames (neglecting the dynamics close to the anchoring point). Finally, the wide-spread G-equation approach was introduced in its 2D non-linear as well as in its 1D linearized form. It was pointed out that it only captures the kinematics of a flame front, but inherently neglects flame-

flow feedback, i. e. hydrodynamic mechanisms. This is a substantial shortcoming of this method, as will be shown in the course of this thesis.

2 Acoustic Response of Burner-Stabilized Flames

A literature review on interactions between acoustics and burner-stabilized premixed flames is provided, which builds upon the concepts outlined in the previous section. Additionally, the notion of convected velocity perturbations is introduced, around which most theoretical predictions of the acoustic flame response evolve.

Chapter. 1 discussed the dynamics of flame sheets far away from any boundary. Four different governing mechanisms were identified, which allowed to break down the overall flame dynamics into their canonical components. This realization lays the foundations for the analyses of acoustically perturbed burner-stabilized flames, which will be conducted in this chapter. Such configurations introduce essentially two new features, that is (i) a burner where the flame is anchored/stabilized and enclosed and (ii) acoustic perturbations interacting with the flame. Furthermore, not only the flame shape but also the change of the global heat release rate will now be an output quantity of interest. Due to these features and requirements, the low-order modeling concepts introduced in the previous chapter need to be extended in order to cope with thermoacoustically relevant setups.

Burner-stabilized flames consist of multiple flame sheets of finite extension that are usually anchored by a separation-induced low-speed region close to a wall. Additionally, they might be confined by a casing and exposed to nonconstant upstream flow profiles. It becomes clear that the rather idealized flame dynamics described in Chap. 1 might be enriched by additional phenomena such as flame-wall or flame-flame interactions. Furthermore, the mean state of a flame is no longer trivial and might significantly impact the dynamics of the overall system. Finally, the existence of acoustic perturbations introduces further complications. The individual flame sheets of the overall flame are now externally forced, which introduces completely new dynamic features. Therefore, the acoustic field inside the respective burner configuration needs to be studied and acoustic-flame sheet interactions have to be considered.

Knowing how a flame reacts to acoustic fluctuations is only half the story when dealing with thermoacoustic interactions. The other half concerns the generation of acoustic perturbations by the flame itself. It can be shown that acoustically compact flames act as a monopole-like source of sound whose strength is proportional to fluctua-

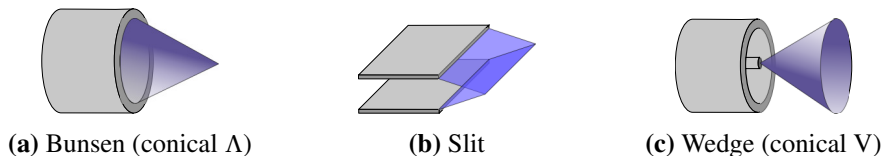


Figure 2.1: Investigated flame geometries (taken from [2]).

tions of their global heat release rate. Consequently, the dynamics of the overall heat release rate is an important feature that has to be discussed in this section, as well.

This chapter is structured as follows: Sec. 2.1 provides a definition of the class of problems that are tackled by this thesis, i. e. the analyzed burner configurations and fuel-oxidizer mixtures are defined. Secs. 2.2 and 2.3 then provide a literature review on the dynamics and low-order modeling concepts of acoustically perturbed flames, respectively.

2.1 Problem Definition

In this thesis laminar lean methane-air flames of different equivalence ratios are analyzed that are operated far away from the region of lean extinction. They all exhibit Lewis numbers close to unity and are hence thermal-diffusively stable. Furthermore, they can in good approximation be assumed to be thin for all analyzed setups, as pointed out in Sec. 1.1.1. The initial temperature of the fresh mixture is always kept constant (300 K).

The geometrical details of all investigated burners shall resemble a backward facing step configuration, which allows for an efficient anchoring of the flame in the low-speed region induced by the separating flow field. Depending on the specific geometrical details of the burner, the boundary and initial conditions, flames of several different geometrical shapes can be stabilized. Three of the most important ones are shown in Fig. 2.1: The Bunsen, the Slit and the Wedge flame. The three illustrations immediately point out that flame sheets of realistic burner setups are not necessarily planar and may also intersect. Furthermore, interactions with combustor walls, e. g. at the anchoring position, imposes new dynamics via quenching, viscous effects and flow separation. Due to advection, any flame front perturbation will eventually reach the flame tip, where it might lead to a pinch-off of burning bubbles of fresh mixture. All of these effects complicate the analysis by adding new dynamic features. Their respective significance for the process of interest, however, might not necessarily be high. Figuring out what is important and what not is one major goal of this work. In order to reduce complexity, this work mainly focuses on Slit configurations.

The combustion region of all of the considered flame configurations shall be limited by lateral constraints. This respects the fact that in technical applications flames are

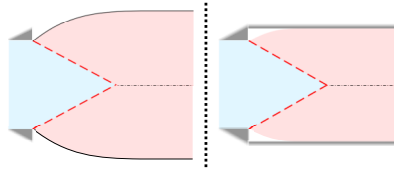


Figure 2.2: Unconfined (left) vs. confined (right) flame.

usually confined in order to use the sensible enthalpy of the hot products or to shield the combustion process from the environment. Fig. 2.2 compares the jet of hot gases of an open flame to the one of a confined flame. It becomes clear that a sufficiently narrow confinement might alter the mean flow field by accelerating the burned gases and, in doing so, also the acoustic flame response.

Finally, all configurations are exposed to acoustic perturbations whose minimum wave length shall be much longer than the height of the respective flame. This limitation demands that all flames are *acoustically compact*, i. e. they are exposed to acoustic pressure or velocity perturbations that are in-phase everywhere along the flame sheets. Furthermore, under such conditions perturbed flames can be approximated as monopole-like sources of sound.

2.2 Acoustics-Flame Interactions

The analysis of the dynamics of acoustically perturbed flame configurations, as described in Sec. 2.1, requires some extensions of the theory of freely propagating flame sheets presented in Chap. 1. A literature review on what has been achieved so far is provided in the preceding section.

Sec. 2.2.1 provides fundamental insights into how flame sheets, as introduced in Chap. 1, respond to acoustic perturbations. These fundamental studies are followed by a review of the literature concerning acoustically perturbed Bunsen flames in Sec. 2.2.2. Here, the focus is put on the shape and the dynamics of acoustically triggered flame front displacements. Section 2.2.3 then provides an overview on how these displacements are connected to variations of the global heat release rate. Crucial thermoacoustic concepts, such as the flame transfer function and its representations in the frequency and time domain are introduced.

2.2.1 Freely Propagating Flame Sheet

In a first step, the interaction of acoustic perturbations with an freely propagating planar flame sheet is analyzed, which should provide guidance on how to deal with the more complex problem of a burner stabilized flame. For all cases studied here, the flame thickness is much smaller than the wave length of any relevant acoustic

perturbation ($\leq \mathcal{O}(10^3)$ Hz). Therefore, we can rely on the flame sheet assumptions introduced in Chap. 1 when assessing acoustics-flame interactions [117]. According to theoretical studies, for the frequency range that is relevant when considering combustion instabilities, the flame speed is supposed to depend on the acoustic forcing [118, 119], i. e. s_L is thought to be a function of the acoustic field. This fact, however, requires further rigorous experimental validation [117] and is, for the sake of simplicity, usually neglected in thermoacoustic studies. The validity of this simplification for many setups of practical relevance is supported by experimental and numerical studies, such as the one of Baillot *et al.* [120] or Michaels and Ghoniem [121], which leads to the conclusion that the impact of acoustics on the flame speed is indeed rather weak.

It is also commonly assumed that premixed flames predominantly respond to velocity perturbations and almost completely ignore changes in pressure [117]. Thus, the flame speed is basically not affected by acoustics. Based on these realizations, it can be concluded that acoustic velocity fluctuations essentially displace a flame front and, in doing so, alter its shape. This may trigger dynamical processes governed by the four mechanisms identified in Chap. 1.

A fundamental study analysing details of acoustic-flame interactions has been performed by Lieuwen [122] for the case of a planar downward propagating flame of infinite extension that is hit by a planar acoustic wave at an angle of incidence θ : Depending on the angle θ , acoustic waves are transmitted and reflected at different ratios at the flame front. As known from optics, when a disturbance travels from a medium of lower to one of higher propagation speed, there exists a “cut-off” angle depending on the density ratio across the flame, where the incident wave is fully reflected at the flame front. This only happens for upstream and never for downstream acoustic excitation. Furthermore, baroclinic production of vorticity at the flame front acts as an acoustic damping mechanism. These results indicate that flame front displacements caused by acoustic perturbations affect the surrounding flow field, for example, by introducing vortical structures. And, indeed, such features are also observed in the vicinity of burner-stabilized flames, as will be shown in the course of this thesis.

2.2.2 Burner-Stabilized Flame

Acoustics-flame interactions are significantly more complex for burner stabilized flames than for freely propagating flame sheets. Although acoustic velocity fluctuations mainly displace a flame, see the previous section, their spatial shape, flame-wall and flame-flame interactions add some important burner-configuration dependent peculiarities. In the following a brief overview of the most important findings is provided. In the first part, the various modes of interactions of acoustic perturbations with flames are covered. Knowing how flame displacements are generated, the review focuses in a second part on the response of a flame to these perturbations. Interestingly, the literature revolves around the notion of convected velocity perturbations

instead of the four canonical mechanisms introduced in Sec. 1.2, which motivates the analysis conducted in this thesis.

Acoustic Interactions with Burner-Stabilized Flames

Based on the fact that flames are usually stabilized in the vicinity of sharp edges where acoustics triggers the shedding of vortices [123–126], it is natural to structure a review on acoustic interactions with burner-stabilized flames according to a decomposition of acoustic perturbations into a potential (irrotational) and a vortical (solenoidal) contribution. This decomposition accounts for the respective nature of the individual flow modes [127] and allows for their separate analysis.

Investigations of the vortical part of the acoustic perturbation field, on the one hand, have not drawn too much attention in the literature. One reason for this might be that perturbed flame sheets generate a reasonable amount of vorticity by themselves [128–130], which makes it hard to isolate effects of acoustically triggered vortex shedding. Schlimpert *et al.* [104] tried to overcome this problem by neglecting flame-induced gas expansion in their numerical model, which suppresses the generation of distracting flame generated vorticity. In doing so, however, they at the same time removed dilatation effects, which significantly dampen the vortical flow component and bend the mean flow shear layer away from the flame. Hence, interactions of separating vortices with the flame were overestimated compared to realistic conditions. According to their analysis, at proper levels of gas expansion and far away from the region of lean extinction, only interactions between the flame base region and shed vorticity remain.

On the other hand, the potential acoustic velocity field in a backward-facing step combustor, as depicted in Fig. 2.2 (right), was closer analyzed in a series of numerical investigations by Lieuwen [131] as well as Lee and Lieuwen [132]. They found that the acoustic velocity field interacting with the flame front is essentially 2-dimensional with a maximum close to the flame anchoring position, even for acoustically compact flames. Since evaluation of the flame response using such a model did — unexpectedly — not yield significant improvements compared to a 1-dimensional description of the velocity field, this study has not drawn too much attention. Their principal finding was later experimentally confirmed by Kornilov *et al.* [133] who did, however, not explicitly mention the connection to the previous study of Lee and Lieuwen [132]. Kornilov *et al.* [133] forced a Bunsen flame, one time by moving the anchoring transversally in and out and, one time by imposing acoustic velocity perturbations. Both kinds of excitation resulted in very similar velocity fields, which are visualized in Fig. 2.3. The authors further evaluated the transfer functions from the forcing to the globally integrated heat release rate for both sets of experiments and found that they also agreed reasonably well. Hence, they indirectly confirmed the findings of Lee and Lieuwen [132] that acoustics interacts predominantly with the flame base region.

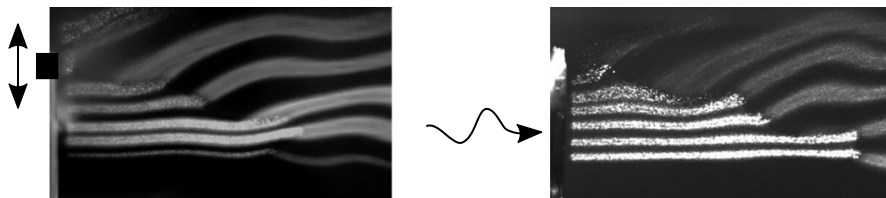


Figure 2.3: TiO_2 smoke trace flow field visualization of two Bunsen flames forced at 200 Hz, one time by transversal movements of the flame holder at which the flame is anchored (left) and one time by acoustic excitation (right) (images are taken from Kornilov *et al.* [133], Figs. 5 and 6).

In summary, (i) the impact of acoustically triggered vorticity on a flame is still unclear and (ii) the potential part of the acoustic velocity field predominantly interacts with the flame base region. It has to be emphasized that, although this review follows said flow decomposition approach, many of the studies mentioned remained side notes in the body of literature on acoustics-flame interactions or they did not explicitly follow such a decomposition-based mindset. Due to the fact, however, that this work is going to revisit such a mindset, the concept of flow decomposition was granted a prominent position in this review.

Flame Response to Acoustically Generated Displacements

As explicated in Sec. 1.2.4, one essential dynamical feature of burner-stabilized inclined flames is the advection of flame front perturbations. In this regard, Cuquel [134] published an instructive experimental investigation of acoustically forced flames. Fig. 2.4 shows four snapshots that were taken at equidistant phases at a frequency of 80 Hz. In accordance with the studies reviewed above, acoustic interactions displace the flame close to the burner mouth. This creates flame wrinkles, which are convected along the flame front until they reach the flame tip. In Fig. 2.4, two of these wrinkles are marked by a red and a green line, respectively. In each successive snapshot, they move by an approximately constant distance and are hence advected downstream by a fixed velocity.

At this point it should be emphasized that the flame is anchored at the burner, i. e. any sudden displacement of the anchoring exerted by acoustic perturbations will eventually be counteracted such that after some time the flame has returned to its original steady state position. The information of the restored flame anchoring will — just like any flame front displacement — be advected along the front and will reach the flame tip after a time τ_r . Accordingly, Blumenthal *et al.* [116] named this period of time the *characteristic time of restoration*. It should, however, be noted that this time scale is characteristic for the advection of *any* flame front feature, not just the restoration. In that sense it should rather be called the characteristic time of advection.

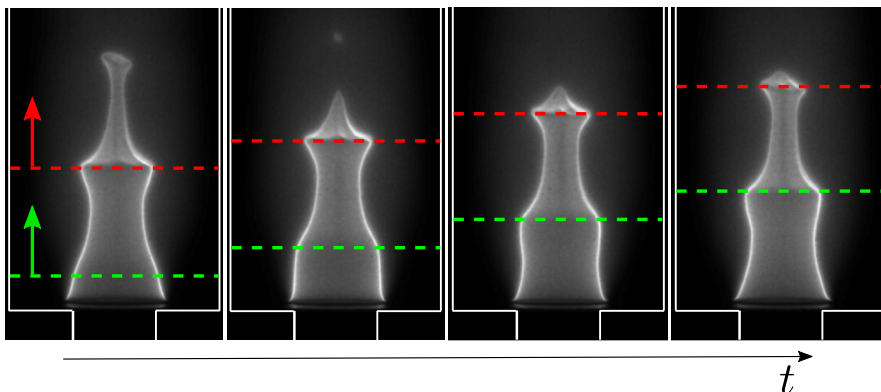


Figure 2.4: Snapshots of an acoustically excited Bunsen flame at 80 Hz, taken at four equidistant phases. Clearly, two distinct wrinkles can be observed that are advected from the flame base towards the tip at a constant speed, marked by a red and green line (images taken from Cuquel [134], Fig. 6.10, left; the red and green lines/arrows were added by the author).

Having a closer look at the snapshots of Fig. 2.4, one notices that the wrinkles grow in amplitude while they are advected downstream. Furthermore, they develop a cusp like structure exhibiting a sharp edge at concave and very smooth contours at convex displacements. This is a consequence of the four governing mechanisms introduced in Sec. 1.2 and corresponds to the non-linear process illustrated in Fig. 1.5. Since the formation of cusps is a non-linear mechanism, it is not analyzed in detail any further here. It should be noted, though, that whenever such cusp-like structures are visible, non-linear mechanisms are at play and, consequently, the dynamics of the respective flame is not purely linear anymore. In this regard, cusps are a good indicator that the linear regime has been left. The transition from the linear to the non-linear regime of acoustically forced Bunsen flames has, for example, been analyzed more closely by Karimi *et al.* [135].

Concerning the dynamics of perturbed burner-stabilized flames, there are essentially two types of studies: those which impose an acoustic forcing and those which mechanically displace the anchoring [45, 63], see the right and left hand side of Fig. 2.3, respectively. The findings of Lieuwen [131] and Kornilov *et al.* [133], stating that acoustics displaces mainly the flame base regions, provides a clear connection between both setups. Consequently, it seems natural that also the observed respective dynamics are very similar and knowledge gathered from one configuration could be transferred to the other.

This potential, however, has not been fully exploit so far. The dynamics of mechanically forced flame sheets has been attributed to the net effect of the destabilizing hydrodynamic mechanism described in Sec. 1.2.3 and the stabilizing thermal-diffusive mechanism described in Sec. 1.2.2 superimpose by advection [45, 63]. Interestingly, this idea has hardly been explicitly formulated in the literature on acoustically forced

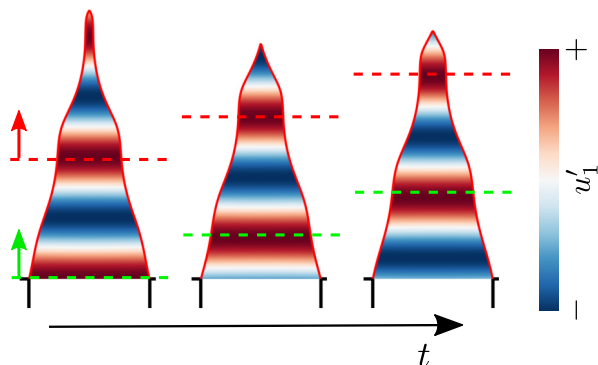


Figure 2.5: Snapshots of a G-equation-based simulation of an acoustically excited Bunsen flame at 120 Hz relying on the convective incompressible velocity model introduced by Baillot *et al.* [120], taken at three equidistant phases. Colors denote the imposed axial velocity fluctuations u'_1 and the green and red horizontal lines tag two maxima of the underlying velocity field visualizing their axial convection (note: other than in Fig. 2.4, here the lines tag axially transported velocity fluctuations not flame wrinkles).

flames. Instead, here the analysis has taken a very different way, centered around purely kinematic observations of the flow field. Baillot *et al.* [120] experimentally detected axially convected velocity perturbations just upstream of an acoustically perturbed flame inside the volume enclosed by the flame sheets and the burner mouth. They explained these observations by both hydrodynamic interactions of the wrinkled flame front with the upstream flow field and the effect of gas expansion across the flame. In principle, this hypothesis was later confirmed by studies of Birbaud *et al.* [136] and Blanchard *et al.* [129].

The important point, however, of the study of Baillot *et al.* [120] is that it could retrieve a good match between experimentally measured perturbed flame sheets and those obtained from a G-equation-based model only if axially convected velocity perturbations upstream of the flame were introduced, resembling the ones that have been measured. Fig. 2.5 depicts three successive snapshots of such a G-equation-based simulation, which illustrates the model of axially convected velocity perturbations and the resulting flame shapes.

Such a convective velocity model results in a linearly decreasing phase of the associated FTF (see next section), which was confirmed by subsequent studies [111, 137, 138]. Hence, Candel wrote in his 2013 review paper “*This behavior [the linearly decreasing phase] is the signature of perturbations convected by the flow often revealing the presence of large structures conveyed by the flow and impinging the flame*” (Candel *et al.* [139], p. 98). In this specific case he was referring to a burner-stabilized Wedge flame that is clearly subjected to vortical structures shed from the burner rim. The notion of this statement, however, was generalized for all types of

flames and it became state-of-the-art that acoustically excited premixed (Bunsen) flames are subject to convected velocity perturbations [140]. The contradictory point here is that Birbaud *et al.* [136] and Blanchard *et al.* [129] as well as even Baillot *et al.* [120] found that these perturbations are a consequence rather than a source of flame front wrinkles. Therefore, the assumption of convected velocity perturbations seems to violate causality (they cannot be source and consequence at the same time) [1, 2]. This point has not explicitly been addressed so far and will be clarified in the course of this work.

In summary, the most important mechanisms governing the linear response of inclined flame fronts to acoustic perturbations have been discussed:

1. Acoustics displaces predominantly the flame base region
2. Flame displacements are advected downstream by a constant speed resulting in a characteristic time of restoration τ_r
3. Flame intrinsic instability mechanisms act on flame displacements, which might lead to their growth in amplitude
4. Acoustically perturbed flames exhibit axially convected velocity perturbations upstream of the flame sheets

What is missing in this overview are features concerning the flame tip (pinch-off) and the anchoring (quenching, vortex shedding). They are, however, either essentially non-linear in nature, of secondary importance or beyond the scope of this work. Furthermore, there is a strong dependency of the flame response on the respective burner configuration. One important point here concerns the confinement of the combustion region [141–144], another the boundary conditions of walls adjacent to the flame sheet [121, 145–149]. Also the burner size is important [150] as well as its geometry [151–153].

2.2.3 Global Heat Release Rate Dynamics

This thesis is devoted to the study of flames in the context of thermoacoustic systems, where the flame constitutes one specific sub-system. Therefore, the input/output relation of interest of the flame module needs to quantify the sound that is produced by an acoustically perturbed flame. In the regime of acoustically compactness, temporal fluctuations of the global heat release act like an acoustic monopole whose dynamics is directly proportional to the normalized fluctuation of the global heat release rate of the flame [22, 154]. In the linear regime, the mentioned input/output relation is established by the flame transfer function (FTF)

$$\frac{\dot{Q}'}{\dot{Q}} = F(\omega) \frac{u'_{\text{ref}}}{u_{\text{ref}}}. \quad (2.1)$$

It relates velocity fluctuations at a reference position u'_{ref} to variations of the global heat release rate. For perfectly premixed flames, a relation

$$\frac{\dot{Q}'}{\bar{Q}} = \frac{A'_f}{\bar{A}_f} + \frac{\int s'_L d\bar{A}_f}{\int \bar{s}_L d\bar{A}_f} \quad (2.2)$$

holds, which connects fluctuations of the global heat release rate \dot{Q}' to fluctuations of the flame surface area A'_f and the mean surface integrated flame speed s'_L [117, 155]. For perfectly premixed flames, as discussed here, the latter term is usually neglected and essentially becomes important at higher frequencies [112, 113].

The thermoacoustic response of premixed flames is the consequence of a great variety of physical mechanisms including everything that has so far been mentioned in this and the previous chapter: hydrodynamic mechanisms leading to the growth of flame front perturbations, thermal-diffusive processes stabilizing the front, non-linear mechanisms leading to the formation of cusps, quenching effects at walls and flame-flame interactions at the flame tip. This section now deals with the final step, which — following Eq. (2.2) — essentially comprises the computation of the flame surface area for a given displaced flame front. While this may sound trivial, it has some non-straightforward consequences, especially concerning flame geometry. This will be examined in greater detail in Chap. 6. For the remainder of this section, some technical details concerning the representation of the linear flame response will be discussed.

A frequency domain representation of the linear response of a laminar Bunsen type flame is depicted in Fig. 2.6. The left half of that figure (a+b) depicts the frequency response in terms of gain and phase, while the right half (c+d) shows the rather untypical representations in terms of a polar plot and a plot of the real and the imaginary part of the FTF over frequency. Note that the gain has a logarithmic scale in Fig. 2.6 (a) and (c). These — sometimes also double logarithmic scales — are adopted from the field of control theory, where this particular choice of scaling allows a simple identification of the corner frequencies, i. e. frequencies above which a signal is attenuated instead of being passed through by the system (in the case of a low pass filter). These frequencies are also known as cut-off frequencies.

Another illustration of the linear flame response is the impulse response (IR), which is shown in Fig. 2.7 (left half). It can be considered as the time domain equivalent to the frequency response (FR) (Fig. 2.7; right half) and relates the heat release rate to fluctuations of a reference velocity via temporal convolution (denoted by the “*“-operator):

$$\frac{\dot{Q}'}{\bar{Q}} = h(t) * \frac{u'_{\text{ref}}}{\bar{u}_{\text{ref}}} \quad (2.3)$$

The axes of Fig. 2.7 have a linear scaling improving the presentation of the low frequency behavior compared to the previously shown logarithmic scale, which usually has a gain and a Strouhal number of order $\mathcal{O}(1)$. The behavior of the gain for values

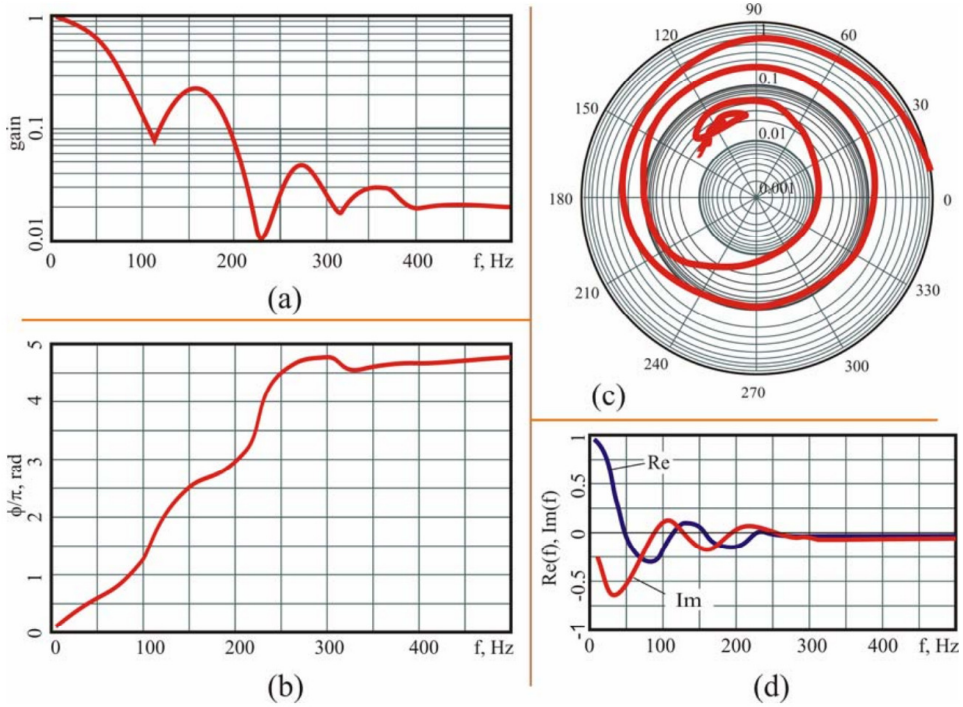


Figure 2.6: Representation of a typical linear flame response of a Bunsen flame in the frequency domain (frequency response) in terms of (a) gain, (b) phase, (c) polar plot with phase determining the angle and gain the radius and (d) real and imaginary part plotted over frequency (taken from Kornilov [156], Fig. 3.1).

lower than $\mathcal{O}(1)$ is of little practical interest. Similarly, from a thermoacoustical point of view, predominantly the flame dynamics at Strouhal numbers of order $\mathcal{O}(1)$ is important. Therefore, in this thesis all frequency response plots exhibit linearly scaled axes.

Characteristic features of the FTF of perfectly premixed laminar flames are (i) a low frequency limit ($f \rightarrow 0$) of unity [157], (ii) an essentially linear decay of phase and (iii) a low-pass behavior featuring reoccurring minima followed by local maxima. The IR of such flames shows a more or less constant positive response that is followed by some strongly damped oscillations. It should however be noted that this characteristic strongly depends on the considered flame geometry, as will be shown in Chap. 6. Keeping the geometry fixed, the responses of several flames are rather similar. Introducing a non-dimensional frequency, a so-called Strouhal number, using the characteristic time of restoration $f^* = f\tau_r$, Ducruix *et al.* [158] found that plotting the responses of the global heat release rate of harmonically forced Bunsen flames of different inclination angles over such a Strouhal number causes the individual curves to collapse on each other. Hence, in this work most representations of flame

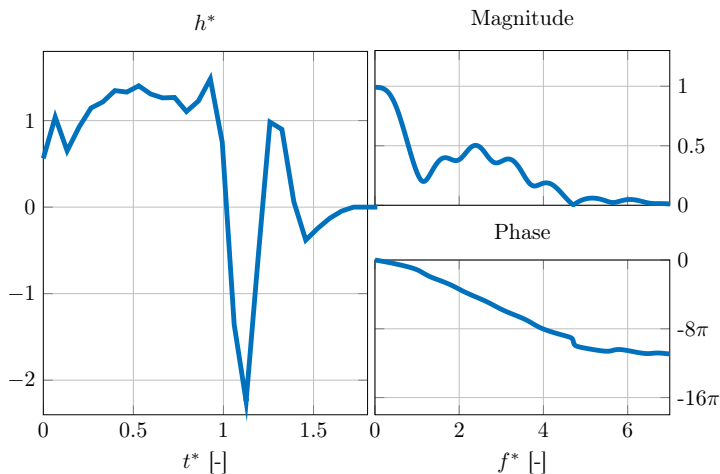


Figure 2.7: Representation of a typical linear flame response of a Bunsen flame in the time domain as impulse response (left) and in the frequency domain as frequency response (right).

responses are either plotted over such a Strouhal number or over a non-dimensional time $t^* = t/\tau_r$.

2.3 Low-Order Models

The dynamics of acoustically perturbed burner-stabilized flames is more complex than the one of freely propagating flame sheets, see the discussion above. Therefore, a less rigorous analysis of the respective dynamics has been conducted for such configurations — mostly due to complexities introduced by the flame anchoring and tip as well as by the acoustic forcing. Probably due to these difficulties, mostly phenomenological models were developed that enabled decent low-order predictions of the global heat release dynamics of acoustically perturbed flames, however, obscured the analysis of the underlying physical processes, since they are not rigorously derived from first principles.

Early studies on the global flame response to acoustic perturbations boiled the complete flame dynamics down to a time lag τ and an interaction index n [159]. This rather simplistic model became to be known in the literature as the n - τ model. It correctly captures the experimentally observed linear decrease of the FTF phase, however, predicts a frequency independent gain of value n . This is a severe oversimplification of the observed low-pass filtering behavior of flames, which was later taken into account by a semi-empirical model developed by Merk [160]. He described the flame front by use of a first order low-pass filter that provided an improved gain prediction at the cost of a poorer phase behavior, which now saturates at $-\pi/2$. Sugi-

moto and Matsui [64] developed a model based on growing convected perturbations, which suffers from the same problem.

Later studies focused on capturing the actual flame front kinematics by use of a G-equation based approach that inherently neglects flame-flow feedback, see Sec. 1.3. One of the first to capture the dynamics of inclined flames using such a (1D linearized) approach were Boyer and Quinard [65]. They imposed an uniform in-phase velocity forcing

$$u'_1 = \hat{A} \exp(i\omega t), \quad u'_2 = 0 \quad (2.4)$$

of amplitude \hat{A} and angular forcing frequency ω , which harmonically displaces the whole flame sheet and found advected flame displacements that propagate inside stationary envelopes. A laboratory coordinate system, as illustrated in Fig. 1.13, is used in this representation. This model will be referred to as the uniform velocity model in the following. By adding an additional growth term $\sigma\xi$ to the 1D G-equation, they artificially included otherwise neglected consequences of flame-flow feedback. The growth rate σ that matched their experiments best, however, was significantly smaller than the one computed from dispersion relations of planar freely propagating flames. They attributed this discrepancy to a confinement related stretching of the flame in combination with a strong sensitivity of the underlying dispersion relation to stretch effects.

Baillet *et al.* [120] assessed the dynamics of acoustically excited Bunsen flames experimentally and analytically. They also relied on the 1D linearized G-equation framework used by Boyer and Quinard [65], however, they dismissed the growth term. As already pointed out in Sec. 2.2.2, they measured velocity fluctuations of the fresh mixture inside the region just downstream of the edge where the flame is anchored, one time without flame (“cold case”) and one time with flame (“hot case”). They observed axially propagating velocity perturbations inside this zone with a speed close to the mean flow velocity for both cases, which they attributed to vortex shedding for the cold and to the upstream influence of the perturbed flame front for the hot case. Motivated by this observation, they imposed axially convected velocity perturbations

$$u'_1 = \hat{A} \exp(ikx_1^L), \quad u'_2 = -ik \frac{x_2^L}{2} \hat{A} \exp(ikx_1^L) \quad (2.5)$$

fulfilling continuity for an axisymmetric frame of reference to their 1D linearized G-equation framework. Here, $k = \omega/\bar{u}_1$ denotes the wave vector of the forcing. Very good agreement between experimentally measured and the modeled transient flame shapes was found. This velocity model is – in accordance with the literature [161] – called the “incompressible convective” model. Results of a G-equation based simulation relying on such a velocity model (with $u'_2 \equiv 0$) are shown in Fig. 2.5.

The first to derive an analytical expression for the FTF using the G-equation framework were Fleifil *et al.* [115]. Based on the observation that acoustic wave lengths

in the frequency range of interest are long compared to the flame height, they assumed an uniform in-phase forcing of the flame sheet by the velocity field, as already applied by Boyer and Quinard [65]. Neglecting variations in flame speed along the flame sheet, they exploit the fact that for perfectly premixed flames the heat release rate is proportional to the instantaneous flame surface area, see Eq. (2.2). Based on this assumption, they could derive an equation for the linearized heat release rate fluctuations by evaluation of the instantaneous flame surface area from a displaced flame front. The resulting FTF showed the desired low-pass behavior, however, the phase saturated at $-\pi/2$ — just as in the model by Merk [160]. Particularly for low frequencies it provided some useful predictions, though. Ducruix *et al.* [158] then generalized the model of Fleifil *et al.* [115] for arbitrary flame angles by introduction of a reduced frequency or Strouhal number ω^* .

Schuller *et al.* [137] revisited the convective velocity model proposed by Baillot *et al.* [120], extended it by imposing an axial decay of the convected waves and combined it with the approach of Fleifil *et al.* [115]. This led to an improved description of the FTF phase, which now resembles that of a system of constant time delay and, hence, does not saturate at $-\pi/2$. Schuller *et al.* [137], however, could only numerically evaluate the model and were not able to provide analytical expressions. In a succeeding publication, Schuller *et al.* [111] simplified this velocity model by neglecting the axial decay and the lateral velocity component satisfying continuity, which led to an analytically solvable problem. Later, Preetham *et al.* [138] and Cuquel *et al.* [161] seized on the original idea of Baillot *et al.* [120] of the incompressible convective velocity model and were able to provide analytical solutions using again the framework of Fleifil *et al.* [115]. They, however, discarded the axial decay of the velocity perturbation imposed by Schuller *et al.* [137]. Their model overpredicts the gain at high frequencies, but provides good estimates of the phase.

The incompressible convective model, became the predominant low-order model for acoustically induced flow-flame interactions. Since Schuller *et al.* [137] introduced it to the field of thermoacoustics, it has been used (with slight modifications) for a great variety of studies. For example, it was used to study non-linear thermoacoustic oscillations [162, 163], the dynamics of bluff-body stabilized flames subjected to longitudinal acoustic forcing [138, 164, 165], the non-linear behavior of the flame response for high amplitude forcing [109, 166, 167] or to study the impact of stretch and exothermicity on the flame response [104, 112, 113, 142]. This model hence became state of the art, however, as already indicated in Sec. 2.2.2, a discussion on the physical justification of the imposed axially convected velocity perturbation arose.

Finally, it should be mentioned that linear models can equally be evaluated in frequency and time domain. In the formulations mentioned above, harmonic velocity forcing was assumed, which leads to a description of the response behavior in frequency domain when combined with the 1D linearized G-equation framework, see Schuller *et al.* [111] or Preetham *et al.* [138]. Blumenthal *et al.* [116] assumed a unit

impulse forcing of the flame following a Dirac distribution $\delta(t)$. For such a forcing, the incompressible convective velocity model of Eq. (2.5) transforms to

$$u'_1 = \delta\left(t - \frac{x_1^L}{\bar{u}_1}\right), \quad u'_2 = \frac{x_2^L}{2\bar{u}_1} \delta'\left(t - \frac{x_1^L}{\bar{u}_1}\right) \quad (2.6)$$

for the two velocity components. Combined with the G-equation formalism, such a forcing leads to a time domain representation of the linear response behavior, which can be transformed to frequency domain. Similarly, any frequency domain representation can be mapped to the time domain. One significant advantage of the time domain perspective regards the improved identification of causalities, see Appendix A.3 for more details. A second related advantage concerns the clear separation and characterization of physical processes: Following Blumenthal *et al.* [116], an impulsive forcing results in two clearly separated processes, an axially moving source of flame front displacement and a process that restores the original flame front. Each of these processes can be associated with a characteristic time scale, which allows for a natural definition of a Strouhal number, for example. Conversely, in frequency domain, one has to deal with the fact that the observable flame front displacement at a certain location is the superposition of past displacements provoked anywhere upstream of that point, which complicates the analysis.

2.4 Summary

In this chapter the body of literature concerning the dynamics of acoustically perturbed burner-stabilized flames was reviewed from an thermoacoustic point of view. In a first step, the problem under consideration was specified by imposing constraints on the burner geometry and the mixture properties. The literature on acoustics-flame interactions was analyzed, starting with freely propagating flame sheets and then moving on to burner-stabilized flames. Subsequently, available low-order modeling concepts were reviewed, which are mostly based on a 1D linearized G-equation approach that is excited by convected velocity perturbations.

One important outcome of this chapter is that not only low-order modeling strategies but also a significant part of the notion of the dynamics of acoustically perturbed flames relies on the concept of convected velocity perturbations. This concept, however is paradoxical: On the one hand, it is assumed that the flame front is locally displaced by axially convected velocity perturbations, on the other, it is stated that these perturbations are a consequence of flame front wrinkling. Obviously, one of these contradictory findings needs to be wrong. Interestingly, studies on flames whose anchoring is displaced mechanically exhibit a very similar dynamics as acoustically perturbed flames, since both ways of forcing essentially act at the flame base region. Nevertheless, the analysis of the mechanically forced configurations does not rely on convected velocity perturbations, but rather on the fundamentals introduced in Chap. 1. This should provide some hints how to resolve the paradox described above.

Part II

Analysis of Acoustics-Flame Interactions of Slit Flames

So far, a review of the fundamental principles and modeling strategies regarding the acoustic response of premixed laminar flames has been provided. A variety of phenomena have been identified that need to be organized in a clear way. For that reason, Chaps. 1 and 2 presented the analysis of acoustically burner-stabilized flames as a continuation and extension of the studies on freely propagating flame sheets. This allows for a clear separation of the relevant canonical governing mechanisms, similar to how it has already been done for the case of flames whose anchoring is displaced mechanically [45, 63].

Contrary to the underlying idea of the structure of Part I, in the field of thermoacoustics, the understanding and modeling of acoustically perturbed burner-stabilized flames is essentially based on the notion of convected velocity perturbations. In order to provide a new perspective on the topic and to resolve the paradox consequences of the assumption of such convected perturbations, this Part of the thesis focuses rather on the dynamics of the acoustic field and the flame sheet than on the kinematics of the flow field upstream of the combustion zone. Therefore, Chap. 3 presents a new first principle-based low-order modeling approach. Based on it, Chap. 4 analyzes the interactions of acoustic perturbations with the flame sheet neglecting flame-flow feedback. Finally, Chap. 5 investigates the consequences of such a feedback from the flame onto the flow.

Parts of Chaps. 3 and 4 have already been published, see Steinbacher *et al.* [1]. Compared to this publication, significant changes have been applied: Essentially, the underlying modeling concept is introduced in more detail, now having a wider scope, and a Kutta condition is applied. Consequently, also the discussion and analysis of the results is updated. Nevertheless, the general statements and results of the original publication remain unchanged.

3 Flow-Decomposition Based Modeling Framework

A new low-order modeling framework for the interaction of acoustics with premixed flames is introduced. It relies on a Helmholtz decomposition combined with a flow-field representation based on flow-field singularities and a conformal mapping technique. The viscous mechanism of vortex shedding is included by use of a Kutta condition.

Low-order modeling approaches naturally require a simplification strategy that is often based on a decomposition of the overall problem into several simpler ones according to a predefined criterion. In this work, a Helmholtz-Decomposition based approach is chosen, which splits the flow into two contributions: an irrotational part that obeys to a flow potential, and a solenoidal or vortical part that identically satisfies continuity. The former is again split into a constant density and a flow expansion part that takes the combustion related density changes and the therewith accompanied acceleration of the flow into account. In doing so, it is easy to switch-off feedback of the flame onto the flow, as will be done in Chap. 4 to analyze primary acoustic-flame interactions. On the other hand, it also allows for a rather straight forward analysis of consequences of flame-flow feedback, which will be discussed in Chap. 5.

Decomposing the flow field into irrotational and solenoidal parts simplifies the flow problem by imposing some structure. For the purpose of allowing for a low-order treatment, however, some more simplifications are required. Hence, a slightly compressible 2D (slit) flow of an ideal fluid is assumed. In doing so, the overall flow-field can be constructed from a number of flow-field singularities, i. e. point sources and vortices. Applying a conformal mapping technique accounting for the boundary conditions, the rather complex dynamics of the overall system boils down to a number of less complex canonical problems. Special focus is put on the implementation of a Kutta condition, which accounts for viscous effects in the vicinity of sharp edges. A Slit flame configuration is chosen since it allows for a significantly simpler analytical treatment than conical ones. It will be explained in Chap. 6 how to relate the obtained results to other flame geometries.

Sec. 3.1 introduces the general idea of the chosen modeling approach that is based on the well-known Helmholtz-Decomposition. Based on this idea, acoustics-flame-flow interactions are analyzed and three perturbation flow modes are identified. In

Sec. 3.2, the considered problem is explicated in detail and the associated governing equations are derived. Sec. 3.3 introduces a low-order method for solving the posed problem relying on a finite number of flow field singularities combined with a conformal mapping technique and a Kutta condition adopted from aero-acoustics.

3.1 Helmholtz Decomposition

Any vector field u can be decomposed into an irrotational u_i and a vortical u_ω part. While the former is defined as the gradient of a potential ϕ

$$u_i = \nabla\phi, \quad (3.1)$$

the latter is computed from the curl of a vector potential ψ

$$u_\omega = \nabla \times \psi, \quad (3.2)$$

where $\nabla = \partial/\partial x_i$ denotes the nabla operator and “ \times ” the cross-product. In doing so, the divergence of the overall field $u = u_i + u_\omega$ solely depends on u_i , since $\nabla \cdot u = \nabla^2\phi$, and the curl of it solely on u_ω , since $\nabla \times u = -\nabla^2\psi$. Here, “ \cdot ” indicates a scalar product and $\nabla^2 = \partial^2/(\partial x_i \partial x_i)$ the Laplace operator. This approach is known as the Helmholtz Theorem or Helmholtz Decomposition [168, 169].

Why is this theorem useful for the analysis of acoustically perturbed flames? The main reason for this is based on the fact that irrotational and vortical flow components exhibit very different characteristics and properties, which help to bring some order into the complex field of acoustics-flame-flow interactions. The flow field of irrotational disturbances depends at every instant in time solely on the prevailing boundary conditions, such as the pressure at the in- and outlet, while the one of vortical perturbations is capable of showing transient phenomena not instantaneously governed by the boundaries. Lord Kelvin reflected this fact in his definition of a vortex as “... *a portion of fluid having any motion that it could not acquire by fluid pressure transmitted through itself from its boundary*” (Thomson [170], p. 225(§20)). It should be kept in mind that here the term vortex is used in order to describe the angular velocity of a point in continuous space, which would nowadays be rather referred to as *vorticity*. It is defined as the curl of the velocity field, i. e. $\omega = \nabla \times u$.

Another important property was found by Chu and Kovaszny [127] who showed that three modes of fluid motion can be identified: sound, vorticity and entropy. Far away from any boundary, they hardly interact with each other, such that any given vorticity or entropy perturbation is convected as a *frozen pattern*. This agrees with the findings of Helmholtz [168] stating that simple vortical structures are rather stable and stay well separated in space while they are transported by the local flow velocity. In this chapter, only the sound and vorticity flow mode shall be considered since our analysis is limited to perfectly premixed flames that should, particularly in the limit of

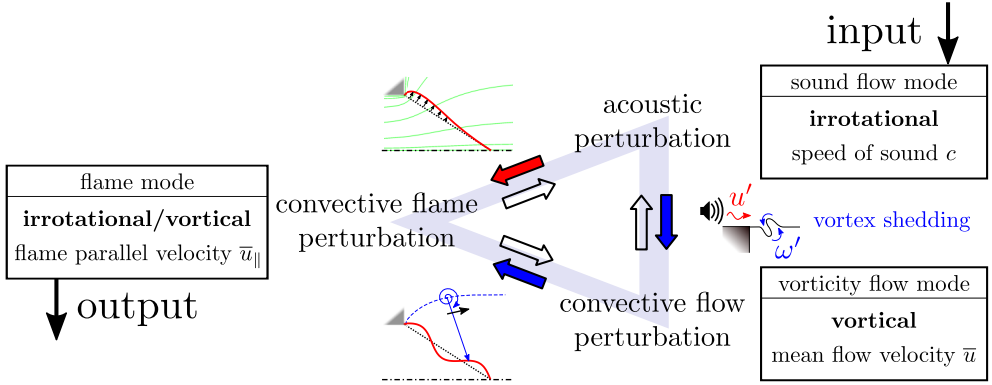


Figure 3.1: Overview of acoustics-flame-flow interactions. For evaluation of the (thermo-) acoustic flame response, sound perturbations serve as an input and fluctuations of the global heat release or the local flame displacement as an output of the considered system.

low Mach numbers and complete combustion, not exhibit any entropic perturbations [171, 172].

To summarize the discussion so far, the irrotational component of a velocity field depends solely on the instantaneous values of pressure and velocity at the boundaries, while the vortical one features convected, well separated structures (note that the analysis is limited to laminar flows!). In order to exploit this knowledge for the sake of bringing some order into the problem at hand, Fig. 3.1 shows an overview of acoustics-flame-flow interactions. Here, additionally to the aforementioned two flow modes, a *flame mode* is introduced, where flame displacements are transported along the steady state flame by a velocity \bar{u}_{\parallel} , see Sec. 1.2.4. It is usually accompanied by both vortical and irrotational flow perturbations proportional to the local flame displacement — details will be provided in Chap. 5. Since we are interested in the (thermo-) acoustic response of a flame, the sound flow mode constitutes the input of the analyzed system and changes of the global heat release rate, which result in a monopole-like source of sound, the output. Any immediate response to an impulsive input forcing of the system can predominately be assigned to direct interactions of the sound field with the flame, while any delayed output has to be attributed to memory-like effects of the vorticity and the flame mode.

We now have a closer look at the irrotational sound flow mode, which inherently neglects flow separation. The perturbation velocity field is thus computed as the gradient of an acoustic potential ϕ , which obeys a non-dimensional wave equation

$$\text{He}^2 \frac{\partial^2 \phi^*}{\partial t^{*2}} - \nabla^2 \phi^* = 0 \quad (3.3)$$

with the Helmholtz number He . The speed of sound is assumed to be constant and Mach numbers are low. Assuming that the characteristic length required for comput-

ing He is the length of the flame, we can express the Helmholtz number as a product of the Mach number Ma and the Strouhal number, i. e. $He = Ma f^*$. Strouhal numbers of interest for FTFs are at maximum of the order $\mathcal{O}(10)$, see Chap. 4, and Mach numbers of order $\mathcal{O}(10^{-2})$. Hence, He can be considered to be of maximum order $\mathcal{O}(10^{-1})$, which allows to safely drop the time dependent term in Eq. (3.3) for further analysis. The domain of interest is hence acoustically compact, which simplifies Eq. (3.3) to the now dimensional equation

$$\nabla^2 \phi = 0. \quad (3.4)$$

Consequently, the acoustic flow mode is governed by a Laplace equation and in the following we refer to the low Helmholtz number regime as the regime of compact acoustics.

Having discussed the properties of a Helmholtz decomposition and having introduced an overview of the relevant interactions governing the flame response in Fig. 3.1, the field is set to explicate the modeling approach pursued In this chapter as well as to introduce the investigated test case setups, which will be provided in the next two sections.

3.2 Problem Formulation and Governing Equations

A symmetric configuration as depicted in Fig. 3.2 shall be considered, where a Slit type flame is stabilized above a jet of perfectly premixed lean air-fuel mixture and excited by upstream velocity perturbations whose bulk value is given by $u'_{1,\text{blk}}(t) = 1/R_i \int_0^{R_i} u'_1(x_2, t) dx_2$. Assuming a high activation energy of the global chemical reaction and a Lewis number of about unity, the overall flow problem is split into a large-scale hydrodynamic and a thin, quasi-1D combustion zone, see Chap. 1.

A low Mach number macroscopic flow is assumed, which is regarded to be *slightly compressible* in the sense that density is only affected by the combustion process [100, 173]. Furthermore, the analysis shall be restricted to a 2D ideal fluid (zero viscosity, thermal and mass diffusivity) without any volume or body forces. Viscous effects will be incorporated by use of a Kutta conditions. This results in a flow problem that is governed by

$$\nabla \cdot u = -\frac{1}{\rho} \frac{D\rho}{Dt} \quad (3.5)$$

$$\frac{Du}{Dt} = -\frac{1}{\rho} \nabla p, \quad (3.6)$$

where $D(\cdot)/Dt = \partial(\cdot)/\partial t + u \cdot \nabla(\cdot)$ is the material derivative and u , ρ and p denote flow velocity, density and pressure, respectively.

The density-gradient dependent source term on the right-hand side of continuity Eq. (3.5) vanishes everywhere but in the immediate vicinity of the flame front. Here

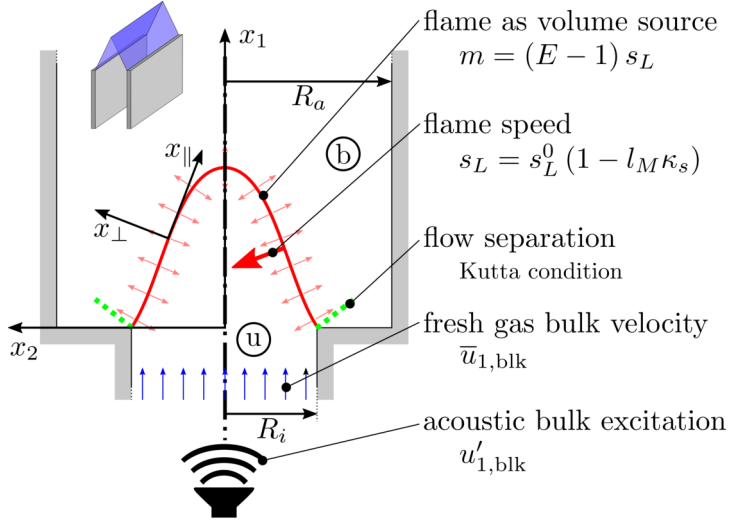


Figure 3.2: A Slit type flame is stabilized above a stream of unburned mixture (“u”) with a bulk flow velocity $\bar{u}_{1,\text{blk}}$ and subjected to upstream bulk velocity perturbations $u'_{1,\text{blk}}$. The flame propagates normal to itself by a flame front curvature κ dependent speed s_L and acts as a volume source of strength m . Two coordinate systems are used, namely laboratory coordinates (x_1, x_2) and flame aligned coordinates $(x_{\parallel}, x_{\perp})$ where x_{\perp} points along the local flame normal direction towards the burned gas (“b”).

it acts as a source of volume, which leads to a volume production per unit length of the flame of $m = Es_L$ [173, 174], where $E = \rho_u / \rho_b - 1$ denotes the non-dimensional density increase and the indices “u” and “b” indicate a quantity of the unburned and burned flow, respectively. Introducing a kernel $D(x_{\perp})$ capturing the spatial distribution of the volume production along the flame normal direction x_{\perp} , see Fig. 3.2, Eq. (3.5) can be rewritten as

$$\nabla \cdot u = mD(d(x, x_f)) \quad (3.7)$$

with $\int_{-\infty}^{\infty} D(x)dx = 1$ and $d(x, x_f)$ denoting the distance from a point x to the flame front x_f .

Taking the curl of the momentum Equation (3.6) leads to a transport equation for vorticity ω

$$\frac{D\omega}{Dt} = \frac{1}{\rho^2} (\nabla\rho \times \nabla p). \quad (3.8)$$

Here, the dilatation term $-\omega(\nabla \cdot u)$ was neglected since it only is non-zero right at the flame front and the unburned flow field is assumed to be free of vorticity. Furthermore, Matalon *et al.* [41] argued that contributions of this term are negligible across the flame sheet. Thus, for 2D inviscid flows, the dominant source term of the vorticity transport equation is the baroclinic torque, which arises from a misalignment of

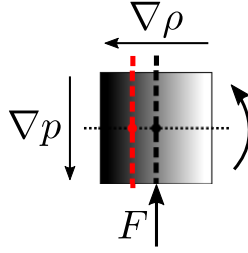


Figure 3.3: Illustration of a parcel of fluid exhibiting a horizontal gradient in density ρ (\propto shade of gray) that is exposed to a vertical gradient in pressure p leading to a force F accelerating the parcel. Due to the density gradient, the center of gravity of the fluid parcel (red line) is shifted away from the geometrical center (black line) and, hence, the parcel of fluid would start to rotate in counter-clockwise direction.

the pressure and density gradients, see Fig. 3.3. For a detailed and rather complete description of how vorticity interacts with a flame sheet, it is referred to the works of Hayes [175] and Berndt [176]. We eliminate the pressure term in Eq. (3.8) by use of Eq. (3.6) and obtain

$$\frac{D\omega}{Dt} = \frac{1}{\rho} \left(\frac{Du}{Dt} \times \frac{\nabla\rho}{\rho} \right) \quad (3.9)$$

[177]. From the left-hand side of this equation it becomes clear that, in the absence of any density gradient $\nabla\rho$, vorticity is transported like a massless particle. The movement of any hypothetical point vortex whose spatial position may be defined by x_ω is governed by

$$\frac{dx_\omega}{dt} = u(x_\omega) \quad (3.10)$$

with $u(x_\omega)$ being the flow velocity right at the vortex position.

Using Eqs. (3.7) and (3.9), the flow problem depicted in Fig. 3.2 is solved by decomposing the flow field u into two irrotational parts u_c and u_e , where the former is caused by a pressure difference between in- and outlet of the domain initiating the volume flux through the combustor. The latter captures effects of the volume expansion across the flame. Further, a vortical part u_ω is introduced that represents the rotational parts of the flow field. In summary, the decomposition is written as

$$u = u_c + u_e + u_\omega, \quad (3.11)$$

see [100, 128, 173, 178]. While the irrotational components each have a potential $u_{c/e} = \nabla\phi_{c/e}$, the vortical component depends on a stream function via $u_\omega = \nabla \times \psi_\omega$. Application of these relations, together with continuity Equation (3.7) and the de-

composition of Eq. (3.11) results in the three Poisson equations

$$\nabla^2 \phi_c = 2 \frac{\dot{V}(t)}{R_i} \delta(x_1 - x_{1,\text{EF}}) \quad (3.12)$$

$$\nabla^2 \phi_e = mD(d(x, x_f)) \quad (3.13)$$

$$\nabla^2 \psi_\omega = -\omega \quad (3.14)$$

with the Laplace operator $\nabla^2 = \partial^2 / (\partial x_i \partial x_i)$. Note that u_c is subject to a line source at $x_{1,\text{EF}} = -\infty$, which generates a volume flux $\dot{V}(t) = [\bar{u}_{1,\text{blk}} + u'_{1,\text{blk}}] R_i \Delta x_3$ through the combustor that is driven by a potential (or pressure) gradient between $x_1 = -\infty$ and $x_1 = +\infty$. All boundaries shall be impermeable and the axial velocity gradients shall vanish far up- and downstream the flame: $\partial u / \partial x_1|_{\pm\infty} = 0$. Note that Eq. (3.12) constitutes the non-homogeneous equivalent to the Laplace Eq. (3.4), which was derived from the acoustic wave equation.

The dynamics of the flame sheet is captured by the G-equation approach, as explicated in Sec. 1.3. The G -field, so far, has no other physical meaning than the fact that its zero iso-line represents the instantaneous position of the flame front. Therefore, we are in principle free to define it to any spatial function as long as the position of the zero iso-line remains untouched (excluding numerical issues). For the problem at hand, it is beneficial to define G to be a signed distance function, i. e. its value at a position $G(x)$ represents the distance from this point to the flame front located at $G(x_f) = 0$. This property allows for a straight forward evaluation of the argument of the function $D(x)$ in Eq. (3.13) as $d(x, x_f) \equiv G(x)$. The G-equation writes

$$\frac{DG}{Dt} = s_L^0 \left(1 + l_M \nabla \cdot \frac{\nabla G}{\|\nabla G\|} \right) \|\nabla G\|. \quad (3.15)$$

and, consequently, its dynamics depends on the underlying flow field as well as on the local, stretch dependent flame speed. Here, only flame stretch related to flame curvature is considered, whose importance is quantified by the Markstein length l_M , which is a length of the order of the flame thickness. Inserting $G = x_\perp - \xi(x_\parallel, t)$ into Eq. (3.15) and linearizing the resulting expression with respect to ξ leads to a 1D description of the flame front in flame aligned coordinates

$$\frac{\partial \xi}{\partial t} + \bar{u}_\parallel \frac{\partial \xi}{\partial x_\parallel} = u'_\perp + l_M s_L^0 \frac{\partial^2 \xi}{\partial x_\parallel^2} \quad (3.16)$$

where \bar{u}_\parallel denotes the mean flow velocity in flame-parallel direction.

Eq. (3.9) together with Eqs. (3.12)-(3.14) and (3.15) define the flow problem. Additionally, in the case of $E > 0$, a volume production kernel D has to be defined. One major difficulty in solving this problem constitutes the impermeability boundary conditions together with the non-trivial considered geometry (backward facing step combustor), another the trailing edge where the flow separates. In this work, we address the former issue by use of a Schwarz-Christoffel mapping technique and the latter by application of a Kutta condition at the trailing edge. Both are introduced in the following.

The coordinate system used to describe the combustor shown in Fig. 3.2 is illustrated in Fig. 3.4. Due to symmetry, we limit ourselves to only one half of the domain. Complex variables are used to describe the 2D problem: Coordinates in the physical domain are represented by $x = x_1 + i x_2$ where x_1 denotes the axial and x_2 the spatial direction, perpendicular to the first. Accordingly, velocities are expressed by $u = u_1 + i u_2$. In the image domain, the complex variable $\xi = \xi_1 + i \xi_2$ is used to specify location.

All corners of the flow domain are named by capital letters (A to E) and are mapped to points on the real axis of the image domain. At edge A, the feed channel opens into the combustion chamber. This edge is mapped to $\xi = 1$. Points E and F are located at $x_1 = -\infty$ in the physical domain and are mapped to $\xi = 0$ in the image domain. The mapping is defined by

$$x(\xi) = \frac{R_a}{\pi} \left[\cosh^{-1} \left(\frac{2C_r^2 \xi - 1 - C_r^2}{1 - C_r^2} \right) - C_r \cosh^{-1} \left(\frac{(1 + C_r^2)\xi - 2}{(1 - C_r^2)\xi} \right) \right] \quad (3.17)$$

with the confinement ratio $C_r = R_i / R_a$ [179]. This mapping can only be inverted numerically, therefore, evaluation of $\xi(x)$ requires the application of a numerical root finding algorithm.

The complex conjugate, denoted by $\tilde{(\cdot)}$, of the velocity in the physical domain is computed by application of the chain rule

$$\tilde{u}(x) = \frac{d\phi(\xi(x))}{d\xi} \frac{d\xi(x)}{dx}. \quad (3.18)$$

The first term in this equation is the derivative of the flow potential ϕ with respect to the image domain coordinate ξ , the second the first derivative of the mapping with respect to the physical coordinate x . The latter writes for the combustor geometry

$$\frac{d\xi(x)}{dx} = \pi \frac{\xi(x)}{R_a} \left[\frac{\xi(x) - C_r^{-2}}{\xi(x) - 1} \right]^{\frac{1}{2}}. \quad (3.19)$$

Using these relations, we are able to compute the velocity field in the physical domain due to any potential $\phi(\xi)$ given in the image domain. Knowing that any point source or vortex maps to its counterpart in the image domain by conserving its strength — i. e. volume production and circulation, respectively — and vice versa, we are able to define a potential field as the superposition of several point sources and vortices. By mapping these points to the image domain, Eq. (3.18) can be used in order to compute the associated physical velocity field that complies with the boundary conditions. This process is explicated in more detail in the following section.

3.3.2 Flow-Field Singularities

The solution of a Poisson equation $\nabla^2 \phi = c$ together with a set of boundary conditions and a Dirac Delta function as non-homogeneous part $c = \delta(x - x')$ is known as

the Green's function $G(x, x')$ of this problem. Here, the Dirac Delta function constitutes a point source whose 2D-spatial position is given by $x' = (x'_1, x'_2)$. Knowing the respective Green's function, the solution of the Poisson equation for an arbitrary non-homogeneous part $c(x)$ is computed as the spatial convolution of the Green's function with a given $c(x)$. Simplifying the problem by assuming free-space boundary conditions, i. e. the potential ϕ asymptots to zero at infinity, a so-called free-space Green's function

$$G(x, x') = \frac{1}{2\pi} \ln \left[\sqrt{(x_1 - x'_1)^2 + (x_2 - x'_2)^2} \right] \quad (3.20)$$

emerges. By mapping the non-homogeneous part of a Poisson equation to the image domain, a solution that is conform with the impermeability boundary conditions at the walls is easily constructed by solely relying on free-space Green's functions. This simplifies the analysis and will be explicated in the following.

First of all, we need to constitute that there are two types of non-homogeneous functions, which are volume sources and vortices, see Eqs. (3.12)–(3.14). Applying Green's Function (3.20) in the image domain (complex coordinate ξ), the complex conjugate of the irrotational velocity component due to a point source of strength S at position ξ' becomes

$$\tilde{u}_{c/e}(\xi, t) = \frac{S}{2\pi} \frac{1}{\xi - \xi'}. \quad (3.21)$$

Similarly, we get for the solenoidal (vortical) velocity due to a point vortex of strength Γ at the same position

$$\tilde{u}_\omega(\xi, t) = -i \frac{\Gamma}{2\pi} \frac{1}{\xi - \xi'}. \quad (3.22)$$

In the image domain, all walls are mapped to the real axis. Therefore, in order to fulfill the impermeability boundary conditions at all walls, mirror sources of equal strength S are placed in the lower half of the complex plane by mirroring the source locations at the real axis. This simply corresponds to computing the complex conjugate of the original source position $\tilde{\xi}'$. Equivalently, mirror vortices of opposite strength are introduced. In doing so, velocity components normal to the real axis vanish and the volume flux through all walls is zero. This is illustrated in Fig. 3.5 for a single vortex.

In the proposed model, the vortical part of the overall perturbation velocity field is approximated by a finite number of N point vortices of strengths $\Delta\Gamma'_n$, which results in an expression for the velocity in the image domain of

$$\tilde{u}_\omega(\xi, t) = -\frac{i}{2\pi} \sum_{n=1}^N \Delta\Gamma'_n \frac{\xi'_n - \tilde{\xi}'_n}{(\xi - \xi'_n)(\xi - \tilde{\xi}'_n)}, \quad (3.23)$$

where mirror vortices of opposite circulation have been placed at the complex conjugate coordinates $\tilde{\xi}'_n$ of all vortices.

The potential part of the perturbation velocity field that drives the volume flux through the combustor can be computed by placing a source of strength

$$S(t) = 2u'_1(t)R_i \quad (3.24)$$

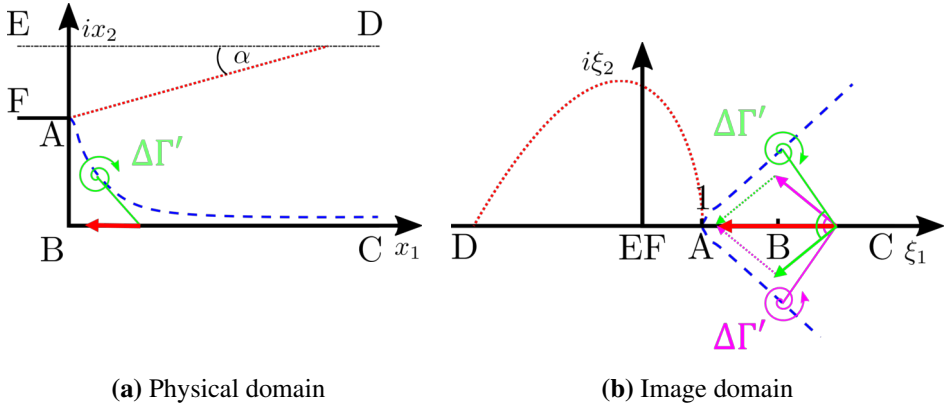


Figure 3.5: Illustration of how impermeability boundary conditions are met by use of a mirror vortex (not to scale): the wall normal velocity component of the original vortex of strength $\Delta\Gamma'$ (green) is canceled by its mirror counterpart (pink) such that the resulting velocity (red) is parallel to the walls in the image (3.5b) as well as in the physical domain (3.5a). Here, the shear layer and the flame front are shown as blue dashed and red dotted lines, respectively.

at $\xi_{EF} = 0$ since all points of $x_1 \rightarrow -\infty$ are mapped to a single point in the image domain (EF). Following Eq. (3.21), the complex conjugate of the associated velocity field is computed in the image domain as

$$\tilde{u}_c(\xi, t) = \frac{S(t)}{2\pi\xi}. \quad (3.25)$$

Resulting stream lines are shown in green in Fig. 3.4, one time in the image and one time in the physical domain.

3.3.3 Kutta Condition

Following Eqs. (3.18) and (3.19), the flow field of the combustor geometry exhibits a $\mathcal{O}((\xi - 1)^{-1/2})$ singularity at edge A, which results from the fact that, in reality, a viscous flow cannot follow the abrupt 90° turn of the wall contour, since this would require an infinitely high pressure gradient. The lack of such high gradients leads to the separation of the flow and vorticity, originally bound in the wall boundary layer, is shed into the inner region of the flow domain. In the modeling framework adopted here, this singularity is removed by employing a Kutta condition. Its application recovers a finite-valued velocity at the edge, which can only be ensured by demanding

$$\left. \frac{d\phi}{d\xi} \right|_{\xi=1} \stackrel{!}{=} 0, \quad (3.26)$$

see Eq. (3.18). In order to meet this condition, vorticity is introduced in the vicinity of edge A, which implies the formation of a thin shear layer. It should be pointed out that in the case of an anchored flame, getting rid of the singularity is compulsory since otherwise the infinitely high velocity at the anchoring would lead to unbound displacement amplitudes at this point.

Concerning the validity of a Kutta condition, at least some qualitative statements can be found in the literature. Crighton [181] published an extensive review article on the Kutta condition in unsteady flows stating that “*within restricted parameter ranges, only those ‘outer’ potential flows that satisfy a Kutta condition are, in general, compatible (in the matched asymptotic expansion sense) with an acceptable multilayered ‘inner’ viscous structure*” (Crighton [181], p.412). Williams [182] made a more cautious statement in a review article on aeroacoustics: “*There is no proof that the solution obtained through the matched-expansion scheme is, in fact, a solution of the real problem — but it usually is [...]*” (Williams [182], p.449). Generally, in the field of aero-acoustics, application of a Kutta condition is considered to be an acceptable principle for modeling flows around sharp edges [183, 184]. The results computed in this chapter compare well with the CFD/SI data and hence confirm the aforementioned assertions, as will be shown below. Nevertheless, it should be kept in mind that a Kutta condition does not naturally appear when simplifying the governing equations of a viscous flow but rather has to be viewed as an ad hoc hypothesis that allows to incorporate viscous effects into an inherently inviscid flow description.

In the literature, several methods have been proposed in order to implement a Kutta condition. A method relying on a single vortex ensuring a finite valued velocity at a sharp edge of an acoustically excited flow of zero mean flow was first developed by Brown and Michael [185, 186]. It was adopted by several later studies, e. g., [187, 188]. The idea of this approach is that during both the positive and negative part of a forcing cycle, shed vorticity accumulates in a single vortex, which represents the rolled up shear layer.

A more advanced method is the *single panel* method [124, 189–191], which introduces a vortex sheet (the *panel*) of length H_x and constant strength γ_x that is attached to the trailing edge. The strength and length of this sheet depend on the instantaneous flow field and are set such that the edge singularity is removed. At each time step, the circulation confined to the sheet is condensed into one point vortex and advected by the local flow velocity. The work presented in this chapter relies on such a single panel method.

The shape of the vortex panel is defined by two geometrical parameters: Its length H_ξ and its angle with respect to the real axis β_ξ , both measured in the image domain as illustrated in Fig. 3.6. Ideally, the strength of the vortex sheet in the physical domain

$$\gamma_x(x) = \frac{d\Gamma(x)}{dx} \quad (3.27)$$

is constant, where $\Gamma = \int_A \omega dS$ is the circulation, defined as the integral of vorticity ω

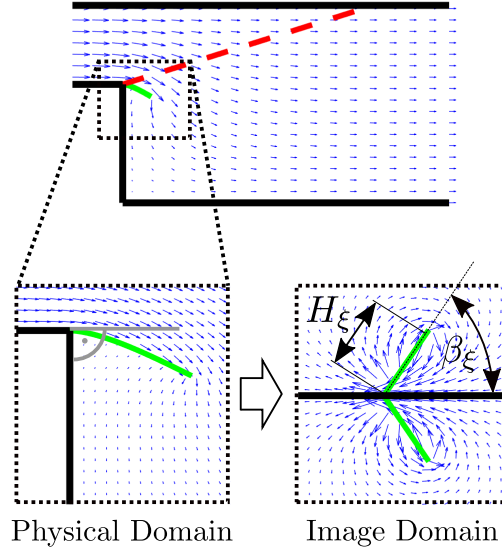


Figure 3.6: Flow field according to source at $\xi = 0$ and a Kutta panel (green), shown for the whole combustor (top). Additionally, a close up view of the Kutta panel is shown in the physical (bottom left) and the image domain (bottom right), with $C_r = 0.4$, $H_\xi = 2.1$ and $\beta_\xi = \pi/3$.

over an area A . We, therefore, need to define the panel strength in the image domain $\gamma_\xi(\xi)$ such that it maps back to a constant distribution in the physical domain $\gamma_x(x)$. Following the chain rule, we get

$$\gamma_x = \gamma_\xi \frac{d\xi}{dx} \quad (3.28)$$

and, hence, we would have to impose a distribution of $\gamma_\xi \propto dx/d\xi$ in the image domain in order to get a constant value in the physical domain. We call this the ideal distribution of vorticity in the following. The flow field corresponding to such a distribution, however, could not be solved analytically (by the author of this thesis). Therefore, a simplified distribution

$$\gamma_\xi(\xi') = c_1 \frac{\sqrt{\xi' - 1}}{\xi'} \quad (3.29)$$

is used, where ξ' parametrizes the vortex sheet and c_1 its strength. Fig.3.7 compares the ideal vorticity distribution of $dx/d\xi$, i. e. $\gamma_\xi = c_1 [s_\xi/(\xi - C_r^{-2})]^{1/2}/\xi$ (—) with the approximation according to Eq. (3.29) (- - - and - · - · -). Here, s_ξ and s_x denote the panel aligned coordinates in the image and the physical domain, respectively. It becomes clear that the approximation is a good model in the limit of short panel lengths and low confinement ratios. Note that the $C_r = 0.4$ and $H_x/R_i = 0.4$ case corresponds

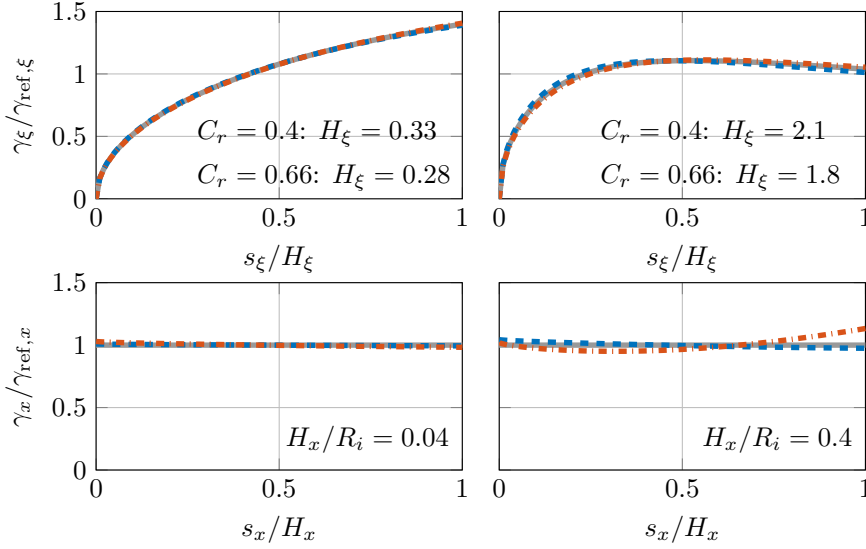


Figure 3.7: Normalized vorticity plotted over panel coordinates in the image (top) and the physical (bottom) domain for two panel lengths $H_x/R_i = 0.04$ (left) and $H_x/R_i = 0.4$ (right), where R_i is kept constant. Shown are two vorticity distributions, $\gamma_\xi = c_1 s_\xi^{1/2}/\xi$ (---, ---) and $\gamma_\xi = c_1 [s_\xi/(\xi - C_r^{-2})]^{1/2}/\xi$ (—). For the former, two confinement ratios $C_r = 0.4$ (---) and $C_r = 0.66$ (---) are depicted, whereas for the latter both coincide to the same line. As reference vorticity $\gamma_{\text{ref}, x/\xi}$, the mean vorticity along the panel was chosen.

to a situation as shown in Fig. 3.6, which should provide a rough feeling of what these numbers mean. It should be kept in mind that, for a given length H_ξ , a lower confinement ratio corresponds to a longer panel in the physical domain. Hence, judging from the results of Fig. 3.7, the lengths of such Kutta panels should be of the order of $H_\xi \leq \mathcal{O}(10^1)$ in order to have a constant distribution of vorticity in the physical domain. Explicitly evaluating the vorticity distribution associated with Eq. (3.29) we get in the physical domain

$$\gamma_x(x) = c_1 \frac{\pi}{R_a} \sqrt{\xi(x) - C_r^{-2}}, \quad (3.30)$$

which states that $\gamma_x(x)$ stays constant along a circle around edge B ($\xi_B = C_r^{-2}$). Thus, the quotient of the distance of the Kutta panel to point B over the panel length H_x needs to be large in order to have an approximately constant vorticity distribution.

The angle of the panel in the image domain β_ξ is determined such that the flow follows the wall contour of the feed duct, see Fig. 3.6. Hence, the angle between the separating shear layer and the back plate of the combustion chamber should be 90° right at the edge. Knowing that the angle between the feed duct wall and the back

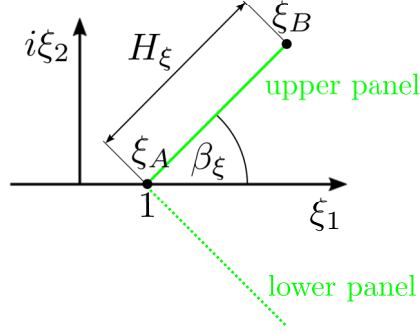


Figure 3.8: Sketch of the Kutta panel (upper) and its mirror counterpart (lower) in the image domain. The starting point of the Kutta panel is named ξ_A and its ending ξ_B .

plate is 270° , which corresponds to an angle of 180° in the image domain, the desired 90° angle corresponds to $\beta_\xi = 60^\circ$ or, in radians, $\beta_\xi = \pi/3$. It will be shown below that this angle is indeed a special one, since imposing such an angle, the velocity right beneath the point where the panel is attached vanishes.

We now evaluate, for a given velocity field, the respective panel strength c_1 that satisfies the Kutta condition. This requires the evaluation of the velocity field imposed by the Kutta panel. In doing so, we firstly need to evaluate the gradient of the potential ϕ_p associated with the panel in the image domain. Assuming a vorticity distribution according to Eq. (3.29) we need to evaluate an integral

$$\frac{d\phi_p}{d\xi} = -\frac{i}{2\pi} \int_{\xi_A}^{\xi_B} c_1 \frac{\sqrt{\xi'-1}}{\xi-\xi'} d\xi', \quad (3.31)$$

where all relevant quantities are sketched in Fig. 3.8. Solving this integral, we get

$$\begin{aligned} \frac{d\phi_{p,up}}{d\xi} = & \frac{i}{\pi} \frac{c_1}{(\xi-1)\exp(-i\beta_\xi)+1} \left[\arctan\left(\sqrt{H_\xi}\right) \right. \\ & \left. - \sqrt{(1-\xi)\exp(-i\beta_\xi)} \arctan\left(\sqrt{\frac{H_\xi}{(1-\xi)\exp(-i\beta_\xi)}}\right) \right] \exp(-i\beta_\xi). \end{aligned} \quad (3.32)$$

Here, the index “*up*” signifies that only the potential of the original Kutta panel is respected, which is found in the upper half of the image domain as depicted in Fig. 3.8. The solution for the associated mirror panel, placed in the lower half of the complex plane (index “*low*”), is the same as the one given by Eq. (3.32), but with a negative sign and a negative angle β_ξ . Accordingly, it writes

$$\begin{aligned} \frac{d\phi_{p,low}}{d\xi} = & -\frac{i}{\pi} \frac{c_1}{(\xi-1)\exp(i\beta_\xi)+1} \left[\arctan\left(\sqrt{H_\xi}\right) \right. \\ & \left. - \sqrt{(1-\xi)\exp(i\beta_\xi)} \arctan\left(\sqrt{\frac{H_\xi}{(1-\xi)\exp(i\beta_\xi)}}\right) \right] \exp(i\beta_\xi). \end{aligned} \quad (3.33)$$

The superposition of both results in the overall expression for the panel, namely $d\phi_p/d\xi$.

Equations (3.32) and (3.33) can now be used in order to compute the strength of the vortex sheet c_1 (including the mirror panel!). From Condition (3.26) we know that the gradient of the overall potential needs to vanish at edge A ($\xi = 1$). Assuming the potential resulting from a superposition of all flow field singularities (vortices and sources) except the Kutta panel may be denoted as ϕ_Σ , this condition translates to

$$\left. \frac{d\phi_p}{d\xi} \right|_{\xi \rightarrow 1} = - \left. \frac{d\phi_\Sigma}{d\xi} \right|_{\xi=1}. \quad (3.34)$$

Combining Eqs. (3.32)–(3.34) and solving for c_1 leads to

$$c_1 = - \left. \frac{d\phi_\Sigma}{d\xi} \right|_{\xi=1} \frac{\pi}{2 \arctan(\sqrt{H_\xi}) \sin(\beta_\xi)}. \quad (3.35)$$

Using these relations and following Eq. (3.18), we can compute the complex conjugate of the resulting flow velocity in the physical domain as

$$\begin{aligned} \tilde{u}(x) &= \frac{d\xi}{dx} \left[\frac{d\phi_\Sigma}{d\xi} + \frac{d\phi_p}{d\xi} \right] \\ &= \frac{d\xi}{dx} \left[\frac{d\phi_\Sigma}{d\xi} + \frac{d\phi_{p,up}}{d\xi} + \frac{d\phi_{p,low}}{d\xi} \right]. \end{aligned} \quad (3.36)$$

This expression respects the Kutta panel as well as its mirror counterpart plus the impact of all other flow field singularities. We now evaluate the right-hand and left-hand limits (with respect to the real part of ξ) of the velocity fields at the separation point A and get

$$\tilde{u}^+ = \lim_{\xi \rightarrow 1^+} \tilde{u}(x(\xi)) = \frac{\pi}{R_a} \sqrt{1 - C_r^{-2}} \left. \frac{d\phi_\Sigma}{d\xi} \right|_{\xi=1} \frac{\pi \cos(\frac{3}{2}\beta_\xi)}{2 \arctan(\sqrt{H_\xi}) \sin(\beta_\xi)} \quad (3.37)$$

and

$$\tilde{u}^- = \lim_{\xi \rightarrow 1^-} \tilde{u}(x(\xi)) = - \frac{\pi}{R_a} \sqrt{1 - C_r^{-2}} \left. \frac{d\phi_\Sigma}{d\xi} \right|_{\xi=1} \frac{i\pi \sin(\frac{3}{2}\beta_\xi)}{2 \arctan(\sqrt{H_\xi}) \sin(\beta_\xi)}, \quad (3.38)$$

respectively. If we insert $\beta_\xi = \pi/3$, the right-hand limit of Eq. (3.37) simplifies to $\tilde{u}^+ = 0$ and the left-hand one of Eq. (3.38) to

$$\tilde{u}^- = - \frac{\pi}{R_a} \sqrt{1 - C_r^{-2}} \left. \frac{d\phi_\Sigma}{d\xi} \right|_{\xi=1} \frac{i\pi}{2 \arctan(\sqrt{H_\xi}) \sin(\frac{\pi}{3})}. \quad (3.39)$$

This reflects the fact that the left-hand limit constitutes the jet velocity at the separating edge, while the right-hand limit evaluates the flow velocity at the side of the recirculation bubble, see Fig. 3.6. From Eq. (3.39) it becomes clear that, at edge A,

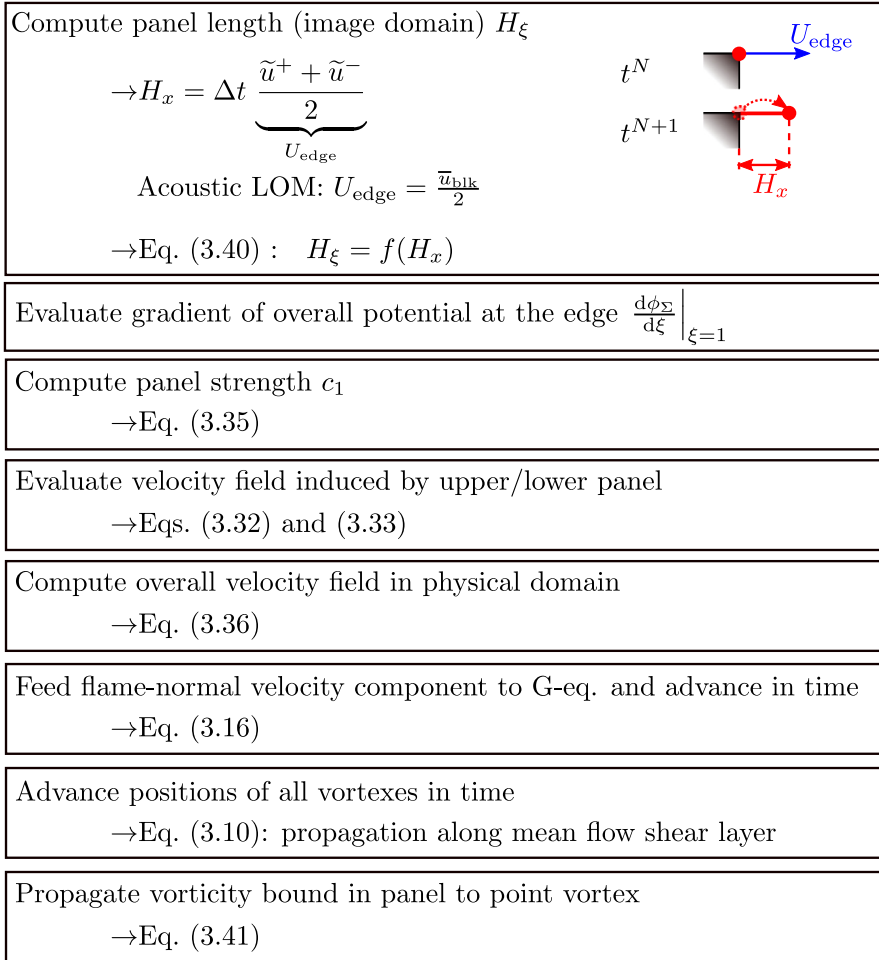


Figure 3.9: Summary of all computations that need to be performed during one time step when considering a Kutta condition.

multiplication of the local velocity $d\phi_\Sigma/d\xi|_{\xi=1}$ with the complex unit i bends the flow by 90° , which leads to the desired separation.

For the sake of completeness, it should be mentioned that one of the major difficulties encountered during the derivation of the Kutta condition concerns branch cuts, which are curves across which the resulting flow field is discontinuous. In this regard a Kutta panel is such a branch cut. Hence it has to be ensured that the branch cuts associated with the Kutta panels used do not exceed their desired lengths and, in doing so, impose spurious discontinuities. In the implementation presented here, this property has been verified.

Finally, it is explicated how the methods described above are used in order to numerically simulate the process of vortex shedding. An overview of all required computations is provided in Fig. 3.9. First of all, in each time step the length of the vortex

sheets H_ξ needs to be computed, which is done by assuming a transport velocity of the vorticity bound in the separating shear layer of $U_{\text{edge}} = (\tilde{u}^+ + \tilde{u}^-)/2$. Multiplication of this velocity with the time step length Δt results in the panel length in the physical domain H_x . Note that in the proposed acoustic LOM, an approximation $U_{\text{edge}} = \bar{u}_{\text{blk}}/2$ is used, which avoids the evaluation of a mean flow state. This approach implicitly assumes a block flow profile in the feed channel and zero velocity in the recirculation zone. Subsequently, H_ξ is numerically evaluated as the root of

$$\int_0^{H_\xi} \left| \frac{dx(s_\xi(t))}{d\xi} \right| dt - H_x = 0, \quad (3.40)$$

where a parametrization $s_\xi(t) = 1 + \exp(i\beta_\xi)t$ of the curve representing the Kutta panel is used (note that, here, t denotes the parametrization parameter not the time). Based on this length, the Kutta condition can be applied according to Eqs. (3.35),(3.32), (3.33) and (3.36). The total circulation of the resulting panel is then provided by

$$\Gamma'_p = \int_0^{H_\xi} c_1 \frac{\sqrt{t}}{|1 + \exp(i\beta_\xi)t|} dt. \quad (3.41)$$

After each time step, this integral is numerically evaluated employing the trapezoidal rule and its respective value of Γ'_p propagated to a new point vortex, which is placed at end of the vortex panel from which it resulted.

3.4 Summary

In this chapter, a low-order modeling approach for the dynamics of acoustically perturbed burner-stabilized 2D flames was derived. It is essentially based on first principles and relies on the assumption of an inviscid, slightly compressible flow whose density is solely affected by the combustion process. Imposing a Helmholtz decomposition, three velocity components need to be modeled: (i) an irrotational field related to the pressure difference between in- and outlet of the domain, (ii) a second irrotational field associated to the volume flux generated by the flame and (iii) a solenoidal velocity field containing all vortical contributions. It is assumed that vorticity is only generated by the flame sheet as well as by a Kutta condition capturing the shedding of vorticity at sharp edges.

Relying on a conformal mapping technique and a finite number of flow field singularities, the overall problem could be split into several canonical problems. This clarifies the solution process and allows to simply switch certain physical mechanisms on and off in order to evaluate their individual contributions. This approach will be applied to the case of a 2D Slit flame in the following.

4 Primary Interactions

Based on a rigorous analysis neglecting flame-flow feedback and relying on methods presented in Chap. 3, it is found that predominantly irrotational velocity perturbations interact with a flame having maximum impact at the base region, while the impact of shed vorticity is negligible. A significant discrepancy between the modeled response and high fidelity CFD data is observed, which is attributed to flame-flow feedback — a mechanism neglected in this chapter.

The basic idea of this chapter is to take a first step towards the identification and modeling of the skeletal processes governing acoustics-flame interactions. To this end, flame-flow feedback as well as thermal-diffusive mechanisms shall be neglected and only the remaining interactions of acoustics with the flame shall be analyzed. More specifically, the modeling approach introduced in the previous chapter shall be exploited in order to resolve the paradoxical finding concerning the convective velocity model explained in Chap. 2. This model assumes that acoustically excited premixed (Bunsen) flames are subject to convected velocity perturbations, which are responsible for the observed wrinkling of the flame front. Several studies, however, demonstrated that these convected perturbations are rather a consequence than a source of flame front wrinkles, caused by a feedback of the flame on the flow. Therefore, the assumption of convected velocity perturbations seems to violate causality (they cannot be source and consequence at the same time). In this chapter, it shall be investigated if vortex shedding imposes significant levels of convected velocity perturbations onto the flame front. If that is the case, causality may at least partly be respected by convective velocity models.

From an analytical point of view, it has to be noted that acoustic perturbations propagate at the speed of sound and, consequently, a convective flow perturbation cannot be assigned to the acoustic flow mode. Thus, an acoustic-to-hydrodynamic mode conversion is required in order to generate perturbations that are transported with the local flow velocity. Following Fig. 3.1, one possible candidate for such a mode conversion mechanism is the process of flow separation, which can happen at sharp corners, e. g. at a backward-facing step or bluff body flame holder. At the separation point, vorticity, originally confined to the wall boundary layers, is shed into the interior of the flow domain. Transient (acoustic) forcing of a separating flow leads to unsteady generation and shedding of vorticity [124, 190, 192]. Vortical structures that are advected

downstream by the flow represent an acoustic damping mechanism [123] and may — more important in the context of this study — interact with the flame front. Using a 2D compressible flow solver, which allowed to artificially modify the gas expansion, Schlimpert et al. [104] showed for an unconfined flame that vortical structures significantly affect the flame front in the case of negligible gas expansion. With realistic gas expansion, however, the influence of shed vorticity is substantial only right at the flame base.

In this Chapter the issue of flow-flame interactions is revisited by decomposing the acoustic velocity disturbance into an irrotational potential and a solenoidal vortical field and analyzing how both interact with the flame. For this purpose, the modeling framework introduced in Chap. 3 is adopted and applied to the analysis of acoustic-flow-flame interactions at a duct singularity. Of particular interest is an assessment of the impact of shed vorticity on the flame front and if and how it contributes to the convective nature of the FTF. In order to suppress the occurrence of vortical structures due to flame-flow feedback, we neglect exothermicity/gas expansion in the perturbations. This assumption is in line with the assumptions of the convective velocity model. The mean flow field, required to compute vortex advection, is nevertheless retrieved from exothermic numerical simulations.

In this chapter, the effect of gas expansion is explicitly excluded from the analysis, i. e. $E = 0$. Thus, due to $m = 0$, Eq. (3.13) drops from the analysis and the baroclinic torque source term vanishes, which eliminates the right-hand side of Eq. (3.9). In the remaining problem, the only source of vorticity is vortex shedding. To simplify the analysis, curvature (stretch) effects are neglected and hence $l_M \equiv 0$.

Sec. 4.1 introduces the specific test case setups as well as the high-fidelity CFD results, which serve as validation cases of the developed model. The resulting low-order model is then analyzed and compared to high fidelity CFD data in terms of flame sheet and global heat release dynamics in Sec. 4.2.

4.1 Test Case Setups

The modeling framework derived in this chapter is applied to a backward facing step combustor, as shown in Fig. 4.1. Configurations of two different confinement ratios $C_r = R_i/R_a$ of $C_r = 0.4$ (upper half) and $C_r = 0.66$ (bottom half) are analyzed, with R_i denoting the feed channel and R_a the combustion chamber half width. The coloring represents the steady state velocity field resulting from a 2D incompressible CFD simulation with a reduced chemical kinetic 2-step mechanism (2S-CM2) as described in Appendix. A. The area of maximum heat release is shown in green color in Fig. 4.1 (■). An estimate of the shear layer position (---) as well as the steady state flame front of length L_f , as predicted by the 1D linearized G-equation approach introduced in Sec. 1.3.2 ($l_M \equiv 0$), (.....) are indicated. Note, that other than for conical configurations [144], the confinement ratio does not impact the flame height of 2D

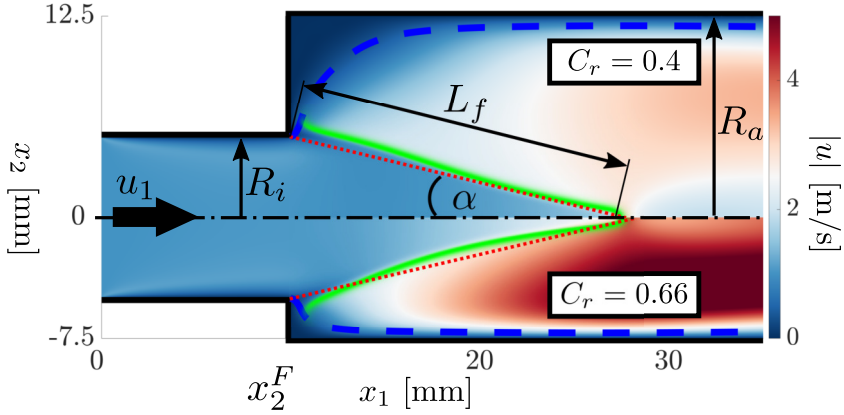


Figure 4.1: CFD steady state snapshots of absolute velocity for a confinement ratio of $C_r = 0.4$ (upper half) and $C_r = 0.66$ (bottom half). For both configurations, the location of maximum heat release (—), the analytically predicted mean flame front (· · · ·) and the approximated location of the shear layer (---) are shown.

Slit flames [142].

The mean inlet velocity of the lean methane-air mixture of equivalence ratio 0.8 is set to 1 m/s. The feed channel half-width is $R_i = 5$ mm for both setups and all boundaries are adiabatic, except the back-plate of the combustion chamber, which is set to a temperature of $T_{BP} = 373$ K. All walls are no-slip walls. The Reynolds number, computed with the mean inlet velocity, the inlet diameter and the kinematic viscosity of the combustion products is $Re \approx 620$ and the expansion ratio, which is the ratio of the unburned to the burned fluid density, is $e \approx 6.7$. For transient simulations, a velocity forcing with an amplitude \hat{u}_1 of $0.02 \bar{u}_1$ is imposed at the inlet. The characteristic time of restoration is estimated to $\tau_r = 19.41$ ms and $\tau_r = 12.08$ ms for the $C_r = 0.4$ and the $C_r = 0.66$ configuration, respectively. For more details it is again referred to Appendix. A.

4.2 Irrotational and Vortical Response Analysis

The low-order modeling approach proposed in this chapter assumes — in accordance with other approaches, such as the ones proposed by Fleifil *et al.* [115] or Schuller *et al.* [111] — a steady mean flow on which a transient velocity perturbation is superposed. The spatio-temporal structure of the latter is computed employing the modeling approach introduced in Chap. 3 neglecting flame-flow feedback. An overview of this approach is provided in Fig. 3.9. The flame dynamics are captured by a linearized 1D G-equation based model that is perturbed by an acoustically compact flow following Eq. (3.12). In order to avoid occurrence of a flow field singularity in the vicinity

of the flame anchoring point and for the sake of capturing the effect of vortex shedding, a Kutta condition is applied. The mean flow is characterized by a constant axial velocity \bar{u}_{blk} and a constant flame speed \bar{s}_L , which in combination lead to the formation of an inclined steady state flame front. The position of the mean flow shear layer is taken from the high-fidelity CFD simulations described in Sec. 4.1. The transport velocity for vorticity along this line is set to the fixed value of $\bar{u}_{\text{blk}}/2$ [126].

The spatial shape of the velocity perturbation associated with the regime of compact acoustics depends on the confinement ratio C_r . This can be seen from the definition of the resulting velocity field provided in Eq. (3.18) and the herein occurring mapping provided by Eq. (3.17). Hence, in this section, the responses of two flame configurations of different confinement ratios are analyzed and the results are compared to CFD/SI data, see Appendix. A.

For this purpose, the two test cases introduced in Sec. 4.1 are simulated. In a first step, simulations under harmonic velocity forcing are conducted and analyzed in Sec. 4.2.1. Realizing that vortex shedding is negligible, the impulse response is computed in Sec. 4.2.2 relying solely on the irrotational velocity component. This requires some non-trivial considerations caused by the Kutta condition. In a final step, in Sec. 4.2.3, analyzes the gathered response data and compares it to CFD/SI results.

4.2.1 Harmonic Forcing

Harmonic forcing of the bulk flow velocity provokes irrotational flow field perturbations and, at edge A, the shedding of vorticity. A Kutta panel attached to this edge ensures that the flow field remains finite and leaves the trailing edge tangentially to the wall contour. In each time step, the vorticity bound by this panel is condensed into a point vortex that is placed right at the panel end. This vortex then becomes part of the vortical flow field and is advected along the mean flow shear layer by a velocity $\bar{u}_{\text{blk}}/2$, whose coordinates are estimated from the CFD data, see Fig. 4.1 (---).

Forcing the $C_r = 0.4$ configuration harmonically at a frequency of 80 Hz and an amplitude of 2% \bar{u}_{blk} results in a response as depicted in Fig. 4.2. Here, four snapshots at different phases of the forcing signal are shown. The upper half of each snapshot visualizes the resulting vortical and the lower half the corresponding irrotational perturbation velocity field. The flame front displacements provoked by the latter (.....) are significantly larger than the vortical ones. Hence, it seems that shed vorticity hardly contributes to the response of the flame and could safely be neglected. The spatial shape of the irrotational perturbation can be deduced from the green arrows shown in Fig. 4.2, which illustrate the flame normal velocity perturbations. According to them, acoustic perturbations mainly displace the flame base region, while the flame tip is hardly affected.

In the literature, a common approach to approximate the amount of vorticity shed

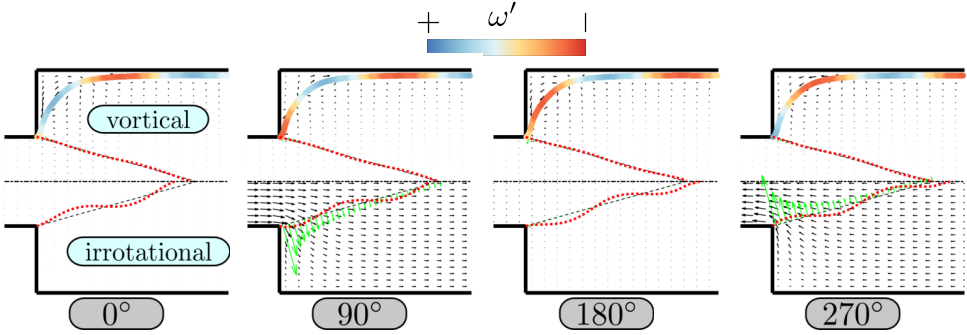


Figure 4.2: LOM predictions of a harmonically forced flame configuration (at 80 Hz and an amplitude of 2% \bar{u}_{blk}) for a confinement ratio of $C_r = 0.4$. Shown are four consecutive snapshots taken at phases from 0° to 270° with respect of the forcing signal. The upper half of each snapshot shows the vortical flow component, where the color along the shear layer corresponds to the strength of the vorticity fluctuations. The lower half shows the respective irrotational flow component. The flame normal velocity, scaled by a factor of 4, is illustrated by green arrows (upper+lower half). The shown flame front displacements are scaled by a factor of 7 (.....).

during a time interval Δt is to evaluate the linearized relation

$$\Delta\Gamma'(t) = \bar{u}_{\text{blk}} \int_t^{t+\Delta t} u'_1(\hat{t}) d\hat{t}, \quad (4.1)$$

which provides an estimate of the created total circulation of the separating vortex sheet [126, 193]. This formula has been used by Steinbacher *et al.* [1] in order to quantify the effects of the free shear layer onto the flame front. Fig. 4.3 compares the resulting strength of the vortex sheet of this approach (—) to the one caused by the aforementioned Kutta condition (· · · · ·). For $C_r = 0.4$, the amplitude of vorticity fluctuations caused by the Kutta condition is more than twice as large as the one computed by Eq. (4.1). Nevertheless, both studies — the one of Steinbacher *et al.* [1] and the one presented here — agree that vortex shedding has only a negligible impact on the flame response. Having a look at the $C_r = 0.66$ configuration, both ways of computing the shed vorticity almost coincide. Therefore, it seems that predictions of Eq. (4.1) agree better with results of the Kutta condition in cases where the flow is less two-dimensional, which is the case if the confinement is getting more narrow ($C_r \rightarrow 1$).

4.2.2 Impulse Forcing

The finding that vorticity shed from the burner mouth has only a negligible impact on the flame response shall now be exploited: It allows to evaluate the impulse response (IR) solely based on the irrotational part of the perturbation velocity field.

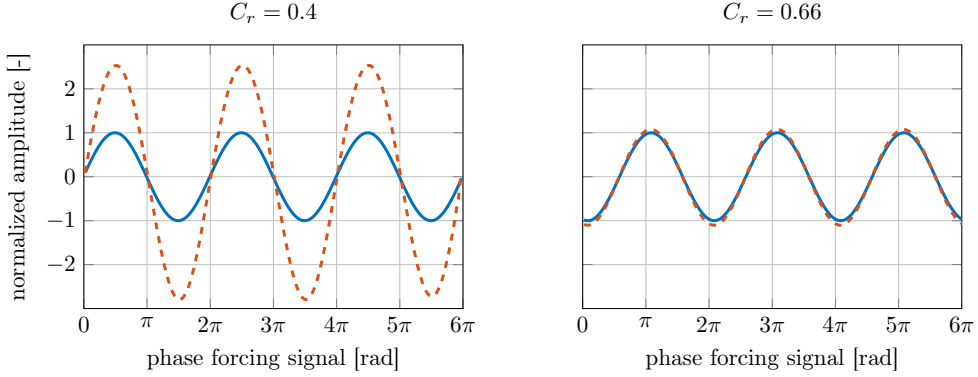


Figure 4.3: Comparison of vorticity distribution resulting from vortex shedding due to a Kutta condition (---) and the linear approximation of Eq. (4.1) (—) for three forcing cycles at 80 Hz and two confinement ratios.

To this end, an impulsive forcing $u'_{\text{blk}} = \epsilon \delta(t)$ of amplitude ϵ is applied to the combustor and the resulting instantaneous flame displacement is computed from the respective irrotational velocity perturbation by evaluation of the temporal integral $\xi(x_{\parallel}) = \int_0^{\infty} u'_{\perp}(x_{\parallel}) dt$. Application of a Kutta panel, however, leads to a situation where $u'_{\perp}(x_{\parallel})$ depends on the panel length, which is computed from the local transport velocity $(\tilde{u}^+ + \tilde{u}^-)/2$ multiplied by the temporal width of the impulse forcing Δt . Assuming a harmonic forcing signal, vorticity is continuously shed from the burner mouth. That means, the panel length H_x is well defined in each time step and continuously varies over time. In the case of an impulsive signal, however, the resulting panel length H_x depends on both the amplitude of the forcing and the width of the impulse signal. This is a problem since in the linear limit, the impulse response maps to a certain frequency response and vice versa. Having a significant dependency of the response to the forcing amplitude ϵ , this property is no longer ensured as will be shown in the following.

Fig. 4.4 analyzes for two confinement ratios how the flame normal velocity perturbation depends on the length of the vortex panel. For this purpose, an impulsive velocity forcing is applied and the resulting flame normal velocity is measured for different panel lengths right at the moment when the impulse hits the flame. A rather strong impact of the panel length on the resulting velocity can be observed: the shorter the panel gets, the higher and more localized the peak velocity becomes. Thus, an impulsive forcing using a very narrow impulse perturbation or a very low amplitude would both lead to a short Kutta panel and, therefore, to a flame displacement that is very localized at the flame holder. The opposite holds for a wide impulse perturbation or a high velocity amplitude. In consequence, this means that the IR is rather sensitive to the specific kind of forcing signal, which is an unfavorable property.

In order to compute an estimate of the IR that robustly captures the linear dynamics of the system in the inviscid limit, an empirical approach is chosen: the panel length

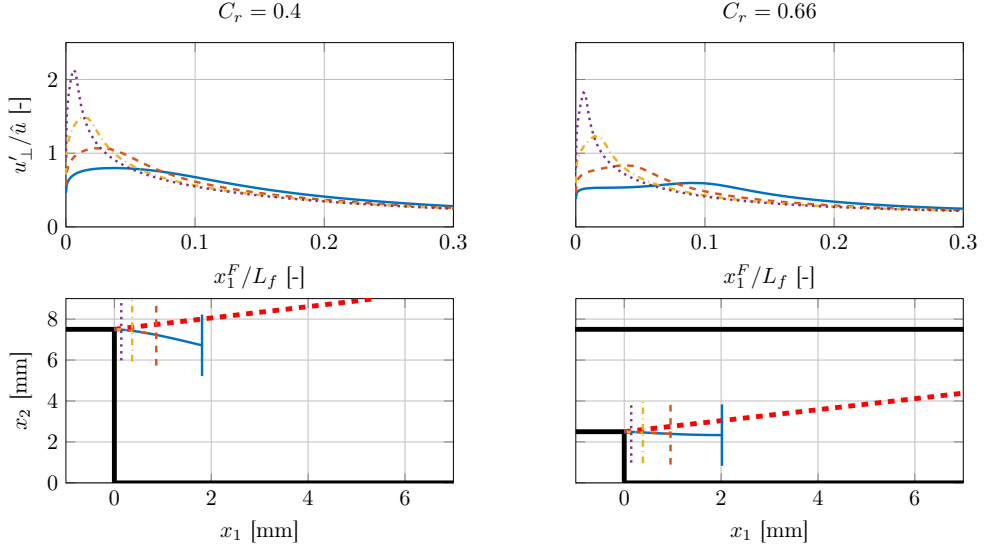


Figure 4.4: Top: Flame normal velocity resulting from a constant mean flow and a Kutta condition evaluated for four panel lengths, H_ξ (—), $H_\xi/2$ (---), $H_\xi/4$ (---) and $H_\xi/8$ (····) plotted over normalized flame coordinate. In accordance with Fig. 3.7, H_ξ is set to 2.1 for $C_r = 0.4$ and to 1.8 for $C_r = 0.66$. Lower: Visualization of the associated panel shapes, where the end of each panel is marked by a vertical line. Additionally, the flame front is shown (· · · ·).

is set to a value such that the frequency response computed from the resulting IR corresponds best to predictions using harmonic forcing. The associated panels fulfilling this requirement best are plotted in Fig. 4.4 for the two investigated confinement ratios (—). Panels of these lengths have already been studied in Sec. 3.3.3. Using the associated flame normal velocity perturbations resulting from such panel lengths, the flame displacement right at the moment when the impulse hits the flame ($t^* = 0$) is computed and plotted in Fig. 4.5. The shown curves are normalized by the displacement amplitude $\hat{\xi} = \int_0^t u'_1 dt$. Indeed, good agreement between the LOM (· · · ·) and the CFD/SI data (—) is found for $t^* = 0$ for both confinement ratios. Details on the processing of the CFD results are provided in Appendix. A.4.

Due to the fact that the resulting flame front has the shape of a triangle at $t^* = 0$, a so-called flame base displacement (FBD) model is introduced:

$$\xi(x_\parallel, t) = \frac{2 \sin(\alpha) \epsilon}{f_b} [\Theta(x_\parallel - t \bar{u}_\parallel) - \theta(x_\parallel - t \bar{u}_\parallel - f_b L_f)] \left[1 - \frac{x_\parallel - t \bar{u}_\parallel}{L_f f_b} \right] \quad (4.2)$$

where f_b measures the length of the triangle relative to the flame length L_f and \bar{u}_\parallel the flame-parallel component of the mean flow velocity \bar{u}_{blk} . The height of the triangle results from conservation of the global volume flux of the perturbation. All the volume provided by the velocity forcing at the inlet is pushed through the mean flame

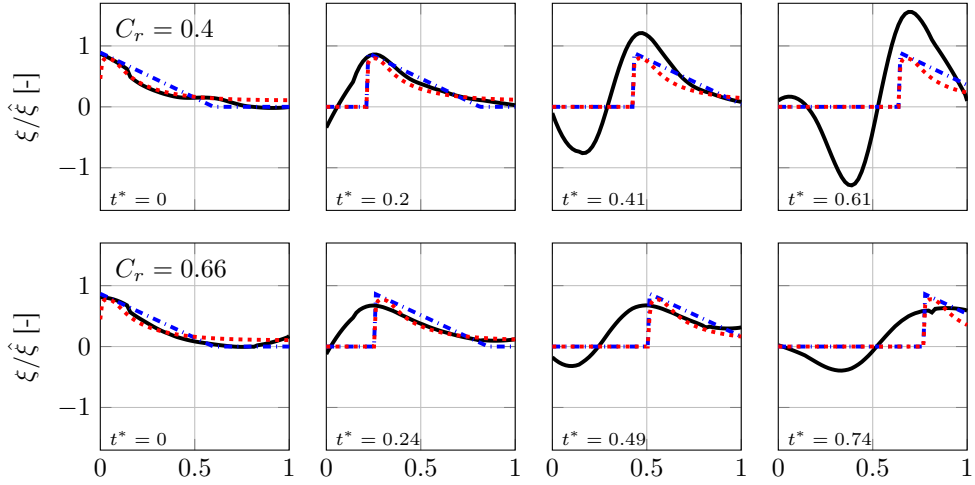


Figure 4.5: Four snapshots taken at equidistant instances in time of the normalized flame displacement resulting from an impulsive velocity forcing at $t^* = 0$ according to CFD/SI results (—), the acoustic LOM (.....) and the FBD model (- - -) at two confinement ratios: $C_r = 0.4$ (top) and $C_r = 0.66$ (bottom).

front and, hence, creates flame displacements, in analogy to the situation depicted in Fig. 6.6. This fixes the height of the triangle to $2 \sin(\alpha) \epsilon / f_b$. For both confinement ratios, a value of $f_b = 0.6$ matches the CFD/SI and LOM data best. This model introduces a simple analytical approximation of the flame response for the limiting case of neglected flame-flow feedback employing one empirical parameter f_b .

4.2.3 Discussion

If we compare the results of all three flame response models illustrated in Fig. 4.5 for $t^* > 0$, we notice that the initial flame front displacements are advected towards the flame tip. While the specific shapes of the acoustic LOM and the FBD model remain unchanged during this process, the CFD/SI data exhibits a spatial growth of the initial displacement amplitude. Furthermore, a secondary negative and a tertiary positive displacement develop. This behavior has most likely to be attributed to flame-flow feedback, which is neglected by the acoustic LOM. The observed growth in amplitude is reminiscent of the Darrieus-Landau mechanism known from planar flames that propagate perpendicular to the unburned flow. In contrast to these setups, the inclined flame geometries investigated here exhibit a characteristic, triangle shaped initial perturbation of significant amplitude as well as (fixed) boundaries. Therefore, the situation at hand is similar, but still different (in terms of initial and boundary conditions) to the one known from classical studies on the Darrieus-Landau instability. It has to be checked carefully how these classical results can be applied for

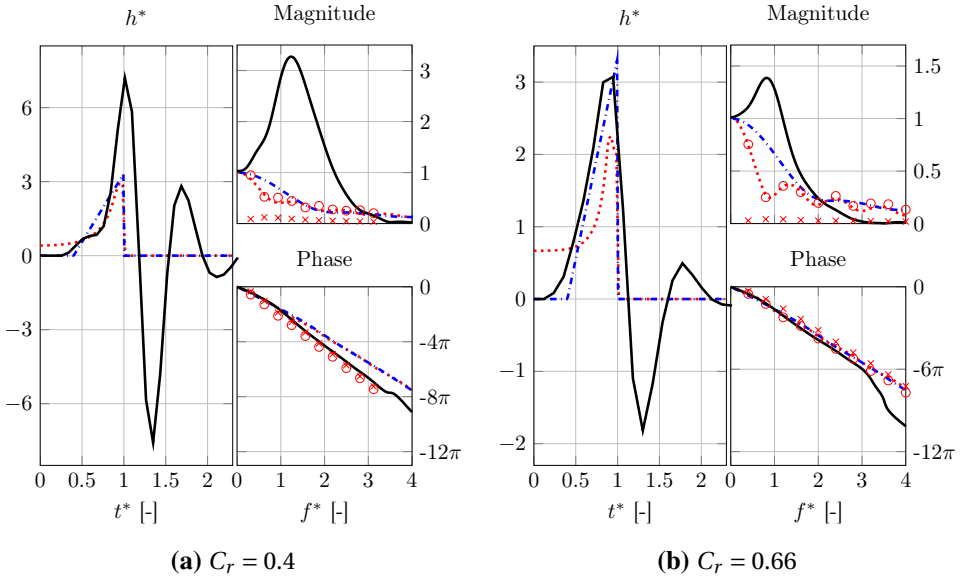


Figure 4.6: IR and FR in terms of gain and phase for $C_r = 0.4$ (left) and $C_r = 0.66$ (right). Shown are results from CFD (—), the FBD model for $f_b = 0.6$ (---) and the acoustic LOM (····). Additionally, results from harmonic forcing of the acoustic LOM are included, split into irrotational (○) and a vortical (×) contributions.

Bunsen-type flames, which will be analyzed in more detail in Chap. 5.

Comparing the transient behavior of the $C_r = 0.4$ to the $C_r = 0.66$ setup, a weaker growth of the initially caused flame displacements can be observed for the latter. It seems that the presence of a confinement delimits the possible displacement amplitudes. Based on the analysis presented in this chapter, which neglects flame-flow feedback, the detailed mechanisms responsible for this behavior cannot be analyzed, though. In Fig. 4.5 it can be seen that the resulting non-dimensional initial displacements as well as the velocity of convection match the CFD data very well.

Based on the results shown in Fig. 4.6, flame-flow feedback is supposed to have a major impact onto the response of the global heat release rate. One of the most prominent discrepancies constitutes the damped oscillatory behavior of the IR predicted by the CFD/SI data (—), especially for the wide confinement case ($C_r = 0.4$). Here, the acoustic LOM only captures the first peak of this curve, significantly underestimating the amplitude. The subsequent positive and negative peaks are not captured at all. In the frequency domain, the damped oscillatory behavior manifests itself as a very high peak gain value at a Strouhal number approximately corresponding to the oscillation frequency. The acoustic LOM, on the other hand, results in a frequency response resembling the gain behavior of a first-order low-pass filter. The almost linearly decaying phase is captured well by all models.

The agreement between the acoustic LOM and the CFD/SI data is better for the narrow confinement configuration ($C_r = 0.66$). Here, the first peak of the IR is captured reasonably well. In contrast to the $C_r = 0.4$ case, the IR exhibits a relatively high level around $t^* = 0$, which cannot be observed in the CFD/SI data. Hence, the initial displacement at the flame tip is overpredicted, which is also seen in Fig. 4.5. The IR of the $C_r = 0.66$ setup shows less pronounced peaks and, thus, the associated FR shows a reduced peak gain value compared to the $C_r = 0.4$ case.

Fig. 4.6 decomposes the frequency response of the acoustic LOM into its irrotational (○) and vortical (×) contributions. The individual frequency response data is gained from harmonic simulations, as depicted in Fig. 4.2. The fact that the former matches the results gained from the impulsively forced configuration (.....), very well cross-validates both approaches. The weak response of the vortical contribution confirms the finding that vortex shedding can be safely neglected.

Finally, an analytical prediction of the response of the FBD model introduced in Eq. (4.2) is provided. Its impulse response writes

$$h_{\text{FBD}}^*(t) = \frac{t^* - 1 + f_b}{2f_b^2} [\Theta(t^* - 1 + f_b) - \Theta(t^* - 1)] \quad (4.3)$$

with the Heaviside Theta function $\Theta(t)$. The associated FR can be mapped to frequency domain by use of Tab. C.2. Following Fig. 4.6, this model captures the overall trend of the acoustic LOM model well. Due to the fact that flame-flow feedback has such an important influence onto the flame response, it can only be used to estimate the cut-off frequency or the phase behavior, but not the gain around a Strouhal number of approximately unity. In this regard it is much simpler to evaluate than the presented acoustic LOM, while it still captures the essential effects.

4.3 Summary and Conclusions

The response of laminar premixed flames stabilized at a backward-facing step to velocity perturbations was scrutinized. One goal was to test the hypothesis that shed vorticity contributes to the so-called convective velocity perturbations, which are an important, widely-used element of low-order flame response models. Analytical methods from aero-acoustics were combined with a flow decomposition approach to quantify the respective contributions of the irrotational and the vortical parts of the disturbance velocity field to the overall flame transfer function (FTF). The complete set of equations derived in Chap. 3 capturing the flow field dynamics of acoustically perturbed flames was used, however, exothermic effects, in particular the effect of flame displacement and wrinkling on the upstream velocity, were neglected in this study.

For the cases considered — a Slit flame geometry with a Péclet number of $Pe = 223$, an expansion ratio of $e \approx 6.7$ and confinement ratios $C_r = 0.4$ and 0.66 — the ir-

rotational part was shown to dominate the flame displacement, which is most pronounced at and near the flame anchoring point. Correspondingly, a flame base displacement (FBD) model was proposed, which captures the early part of the impulse response well, particularly for high confinement ratios. Discrepancies for later times and for low confinement ratios were attributed to exothermic flame-flow-flame feedback mechanisms not taken into account by the low-order modeling approach. For the configurations investigated, vortex shedding is found to only have a negligible impact on the flame response.

The main findings of the present analysis are:

1. Vortex shedding due to an oscillatory flow in the vicinity of a sharp corner is found to have only negligible impact on the flame response.
2. Hence, the shedding of vorticity was ruled out as a possible candidate to physically justify the assumption of convected velocity perturbations as a source of flame wrinkling. Consequently, one must conclude that models based on this assumption do not faithfully represent acoustics-flame-flow interactions.
3. The irrotational part of an acoustic perturbation essentially interacts with the flame base region, which is captured by an analytical model proposed in this study, namely, the FBD model.

Flame-flow feedback is supposed to have a substantial impact on the flame response, particularly, at Strouhal numbers of order $\mathcal{O}(1)$. It might lead to rather high and distinct peaks in the gain of an FTF, particularly, for high confinement ratios. This will be analyzed in more detail in the next chapter.

5 Secondary Interactions

The previously introduced low-order modeling framework is extended such that it can cope with two important types of flame-flow feedback: (i) vortical flame-flow feedback resulting from flame generated vorticity and (ii) irrotational flame-flow feedback resulting from a flame normal acceleration of the flow across a flame sheet. Both contribute to the convective growth of flame sheet disturbances and account for the appearance of FTF gain values exceeding unity as well as convected velocity perturbations upstream a perturbed flame.

In the previous chapter, interactions of acoustic perturbations and burner-stabilized Slit flames were analyzed in the limit of negligible flame-flow feedback (no gas expansion) and flame stretch (constant flame speed). While the latter is expected to dampen flame front displacements ($Le > Le_{c,TD}$), flame-flow feedback leads to convective growth of flame perturbations ($e > 1$). Consequently, the observed significant discrepancy between the low-order model developed in the previous chapter and high fidelity CFD data was attributed to flame-flow feedback. This hypothesis shall be analyzed in more detail in the following.

In order to clarify the discussion, we want to agree upon the terminology first. The term “*secondary interactions*” has already been specified before and refers to phenomena/flame displacements, which are not directly caused by acoustic perturbations, but by incompressible flame intrinsic processes. It can be distinguished most easily between primary and secondary interactions for the case of impulsively forced flames, since any change in flame shape occurring after an acoustic impulse has hit the flame ($t > 0$) is subsumed as a secondary interaction (except advection). In principle, all phenomena discussed in Chap. 1 governing the dynamics of a flame sheet are potentially important here. It was observed in the previous chapter by inspecting high fidelity CFD data that the primary displacement, caused by acoustics, grows in amplitude and, additionally, secondary displacements develop. Such a growth is the signature of a hydrodynamic mechanism, described in Sec. 1.2.3, which is sometimes also referred to as the *Darrieus-Landau* mechanism. It arises due to interactions of the flow field with the flame sheet, captured by a set of jump conditions. It is driven by the change in specific volume across the flame, i. e. it is a consequence of gas expansion. Hence, this phenomenon relies on *flame-flow feedback*.

The role of flame-flow feedback for the (linear) response has already been pointed out by some previous studies. Already Baillot *et al.* [120] attributed the occurrence of convected flow perturbations upstream a wrinkled flame front to the “*retroactive hydrodynamic effects of the flame on the flow of the unburned gases*” (Baillot *et al.* [120], p. 164). This was later confirmed by Birbaud *et al.* [136], who conducted a series of demonstrative experiments. Blanchard *et al.* [129] numerically showed that a perturbed flame sheet acts as a vortex sheet whose upstream influence contributes to the formation of axially convected velocity perturbations. They related this phenomenon to the Darrieus-Landau mechanisms. The relevance of this hydrodynamic mechanism for the flame response of perturbed burner-stabilized flames was further confirmed by the studies of Hemchandra [103] and Schlimpert *et al.* [104]. Both reported a strong impact of hydrodynamic mechanisms leading to the spatial growth of flame front perturbations. Hemchandra [103] conjectured that this mechanism may be responsible for the occurrence of high FTF gains exceeding unity.

Flow instabilities often trigger the development of large coherent structures. In consequence, characteristic flow features develop, which have important consequences for technical applications. Oberleithner *et al.* [79] as well as Oberleithner and Paschereit [80] found for swirl-stabilized flames that the gain of the flame response scales with stability properties of the respective shear layers. According to these studies, a Kelvin-Helmholtz-type hydrodynamic instability triggered by acoustic perturbations leads to the formation of large scale coherent structures that interact with the flame and, thus, provoke fluctuations of the global heat release rate. Similar to flames, shear layers (or vortex sheets) can be idealized as discontinuities. While flame related discontinuities exhibit jumps in normal and tangential velocity, shear layers only show changes in tangential velocity. In their most idealized versions, both entities are unconditionally (convectively) unstable [180, 194] and may hence both contribute to the formation of coherent structures that may impact the flame response. Hence, the Darrieus-Landau mechanisms or instability should be analyzed in more detail and clearly demarcated from shear layer instabilities. As a first step, flame-flow feedback related mechanism will be analyzed for laminar flames in this chapter.

Although thermal-diffusive mechanisms might have a crucial impact on secondary acoustics-flame interactions, as well, the following discussion focuses on the hydrodynamic ones. They are the drivers for all observable secondary phenomena, while thermal-diffusive mechanisms only exert a damping influence (assuming lean methane-air flames). It can already be anticipated that a consideration of driving mechanisms will create a need for damping and, therefore, displacement amplitudes are likely to be overestimated if damping mechanisms are neglected. It will be shown in the course of this chapter that this expectation is true indeed, however, this point is beyond the scope of this work and shall be left for succeeding studies. This chapter strives to take one step forward towards a comprehensive understanding of the flame dynamics by assessing mechanisms that provoke the convective growth of flame front perturbations. These mechanisms are expected to be associated with flame-flow feedback.

In a first step, Sec. 5.1 revisits flame response predictions from high fidelity CFD simulations as well as from low-order models relying on convected velocity perturbations in the light of flame-flow feedback. Section 5.2 then shows how flame-flow feedback is integrated into the modeling framework introduced in Chap. 3. Finally, Sec. 5.3 discusses and analyzes flame response predictions computed with this new framework and compares them to high fidelity CFD simulations.

5.1 Flame Response Revisited in the Light of Flame-Flow Feedback

As already discussed in Chap. 2, the understanding and modeling of interactions between acoustics and burner stabilized flames often relies on the notion of convected velocity perturbations. Conversely, in the case of flames whose anchoring is mechanically displaced, it essentially follows the concepts of flame-sheet dynamics outlined in Chap. 1. Based on this point of view, flame-flow feedback — namely the hydrodynamic mechanism explicated in Sec. 1.2.3 — is not explicitly considered in the analysis of acoustically perturbed flames. Nevertheless, it is implicitly contained in the models since, according to the literature [120, 129, 136], the observed convected perturbations are supposed to be induced by the upstream influence of a wrinkled flame. In the following, the response of acoustically perturbed flames is revisited focusing on consequences of flame-flow feedback. The goal is to provide links between the notion of convected velocity perturbations and the dynamics of flames driven by gas expansion.

To this end, high fidelity CFD data is evaluated in Sec. 5.1.1. Special focus is put on how the impulse response is linked to the flame sheet dynamics and how strong the expected effects of flame-flow feedback are. This provides further evidence for the conjecture made in Chap. 4, which states that the oscillatory nature of the IR and the high gain values are caused by gas expansion driven flame-flow feedback. Subsequently, the convective velocity model is revisited in Sec. 5.1.2 and analyzed in the light of these findings.

5.1.1 High Fidelity CFD/SI Data

The snapshots shown in Fig. 4.5 (—), which are taken from high fidelity CFD data, clearly indicate convectively growing flame displacements amplitudes. Furthermore, three distinct positive and negative peaks emerge in the final snapshot, although — following the analysis of Chap. 4 — acoustics caused only one of them directly (the one at $t^* = 0$). Consequently, the other peaks have to be caused by flame sheet intrinsic mechanisms. Flame-flow feedback due to exothermic gas expansion is one promising candidate for such a mechanism, since it was explicitly neglected in the low-order modeling approach analyzed in the previous chapter, see Fig. 4.5 (.....).

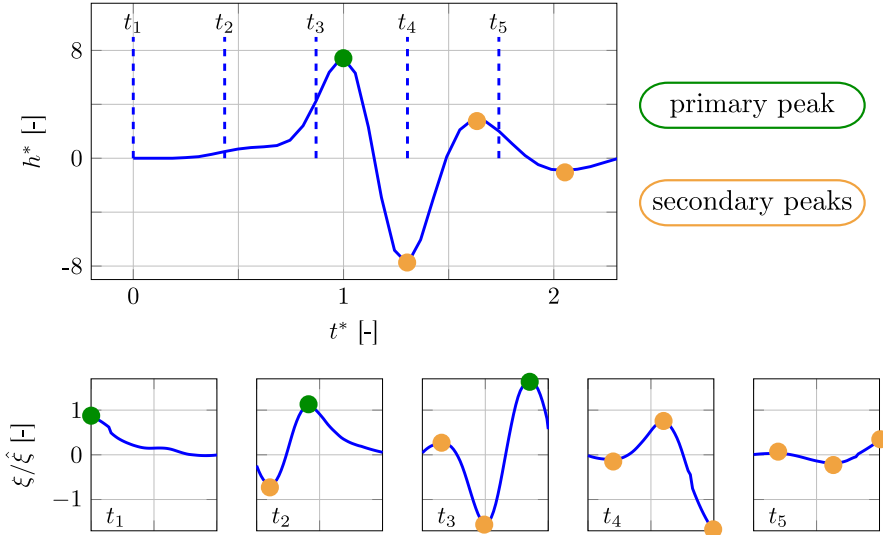


Figure 5.1: Top: Impulse responses for the $C_r = 0.4$ (—) configuration depicted in Fig. 4.1 (but with $T_{BP} = 700$ K). Instants in time corresponding to one of the snapshots shown in the bottom blot are marked by vertical lines. Bottom: Consecutive snapshots of the normalized flame-normal flame front displacement caused by an impulsive acoustic forcing of a flame setup with $C_r = 0.4$ (—). Depicted are five instants in time, where t_1 matches the time the acoustic impulse hits the flame. Primary and secondary peaks in flame shape are marked by colored dots.

It is shown in Appendix. A.3 that the global heat release signal of a flame subjected to an impulsive forcing (Fig. 4.5; —) coincides well with the IR identified from broad band data for all analyzed setups (Fig. 4.6; —). Consequently, the analysis of the flow field and flame dynamics resulting from an impulsive forcing provides valuable physical insights into the linear flame dynamics. In order to relate the flame displacement data with the respective IR, it is necessary to know how the global heat release rate is linked to flame sheet displacements. As will be detailed in Chap. 6, in the limit of stiffly anchored Slit flames, the linear dynamics of the global heat release rate depends only on the displacement of the flame tip. That means, the heat release rate stays constant as long as the flame tip is not perturbed.

Exploiting this relation, Fig. 5.1 compares the IR of the Slit flame configuration to the associated flame front displacements¹. At the very moment the acoustic impulse hits the flame ($t = 0$), the flame front is displaced in the previously described triangle-like manner and a primary displacement peak is formed. At this time, the IR of the global heat release rate h^* shows no signal since the flame tip was not displaced.

¹The data shown corresponds to the same setup as discussed in Chap. 4, only the temperature of the anchoring wall is changed to $T_{BP} = 700$ K. As discussed in App. B, this hardly affects the overall characteristics of the flame response, which allows to directly compare both setups.

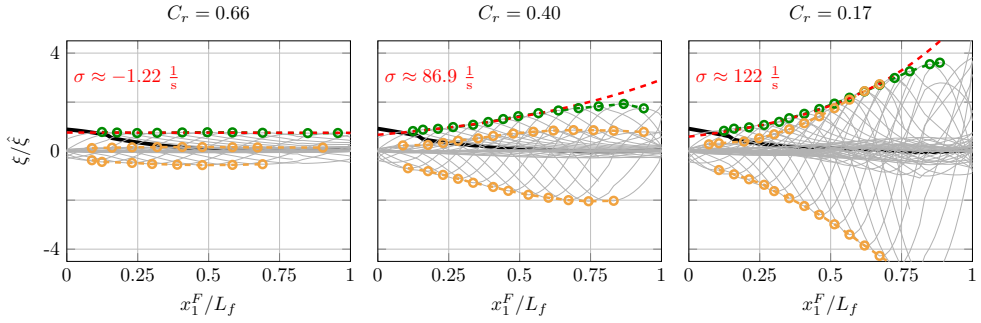


Figure 5.2: Normalized flame displacements shown for three confinement ratios corresponding to the cases shown in Fig. 5.1. Additionally, a case with $C_r = 0.17$ is added. The thick black line signifies the displacement immediately caused by an impulsive velocity forcing of the flame and the gray lines its subsequent spatio-temporal development. The primary positive displacement peak is tracked and marked in each time step (● ● ●). Similarly, the positive and negative secondary peaks are tracked (○ ○ ○). An exponential function is fitted to the spatial trace of the primary peak (---) and from it a temporal growth rate σ is computed.

Only around t_3 ($C_r = 0.4$; —) the heat release rate starts to increase, which corresponds to the time the initially created primary displacement reaches $x_1^F/L_f = 1$. Accordingly, the subsequent negative secondary displacements causes the heat release to decrease to negative values at t_4 . We note that (i) the convective growth of flame front displacements directly leads to higher peak values of the associated IR and (ii) the presence of the numerous positive and negative displacement peaks of decreasing amplitude is responsible for the damped oscillatory IR behavior. Those two observations are supposed to be caused by flame-flow feedback and shall be quantified in the following.

To this end, the spatial growth of the convected displacement peaks is evaluated. Fig. 5.2 combines several snapshots of the displaced flame front at different instants in time in one single plot (thick black line for $t^* = 0$ and gray lines for $t^* > 0$). Additionally, for each snapshot, the maximum of the primary displacement — caused by acoustics at $t^* = 0$ — is marked by a green circle (● ● ●). The subsequently developing first two positive and negative secondary peaks are marked by orange circles (○ ○ ○). Due to the fact that all of these maxima are convected downstream towards the flame tip at $x_1^F/L_f = 1$, their traces form lines of growing amplitude. Assuming this growth is governed by linear dynamics (no sharp edges in concave regions!) and the initial shape approximately resembles a sine (see particularly the shapes at $t \geq t_2$ in Fig. 5.1), the growth should be exponential. Fitting an exponential function to the distribution of the primary peaks, a spatial growth rate σ_x is computed. In order to avoid to capture anchoring and tip related effects, points close to one of these two exceptional points are excluded from the respective data sets. By use of the advection

velocity \bar{u}_{\parallel} , these spatial growth rates can be converted to temporal ones via $\sigma = \sigma_x \bar{u}_{\parallel}$ [63, 66].

Before the results of this kind of analysis are discussed, it should be emphasized that impulsively forced data is used here. Such kind of analysis, however, is usually performed based on harmonically forced data, see for example Truffaut and Searby [66]. Assuming that harmonic forcing also results in harmonic flame sheet perturbations of a single wave number, growth rates can be evaluated for each wave number separately. Repeating this for several frequencies, samples of the underlying dispersion relation are computed. Imposing an impulsive acoustic forcing excites perturbations of several wave numbers at the same time, see the triangle-shaped initial displacement shown in Fig. 5.1. Subsequently, each excited wave number perturbation will independently grow in amplitude at a rate given by the underlying dispersion relation (we assume we are still in the linear regime). This means that the flame displacements shown in Fig. 5.1 are a superposition of all of these individual perturbations. Therefore, the computed overall growth rate can not directly be related to frequency-specific growth rates of the associated dispersion relation. Nevertheless, the displacements resembles a sine-like shape already in the second snapshot (t_2). Therefore, it is possible to get, at least, a rough idea of the order of magnitude of the maximally expected growth rates from impulsively forced data. In the scope of this section, this shall be sufficient.

Evaluating the temporal growth rates σ for three confinement ratios in Fig. 5.1, it is found that they strongly depend on confinement ratio. While the growth of displacements is suppressed at the narrowest confinement, it reaches a value of about 120 1/s for $C_r = 0.17$. In order to put this number into perspective, it is non-dimensionalized by the flame transition time $\tau_t = \delta_D/s_L$ to $\sigma\tau_t = 0.038$. Truffaut and Searby [66] experimentally determined non-dimensional growth rates between approximately 0.03 and 0.09 for rich propane-air flames stabilized at a harmonically displaced rod, see Fig. 1.4. The order of magnitude of their results is hence the same as the ones obtained here. Further, Truffaut and Searby [66] attributed the observed growth to the Darrieus-Landau mechanism, which is denoted as the hydrodynamic mechanism in Chap. 1. This provides evidence that similar, flame-flow feedback related processes are at work for the configurations studied in this thesis. For future studies it should be kept in mind that displacement amplitude growth rates may significantly be influenced by lateral constraints of the flow, such as a confinement.

5.1.2 Convective Velocity Model

If flame-flow feedback really has the decisive impact on the flame dynamics as asserted above, why is it possible that G-equation based approaches relying on convective velocity models, which do not explicitly account for flame-flow feedback, are capable of correctly reproducing essential aspects of the dynamics of acoustically perturbed flames? The answer is that they implicitly do, which is analyzed in the

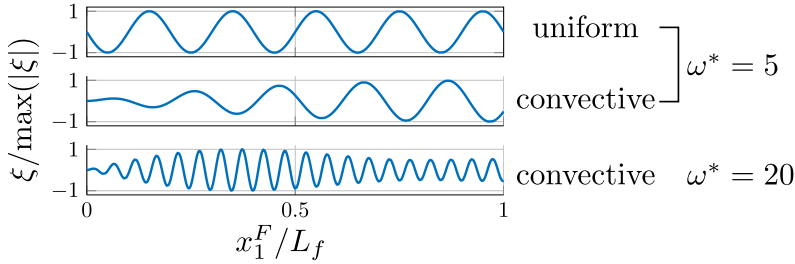


Figure 5.3: Normalized flame front displacements as predicted by the uniform (top) and the incompressible convective (middle and bottom) velocity model for a harmonic velocity forcing at a Strouhal number of $\omega^* = 5$ (top and middle) and one of $\omega^* = 20$ (bottom).

following.

Having a closer look at the convective velocity model of Eq. (2.5), one recognizes that this model indeed leads to a spatial growth of flame front displacements. This is illustrated in Fig. 5.3, which shows the response of a flame front exposed to harmonic velocity forcing at a fixed frequency according to the 1D linearized G-equation approach introduced in Sec. 1.3.2. Three response predictions are shown for two velocity models and two Strouhal numbers. While, for a Strouhal number of 5, the uniform velocity model of Eq. (2.4) (Fig. 5.3, top) shows a constant amplitude of the wrinkled flame surface, the incompressible convective velocity model (Fig. 5.3, middle) exhibits a clear spatial growth of the respective flame front displacements. Hence, the convected velocity perturbation mimics the effects of flame-flow feedback, which explains their agreement with experimental data.

At a Strouhal number of 20, however, the spatial distribution of displacement amplitudes grows only up to $x_1^F / L_f \gtrsim 0.5$ and subsequently decreases again. Overall, a low frequency modulation on top of a high frequency oscillation becomes visible (Fig. 5.3, bottom), which is also known as a beat. This might explain the decreasing predictive capabilities of such models at high frequencies, which was reported by Cuquel *et al.* [161]. But even at sufficiently low frequencies, the model deviates from a realistic behavior. Theoretically, it is possible to evaluate spatial growth rates relying on a convective velocity model by post-processing displacement predictions as the one shown in Fig. 5.3, middle. Doing this for several forcing frequencies, this will eventually result in a dispersion relation that, ideally, coincides at low frequencies with the realistic flame sheet behavior. If that is true, we can expect that the convective velocity predicts the actual acoustic flame response very well. The study of Kashinath *et al.* [167], however, suggests that convective velocity models do not capture the real physical behavior. In this work, the authors fitted the convection speed of the velocity perturbations to high fidelity CFD data and found a significant dependency of this speed to frequency. Knowing that this speed influences the resulting growth rates, their study indicates that the dispersion relation naturally resulting from

a convective model does not agree with the one of the underlying physical process, but requires a non straight forward fitting procedure.

It can be concluded that models relying on convected velocity perturbation mimic the flame-flow feedback related spatial growth of displacement amplitudes, however, only up to a certain frequency. Furthermore, the associated (theoretical) dispersion relation of these kind of models does in general not reproduce the real physical behavior.

5.2 Modeling of Flame-Flow Feedback

The previous section pointed out the importance of flame-flow feedback by analyzing high fidelity CFD data. Furthermore, hints of such a feedback were found in the convective velocity model, which is commonly applied in G-equation based modeling approaches. Motivated by these findings, the goal of this section is to integrate flame-flow feedback into the modeling framework introduced in Chap. 3 such that it can be used to analyze its impact on the linear flame response.

According to the concepts outlined in Chap. 1, flame-flow feedback is a hydrodynamic mechanism related to density changes across the flame sheet. It necessarily results in the unconditional growth of flame front displacements, if it is not stabilized by thermal-diffusive mechanisms [44]. Following the analysis of Darrieus and Landau, in the framework of gasdynamic discontinuities, this growth emerges from the jump conditions of mass and momentum across the flame. Hence, it can be expected that analyzing these conditions in more detail contributes to the understanding of the basic mechanisms at play.

Having done this, it should be possible to integrate gas expansion into the existing modeling framework of Chap. 3. It explicitly appears at two positions, (i) as volume source in the gas expansion related flow component u_e of Eq. (3.13) and (ii) in form of a density gradient in the baroclinic source term of the vorticity transport equation, i. e. Eq. (3.9). The modeling concept proposed in this section concerning point (i) relies on the specification of a volume production kernel. This kernel function distributes the volume produced by the flame in space and serves as a source to the gas expansion related flow field component u_e . Based on a study conducted by Zimmermann [195], a Gaussian kernel function will be introduced. Concerning the modeling concept for the baroclinic source term, see point (ii), it will be shown that a candidate for such a concept can be derived from the analysis of the jump conditions.

Following these ideas, Sec. 5.2.1 derives and analyzes a set of jump conditions, including and excluding flame stretch effects, respectively. Based on these results, Sec. 5.2.2 introduces a concept for how flame generated (baroclinic) vorticity can be included into the modeling framework. Finally, a kinematic modeling approach of gas expansion is introduced in Sec. 5.2.3.

5.2.1 Jump Conditions Across a Flame Sheet

In the subsequent analysis it is assumed that the fluxes of mass and momentum through the flame front are constant, i. e. the fluxes of mass, normal and tangential momentum are conserved across the flame sheet

$$[m]_u^b = 0, \quad [p + mu_i n_i]_u^b = 0, \quad [mu_i t_i]_u^b = 0, \quad (5.1)$$

where u_i , n_i and t_i denote the i -th component of the flow velocity, the local flame normal and flame tangential vectors, respectively. Further, the Einstein summation convention is employed and $m = u_i n_i - \partial \xi / \partial t$ denotes the local mass flux across the flame sheet. This essentially follows the original ideas of Landau [27] and Markstein [44], who derived the set of jump conditions shown in Eq. (1.7). All of the relations shown below are derived from the formulation of the fluxes as they are stated in Eq. (5.1). They are evaluated right at the mean flame position, which is, per definition, fixed in space and time. This simplification imposes an error that scales with the displacement amplitude and the inverse of the perturbations wave length.

A flame aligned coordinate system $[x_1, x_2]$ as depicted in Fig. 1.9b is assumed. The mean flow field in which a freely propagating flame sheet is stabilized points towards the positive x_2 -direction. Application of the jump conditions Eq. (5.1) requires the computation of the velocity components tangential and normal to the flame front. The linear analysis presented in the following shall be limited to perturbation wave lengths λ that are long compared to the convective-diffusive length scale δ_D in order to avoid the occurrence of significant levels of flame stretch and to not trigger significant 2D effects. Mathematically, this fact is reflected by limiting the analysis to large Péclet numbers $Pe = \delta_D / \lambda$. Furthermore, flame displacement amplitudes shall be small, that is $\xi \ll \lambda$. We assume $\xi = \mathcal{O}(\epsilon)$, where ϵ may be a small quantity, such that all terms $\mathcal{O}(\epsilon^2)$ are negligible. Accordingly, they are dropped in the following analysis. Developing all quantities in powers of Pe^{-1} shifts perturbations that exhibit a short wave length compared to the flame thickness to higher order terms in the expansion parameter. Based on this expansion, only zeroth order terms are considered in the following. Using this method, the flame normal and tangential vectors resulting from the perturbed flame are given by

$$\mathbf{n}_f = [n_{f,1}, n_{f,2}] = \left[-\frac{\partial \xi}{\partial x_1}, 1 \right] + \mathcal{O}(Pe^{-1}) \quad \text{and} \quad \mathbf{t}_f = [t_{f,1}, t_{f,2}] = \left[1, \frac{\partial \xi}{\partial x_1} \right] + \mathcal{O}(Pe^{-1}), \quad (5.2)$$

respectively.

A perturbed flame sheet goes along with perturbations of all other flow variables, that is velocity and pressure. Assuming a flow field of the fresh mixture $u_u = [u'_{u,1}, \bar{u}_{u,2} + u'_{u,2}] + \mathcal{O}(Pe^{-1})$, the flame normal and tangential velocity components just upstream of the flame sheet can be computed from $n_{f,i} u_{u,i}$ and $t_{f,i} u_{u,i}$, which results in

$$u_{u,\perp} = \bar{u}_{u,2} + u'_{u,2} + \mathcal{O}(Pe^{-1}) \quad \text{and} \quad u_{u,\parallel} = \bar{u}_{u,2} \frac{\partial \xi}{\partial x_1} + u'_{u,1} + \mathcal{O}(Pe^{-1}), \quad (5.3)$$

respectively. Using these equations together with Eq. (5.1), we get for the mean quantities

$$[\bar{u}_2]_u^b = s_L^0 E \quad (5.4)$$

$$[\bar{p}]_u^b = -(s_L^0)^2 \rho_u E \quad (5.5)$$

$$[\bar{u}_1]_u^b = 0, \quad (5.6)$$

where the assumption of a stationary flame front of the unperturbed flow requires $\bar{u}_{u,2} = s_L^0$ and $E = \rho_u / \rho_b - 1$ denotes the non-dimensional increase of specific volume. Hence, across the flame front the flow is accelerated by a factor $e = (E + 1)$ in x_2 -direction and the static pressure decreases by a term $(s_L^0)^2 \rho_u E$. Application of the jump conditions for the perturbed flow field results in

$$[u'_2]_u^b = E \left(u'_{u,2} - \frac{\partial \xi}{\partial t} \right) + \mathcal{O}(\text{Pe}^{-1}) \quad (5.7)$$

$$[p']_u^b = -2\rho_u s_L^0 [u'_2]_u^b + \mathcal{O}(\text{Pe}^{-1}) \quad (5.8)$$

$$[u'_1]_u^b = -s_L^0 E \frac{\partial \xi}{\partial x_1} + \mathcal{O}(\text{Pe}^{-1}), \quad (5.9)$$

while the equation governing the kinematics of the flame sheet $s_L = u_{u,\perp} - \partial \xi / \partial t$ leads to

$$u'_{u,2} - \frac{\partial \xi}{\partial t} = s_L - \bar{u}_{u,2} + \mathcal{O}(\text{Pe}^{-1}). \quad (5.10)$$

Neglecting Flame Stretch

When Landau [27] assessed the stability of planar flames, he assumed a constant flame speed $s_L = s_L^0 + \mathcal{O}(\text{Pe}^{-1})$ and, thus, neglected stretch effects. Note that this assumption is perfectly in line with the neglect of terms that are of higher than zeroth order in $1/\text{Pe}$. Inserting the constant flame speed assumption into Eqs. (5.7)–(5.9), the jump conditions write

$$[u'_2]_u^b = \mathcal{O}(\text{Pe}^{-1}) \quad , \quad [p']_u^b = \mathcal{O}(\text{Pe}^{-1}) \quad \text{and} \quad [u'_1]_u^b = -s_L^0 E \frac{\partial \xi}{\partial x_1} + \mathcal{O}(\text{Pe}^{-1}). \quad (5.11)$$

From Eq. (5.10) it follows that the flame front moves in response to upstream velocity perturbations according to $\partial \xi / \partial t = u'_{u,2} + \mathcal{O}(\text{Pe}^{-1})$. While pressure and flame-normal velocity fluctuations are continuous across the flame, flame-tangential velocity perturbations change, as stated by Eq. (5.11).

Considering Flame Stretch

Now consequences of flame stretch shall be investigated by including terms up to $\mathcal{O}(\text{Pe}^{-1})$ to the analysis. As already mentioned in Sec. 1.2.3, in the limiting case of

high activation energies of the global reaction, this shall only add a new stretch dependent term to the flame speed relation, while the jump conditions Eqs. (5.7)–(5.9) remain the same. This approximation is in line with the phenomenological stretch-related correction of Markstein [44] and justified by the strong dependency of the flame speed to temperature in the case of a high activation energy of the global reaction [42].

Assuming that the Markstein number for flow strain and flame curvature is the same, the equation for the flame speed writes

$$s_L = s_L^0 (1 - l_M \kappa_s) \quad (5.12)$$

with the Markstein length l_M and the flame stretch κ_s . Using this relation together with Eq. (5.10) we get

$$u'_{u,2} - \frac{\partial \xi}{\partial t} = -l_M \kappa_s. \quad (5.13)$$

This extended relation of the flame sheet kinematics is now inserted to the jump conditions Eqs. (5.7)–(5.9) and we obtain

$$[u'_2]_u^b = -E l_M \kappa_s \quad (5.14)$$

$$[p']_u^b = -2\rho_u s_L^0 [u'_2]_u^b \quad (5.15)$$

$$[u'_1]_u^b = -s_L^0 E \frac{\partial \xi}{\partial x_1}. \quad (5.16)$$

While the jump conditions (5.16) for the tangential velocity u'_1 remain unchanged compared to the case without flame stretch, the other two now contain flame stretch related quantities. These new terms reflect the fact that changes in the flame speed affect the local volume production per unit length $m = E s_L$ of the flame sheet, see Eq. (3.7). Hence, concave parts of the flame now produce more volume since the flame propagation speed is increased here, and vice versa for convex parts.

A stretch dependent flame speed, as expressed in Eq.(5.13), is one of the most important mechanisms that dampens flame front displacements by imposing flame speed variation in convex/concave regions. Following the analysis conducted in Sec. 1.3.2, it has a diffusion-like effect on the flame dynamics. Consequently, sharp displacements are smeared in space.

5.2.2 Modeling of Flame Generated Vorticity

Based on the jump conditions derived in the previous section, a model for the production of vorticity by a perturbed flame sheet shall now be deduced. To this end, the jump in the tangential velocity component of Eqs. (5.9) or (5.16) is revisited, since it quantifies the amount of vorticity generated across the flame sheet. This can be shown by computing the circulation around a closed surface as depicted in Fig. 5.4.

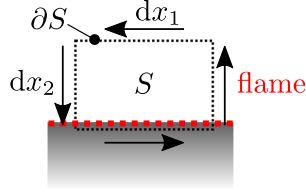


Figure 5.4: Illustration of the line integral of Eq. (5.17) along a path ∂S enclosing a surface S .

The lower side of this rectangular surface is assumed to be just inside the domain of the unburned fluid, whereas all other sides are inside the burned region. We obtain for the circulation of an infinitesimally small surface

$$\begin{aligned}
 d\Gamma &= \oint_{\partial S} u_i dx_i \\
 &= -u'_{b,1} dx_1 - u'_{b,2}(x_1) dx_2 + u'_{u,1} dx_1 + u'_{b,2}(x_1 + dx_1) dx_2 \\
 &= \frac{\partial u'_{b,2}}{\partial x_1} dx_1 dx_2 - [u'_1]_u^b dx_1,
 \end{aligned} \tag{5.17}$$

where it is assumed that the streamwise component of the flow just upstream of the flame does not vary along the flame sheet, i. e. $\partial u'_{u,2}/\partial x_1 \equiv 0$. Furthermore, also the flame tangential velocity is assumed to be constant along the sheet. This results in an expression for the circulation, which is related to vorticity by a surface integral $d\Gamma = \int_S \omega dA$. Hence, a perturbed flame acts as a vortex sheet of strength

$$\frac{\partial \Gamma}{\partial x_1} = \frac{\partial u'_{b,2}}{\partial x_1} dx_2 - [u'_1]_u^b. \tag{5.18}$$

As shown in Sec. 5.2.1, variations of flame-normal velocity of combustion products $u'_{b,2}$ along the flame sheet result only from flame stretch effects, i. e. consequences of flame curvature and flow strain. Combining Eq. (5.18) with the jump condition of Eq. (5.14) and (5.16) assuming $\partial u'_{u,2}/\partial x_1 \equiv 0$, the stretch dependency of the first term in Eqs. (5.18) becomes clear:

$$\frac{\partial \Gamma}{\partial x_1} = -E l_M \frac{\partial \kappa_s}{\partial x_1} dx_2 + s_L^0 E \frac{\partial \xi}{\partial x_1}. \tag{5.19}$$

Assuming the flame front displacement may be of order $\mathcal{O}(\epsilon)$ and dx_2 of order of the flame thickness, the first term in Eq. (5.19) is of the order $\mathcal{O}(\epsilon l_M^2)$. The second term in Eq. (5.19) is of order $\mathcal{O}(\epsilon)$. Knowing that the Markstein length l_M is a quantity of similar length as the flame thickness, it becomes clear that the first term in Eq. (5.19) is much smaller than the second one. Therefore, in the scope of this thesis, only the second term in Eq. (5.19) shall be of interest and, thus, flame stretch related effects on flame generated vorticity are neglected. This is in line with the analysis conducted by Matalon *et al.* [41]. They reported that significant jumps in vorticity result only from

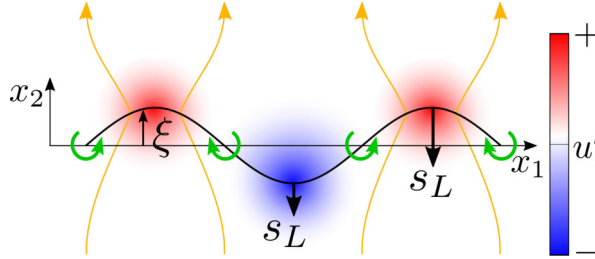


Figure 5.5: Sketch of a harmonically perturbed flame sheet including an illustrations of the consequences of flame-generated vorticity, indicated by green circular arrows. Together with the mechanism of geometrical focusing, see Sec. 5.2.3, this leads to the formation of in- and decreased flow speeds at the flame front, illustrated by the red and blue colored areas as well as the orange stream tubes. Flame stretch related variations of flame speed are indicated by downward pointing small arrows of various lengths.

baroclinic production assuming the flow field upstream of the flame is vortical-free (irrotational). For a more complete analysis of the generation of vorticity by gasdynamic discontinuities see the work of Hayes [175]. More detailed considerations of flame generated vorticity due to flame stretch are, for example, found in the works of [100, 173, 174, 196].

From Eq. (5.19) it follows that flame generated vorticity is maximum at inflection points of the flame displacement. In Fig. 5.5 the effect of this vorticity is indicated by green circular arrows placed at points of $\xi = 0$. They lead to an acceleration and deceleration of the contracting (red) and expanding (blue) flow tubes, respectively, and thus destabilize the perturbed flame sheet. Since the work of Darrieus and Landau was based on the jump conditions shown in Sec. 5.2.1 neglecting flame stretch, it can be concluded that flame-generated vorticity is the driving mechanisms of the Darrieus-Landau instability. The modeling concept pursued in this work follows this result: Vorticity, in form of point vortices, is distributed along the mean flame sheet satisfying Eq. (5.19). These vortices would subsequently be advected by the mean flow field following Eq. (3.10). This advection process, however, shall be neglected.

The suggested modeling concept distributes vorticity along the mean flame position in form of point vortices. Such vortices, however, exhibit a flow field singularity at their center, which would lead to unbounded velocity magnitudes close to it. Since these vortices are placed very close to the flame sheet, this could lead to undesired distortions of the resulting flame front. Hence, viscous vortices will be used, where the vorticity is not concentrated in one singular point, but spatially distributed according to a Gaussian-like function. Such a vortex is known as the Lamb-Oseen vortex [197]. Its vorticity distribution is obtained as an exact solution of the Navier-Stokes equations for an initially singular point vortex. The complex conjugate of the vortical

velocity field of a Lamb-Oseen vortex is written as

$$\tilde{u}_\omega(\xi) = -i \frac{\Gamma}{2\pi} \frac{1}{\xi - \xi'} \left[1 - \exp\left(-\frac{|\xi - \xi'|^2}{r_{0,\omega}^2}\right) \right], \quad (5.20)$$

where the velocity drops to zero at the vortex center ($\xi \rightarrow \xi'$). The vortex radius $r_{0,\omega}$ specifies the radius where the induced circumferential velocity is maximum. For radii greater than $r_{0,\omega}$, the velocity distribution asymptotically approaches the one of a singular vortex, see Eq. (3.22). The vortex sheet assumed by this modeling approach has a thickness of the order of the flame displaced $\mathcal{O}(\epsilon)$. Hence, the vortex radius is always set to the prevailing displacement amplitude. The Markstein length l_M , which quantifies the thickness of a flame sheet, is hereby used as a lower threshold for the vortex radius, i. e. $r_{0,\omega} > l_M$. It is finally emphasized that such an approach mimics the Darrieus-Landau mechanism, which also relies solely on flame-generated vorticity.

5.2.3 Modeling of Geometrical Focusing

In the case of acoustically excited burner-stabilized flames, flame front displacements may be imposed whose amplitudes are not small compared to a characteristic length scale of the perturbation. As shown in Eq. (4.2), acoustics interacts predominantly with the flame base region exhibiting a characteristic length scale of about $0.6L_f$. Knowing that the Darrieus-Landau mechanism will lead to a convective growth of the primary displacements, after some time a situation may occur where the displacement amplitude ϵ is no longer negligible compared to the characteristic perturbation length scale. Then the theory based on two flow domains of constant spatial extension, which are coupled via the jump conditions introduced in Sec. 5.2.1 does not hold any more. In addition to the Darrieus-Landau mechanism, new phenomena may occur. One of them is geometrical focusing, which will be introduced in this section.

The proposed extended modeling approach is based on a method that captures consequences of gas expansion across a perturbed flame sheet. It essentially relies on existing modeling strategies, which represent a flame sheet as a localized source of volume [100, 173, 174, 198, 199]. Most studies realize such a volume production relying on discontinuous source panels, which are placed along the instantaneous flame front position. The herein proposed method seizes this idea and extends it by using spatially distributed (Gaussian) volume sources instead of panels, which allow to resolve the inner structure of the flame sheet and avoid unbounded velocity magnitudes. More specifically, a Gaussian volume production kernel $D(x)$ is proposed and included into the modeling framework introduced in Chap. 3. Based on this general idea, a modeling concept is derived in the following, which has already successfully been implemented and tested by Zimmermann [195] in the scope of his Bachelor's thesis. To the best knowledge of the author, no prior efforts have been made to analyze acoustics-flame interactions based on such an approach.

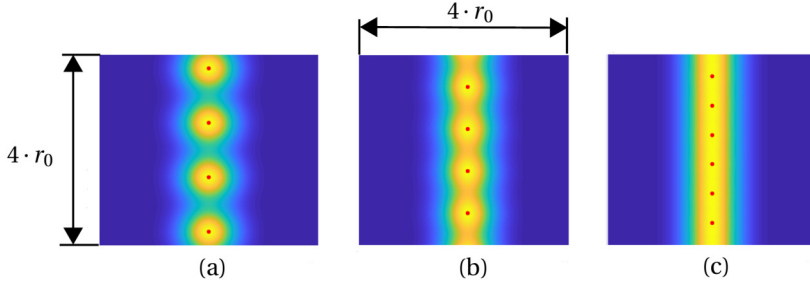


Figure 5.6: Each of the three figures shows the amount of volume produced according to a number of Gaussian sources with kernel radius r_0 distributed along a vertical line, where blue denotes zero and yellow maximum volume production. The center of each Gaussian source is marked by a red dot (\bullet). The number of sources per length increases from left to right, while the sum of all source strengths is kept constant (taken from Zimmermann [195], Fig. 5.8).

The most elementary kernel, which could be used to represent the volume production kernel $D(x)$, is a Dirac Delta distribution $\delta(x)$. Here, volume is produced only at one singular point. By continuously placing such point sources along a line, a line source emerges. Approximating the flame front by a finite number of such lines results in a kinematic description of an infinitely thin flame sheet, since the flow velocity immediately increases at the flame by a fixed value that depends on the respective line source strength. This approach has, for example been applied by Pindera and Talbot [173]. Here, another method is pursued, which is inspired by the Lamb-Oseen vortex introduced in the previous section. In analogy to this kind of vortex, a Gaussian-like volume source distribution is assumed. Computing the flow field associated to such a source in free space, results in an irrotational velocity field

$$\tilde{u}_e = \frac{S}{2\pi} \frac{1}{\xi - \xi'} \left[1 - \exp\left(-\frac{|\xi - \xi'|^2}{r_{0,e}^2}\right) \right], \quad (5.21)$$

where S denotes the strength of the Gaussian source, just as in the case of a point source, see Eq. (3.21). Again, the flow field is finite-valued everywhere. Placing several such sources right next to each other results in a discretized version of a line source, but now with a smooth increase of velocity across it. This is illustrated in Fig. 5.6, where three different source distributions of increasing density, i. e. sources per length, are shown. While the individual sources are clearly distinguishable in the left figure, in the figure to the very right the given source distribution already resembles a line source very well — although only six sources are used. Generally, modeling approaches relying on Gaussian sources have to ensure that the distance between the individual sources is sufficiently smaller than $r_{0,e}$.

A distribution of volume sources along a line leads to an increase of the velocity component normal to that line. Fig. 5.7 visualizes this for a steady state flame front along

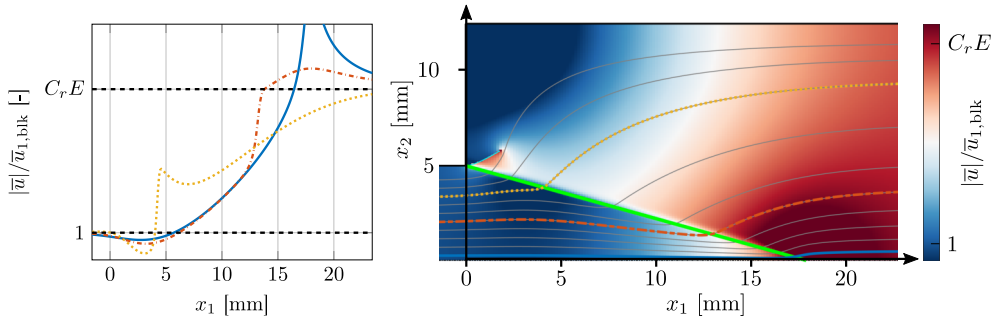


Figure 5.7: Left: Magnitude of flow velocity evaluated along three stream lines (see right plot) plotted over the axial coordinate x_1 . The theoretical velocities far up- and downstream of the flame are marked by horizontal black dashed lines. Right: Steady state flow field for $C_r = 0.4$. The flame front (green) is represented by a number of Gaussian sources of kernel radius r_0 . The three stream lines (gray lines) referenced in the left plot are marked by corresponding line styles.

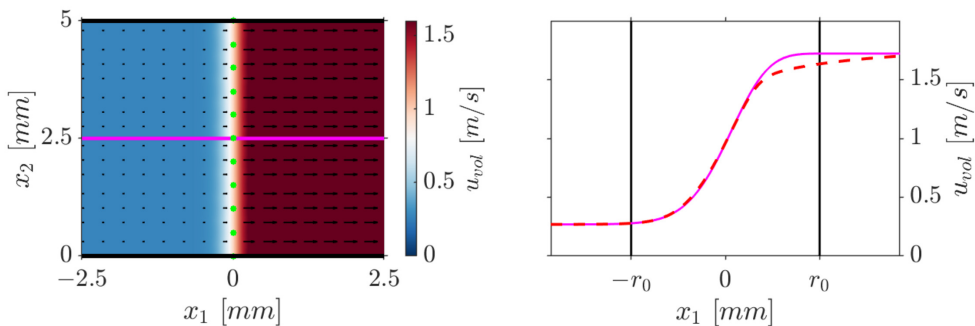


Figure 5.8: Left: Axial velocity of a channel flow including a vertical flame sheet (methane-air, $\phi = 0.8$) represented by Gaussian sources with kernel radius r_0 (\bullet). Right: Flame normal velocity evaluated along the pink line shown in the left plot (pink line) compared to results of a 1D simulation employing detailed chemical mechanism (red dashed line). The Gaussian sources are placed at $x_1 = 0$ and have a kernel radius of $r_{0,e} = 0.53$ mm (taken from Zimmermann [195], Fig. 5.6).

which Gaussian volume source of strength S and radius $r_{0,e}$ are distributed. Plotting the absolute velocity along three selected stream lines illustrates the acceleration of the flow across the flame sheet. Therefore, $r_{0,e}$ has to be chosen such that the flame normal velocity induced by the Gaussian sources optimally resembles the behavior imposed by a realistic combustion zone. In order to archive this, 1D simulations of a steady flame are conducted employing a detailed chemical reaction scheme. Re-

sults are compared to the fields relying on Gaussian sources in Fig. 5.8¹. The left plot of this figure shows a straight flame stabilized inside a duct, along which Gaussian sources are uniformly distributed. The plot on the right hand side of Fig. 5.8 shows the flame normal velocity inside the duct evaluated along the pink horizontal line shown in the left plot (pink line). Additionally, results of the detailed 1D simulations are shown (red dashed line). Both curves coincide very well and only deviate on the downstream side of the flame sheet, where the secondary reaction layer is placed, see Sec. 1.1.1. All in all, for the given value of $r_{0,e}$, very good agreement between both combustion models is found.

The velocity fields depicted in Figs. 5.7 and 5.8 are retrieved by placing a number of Gaussian sources of kernel radius $r_{0,e} = 0.53$ mm along a given steady state flame front and placing a source of strength $S = 2\bar{u}_{1,\text{blk}}R_i$ at $x_1 = -\infty$ (corresponds to $\xi = 0$ in the image domain). A Kutta condition is employed at the trailing edge for the setup shown in Fig. 5.7. Besides this, the only difference in the computations involved to create both figures is the choice of the respective Schwarz-Christoffel mapping (see Zimmermann [195] for details). Considering the fact that the Gaussian sources should impact the flow velocity down- *and* upstream of the flame, it may be surprising that the velocity far upstream of the flame asymptotes to $\bar{u}_{1,\text{blk}}$ while it approaches $C_r E \bar{u}_{1,\text{blk}}$ on the downstream side. This point can be clarified as follows: As shown in Fig. 3.4, the Gaussian sources are placed in the image domain along an arc starting from $\xi = 1$ and extending to negative values of ξ_1 . Impermeability boundary conditions demand a second arc of sources mirrored at the real axis. These two arcs enclose the flow domain upstream of the flame, where the flow field contributions of the individual Gaussian sources mostly annihilate each other. Considering a duct flame, the superimposed contributions of all sources even perfectly vanish on the upstream side of the flame. This is a consequence of the fact that here the flame front maps to a sphere around the origin in the image domain, which is symmetric with respect to the imaginary and the real axes. For the burner-stabilized flame of Fig. 5.7, the arc shown in Fig. 3.4 is only symmetric with respect to the real axis. In consequence, a slightly negative flow upstream of the flame is induced by the Gaussian sources, which however is negligible as illustrated in Fig. 5.7 (the absolute velocities almost approach 1 for $x_1 \rightarrow -\infty$).

Representing a flame front by a number of Gaussian sources, leads to an unconditional growth of flame front displacements, as will be shown in the next section. Hence, together with the destabilizing effect of flame-generated baroclinic vorticity, discussed in Sec. 5.2.2, two hydrodynamic mechanisms of flame-flow feedback are found — a vortical and an irrotational one. The former has already been covered in the discussion above. The latter can be understood by considering a perturbed flame sheet, as depicted in Fig. 5.9. The combustion process imposes a volume production onto the flow, which is an irrotational effect, and which can be captured by distributing sources along the flame sheet. This imposes, on the one hand, a discontinuity in

¹Computed with Cantera [29] using the GRI-Mech 3.0 reaction mechanism [30]

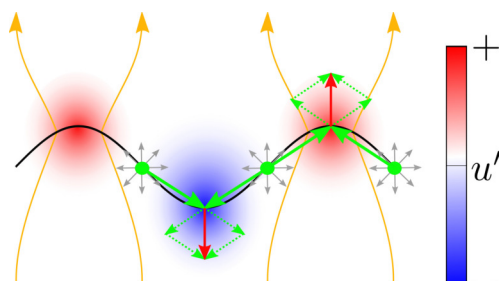


Figure 5.9: Illustration of the perturbed flow field imposed by a displaced flame sheet, which is represented by a number of Gaussian volume sources. The overall effect of these sources leads to a geometrical focusing of the flow, i. e. an acceleration of the flow in the vicinity of concave and a deceleration in the vicinity of convex parts of the flame, amplifying already existent flame perturbations.

flame normal velocity across the flame. On the other hand, additionally the flow field in the vicinity of the flame is modified. This is illustrated in Fig. 5.9: Three sources placed at the inflection points of the perturbed flame sheet are exemplarily highlighted (gray). Each imposes a velocity field that points away from the center of the respective source. Overall, this results in an increase of flow velocity in the vicinity of the maxima of the displaced flame sheet and, vice versa, a decrease at the minima. Altogether, this results in an accelerated flow at concave and a decelerated flow at convex parts of the flow field. Due to this dependency on flame shape, this process is referred to as *geometrical focusing* in the following. Just like the Darrieus-Landau mechanism relying on flame-generated vorticity, geometrical focusing amplifies flame perturbations and constitutes a hydrodynamic flame-flow feedback mechanism. It essentially relies on movements of the mean flame shape and is, hence, not accounted for if two coupled flow domains of constant boundaries are assessed, as it is assumed in the scope of Darrieus-Landau's problem discussed in Sec. 1.2.3.

For the sake of completeness, it should be mentioned that geometrical focusing also leads to the occurrence of spatially varying tangential velocity perturbations, associated with flow strain. Their consideration, however, is explicitly neglected here.

5.3 Analysis of the Impact of Flame-Flow Feedback

The modeling framework introduced in Chap. 3 supplemented with the approaches outlined in this chapter shall now be applied to the flame configurations analyzed in Chap. 4 (primary interactions). Since vortex shedding was found to only have a negligible impact on the flame response, it is excluded from the analysis presented in the following.

Parameter	Value
Expansion ratio e	6.68
Flame speed s_L^0	0.2686 m/s
Flame thickness δ_D	83.95 μm
Markstein number M_a	4
Gaussian source kernel radius $r_{0,e}$	0.53 mm

Table 5.1: Flame parameters used for the computations of this chapter.

An overview of the flame parameters used for the computations of this chapter is provided in Tab. 5.1. The values for e , s_L and δ_D are retrieved from 1D simulations of lean methane-air flames at $\phi = 0.8$ relying on the software Cantera [29] employing the GRI-Mech 3.0 reaction mechanism [30]. The flame thickness is estimated by a diffusion length $\delta_D = D_{th}/s_L$, where D_{th} denotes the thermal diffusivity. Following Eq. (5.12), the definition of the stretched flame speed depends on the Markstein length l_M , which is computed from δ_D and the Markstein number M_a via $l_M = \delta_D M_a$.

Following Matalon *et al.* [41], methane-air mixtures exhibit Markstein numbers roughly between 3 and 4. As mentioned in the introduction of this chapter, we should expect an overprediction of displacement amplitudes when including flame-flow feedback into the modeling approach, since only driving and no damping mechanisms are considered. Damping mechanisms are usually associated with flame stretch. In the modeling approach proposed here, only consequences of curvature-related stretch for the flame speed are considered. Flow strain as well as stretch generated vorticity are neglected, which might significantly underestimate the damping, as indicated by the study of Pindera and Talbot [174]. Hence, in the scope of this thesis only a qualitative analysis of flame-flow feedback mechanisms is possible and therefore, in a first approximation, a Markstein number of 4 is assumed. Following Fig. 5.8, the kernel radius of all Gaussian sources is fixed to $r_{0,e} = 0.53$ mm.

Based on these assumptions, the model relying on the 1D linear representation of the flame dynamics of Eq. (3.16), a Schwarz-Christoffel mapping, a representation of the flow field by a finite number of flow field singularities and a Kutta condition is ready to be solved. Exactly the same setup as discussed in Chap. 4 is analyzed, but this time flame-flow feedback is included. Concerning the numerical details, Eq. (3.16) is integrated in time relying on an explicit Euler method together with a first-order upwind discretization scheme for the advection and a second-order central scheme for the diffusion term. The flame sheet is discretized using 100 sample points and the time step width is set such that a mesh Fourier number of $l_M s_L^0 \Delta t / \Delta x^2 \approx 0.05$ is achieved [200]. In each time step, Lamb-Oseen vortices are distributed along the mean flame position (one vortex per sampling point), with their respective strength being computed from Eq. (5.16). Furthermore, Gaussian sources of kernel radius $r_{0,\omega}$ are placed along the instantaneous flame front, with a density of 10 sources per millimeter. Their strengths depend on the local flame speed, on the expansion ratio

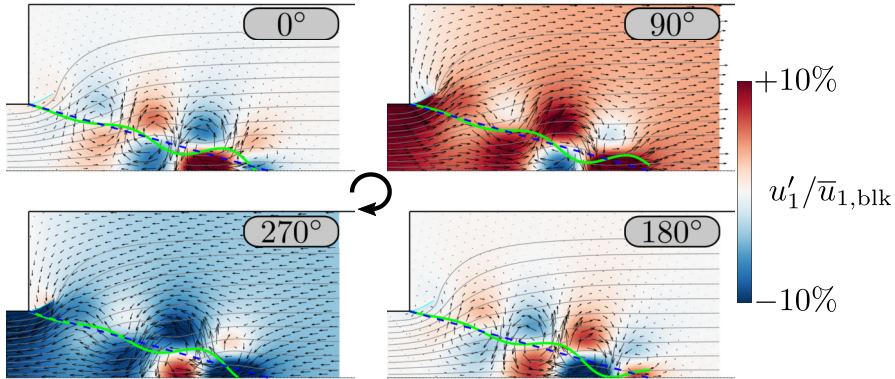


Figure 5.10: LOM predictions including flame-generated vorticity of a harmonically forced flame configuration (at 120 Hz and an amplitude of 10% \bar{u}_{blk}) for a confinement ratio of $C_r = 0.4$. The minimum vortex kernel radius is set to $r_{0,\omega,\text{min}} = 4.25 l_M$. Shown are four consecutive snapshots taken at phases from 0° to 270° relative to the forcing signal. Each shows the current axial velocity perturbations u'_1 (color), the mean flame front position (---), the perturbed flame (—) and, attached to the trailing edge, the Kutta panel.

e as well as on the number of sources per millimeter. The global heat release is evaluated using the linearized relations introduced in Chap. 6. The Kutta condition is applied as described in Sec. 4.2.2. The run times of the simulations shown in this chapter are of the order of one minute, if solely flame generated vorticity is considered (Sec. 5.3.1), and of 10 minutes if gas expansion via Gaussian sources is taken into account (Secs. 5.3.2).

The analysis is split into two parts: in the first one, consequences of flame generated vorticity are assessed in Sec. 5.3.1, which is analog to the Darrieus-Landau mechanism. In the second part, Sec. 5.3.2 focuses on irrotational feedback mechanisms, namely geometrical focusing, by representing the flame sheet by a number of Gaussian sources, which impose a jump in flame normal velocity across the flame sheet. All simulations are put into perspective by comparing them to the results of Chap. 4, where flame-flow feedback was neglected.

5.3.1 Flame Generated Vorticity

In a first step, the role of flame generated vorticity is investigated and the flame normal acceleration across the flame sheet, captured by Gaussian sources, is not taken into consideration. Lamb-Oseen vortices are placed along the mean flame front. According to Eq. (5.16), their strength is proportional to the local flame displacement gradient $\partial \xi / \partial x_1^F$, the non-dimensional increase of specific volume E and the un-

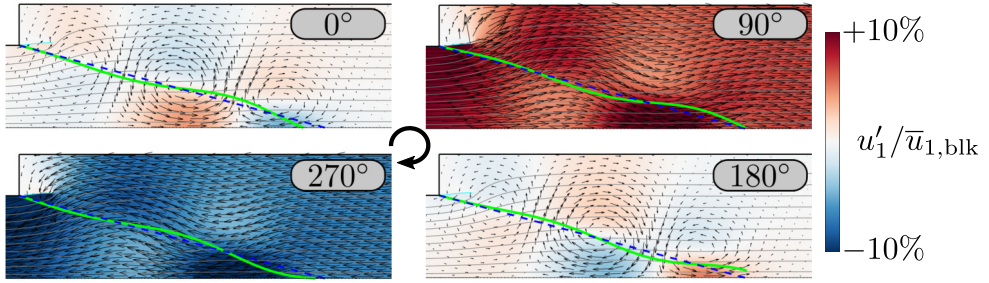


Figure 5.11: Results of a simulation as described in Fig. 5.10, but for a confinement ratio of $C_r = 0.66$.

stretched flame speed s_L^0 . Since vorticity is generated all along the perturbed flame sheet with maxima at the inflection points of ξ , its spatial distribution is modeled by Lamb-Oseen vortices whose kernel radii are set to the current maximum displacement amplitude. Furthermore, a minimum radius of $r_{0,\omega,\min} = 4.25 l_M$ is assumed in order to avoid an overprediction of the imposed vortical velocity perturbations at the flame sheet. Applying such a definition for $r_{0,\omega,\min}$ ensures that the order of magnitude of the kernel radius cannot become smaller than the flame thickness. Nevertheless, $r_{0,\omega,\min}$ has to be regarded as an empirical parameter whose value is not rigorously derived from first principles. Unfortunately, it significantly affects the computed flame response, as will be shown below.

Figs. 5.10 and 5.11 show four snapshots of harmonically forced simulations of this model at $C_r = 0.4$ and $C_r = 0.66$, respectively. It is evident that consideration of flame generated vorticity leads indeed to a convective growth of flame front perturbations: right at the anchoring, hardly any flame displacement is visible, whereas the flame tip oscillates with significant amplitude. Comparing the results of both confinement ratios, we observe that the wave length and maximum displacement amplitude of the resulting flame front perturbations varies: A more narrow confinement seems to promote perturbations of longer wave lengths and lower displacement amplitudes. Furthermore, a considerable impact of the flame sheet on the flow of premixture is observable for both setups. Positive and negative axial velocity perturbations propagate from the flame base region to its tip, similar as reported by Blanchard *et al.* [129]. It has, however, to be noted that, other than claimed by Blanchard *et al.* [129], the vortical component of flame-flow feedback does most probably not fully explain the observed convected velocity perturbations, since the irrotational component has a significant impact, as well, which will be shown in Sec. 5.3.2.

Imposing an impulsive forcing, results in a response as depicted in 5.12. As expected, the response with and without flame-flow feedback agree at $t^* = 0$ and then increasingly deviate from each other. Similar to the CFD data, negative and positive secondary peaks develop and subsequently grow in amplitude while they are advected towards the flame tip. The most apparent deviation between the LOM (---) and

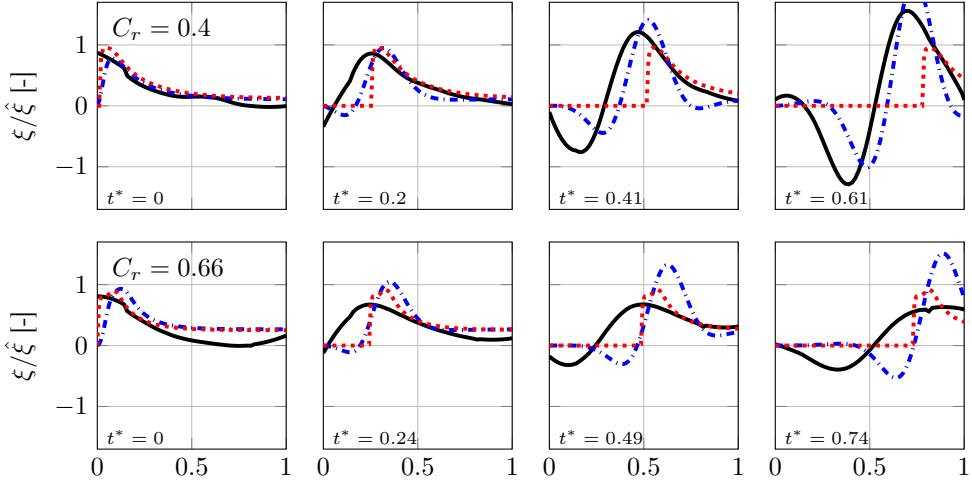


Figure 5.12: Four snapshots taken at equidistant instances in time of the normalized flame displacement resulting from an impulsive velocity forcing at $t^* = 0$ taken from CFD/SI results (—), the acoustic LOM excluding flame-flow feedback (.....) and the acoustic LOM including flame-generated vorticity with $r_{0,\omega,\min} = 4.25 l_M$ (-.-.-) at two confinement ratios: $C_r = 0.4$ (top) and $C_r = 0.66$ (bottom).

the CFD data (—) is the position where the negative and positive peaks develop, which is slightly too far downstream in the low-order representation. Furthermore, the responses predicted by the LOM is stronger than the respective CFD counterpart. Overall, the $C_r = 0.4$ low-order predictions match the respective CFD results better than the $C_r = 0.66$ ones. The damping behavior, presumably imposed by the presence of a rather narrow confinement, seems to be underpredicted for the $C_r = 0.66$ setup. Nevertheless, a — compared to the acoustic LOM — improved agreement can be observed for both configurations.

This improved agreement is also reflected by the corresponding impulse and frequency response data of the global heat release rate, which is shown in Fig. 5.13. At $C_r = 0.4$, CFD/SI (—) and LOM (-.-.-) predictions agree well, only small deviations in phase/gain and the impulse response are observable. At $C_r = 0.66$, the acoustic LOM correctly captures the oscillatory behavior of the IR, however, the response deviates significantly from the CFD/SI data around $t^* = 0$, see Fig. 5.13b. Accordingly, the corresponding FTF gain curves are qualitatively different. The drastic reduction of the peak gain value of the $C_r = 0.66$ setup (compared to $C_r = 0.4$), can also be found in the acoustic LOM data (-.-.-). All in all, the suggested low order modeling strategy results in reasonable response predictions, even at $C_r = 0.66$.

Interpreting the results of the acoustic LOM including flame generated vorticity, it should be kept in mind that they are based on an empirical parameter $r_{0,\omega,\min}$. Evaluating the flame responses for 10% lower and larger values of $r_{0,\omega,\min}$ results in the

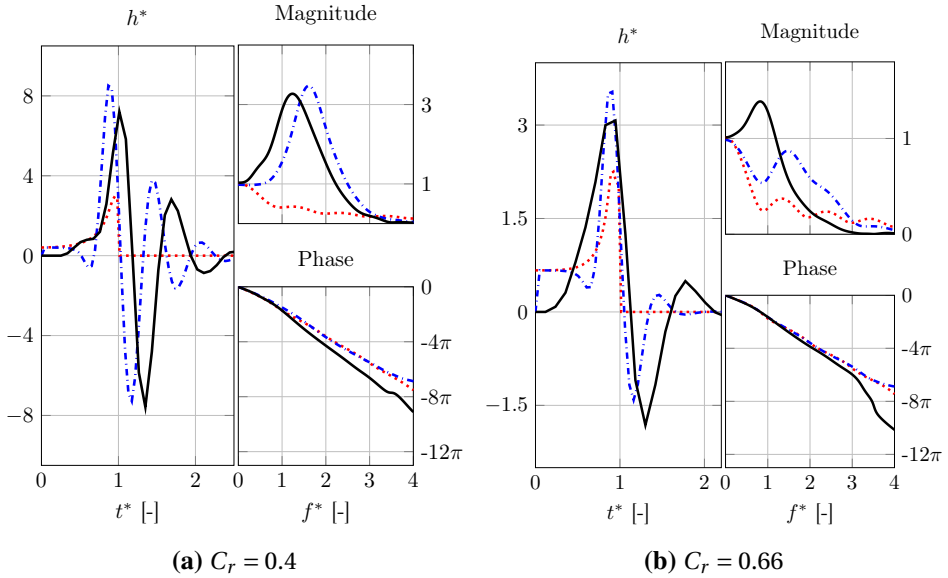


Figure 5.13: IR and FR in terms of gain and phase at $C_r = 0.4$ and $C_r = 0.66$ as predicted by CFD/SI (—) as well as by the acoustic LOM with (— · —) and without (· · ·) consideration of flame-generated vorticity ($r_{0,\omega,\min} = 4.25l_M$).

responses visualized in Figs. 5.14a and 5.14b, respectively. A reduction of the minimum kernel radius leads to higher velocity amplitudes and, thus, to an increase of the FTF gain. Exactly the opposite behavior can be observed when the radius is increased. We have to recognize that the low-order predictions are rather sensitive to variations in $r_{0,\omega,\min}$. That means that the quantitatively good agreement with the reference CFD/SI data is the result of a parameter tuning, i. e. finding an optimal value for $r_{0,\omega,\min}$. Nevertheless, the fact that the model shows reasonable results for both confinement ratios and, additionally, leads to qualitatively correct response predictions indicates that flame generated vorticity may indeed be one important driving mechanism resulting from flame flow feedback.

The rather simplistic treatment of flame generated vorticity proposed in this section resulted in valuable insights in consequences of flame-flow feedback. Its impact on the FTF could be shown to lead to gains exceeding unity. Furthermore, the findings of Blanchard *et al.* [129] could be corroborated stating that a perturbed flame sheet acts as a vortex sheet whose upstream influence is responsible for the observed convected velocity perturbations. The present analysis contains the empirical parameter $r_{0,\omega,\min}$ and it was shown that response predictions are quite sensitive to its exact value. Therefore, all results presented in this section are qualitative in nature. Quantitatively good agreement between LOM and CFD/SI data could be achieved by tuning $r_{0,\omega,\min}$. Future studies could refine the analysis of flame-generated vorticity by implementation of more detailed vorticity source terms, for example, relying on the

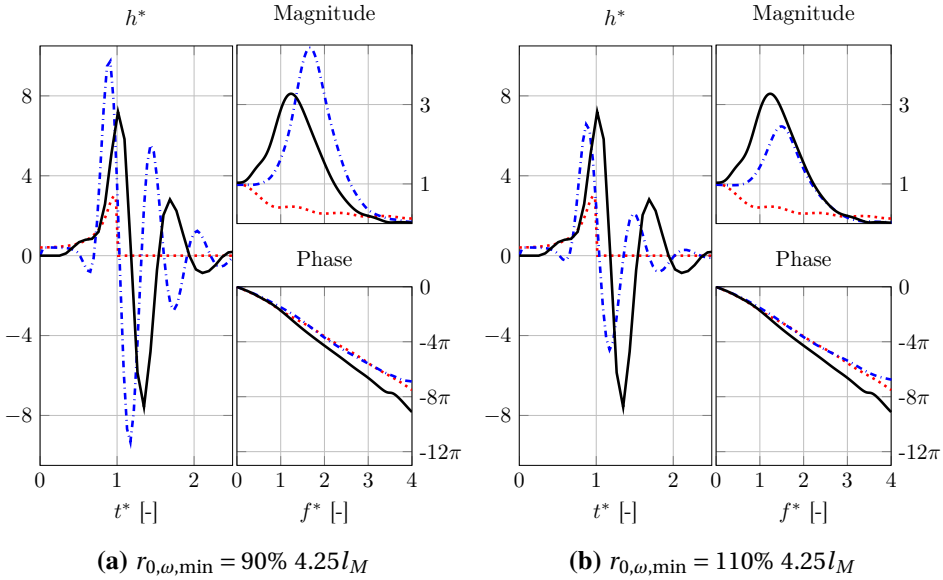


Figure 5.14: IR and FR in terms of gain and phase at $C_r = 0.4$ as predicted by CFD/SI (—) as well as by the acoustic LOM with (---) and without (····) consideration of flame-generated vorticity. Shown are results for two minimum vortex kernel radii $r_{0,\omega,\min}$.

work of Hayes [175]. This might possibly enable a quantitative assessment of the vortical component of flame-flow feedback.

5.3.2 Irrotational Flame-Flow Feedback

A flame usually imposes a significant change in density on a flow, which is caused by exothermic reactions releasing reasonable amounts of sensible enthalpy. Such a density change is accompanied by an expansion and, thus, an acceleration of the flow across the flame zone. This process is captured by means of Gaussian sources, which are placed along the perturbed flame sheet and, hence, provoke a jump in flame normal velocity. Their kernel radii $r_{0,e}$ are adjusted in order to optimally match a realistic velocity profile through the flame front, see Fig. 5.8.

Applying this technique, the problem arises that the steady state position of the flame is a priori unknown, since the presence of a confinement together with an combustion-induced expanding flow alters the steady state flow field and, hence, also the corresponding flame shape [142, 144]. This circumstance would require the computation of the steady state in a first step, before the displacement dynamics could be evaluated in a second. Employing a 2D non-linear G-equation solver combined with a representation of the flame by Gaussian sources, the steady state solution was computed by Zimmermann [195]. Since this requires the availability of another solver as

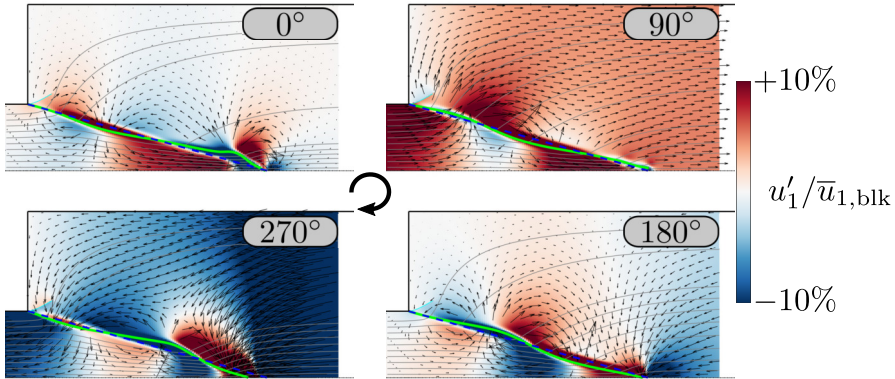


Figure 5.15: LOM predictions including irrotational flame-flow feedback of a harmonically forced flame configuration (at 120 Hz and an amplitude of 10% \bar{u}_{blk}) for a confinement ratio of $C_r = 0.4$. Shown are four consecutive snapshots taken at phases from 0° to 270° with respect of the forcing signal. Each shows the current axial velocity perturbations u'_1 (color), the mean flame front position (---), the perturbed flame (—) and, attached to the trailing edge, the Kutta panel.

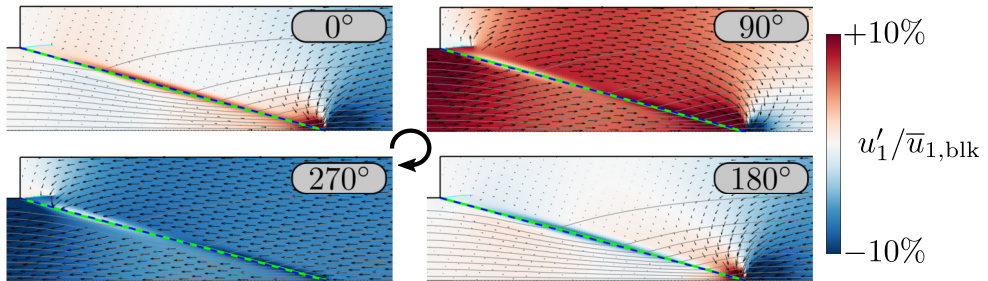


Figure 5.16: Results of a simulation as described in Fig. 5.15, but for a confinement ratio of $C_r = 0.66$.

well as its seamless compatibility with the present framework, another approach is pursued here: The flame normal flow velocity resulting from the distributed sources is evaluated at all flame points based on the initially specified steady state flame front position before the simulation starts. The resulting values are then subtracted from the respective values at all later times. This ensures that the initially specified flame position becomes a steady state of the posed problem and it is possible to apply the method introduced above without any further adjustments. The employed steady state of the $C_r = 0.4$ configuration is illustrated in Fig. 5.7.

Figs. 5.15 and 5.16 show results for a harmonically forced flame. These configurations exactly corresponds to the setups shown in Figs. 5.10 and 5.11, but this time Gaussian sources are used to represent the generation of volume across a flame. As

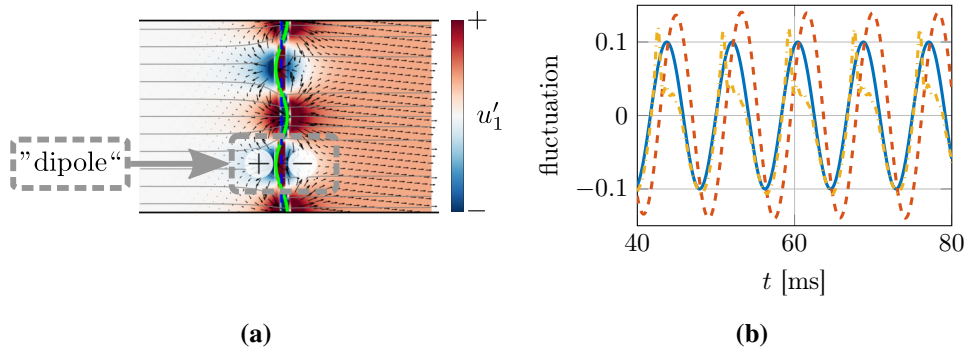


Figure 5.17: (a): Illustration of the dipole-like flow structure in the vicinity of a perturbed duct flame, which results from an acceleration of flame-normal velocity across a flame sheet (geometrical focusing). (b): Fluctuation of the global heat release rate for a harmonic velocity forcing at 120 Hz at an amplitude of $10\% \bar{u}_{1,\text{blk}}$ (—) for $C_r = 0.4$, resulting from simulations respecting flame-generated vorticity (- - -), see Fig. 5.10, and irrotational gas expansion (· · ·), see Fig. 5.15.

in the vortical case, the displacement amplitude convectively increases towards the flame tip. Due to the now significantly larger wave lengths of the imposed flame sheet perturbations, this fact is harder to recognize. The $C_r = 0.66$ case shows hardly any spatial variations of the local displacement phase and only a rather small convective growth in perturbation amplitude. When interpreting the u'_1 field, it should be considered that the deep red and deep blue parts right at the flame front are caused by the fact that the flame sheet moves: if the flame propagates into the fresh mixture, the velocity at points placed inside the originally unburned flow will be strongly increased compared to the steady state and, vice versa, if the flame is pushed into burned parts. Hence, consequences of the sources for the flow field become only apparent further away from the flame sheet.

Respecting this fact, it is interesting to note that also the irrotational part of the flame-flow feedback imposes distinct convected velocity perturbations upstream of the flame, at least for $C_r = 0.4$. Dipole-like irrotational perturbations are imposed onto the surrounding flow field, which is shown for the case of a perturbed duct flame in Fig. 5.17a²: regions where the displacement shows local maxima (concave parts) behave as sources on the burned and as sinks on the unburned side of the flame sheet. For regions at local minima (convex parts), it is the other way round. In consequence, the overall perturbation flow field might appear vortical, while it is irrotational in reality. This complicates a visual analysis of the flow field in the vicinity of perturbed flames. Based on these findings, it has to be concluded that the description of Blan-

²The computation of this figure employs exactly the same framework as the ones of Figs. 5.15 and 5.16, however, a different Schwarz-Christoffel mapping was applied in order to cope with the depicted duct geometry, see Zimmermann [195] for details.

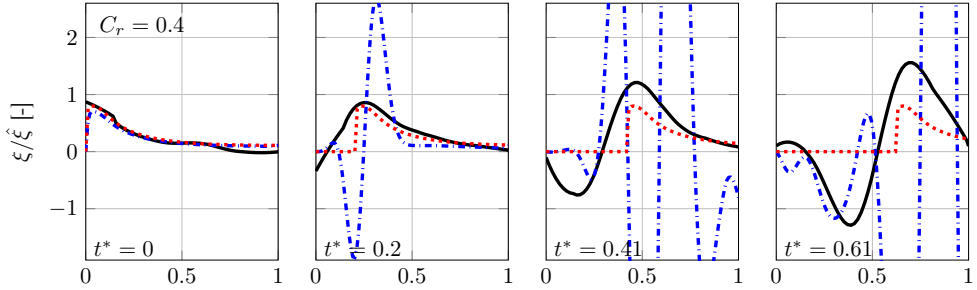


Figure 5.18: Four snapshots taken at equidistant instances in time of the normalized flame displacement resulting from an impulsive velocity forcing at $t^* = 0$ taken from CFD/SI results (—), the acoustic LOM excluding flame-flow feedback (· · · · ·) and the acoustic LOM including irrotational gas expansion (- · - · -) at a confinement ratio of $C_r = 0.4$.

chard *et al.* [129] is incomplete: a perturbed flame sheet is more than just a vortex sheet of varying strength.

One important difference between the setup respecting flame-generated vorticity and the setup respecting irrotational gas expansion is that at $C_r = 0.4$ the latter exhibits a clearly non-linear output behavior of the global heat release, even for small amplitudes of the input velocity. The time series data of the global heat release rate associated with the simulations shown in Fig. 5.10 and 5.15 are depicted in Fig. 5.17b. While the vortical output data (- · - · -) is sinusoidal, the irrotational output (- · - · -) shows a drop of the global heat release signal every time a maximum is reached. Such a behavior is non-linear in nature and can be associated with the dynamics of the flame tip. Once a positive flame front perturbation reaches the flame tip, this will eventually lead to a pinch-off of a bubble of unburned fluid. When this bubble is burned, a rapid change in the global heat release rate is provoked. This process is not faithfully captured by the model at hand, nevertheless, qualitatively something similar happens: A positive flame displacement is usually followed by a negative one. In flame coordinates, this might lead to the occurrence of negative displacements exceeding the symmetry line at $x_2 = 0$. This, of course, is not possible and the numerical algorithm disregards portions of the flame sheet that are outside the flow domain, i. e. $x_2 < 0$. That means, the heat release drops overproportionally fast, which manifests itself as the observed rapid drop of the global heat release rate. Regarding the simulations that respect only flame generated vorticity, vortices are distributed along the *mean flame position* and not the displaced one, and hence also displacements with $x_2 < 0$ where allowed. This results in the good-natured output of this model. At $C_r = 0.66$ all forced simulations exhibited an essentially harmonic output signal at the forcing frequency (not shown), which shows that the presence of a confinement significantly dampens the impact of flame-flow feedback, particularly its irrotational component.

The observed convective growth of displacement amplitudes resulting from an im-

pulsive velocity forcing is significantly stronger for the irrotational gas expansion model than for the model that respects only flame-generated vorticity. The resulting flame displacements of the former model are depicted in Fig. 5.18. Already at the second snapshot ($t^* = 0.2$) very high displacement amplitudes have formed. They subsequently grow even further in amplitude and, additionally, a variety of secondary displacements develop. This emphasizes the point made in the introduction of this chapter: capturing mainly mechanisms that are responsible for a growth of flame front perturbations will most probably result in an overprediction of displacement amplitudes. This could possibly be fixed by including damping mechanisms. In the study shown here, consequences of flame curvature were respected, however, the results clearly suggest that this is not sufficient. An appropriate consideration of damping mechanisms is out of the scope of this work and should be analyzed in future studies.

Finally, it should be pointed out that a joint analysis of both flame-flow feedback mechanisms, i.e. the irrotational and the vortical one, results in even higher displacement amplitudes than the ones shown here (not shown). Therefore, such a combined study is only instructive once damping mechanisms are adequately included into the modeling framework. This situation is very similar to what happened to the works of Darrieus [26] and Landau [27]: since their model included only driving mechanisms leading to the unconditional growth of flame front perturbations, it was later complemented by Markstein [44] introducing the empirical assumption of a curvature-dependent flame speed. Concerning the present modeling approach, similarly, it turned out that there is a significant lack of damping mechanism in order to achieve quantitative agreement with CFD/SI data. Therefore, in addition to the curvature dependency of the flame speed, other mechanisms need to be assessed.

5.4 Summary and Conclusions

In this chapter, consequences of flame-flow feedback for the acoustic flame response were modeled and analyzed. A vortical and an irrotational mechanism resulting from gas expansion were found to be the driving forces that govern secondary acoustics-flame interactions. While the former is known as the Darrieus-Landau mechanism relying on flame-generated vorticity, the latter results from a geometrical focusing of accelerating effects of a perturbed flame sheet and has, so far, not been analyzed in the context of acoustics-flame interactions. Based on these two mechanisms, perturbed flames act as vortex sheets of varying strength (flame-generated vorticity) as well as sheets of advected dipoles (irrotational gas expansion), which explains the occurrence of convected velocity perturbations upstream of the flame. Furthermore, both mechanisms lead to the formation of secondary convectively growing displacements causing FTF peak gain values that significantly exceed unity — just like it was predicted by the CFD/SI results. The presence of a narrow confinement significantly impacts the consequence of flame-flow feedback, leading to flame front displacements of longer wave lengths and lower amplitudes. Accordingly, the maximum FTF

peak gain values are reduced.

Qualitatively, mechanisms that could explain the discrepancies observed in Chap. 4 were found and promising modeling strategies were proposed. Contrary to the MS equation, as used by Searby *et al.* [63], the modeling framework proposed here allows to capture confinement induced consequence for the flame response. Relying on this new modeling approach, it was found that the previously neglected irrotational consequences of gas expansion led to an unphysically fast growth of flame front displacements, such that the response dynamics left the linear regime. It is conjectured that this growth is in reality limited by some damping mechanisms, which were not included in the present study. Their investigation should be subject of future research, which then might also allows for quantitative assessments of the flame dynamics. Furthermore, relying on the works of Oberleithner *et al.* [79] and Oberleithner and Paschereit [80], it would be interesting to analyze the role of flame-flow feedback driven instability mechanisms for technically relevant configurations, in analogy to shear layer instabilities.

The main findings of the present analysis are:

1. Compact acoustics imposes irrotational flow perturbations, which predominantly displace the flame base region.
2. These primary flame front displacements are advected downstream by the mean flow and are exposed to mechanisms of flame-flow feedback along their way to the flame tip.
3. This feedback leads to the convective growth of displacement amplitudes and, additionally, creates new secondary flame front perturbations.
4. These secondary perturbations lead to an oscillatory behavior of the impulse response (IR) of the global heat release rate. This, in turn, creates a pronounced peak in the gain of the associated frequency response at a frequency close to the oscillation frequency of the IR.
5. For the flame configuration at hand, two mechanisms of flame-flow feedback were identified: (i) the Darrieus-Landau mechanism relying on flame generated vorticity and (ii) geometrical focusing resulting from a flame-normal acceleration of the flow across a perturbed flame sheet.
6. Both mechanisms lead to the convective growth of flame front perturbations and impose convected velocity perturbations upstream of the flame front.

Part III

Generalization to Other Burner Configurations

The analysis conducted so far analyzed Slit flame setups. Most experimental and theoretical studies, however, report on Bunsen flames. In order to provide a connection of both configurations, the impact of flame geometry onto the acoustic flame response shall be investigated in the following. For the sake of completeness, also Wedge flames are considered. The results should provide guidance how to generalize the findings made for Slit flame configurations as well as how to interpret data obtained using arbitrary flame configurations.

Major parts of Chap. 6 have already been published, see Steinbacher *et al.* [2]. Compared to this publication, Sec. 6.3 is newly added and some minor changes have been applied (wording, grammar).

6 Consequences of Flame Geometry

Flame geometry (Slit, Wedge or Bunsen) determines how flame front displacements translate to global heat release rate fluctuations, which defines geometry-specific response characteristics. Low-order models relying on a Gaussian kernel function are able to adequately capture the FTFs of all three geometries.

Various types of laminar flame configurations are used in academia and technical applications, which often exhibit very different response characteristics [146, 153, 201]. Three of the most prominent geometries are depicted in Fig. 2.1: Bunsen, Wedge (or V-) and Slit flames. Most theoretical studies on analytical FTF models are concerned with Bunsen and Wedge flames [31, 113, 138, 202], while only very few deal with Slit flames [112, 142, 203]. One reason for this might be that the latter are technically less relevant. Particularly for academic studies, however, Slit flames are very interesting due to the simpler analytical treatment of the governing equations [112, 132, 148], see also the works presented in Part II of this thesis.

To date, no study has strictly and comprehensively analyzed the differences in the linear flame response that result from flame geometry. Schuller *et al.* [111] and Blumenthal *et al.* [116] compared analytical response predictions of Wedge and Bunsen flames, but did not include Slit flames. Schuller *et al.* [111] provided validation data from experiments solely for the Bunsen configuration. Durox *et al.* [152] compared experimental response results of Bunsen, Wedge and M-flames, where the last one is a hybrid of the first two types of flames. They focused on the nonlinear behavior of the frequency response for increasing forcing amplitude levels and did not compare measurements to analytical predictions. Other studies assessing the consequences of flame geometry examined the production of combustion noise of turbulent Slit and Bunsen flames. Kotake and Takamoto [151] experimentally investigated the impact of the nozzle shape (or burner mouth shape) on the acoustic power of the associated combustion noise for constant cross-sectional areas. They found that for lean conditions, rectangular nozzles (“slits”) produce significantly higher levels of acoustic power than square and circular (Bunsen) shapes. A similar conclusion was drawn from numerical results by Pausch *et al.* [153], who additionally found that Slit burners exhibit a lower peak frequency than Bunsen type ones. Further, they located the position of maximum heat-release of the rectangular flame at its tip, while it is a bit further upstream for the Bunsen flame. Neither study analyzed the corresponding FTFs. Due to this lack of comprehensive studies on consequences of flame geometry

for the respective FTFs, a literature review for each of the three investigated configurations is provided in the following.

For Bunsen type flames, results for both experimentally determined and theoretically modeled FTFs are readily available, see e. g. [111, 115, 133, 144, 145, 158, 204–206]. Low-order models based on the so-called convective or incompressible-convective velocity model agree reasonably well with experimental data, see Sec. 2.2.1 (Low-Order Models) for details.

To the best knowledge of the author, there is a lack of literature regarding FTF analysis and models for laminar Slit flames that are validated against experimental or high fidelity numerical data. On the one hand, several theoretical studies develop and investigate analytical models for the FTF of Slit flames [112, 138, 142, 207], however, none of them compares results to experimental/high fidelity numerical data. On the other hand, experimental and/or numerical investigations reporting on measured FTFs of Slit flames [147–149, 208–210] do not compare their measurements to analytical predictions. Only Duchaine *et al.* [146] presented an empirical model for the phase of Slit and Bunsen FTFs and compared it to experimental data, finding that the effective time lag of a Bunsen flame is about half the value of a Slit configuration. Further, Kornilov *et al.* [209] visually compare measured gain and phase values of a Bunsen and Slit setup, which shows a significantly higher gain — even exceeding unity — of the Slit flame. But again no model was developed and validated against this data.

Finally, there is a group of studies that compared analytically predicted instantaneous flame front positions of harmonically perturbed Slit flames to experimental or high fidelity numerical data, however, they did not evaluate transfer functions of the global heat-release rate [104, 164, 165, 211, 212]. All of them rely on a G-equation based approach where the speed of a convective velocity perturbation was fitted in order to achieve good agreement of the resulting perturbed flame front with the comparison data. From the good match in terms of flame front position, a very similar behavior of the corresponding global heat-release dynamics at the considered forcing frequency can be inferred. However, since the responses were only computed at a few forcing frequencies, it is not possible to deduce an FTF from those studies.

There are several experimental studies reporting measured FTFs of Wedge flames, e. g., [152, 201, 213], but they are all lacking a comparison to theoretical predictions. The studies performed by Schuller *et al.* [111] and Blumenthal *et al.* [116] develop analytical FTF models for Bunsen and Wedge flames, but compare only the response of the Bunsen type setup to experimental data. Finally, Schuller [214] developed a modeling approach, which was validated against experimental data. At the same time, however, he mentions the difficulties in deriving an analytical model for such burner stabilized Wedge flames, which essentially arises from a strong interaction of the flame with vortical structures shed from the burner mouth [202]. Other Wedge type flames found in the literature are swirl stabilized flames, which depend on variations

of the turbulent burning velocity, axially convected velocity disturbances, as well as on convected swirl waves [79, 215–217]. Modeling of the FTF requires an adequate description of all those effects. This complicates the analysis and shifts the focus away from geometrical consequences.

The study presented in the following aims to generate a more profound understanding of the consequences of flame geometry by comparing analytical FTF predictions of Slit, Wedge and Bunsen type flames to each other and analyzing the origin of the discrepancies found. For the first time, Slit and Wedge flame FTF predictions resulting from high fidelity computational fluid dynamics (CFD) simulations are compared to analytical model predictions. The unique feature of the Wedge flame setup considered in our study is that it is not dominated by vortex-flame interaction, as it is the case for a burner stabilized flame [202], since no burner mouth is involved. Therefore, a clean validation basis for analytical models is provided for all three geometries. It is found that the widespread G-equation framework, combined with a convective velocity model, is not able to adequately predict the flame response of Slit flames. In order to overcome this limitation, an extension of the well-known velocity models is introduced, which relies on a Gaussian kernel function in order to add some temporal dispersion to the transfer function model.

The analysis is structured as follows: In Sec. 6.1 the three test case setups are introduced, which are used to validate the theoretical models. For each flame configuration steady-state and transient numerical simulations are performed and the respective flame transfer function are identified from broad-band input/output data using means of system identification (SI). The overall heat-release rate, evaluated as the integral over the flame surface, plays a crucial role in the analysis of flame geometry-related response differences. Peculiarities of the various flame configurations on the one hand, and of the coordinate system on the other hand are detailed in Sec. 6.2. The here gained mathematical expressions are elucidated by descriptive physical reasoning based on a model that solely relies on displacements of the flame anchoring in Sec. 6.3. In Sec. 6.4, incompressible-convective velocity models with Dirac and Gaussian kernel functions are introduced, respectively for all flame configurations considered. Properties of the Dirac kernel based models are discussed in Sec. 6.5 and, in particular, the flame geometry-related differences in the flame response are explicated. Finally, in Sec. 6.6 FTF predictions of the various velocity models are validated against CFD data, as well as against experimental data taken from the literature.

6.1 Test Case Setups

Transient and steady state numerical simulations employing well-established means of computational fluid dynamics of three flame configurations are performed and serve as a validation basis, see Appendix A.2.1 for details. Using input-output time

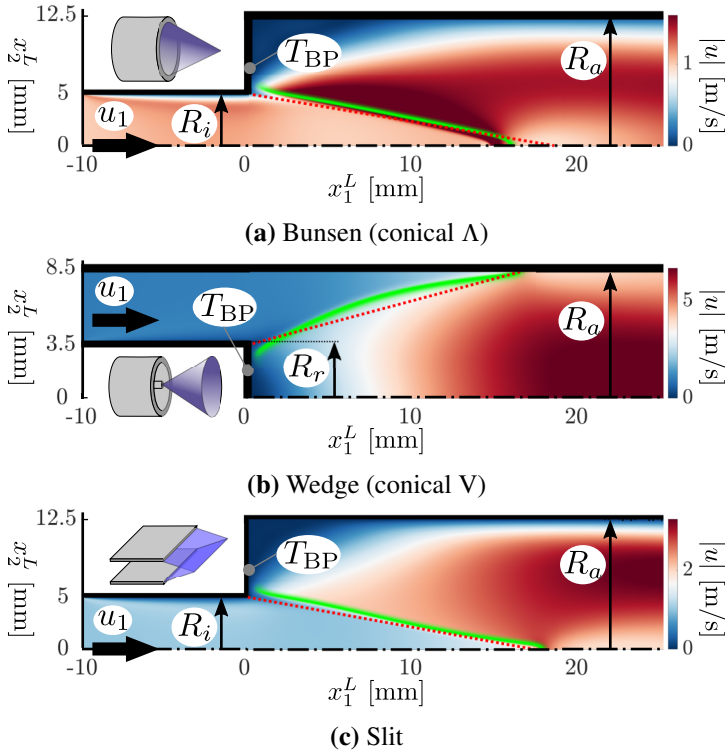


Figure 6.1: CFD steady state snapshots of absolute velocity for the three investigated flame test cases of different flame geometries. For all configurations, the location of maximum heat release (green) and the analytically predicted mean flame front (.....) are shown (taken from [2]).

series data resulting from broad-band forced simulations, FTFs are identified by means of system identification (SI) employing a finite impulse response (FIR) model as described in Appendix A.2.2.

Three setups are considered and the respective steady state solutions are depicted in Fig. 6.1. All setups are chosen to be as simple as possible in order to serve as a clean reference that exhibits any geometry-related characteristics in a clear manner. Further, the mechanisms governing the flame response to acoustic perturbations should be similar for all cases, i. e. similar Reynolds numbers and negligible interaction with vortical structures shed from the burner mouth for the Wedge configuration [1, 104, 201]. This shedding process is suppressed by adding a straight lateral wall constraining the flame, see Fig. 6.1b. Note that all configurations exhibit a small recirculation zone since the flow cannot follow the sharp edge at the inlet to the combustion chamber. Following Chap. 4, however, acoustically triggered shedding of vorticity from this edge has only a negligible impact on the linear flame response.

For the Slit and Bunsen setups, a feed duct and combustion chamber with a half-diameter of $R_i = 5$ mm and $R_a = 12.5$ mm are used, respectively (Fig. 6.1). The

Wedge flame setup has the same feed duct height of 5 mm as the other two cases and a rod radius of $R_r = 3.5$ mm, which results in a combustion chamber radius of $R_a = 8.5$ mm. At the inlet, a uniform flow profile of axial velocity $u_1 = 1$ m/s with a temperature of 300 K is imposed for all setups. Further, zero pressure gradients at the inlet and a fixed pressure are assumed, as well as a zero axial velocity gradient at the outlet. No swirl of the flow is imposed. All walls are set to be adiabatic, except from the feed duct wall, which is set to a fixed temperature of 300 K, and the combustion chamber back plate, which is set to $T_{BP} = 700$ K. This configuration correspond to a Reynolds number of $Re = 620$, which is computed with the mean inlet velocity, the feed duct diameter and the kinematic viscosity of the fresh mixture.

6.2 Integral Heat-Release

For all three geometrical configurations considered, the integral heat-release rate is proportional to the respective flame surface area $A_f(t) = \int_A dS$. Hence, evaluation of surface area fluctuations $A'_f(t) = A_f(t) - \bar{A}_f$ of a perturbed flame up to contributions of order $\mathcal{O}(\epsilon)$ allows to retain the flame geometry specific heat-release dynamics. This leads to qualitatively very different results for the three flame geometries, as shown in the following.

One assumption made in this analysis is that the flame is stiffly anchored at its base, i. e. this point is not allowed to move. This assumption is justified by the fact that the impulse response for Slit flames shows no signal around $t = 0$, see Sec. 6.6. If the flame base would move, a displacement would directly lead to a fluctuation of the heat-release rate¹. A second assumption is that all flames considered are symmetric, i. e. it is sufficient to analyze only one half of the flame front, see Fig. 1.13. A point on the flame front at the symmetry axis consequently fluctuates in axial direction, which is best captured using laboratory coordinates and the flame front displacement η' . These two assumptions are important, since they define the possible directions of movement of the flame boundaries (tip and anchoring), which is crucial for the evaluation of the linearized surface area, as will be shown below.

For the computation of the FTF a variety of coordinate systems have already been adopted in the literature, see e. g. [111, 112, 115]. However, to date no study has comprehensively scrutinized the derivations of the flame surface area with respect to the coordinate systems used, nor have the geometry dependent peculiarities ever been pointed out explicitly. Indeed, a technical note by Humphrey *et al.* [218] provides evidence that this issue deserves more attention: They reported that the expression for

¹Purely flame normal displacements of the flame-anchoring would also not cause any $\mathcal{O}(\epsilon)$ fluctuations of the flame surface area, see discussion on Fig. 6.3 below. Hence, strictly speaking, it is not possible to infer from a zero response at $t = 0$ of the Slit IR that the flame base is actually stiffly anchored — it could also be displaced normally. In the 1D linearized G-equation framework, however, the implications for the modeling are the same in both cases and, hence, it is decided to proclaim the more straight forward assumption of a stiffly anchored flame.

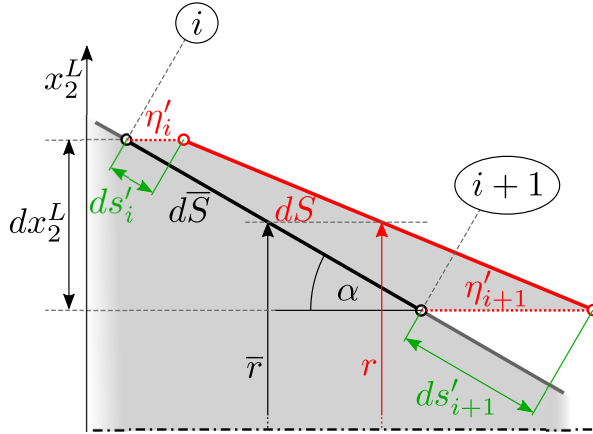


Figure 6.2: Illustration of the dependency of the change of the flame line segment length $dS' = dS - \bar{dS}$ on the displacements $d\eta'_i$ and $d\eta'_{i+1}$ up to $\mathcal{O}(\epsilon)$ contributions. For conical flames, also the radii r and \bar{r} of the geometrical centers of the line segments are important. The region of the unburned fluid is filled in gray.

the linearized flame surface area of a Slit flame seems to depend on the coordinate system used. To resolve this counterintuitive finding, Humphrey *et al.* [218] proposed to use frequency dependent integration limits, which result in coordinate system specific correction terms. In this section, this issue is revisited and it is sought to provide a more intuitive understanding by not limiting our analysis to the frequency domain. Further, a more global context is provided by considering three technically relevant flame geometries.

The geometrical analysis starts by focusing on a single 1D line segment dS of a flame front, see Fig. 6.2. The notation used in the following is illustrated in Fig. 1.13, where η' denotes the axial displacement of the flame front using laboratory coordinates. It is displaced by η'_i at node i and η'_{i+1} at node $i+1$ with reference to the corresponding steady-state line segment \bar{dS} . Hence, we write the length of the displaced segment, using the Pythagorean theorem, up to the leading order in the axial displacement as

$$\begin{aligned} dS &= \sqrt{(dx_2^L)^2 + (\bar{\eta}_{i+1} + \eta'_{i+1} - \bar{\eta}_i - \eta'_i)^2} \\ &= \underbrace{\sqrt{1 + \left(\frac{d\bar{\eta}}{dx_2^L}\right)^2} dx_2^L}_{\bar{dS}} + \underbrace{\frac{\frac{d\bar{\eta}}{dx_2^L} d\eta'}{\sqrt{1 + \left(\frac{d\bar{\eta}}{dx_2^L}\right)^2}}}_{dS'} + \mathcal{O}((d\eta')^2) \end{aligned} \quad (6.1)$$

with the difference of the steady-state axial distances $d\bar{\eta} = \bar{\eta}_{i+1} - \bar{\eta}_i$ and the transient distances $d\eta' = \eta'_{i+1} - \eta'_i$, as well as the lateral distance dx_2^L . The second line results from a Taylor series development of the term in the first line around $d\eta' = 0$. The first term in Eq. (6.1) denotes the length of the steady-state line segment and the second

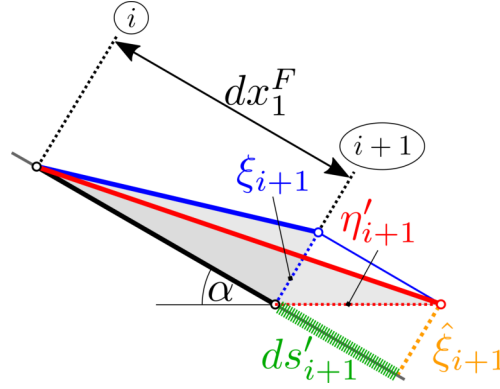


Figure 6.3: Displaced flame segment in flame aligned (blue) and laboratory (red) coordinates.

its change due to $\eta'_{i/i+1}$. By applying the trigonometric relation $\cot(\alpha) = d\bar{\eta}/dx_2^L$, the linearized variation of the line segment length is transformed to

$$dS' = ds'_i + ds'_{i+1} = \cos(\alpha) (\eta'_{i+1} - \eta'_i). \quad (6.2)$$

From this expression it can directly be deduced that up to the first order in $d\eta'$ the change of the line segment depends on the flame parallel (x_1^F -) component of the displacements $ds'_{i/i+1}$, see Fig. 6.2. The elongation ds'_{i+1} counts positive, while ds'_i contributes with a negative sign.

As pointed out in Sec. 1.3.2, for small displacements, the perturbed flame front can equivalently be described in flame aligned and laboratory coordinates. In order to analyze the consequences of a change of the coordinate system for the computation of the linearized surface area fluctuations, again a single displaced flame segment shall be analyzed (Fig. 6.3, red). Node i may be fixed and node $i+1$ be axially displaced by η'_{i+1} . Following Eq. (6.2), this would result in a linearized change of the segment length of $dS' = \cos(\alpha)\eta'_{i+1}$. Transforming this situation to flame aligned coordinates by application of a relation $\xi_{i+1} = \eta'_{i+1} \sin(\alpha)$ results in the segment shown in blue. However, the linearized change of the resulting segment length

$$\begin{aligned} dS^F &= \sqrt{(dx_1^F)^2 + d\xi^2} \\ &= \underbrace{dx_1^F}_{dS^F} + \underbrace{\mathcal{O}(d\xi^2)}_{dS^F} \end{aligned} \quad (6.3)$$

vanishes to leading order since the displacement ξ_{i+1} has no component parallel to the mean flame front. Hence, paradoxically, a displacement η'_{i+1} only imposes a change of the linearized line segment length in laboratory coordinates, and not in flame aligned coordinates.

This can be resolved by realizing that the aforementioned transformation from η' to ξ is incomplete: In order to equivalently describe the axially displaced flame front

(Fig. 6.3, red) using flame aligned coordinates, the displacement $\hat{\xi}_{i+1} = \eta'_i \sin(\alpha)$ should not be applied at node $i + 1$, but at a position shifted by a distance ds'_{i+1} further to the right (Fig. 6.3, orange). Vice versa, in order to describe a normally displaced flame front (Fig. 6.3, blue) using laboratory coordinates, the respective node $i + 1$ for η'_{i+1} would have to be shifted to the left by ds'_{i+1} . In doing so, the first order change of the segment length stays the same in both coordinate systems.

Therefore, it is concluded that — other than for the flame dynamics described by Eq. (1.32) — a transformation of the coordinate system has non-trivial implications regarding the evaluation of the linearized change of the flame length and, thus, also the respective flame surface area. Depending on the given behavior of the flame, possible elongations or shortenings of the flame length not covered by the chosen coordinate system have to be accounted for correctly. Adding contributions of flame movement not parallel to one of the employed coordinates is equivalent to imposing varying integration limits when evaluating the flame surface integral. Other than proposed by Humphrey *et al.* [218], terms resulting from such varying limits should not be regarded as correction terms since they are a mathematical necessity for solving a well defined problem. This will be explicated in the following for the individual flame geometries.

Slit Flames

The flame surface area of Slit flames (index “slit”) is given by an integral

$$A_{f,\text{slit}}(t) = \Delta x_3 \int_0^{l_f(t)} ds, \quad (6.4)$$

where $l_f(t)$ is the length of the displaced flame surface profile line and Δx_3 the extension of the flame in x_3^L direction. Using laboratory coordinates, the arc length ds (Fig. 6.4) is expressed as $ds = \sqrt{1 + (d\eta/dx_2^L)^2} dx_2^L$, see Eq. (6.1). Linearization results in a surface area fluctuation

$$\begin{aligned} A'_{f,\text{slit}}(t) &= -\cos(\alpha) \Delta x_3 \int_0^{R_i} \frac{\partial \eta'}{\partial x_2^L} dx_2^L \\ &= \Delta x_3 \cos(\alpha) \eta'(0, t), \end{aligned} \quad (6.5)$$

where the anchoring boundary condition $\eta'|_{x_2^L=R_i} = 0$ has been applied and R_i is the base half-diameter of the flame. This leads to the result that surface area fluctuations of stiffly anchored Slit flames, to leading order, *only* result from movements of the flame tip.

As stated above, in flame aligned coordinates a varying upper integration limit has to be considered for evaluation of the flame surface integral. Inserting the corresponding

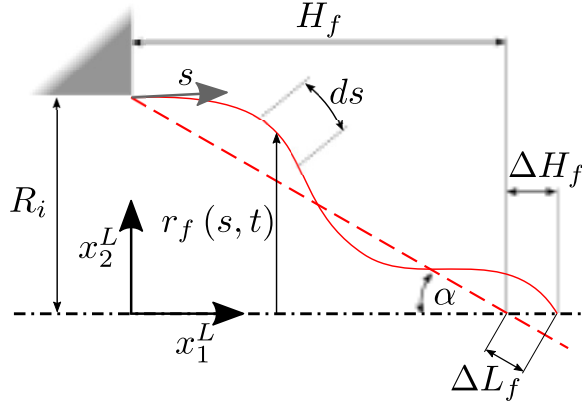


Figure 6.4: Geometric measures required for the computation of the flame surface area of Bunsen flames.

arc length, see Eq (6.3), and integration limits, the respective surface integral becomes

$$\begin{aligned}
 A_{f,\text{slit}}(t) &= \Delta x_3 \int_0^{L_f + \Delta L_f(t)} \underbrace{\sqrt{1 + \left(\frac{\partial \xi}{\partial x_1^F}\right)^2}}_{=1 + \mathcal{O}(\epsilon^2)} dx_1^F \\
 &= \Delta x_3 \left[\int_0^{L_f} dx_1^F + \int_{L_f}^{L_f + \Delta L_f(t)} dx_1^F + \mathcal{O}(\epsilon^2) \right], \quad (6.6)
 \end{aligned}$$

with the elongation/shortening of the flame length $\Delta L_f(t)$ (Fig. 6.4). The first term in Eq.(6.6) denotes the mean flame surface area, the second one the contribution due to the elongation of the flame. As illustrated in Fig. 6.3, the flame tip contribution is of the same order as ξ and has, thus, to be considered for the linear analysis.

The variation of the flame length $\Delta L_f(t)$ has to be determined from the flame normal displacement ξ in order to close the flame aligned modeling approach. From Fig. 6.3 we recall the relation between ξ and η' at the flame tip: $\xi(L_f, t) = \eta'(0, t) \sin(\alpha)$. Using this relation, we compute the variation of the flame length, which corresponds to an elongation $ds'_{i+1} = \cos(\alpha)\eta'_{i+1}$ in Fig. 6.3. Hence, we get $\Delta L_f(t) = \xi(L_f, t) \cos(\alpha) / \sin(\alpha)$, which, with use of Eq. (6.6), results in an expression for the surface area fluctuation

$$A'_{f,\text{slit}}(t) = \frac{\Delta x_3}{\tan(\alpha)} \xi(L_f, t) \quad (6.7)$$

that is equivalent to Eq. (6.5). The only coordinate system that does not require a varying upper integration limit is the laboratory one, which is therefore considered to be the most natural one for the flame surface area integral for the configuration considered (symmetric, stiffly anchored Slit flame).

Bunsen Flames

For conical flames in general (index “con”) we have to consider the radius r of the geometrical center of a line segment. Using the steady-state flame segment radius \bar{r} , we retrieve $A'_{\text{con}} = 2\pi\bar{r} dS'$ for the change in flame surface area of one single flame element, see Fig. 6.2. The flame surface integral is written as

$$A_{f,\text{con}}(t) = 2\pi \int_0^{l_f(t)} r_f(s, t) ds \quad (6.8)$$

where s is the parametrization of the flame front profile, $l_f(t)$ its transient length and $r_f(s, t)$ its local radius, see Fig. 6.4. For Bunsen flames (index “ Λ ”), using flame aligned coordinates, with a decomposition into mean and fluctuating quantities, this results in an expression

$$A_{f,\Lambda}(t) = 2\pi \int_0^{L_f + \Delta L_f(t)} [R_i - x_1^F \sin(\alpha) + \xi \cos(\alpha)] dx_1^F. \quad (6.9)$$

Here, L_f is the mean flame length, $\Delta L_f(t)$ its transient variation in flame coordinates and R_i the flame base radius. As in the Slit flame case, the upper integration limit is time dependent: Wrinkles reaching the flame tip impose a change in flame height H_f and, hence, also in the upper integration limit, which is required to capture this effect, see Fig. 6.4. For Bunsen flames, this additional transient contribution to the flame surface area, however, does not contribute to the linear approximation of the flame surface area fluctuation. An increase of the flame height by $\Delta H_f(t) = \Delta L_f(t) / \cos(\alpha)$ would add the surface of a cone with both base radius and height of order $\mathcal{O}(\epsilon)$. Therefore, the lateral surface area of this cone is of the order $\mathcal{O}(\epsilon^2)$ and is thus neglected in linear considerations for anchored flames:

$$A'_{f,\Lambda}(t) = 2\pi \cos(\alpha) \int_0^{L_f} \xi dx_1^F. \quad (6.10)$$

Hence, the global linearized flame surface fluctuation is computed from the integral of the displacements.

Wedge Flames

Wedge flames (index “V”) are conical flames, as well. Hence, the surface integral of Eq.(6.8) also holds for them and, using a flame aligned coordinate system and a corresponding parametrization of the local flame radius $r_f(s, t)$, we retrieve the linearized flame surface area

$$\begin{aligned} A_{f,V}(t) &= 2\pi \int_0^{L_f + \Delta L_f(t)} [R_r + x_1^F \sin(\alpha) - \xi \cos(\alpha)] dx_1^F \\ &= \bar{A}_{f,V} + 2\pi \left[R_a \Delta L_f(t) - \cos(\alpha) \int_0^{L_f} \xi dx_1^F \right], \end{aligned} \quad (6.11)$$

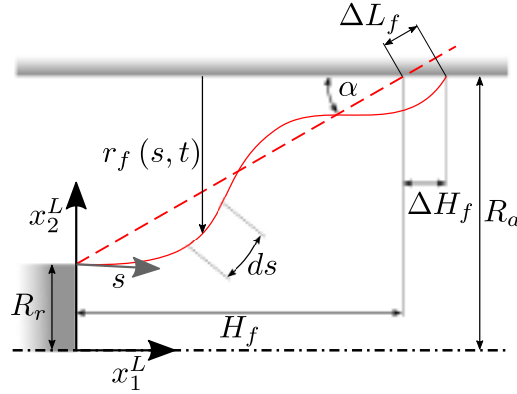


Figure 6.5: Geometric measures required for the computation of the flame surface area of Wedge flames.

which results with $\Delta L_f(t) = \xi(L_f, t) / \tan(\alpha)$ in a surface area fluctuation

$$A'_{f,V}(t) = 2\pi \cos(\alpha) \left[\frac{R_a}{\sin(\alpha)} \xi(L_f, t) - \int_0^{L_f} \xi dx_1^F \right]. \quad (6.12)$$

Similar to the Slit case, fluctuations in the flame height add or subtract the surface of a cone with a base radius of the order of the maximum flame radius R_a and a height of the order $\mathcal{O}(\epsilon)$, see Fig. 6.5. In total, the flame tip movement $\Delta H_f(t)$ would add a $\mathcal{O}(\epsilon R_a)$ contribution to the flame surface area fluctuations, which is significant. As a result, the linearized surface fluctuations of stiffly anchored Wedge flames is expressed as the (negative) integral of the deflection from the mean, plus the flame tip movement.

Coordinate System	with $\bar{u}_\parallel = \bar{u}_1 \cos(\alpha)$ $u'_\perp = u'_1 \sin(\alpha) + u'_2 \cos(\alpha)$
Flame	<p>Velocity of convective disturbance:</p> $u_c = \frac{K\bar{u}_1}{\cos(\alpha)}$ <ul style="list-style-type: none"> Surface Integral Slit $\frac{A'_{f,\Lambda}(t)}{\bar{A}_{f,\text{slit}}} = \frac{1}{L_f \tan(\alpha)} \xi(L_f, t)$ <p>Flame Front Dynamics, Eq. (1.32) ($I_M = 0$)</p> $\xi(x_1^F, t) = \frac{1}{\bar{u}_\parallel} \int_0^{x_1^F} u'_\perp \left(\bar{x}_1^F, t - \frac{x_1^F - \bar{x}_1^F}{\bar{u}_\parallel} \right) d\bar{x}_1^F$ <ul style="list-style-type: none"> Surface Integral Conical $\frac{A'_{f,\Lambda}(t)}{\bar{A}_{f,\Lambda}} = \frac{2 \cos(\alpha)}{R_f L_f} \int_0^{L_f} \xi(x_1^F, t) dx_1^F$ $\frac{A'_{f,V}(t)}{\bar{A}_{f,V}} = \frac{2 \cos(\alpha)}{L_f (R_r + R_a)} \left[\frac{R_a}{\sin(\alpha)} \xi(L_f, t) - \int_0^{L_f} \xi(x_1^F, t) dx_1^F \right]$
Laboratory	<p>Velocity of convective disturbance:</p> $u_{c,\Lambda} = -K\bar{u}_1 \tan(\alpha)$ $u_{c,V} = K\bar{u}_1 \tan(\alpha)$ <ul style="list-style-type: none"> Surface Integral Slit $\frac{A'_{f,\text{slit}}(t)}{\bar{A}_{f,\text{slit}}} = \frac{\cos(\alpha)}{L_f} \eta'(0, t)$ <p>Flame Front Dynamics, Eq. (1.34)</p> $\eta'_\Lambda(x_2^L, t) = -\frac{1}{\sin^2(\alpha)\bar{u}_\parallel} \int_0^{x_2^L} u'_\perp \left(\bar{x}_2^L, t + \frac{x_2^L - \bar{x}_2^L}{\sin(\alpha)\bar{u}_\parallel} \right) d\bar{x}_2^L$ $\eta'_V(x_2^L, t) = \frac{1}{\sin^2(\alpha)\bar{u}_\parallel} \int_0^{x_2^L} u'_\perp \left(\bar{x}_2^L, t + \frac{x_2^L - \bar{x}_2^L}{\sin(\alpha)\bar{u}_\parallel} \right) d\bar{x}_2^L$ <ul style="list-style-type: none"> Surface Integral Conical $\frac{A'_{f,\Lambda}(t)}{\bar{A}_{f,\Lambda}} = \frac{2 \cos(\alpha)}{R_f L_f} \int_0^{R_f} \eta'(x_2^L, t) dx_2^L$ $\frac{A'_{f,V}(t)}{\bar{A}_{f,V}} = \frac{2 \cos(\alpha)}{L_f (R_r + R_a)} \left[R_a \eta'(R_a, t) - \int_{R_r}^{R_a} \eta'(x_2^L, t) dx_2^L \right]$

Table 6.1: Overview of analytic expressions required to compute the linear response of stiffly anchored flames, provided for two coordinate systems.

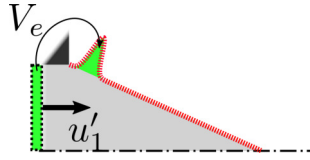


Figure 6.6: Illustration of a thought experiment: A Bunsen-type flame shall be supplied with an extra amount of fresh fluid V_e (green) by means of an impulsive velocity forcing u'_1 , which shall lead to a displacement of the flame base region.

It is concluded that the computation of the linearized flame surface area fluctuation requires a consideration of the possible flame movements at the boundaries for all geometrical configurations. A coordinate system should be chosen that allows a proper description of this movement, otherwise, the elongation/shortening of the flame necessitates varying integration limits. This procedure is in particular important for Slit and Wedge flames, where the flame tip adds a leading order contribution to the linearized fluctuation of the flame surface area. All formulas concerning the flame front and the integral heat-release are summarized in Tab. 6.1 for the three geometries and the two coordinate systems considered. Also expressions for the convection speed, required for the convective velocity models, are provided in this table. They will be explained in detail in Sec. 6.4.

6.3 Physics Based Illustration of the Heat Release Dynamics

So far, formulas for flame surface area fluctuations up to contributions of order $\mathcal{O}(\epsilon)$ have been derived mathematically for three flame geometries. In this section, these formulas shall be elucidated by physical reasoning based on a model that solely relies on displacements of the flame anchoring. Instead of assessing variations in the flame surface area, changes of the volume of unburned fluid upstream of the flame shall be considered [219, 220]. This concept allows for a descriptive and simple way to grasp the mathematical results of the previous section.

Let us set up a thought experiment: a stationary Bunsen-type flame shall be supplied with an extra amount of fresh mixture of the volume V_e by impulsively increasing the inflow velocity for a short amount of time. Since this process shall happen very fast, the flame cannot immediately consume this extra volume of premixture and, thus, it shall solely lead to a very narrow displacement of the flame front at its anchoring position, as illustrated in Fig. 6.6. Effects of non-linear flame propagation (Huygens's Principle; see Fig. 1.6) and flame stretch shall be neglected, which means that this newly created flame pocket is advected downstream without changing its shape, as predicted by Eq. (1.32) for $I_M \equiv 0$. Note, that this does not faithfully represent what

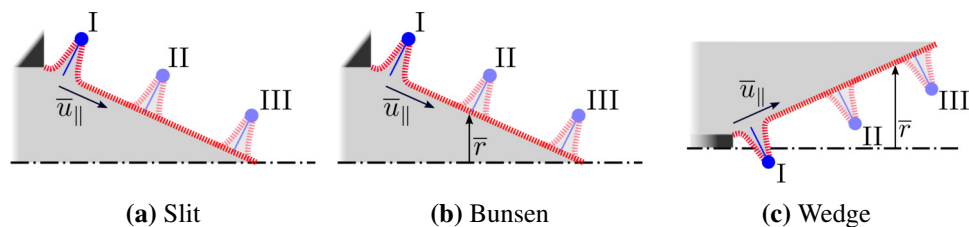


Figure 6.7: Sketch of an advected flame pocket, which is generated by an impulsive deflection of the flame base, shown for three flame configurations (see Fig. 6.6). Assuming a Dirac impulse forcing, the flame is displaced only at one point (indicated in blue), while a Gaussian impulse would impose a smooth flame displacement as visualized here.

would happen in reality, but let us disregard this fact for a moment in order to create a simple model that helps to understand geometry related differences of the flame response.

The flame shapes resulting from such a forcing are plotted for all three flame geometries in Fig. 6.7. For all cases, a small pocket of unburned fluid is formed (position I), which is advected along the flame front with the velocity \bar{u}_{\parallel} such that it reaches positions II and III at subsequent times. The extra fluid, trapped in the pocket, will lead to an increase of the global heat release rate of the flame at the very moment it is burned. Since all of the initially supplied extra volume V_e is conserved, the global heat release rate does not change with respect to the steady state at $t = 0$. We will see in the following that the process of how the pocket is burned depends strongly on flame geometry.

Firstly a Slit type flame, as depicted in Fig. 6.7a, is analyzed. Here, the volume of unburned fluid inside the pocket remains constant during the advection process. The rate at which fuel is burned by the flame is the same as in the steady state case and is not affected by the presence of the described pocket. Hence, the integral heat release rate remains constant for all pocket positions I, II and III. Once the pocket reaches the flame tip, however, the volume of fluid trapped inside the pocket is consumed since it cannot be advected any further. In real flames this might lead to pinch-off effects or an elongation of the flame front. In any case, the pocket is burned and the integral heat release rate of the flame is increased at the moment when the displacement reaches the flame tip. This agrees with the mathematical result of Sec. 6.2, which states that \dot{Q}' is proportional to movements of the flame tip.

The situation is different for Bunsen flames, see Fig. 6.7b. While the pocket is advected, its radial position \bar{r} is reduced and, hence, the trapped volume of fluid is constantly depleted along the way from position I to III. Thus, volume V_e is continuously reduced, which leads to an increase of the heat release rate compared to the steady state. Once the pocket reaches the flame tip (at $\bar{r} \rightarrow 0$), all of the fluid has been consumed and the heat release rate returns to the steady state value. This cor-

responds to the finding made in Sec. 6.2 that \dot{Q}' is proportional to the integral of the instantaneous flame front displacements.

If we, finally, assume a Wedge flame, we have a situation as illustrated in Fig. 6.7c. Position I now is at a small and III at a large radius. The initially created pocket, therefore, gathers more and more unburned fluid while it is advected downstream. Due to mass conservation, this has to lead to a reduction of the global heat release rate compared to the steady state, since the flame stores more and more premixture instead of burning it. This is exactly the inverse behavior of a Bunsen flame and explains the negative sign of the integral in Eq. (6.12), which is positive for Bunsen flames. When the growing pocket ultimately reaches the flame tip, all of the gathered fluid is burned all of a sudden, similarly to Slit flames.

The described behavior is now assessed analytically. Therefore, an unit impulse velocity forcing at the flame base $u'_{\perp} = a\delta(x_1^F)\delta(t)$ is assumed, which leads to an infinitely thin pocket of unburned gas (see blue line/dot in Fig. 6.7) which is advected along the mean flame front according to

$$\xi(x_1^F, t) = \frac{a}{u_{\parallel}} \delta\left(t - \frac{x_1^F}{u_{\parallel}}\right) \quad (6.13)$$

with the Dirac delta function $\delta(t)$ and the geometry dependent amplitude a . All the volume of the impulsively supplied unburned fluid V_e is now condensed to one point. The amplitude a is chosen such, that all of the extra volume flux provided at the inlet of the domain (Index “i”) is displacing the flame and hence is conserved: $\int_{\bar{A}_f} a\delta(x_1^F)dS = \int_{A_i} u'_1 dS$. Therefore, we get $a = R_i$ for Slit flames, $a = R_i/2$ for Bunsen Flame and $a = R_r/2(1/\tilde{r}^2 - 1)$ for Wedge flames, with the non-dimensional rod radius $\tilde{r} = R_r/R_a$. By integrating Eq. (1.32) ($I_M = 0$) and applying a flame base movement as described above as a boundary condition, a transfer function connecting the normalized upstream velocity perturbation u'_1 and the normalized flame surface area fluctuation is evaluated:

$$F_{\delta}(\omega) = \frac{A'(\omega)/\bar{A}}{u'_1(\omega)/\bar{u}_1} \quad (6.14)$$

The impulse responses resulting from this approach are provided in Appendix C.2 for all three geometries.

$F_{\delta}(\omega)$ can be viewed as an FTF where the velocity perturbation is imposed only at the flame base. Therefore, it shares some basic properties with conventional FTFs, for example, that it has a low-frequency limit of unity [157]. The resulting response functions are plotted for all three flames in Fig. 6.8, on the left hand side in time domain (impulse response h_{δ}) and on the right in frequency domain in terms of gain and phase. All quantities are non-dimensionalized by the characteristic flame time: $h_{\delta}^* = h_{\delta}\tau_r$, $t^* = t/\tau_r$ and $f^* = f\tau_r$. For Wedge flames, a non-dimensional rod radius of $\tilde{r} = 0.5$ is assumed. It should be noted that the IRs of the Slit and the Wedge configuration both contain a Dirac delta function. The strength of such a δ -function

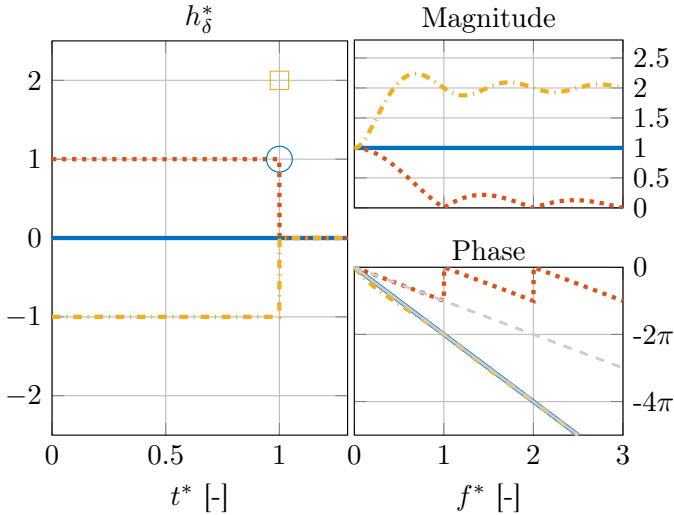


Figure 6.8: Transfer function in terms of impulse response h_δ and frequency response F_δ from flame base velocity perturbations to heat release shown for three flame configurations: Slit (—, impulses as \circ), Bunsen (---) and Wedge flames (— · —, impulses as \square). The phase curves corresponding to a fixed time delay of τ_r (—) and the one corresponding to $\tau_r/2$ (---) are added to the phase plots. For Wedge flames a non-dimensional rod radius of $\tilde{r} = 0.5$ is assumed.

is characterized by its integral and it is hence decided to plot this integral value in all IR visualizations. That means, for example, that the yellow square in Fig. 6.8 (\square) represents a $2\delta(t^* - 1)$ contribution.

The impulse response (IR) of the Slit flame (—, impulses as \circ) only consists of a Dirac impulse at $t^* = 1$, which is exactly the time it takes for a flame front perturbation to be advected from the base to the tip. Since a very localized response in time domain leads to a very spread out response in frequency domain (and vice versa), the gain of Slit flames is unity for all frequencies, see also Tab. C.2 in Appendix C.1. The phase linearly decays, as it is expected for systems with a single, constant time delay τ_r .

A Bunsen flame (---) spreads the response in time, as it continuously burns the supplied pocket of fluid. This leads to a constant positive value of the IR until $t^* = 1$, where the pocket has reached the flame tip. Consequently, the gain of the associated frequency response (FR) drops to zero at that frequency whose period fits the characteristic flame time, which is $f = 1/\tau_r$. Up to a Strouhal number of $f^* = 1$, the phase decays with a constant slope which corresponds to that of a system with a fixed time delay $\tau_r/2$. This delay is defined by the geometrical center of the IR. At multiples of $f^* = 1$ the phase jumps by π since the gain drops to zero. The smearing of the heat release fluctuation in time leads to a, compared to Slit flames, reduced cut-off fre-

quency of the corresponding transfer function. Mathematically, this can be explained by the low-pass filter behavior of an integrator ($\propto 1/\omega$).

Finally, a Wedge flame (—, impulses as □) increases the initially supplied pocket of fresh fluid and, hence, shows a negative response in the time domain up to $t^* = 1$. At the time the pocket reaches the tip, all of the accumulated and excitation supplied premixture is burned at once and leads to a strong impulse at $t^* = 1$. The magnitude of this impulse is higher than the one of the Slit flame, since the fluid pocket grew in size along its way to the flame tip. Hence, Wedge flames have two intrinsic time scales, τ_r from the impulse and $\tau_r/2$ from the integration. Through interference effects this leads to recurring peaks in the gain [116]. In particular at high frequencies, the phase is dominated by the characteristic flame time τ_r .

Using the example of a (infinitely narrow) pocket of fluid, which is advected from the flame base to the tip, it was possible to intuitively confirm the analytical results from Sec. 6.2. Further, some fundamental consequences of different flame geometries on the flame response in frequency and time domain could be illustrated. One example are the different time lags of Bunsen and Slit flames ($\tau_r/2$ vs. τ_r), which lead to different slopes in the transfer function phase. This is in accordance with the findings by Duchaine *et al.* [146], which leads to the conclusion that even such a simple flame response model as the one described here correctly predicts some features of realistic FTFs. In the next section we derive analytical predictions for the FTF for all configurations, using the most widespread velocity models from the literature, and compare the results to CFD/SI data, see Sec. 6.1, as well as to measurement data from the literature. It will be shown that the respective results, although being more complex, will qualitatively be very similar to those retained by the aforementioned simple model.

6.4 Incompressible-Convective FTF Models

Integration of Eq. (1.32) ($l_M = 0$) requires a model for the flame normal velocity perturbation u'_\perp . State of the art models, which allow the analytical evaluation of the FTF, are based on axially advected flow perturbations emanating from the flame base, see Sec. 2.2.1 (Low-Order Models). The two most common ones are the “convective velocity model” [111, 116] and the “incompressible-convective velocity model” [138, 161]. The flow field of the former consists of axial flow perturbations, which are transported with mean flow velocity \bar{u}_1 and lead to the generation of wrinkles at the momentary location of the perturbation along the flame. The flow field of the latter introduces a matching lateral flow perturbation to fulfill continuity equation. Using the Einstein summation convention, the incompressibility condition reads for

symmetric configurations:

$$\begin{array}{ll}
 \text{Slit:} & \text{Conical:} \\
 \frac{\partial u'_i}{\partial x_i} = 0 & \frac{\partial u'_i}{\partial x_i^L} + \frac{u'_2}{x_2^L} = 0 \\
 \rightarrow u'_2 = -x_2^L \frac{\partial u'_1}{\partial x_1^L} & \rightarrow u'_2 = -\frac{x_2^L}{2} \frac{\partial u'_1}{\partial x_1^L}.
 \end{array}$$

A Cartesian and a cylindrical coordinate system is applied here for Slit and conical flames, respectively. A general formulation that combines slit and conical cases reads

$$u'_2 = -x_2^L f_g \frac{\partial u'_1}{\partial x_1^L}, \quad (6.15)$$

where the geometrical factor f_g is set to $f_g = 1$ for slit and to $f_g = 1/2$ for conical flames. By setting $f_g = 0$, the plain convective velocity model is recovered. As stated in Sec. 2.2.3, in order to derive an analytical expression for the FTF, either a harmonic [111] or an unit impulse signal [116] has to be imposed on the reference velocity position. In the following the latter method is applied, the impulse response is evaluated and the frequency response is derived from that.

In the time domain (unit impulse excitation), convective velocity models exhibit an advected Dirac velocity perturbation $u'_1 = \delta(t - x_1^L/\bar{u}_1)$, which locally perturbs the flame front, see Eq. (2.6). It is shown below that such a velocity model leads to the occurrence of Dirac impulses in the corresponding IRs of Slit and Wedge flames. This, in turn, results in frequency responses lacking a cut-off frequency, i. e. the associated FTF does not feature the characteristic low-pass behavior. In order to remedy this unrealistic shortcoming, we assume a general velocity kernel function $g(\tau)$, which determines a characteristic spatial shape of the convected velocity fluctuations $u'_1 = g(\tau)$. In the convective model described above, this kernel is a Dirac delta function: $g_\delta(\tau) = \delta(\tau)$, with $\tau = t - x_1^L/\bar{u}_1$. A natural extension to this model is the assumption of a Gaussian kernel

$$g_\sigma(\tau) = \frac{1}{\sqrt{2\pi\sigma^2}} \exp\left(-\frac{\tau^2}{2\sigma^2}\right) \quad (6.16)$$

with the standard deviation σ . Applying such a kernel is effectively a low-pass filtering of the results computed from a Dirac kernel and, therefore, leads to the desired low-pass behavior of the FTFs. Furthermore, it allows for more realistic predictions of acoustically induced flame front displacements as will be shown in Sec. 6.6.

Employing the general kernel and applying Eq. (6.15), the two advected components

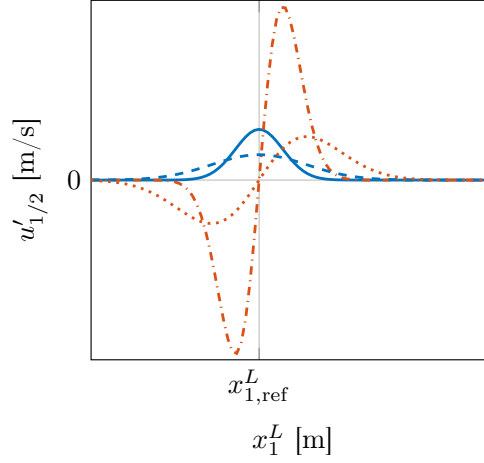


Figure 6.9: Qualitative illustration of the velocity field resulting from unit impulse forcing and a Gaussian velocity kernel function $g(\tau)$ at position $x_{1,\text{ref}}^L$. Shown are x_1^L (—) and x_2^L (---) components for a standard deviation of σ_1 , as well as x_1^L (- - -) and x_2^L (· · · ·) components for $\sigma_2 = 2\sigma_1$.

of the velocity perturbation of Eq. (2.6) are written as

$$u'_1 = g\left(t - \frac{x_1^L}{K\bar{u}_1}\right) \quad (6.17)$$

$$u'_2 = f_g \frac{x_2^L}{K\bar{u}_1} g'\left(t - \frac{x_1^L}{K\bar{u}_1}\right), \quad (6.18)$$

with $g'(\tau)$ denoting the first derivative of the kernel function with respect to τ . Here, a parameter K is introduced, which defines the axial advection speed of the velocity perturbation as a multiple of the mean flow velocity (inverse definition as in [138, 163, 167]). For $K = 1$ the standard convective velocity model is retrieved. Fig. 6.9 qualitatively shows the spatial shape of the x_1^L and x_2^L velocity components of the convected perturbation for a Gaussian velocity kernel function of two different standard deviations σ . For $\sigma \rightarrow 0$, the velocity perturbation becomes more and more localized as it approaches a Dirac impulse.

From Fig. 6.9 it is deduced that the integral of u'_2 over x_1^L is zero. Indeed, the associated velocity field has a solenoidal character and thus corresponds to a vortical velocity field. Fig. 6.10 exemplarily illustrates the qualitative two-dimensional (2D) velocity (u'_1, u'_2) and vorticity (ω'_3) field associated with the convective Gaussian disturbance for a Bunsen flame. The axial velocity component u'_1 provides fresh fluid, which generates a positive displacement of the flame front, while the u'_2 component leads to positive as well as negative displacements of equal magnitude. From the arrows in Fig. 6.10 it becomes clear that the u'_2 component redistributes flame front deflections. When interpreting the shown velocity field, it has to be kept in mind that

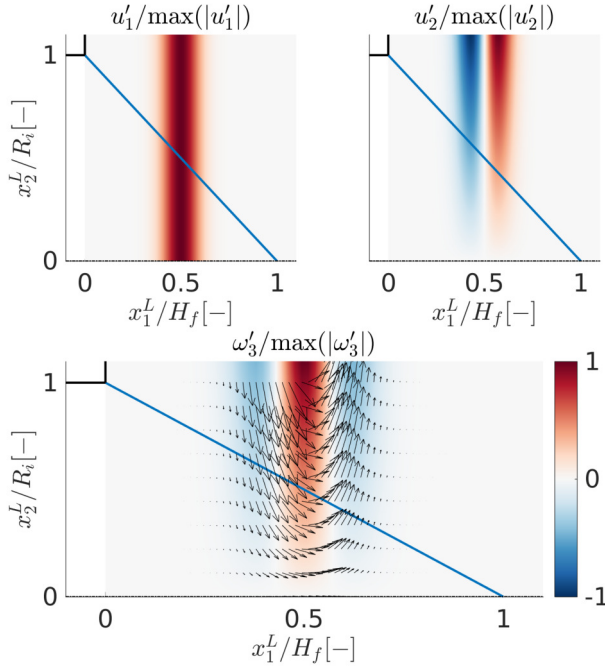


Figure 6.10: Snapshot of the velocity and vorticity field resulting from unit impulse response forcing and a Gaussian velocity kernel for a Bunsen flame. Shown are the two velocity components u'_1 (top left), u'_2 (top right) and the correspond x_3^L vorticity component ω'_3 (bottom), all of them normalized by their maximum absolute value.

only the velocity right at the mean flame front interacts with the flame. The spatio-temporal structure far away from the flame is not important and should, hence, not be misinterpreted as a strange kind of shear layer vortex.

In order to derive analytical expressions for the IRs of all three configurations, we firstly evaluate the flame normal velocity perturbation associated with Eqs. (6.17) and (6.18), which is

$$\begin{aligned}
 u'_{\perp, \Lambda / \text{slit}} = & g \left[t - \frac{x_1^F}{L_f} \tau_c \right] \sin(\alpha) + \\
 & f_g \tau_c \frac{R_i - x_1^F \sin(\alpha)}{L_f} g' \left[t - \frac{x_1^F}{L_f} \tau_c \right]
 \end{aligned} \tag{6.19}$$

for Slit and Bunsen flames and

$$u'_{\perp,V} = g \left[t - \frac{x_1^F}{L_f} \tau_c \right] \sin(\alpha) + f_g \tau_c \frac{R_0 + x_1^F \sin(\alpha)}{L_f} g' \left[t - \frac{x_1^F}{L_f} \tau_c \right] \quad (6.20)$$

for Wedge flames. A second characteristic time τ_c is introduced here, which denotes the time it takes for an axially advected velocity perturbation to be transported from the flame base to its tip. This introduces the velocity of the convective disturbance in flame coordinates u_c , which is provided for both coordinate systems in Tab. 6.1. The characteristic flame times τ_r and τ_c are related to flame speed, the flame angle and the feed duct half-diameter by

$$\tau_r = \frac{R_i}{s_L \cos(\alpha)}, \quad (6.21)$$

$$\tau_c = \frac{\cos^2(\alpha)}{K} \tau_r, \quad (6.22)$$

where the relation $\cos^2(\alpha) = 1 - s_L^2/\bar{u}_1^2$ could be applied to estimate the flame angle. For Wedge flames, a length $R_i = R_a - R_r$ has to be used in Eq. (6.21). Using the described perturbation velocity field, analytical expressions for the IRs of all three flame geometries are derived by solving Eq. (1.32) ($l_M = 0$) and, subsequently, Eq. (2.3) for the unit impulse response $h(t)$ using the flame surface integrals summarized in Tab. 6.1. Results are provided in Appendix C.1 and are functions of τ_r and τ_c only (ignoring f_g and possible kernel parameters). The FTF of Wedge flames has the non-dimensional rod radius $\tilde{r} = R_r/R_a$ as a third parameter. All FTFs are derived in terms of a general kernel g and are hence ready to be used with arbitrary functions.

We introduce the abbreviation DIC for the Dirac kernel based incompressible-convective velocity model and GIC for the Gaussian kernel based counterpart. The GIC model relies on the two additional empirical parameters K and σ , which need to be fitted to experimental observations. As will be shown later, K is primarily used to modify the frequency of maximum gain and σ to set the cut-off frequency of the FTF.

6.5 Geometry-Dependent Analysis of the Incompressible-Convective Model

Above, the incompressible-convective velocity models for three flame configurations were introduced. We now want to analyze the DIC model for all geometries in order to gain some insights into the respective flame responses. To date, expressions of the DIC model have solely been evaluated for Bunsen flames. While Cuquel [134]

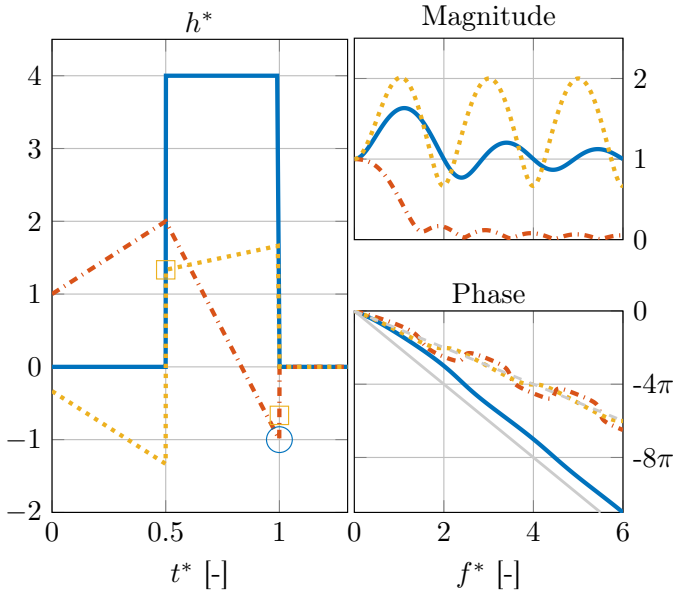


Figure 6.11: FTF predictions of the DIC model for $\alpha = \pi/4$ and $K = 1$ in terms of impulse response $h(t)$ (left) and frequency response $F(\omega)$ (right) shown for three flame configurations: Slit (—, impulses as \circ), Bunsen (---) and Wedge flames (....., impulses as \square). The phase decay corresponding to a fixed time delay of τ_r (—) and the one corresponding to $\tau_r/2$ (---) are added to the phase plots. For Wedge flames a non-dimensional rod radius of $\tilde{r} = 0.5$ is assumed.

analyzed them in time and frequency domain, Preetham *et al.* [138] and Orchini and Juniper [163] focused only on frequency domain representations. The following discussion seeks to close this gap in the literature.

FTF predictions of the DIC model for $\alpha = \pi/4$ and $K = 1$ are shown in Fig. 6.11 for all three flame geometries. For Wedge flames, a non-dimensional rod radius of $\tilde{r} = 0.5$ is assumed. The IRs are shown on the left-hand side of this figure and the associated FRs, in terms of magnitude and phase, on the right. All quantities are non-dimensionalized by the characteristic flame time: $h^* = h\tau_r$, $t^* = t/\tau_r$ and $f^* = f\tau_r$. The IRs of the Slit and the Wedge flame contain Dirac delta functions. This kind of function (strictly speaking distribution) is characterized by its integral and it is hence decided to indicate this integral value in all IR visualizations whenever a Dirac Impulse is present. That means, for example, that the blue circle \circ in Fig. 6.11 represents a $-\delta(t^* - 1)$ contribution. Since the integral of this expression is -1 , the circle indicates this value in the graphical representation of the IR at $t^* = 1$.

The respective behavior of the FTF for the various geometries becomes more clear when analyzing the transient flame front deflection $\xi(x_1^F, t)$ caused by an impulse forcing. An illustration of a snapshot is shown in Fig. 6.12a for Slit and Bunsen and in

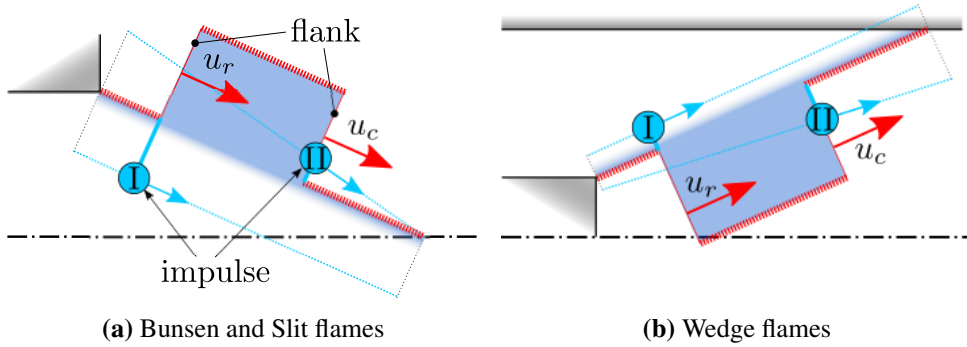


Figure 6.12: Illustration of the displaced flame front deflection $\xi(x_1^F, t)$ of the DIC model for an impulse velocity perturbation. Shown are two flanks, which propagate with the velocity u_r (restoration) and u_c (convective flow disturbance), and two impulses I and II both propagating with the velocity of the respective flank.

Fig. 6.12b for Wedge flames. As expounded by Blumenthal *et al.* [116] for the plain convective velocity model, two flanks are formed (see Fig. 6.12), which delimit a pocket of unburned gas. This pocket grows in extent, since the downstream flank propagates with a higher velocity than the upstream one ($u_c > u_r$). In case of the incompressible-convective velocity model, additionally, two flame front displacements of the shape of a Dirac impulse are formed (see Fig. 6.12), which are not present in the plain convective velocity model and also propagate along the flame front. They result from the lateral, solenoidal velocity component of the convected perturbation. In agreement with Fig. 6.12 we refer to those impulses as Impulse I and Impulse II. Their propagation speed equals the speed of the adjacent flank, i. e. u_c for impulse II and u_r for impulse I.

First let us consider a Bunsen flame. Here, Impulse I forms a negative flame front displacement and its amplitude stays constant while it is advected downstream with u_r , see Fig. 6.12a. Impulse II constitutes a positive displacement and its amplitude decreases when advected downstream by the velocity u_c , until it reaches zero right at the flame tip. According to Sec. 6.2, the linearized flame surface area fluctuation of a Bunsen flame depends on the integral of the instantaneous flame front deflections. Hence, advected Dirac impulses are transformed to Heaviside Step functions in time when evaluating the IR, see Appendix C.1. Consequently, the IR of a Bunsen flames does not show any Dirac Impulses as depicted in Fig. 6.13a. Impulse I adds a constant negative contribution to the overall IR (.....), while Impulse II adds an decreasing, positive value to the overall IR, which disappears at $t^* = 0.5$, i. e. in dimensional time at $t = \tau_c$ (- - -). The specific nature of the Bunsen flame heat-release dynamics (integral of ξ) leads to a dispersion of the flame response in time. This, in turn, goes along with a relatively low cut-off frequency of the associated FTF, see Fig. 6.11 (- - -). This can be explained by the fact that integration imposes a $1/\omega$ behavior in

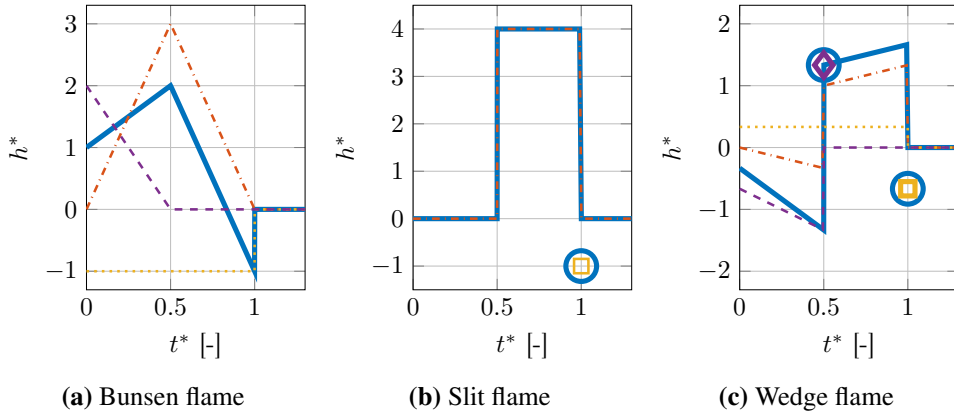


Figure 6.13: Impulse responses of the three different flame configurations. Shown are the overall IR (—, impulses as \circ), as well as the contributions of the flanks (---), Impulse I (····, impulses as \square) and Impulse II (---, impulses as \diamond) of $\xi(x_1^F, t)$ to the overall IR. Parameters are the same as those described in Fig. 6.11.

frequency domain, see Tab. C.2 in Appendix C.1: The integral of a Dirac impulse is the Heaviside step function and, consequently, the amplitude of the one-sided Fourier transform of the latter shows an $1/\omega$ behavior while it is unity for the former.

The situation is very different when a Slit flame is considered. The instantaneous flame front displacement according to the DIC model is qualitatively the same as for a Bunsen flame, see Fig. 6.12a. However, since the flame surface area fluctuation of Slit flames depends to leading order only on the flame tip movement, see Sec. 6.2, Dirac impulses in ξ lead to the appearance of Dirac impulses in the IR. More specifically, as shown in Fig. 6.13b, Impulse I adds a negative Dirac impulse at $t^* = 1$ (in dimensional time at $t = \tau_r$). Impulse II has no impact as it vanishes at the flame tip. The negative impulse at $t^* = 1$ leads to an FR gain tending to unity instead of zero for $f \rightarrow \infty$, see Fig. 6.11 (—). All in all, the response of a Slit flame constitutes a time delayed, direct effect of flame front perturbations. No spatial integration of flame displacements, as in the Bunsen case, is present, which leads to an FR lacking a low-pass filtering behavior.

The global heat-release rate of Bunsen flames responds to the integral of a flame front perturbation, while Slit flames react to flame front deflections directly once they reach the flame tip. Bunsen flames are, in consequence, a more sedate source of sound than Slit flames for a given flame front perturbation. This fact might, besides other effect such as flame curvature or burner-plenum acoustics, contribute to the lower sound pressure levels of combustion noise produced by turbulent Bunsen type flames compared to Slit ones, as reported by Kotake and Takamoto [151] and Pausch *et al.* [153].

In terms of response characteristics, Wedge flames are in some aspects similar to Slit flames and in others more close to Bunsen flames. A snapshot of the resulting flame front deflection due to an impulse velocity forcing is shown in Fig. 6.12b. Again, two flanks appear, which are advected downstream. Impulse I depends on the non-dimensional rod radius \tilde{r} and has a constant, non-zero value for $\tilde{r} > 0$. Contrary to Bunsen and Slit flames, Impulse II now increases in amplitude while it is advected downstream. Consequently, both impulses lead to the occurrence of Dirac impulses in the IR of Wedge flames, see Fig. 6.13c. Thus, the gain of the corresponding FR never reaches zero and shows several recurring peaks of high magnitude, similar to a Slit configuration, see Fig. 6.11 (•••••). While the phase of a Slit flame decays with a constant slope, which corresponds to the one of a system with a fixed time delay τ_r , the phase of a Bunsen flames decays with a slope corresponding to a time delay $\tau_r/2$. The phase of a Wedge flame with $\alpha = \pi/4$ behaves similar to the one of a Bunsen flame, as depicted in Fig. 6.11. For longer flames ($\alpha \downarrow$) the phase of a Wedge flame would approach the one of a Slit flame (not shown).

The response of Wedge flames integrates flame front perturbations *and* also directly responds to them once they reach the flame tip. In that sense they are a hybrid of Slit and Bunsen flames. Since, however, their flame front deflection according to the DIC model is different to that of Bunsen and Slit flames, see Fig. 6.12, they are not a pure hybrid and additionally bring some individual response characteristics, such as the presence of pronounced positive and negative contributions in their IR. As explicated by Blumenthal *et al.* [116], this is a necessary condition for the occurrence of peak gain values exceeding unity. Indeed, the gain shown in Fig. 6.11 affirms this statement.

In this section it is illustrated that each of the three considered flame configurations has its own peculiar response characteristics. As will be shown in the following, the incompressible-convective velocity model is able to predict frequency and impulse responses, which qualitatively and also quantitatively agree with CFD and experimental data, if a Gaussian instead of a Dirac kernel is used. In doing so, the Dirac impulses, appearing in the IRs of Slit and Wedge flames, are transformed to Gaussian impulses. This corresponds to a dispersion in time and, hence, to a decreased cut-off frequency, which brings the desired low-pass behavior of the predicted FTFs.

6.6 Validation of Flame Response Models

Figs. 6.14, 6.15 and 6.16 visualize FTFs identified from the CFD simulations introduced in Sec. 6.1 for all three flame configurations (•••••). Additionally, predictions from the convective and the incompressible-convective velocity model (DIC and GIC) are shown. The free parameters τ_r , τ_c and \tilde{r} are computed according to Eqs. (6.21) and (6.22) using the physical and geometrical quantities introduced in Sec. 6.1 and a laminar flame speed of $\bar{s}_L = 0.278$ m/s. Due to confinement effects

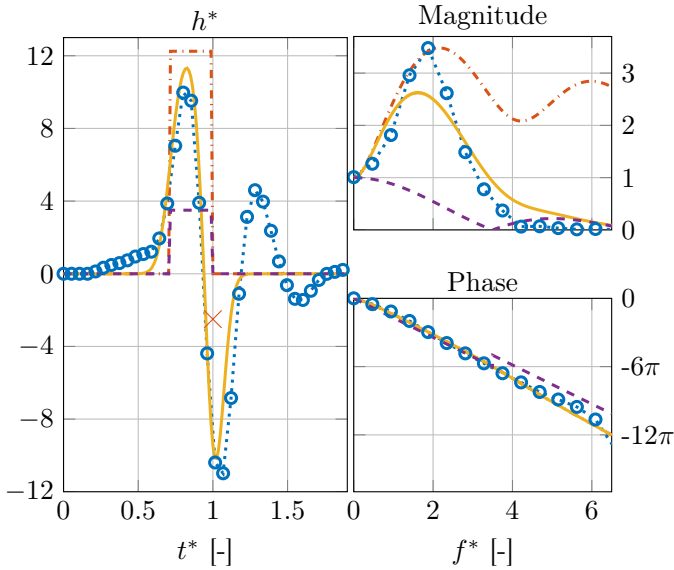


Figure 6.14: Comparison of FTF predictions for **Slit flames** visualized in time (left) and frequency domain (right) from CFD/SI data (●○●), as well as from the plain convective (---) and the incompressible-convective velocity model using a Dirac (· · ·, impulses as ×) and a Gaussian kernel with $\sigma = 1.2$ ms and $K = 1.3$ (—) for $\tau_r = 18.7$ ms.

(see e. g. [144]), we have to adjust τ_r for the Slit and the Wedge setup compared to the results provided by Eq. (6.21) in order to match the CFD/SI data. This correction is applied by fitting the reduced order models to the CFD/SI IR data such that the position of the first negative part of the IRs coincide. Confinement effects are negligible for the Bunsen flame setup. The respectively values of τ_r are provided in the figure captions of the FTF data.

Concerning the empirical parameters of the GIC model, for the Bunsen and the Slit results presented here, we chose $\sigma = 1.2$ ms and $K = 1.3$ in order to match the CFD data. For the Wedge case, $K = 1.3$ could be applied as well, however, we use an increased standard deviation of $\sigma = 1.9$ ms. This results in a non-dimensionalized standard deviation $\sigma^* = \sigma/\tau_r$ of $\sigma^* \approx 0.064$ for the Slit and Bunsen setup and $\sigma^* \approx 0.142$ for Wedge case. Hence, at least for the three cases discussed here, some universality of these parameter values can be assumed.

By evaluating the FTF for both a Dirac and a Gaussian kernel, the importance of the dispersion in time, which was mentioned in Sec. 6.4, becomes apparent. Wedge and Slit flames have Dirac impulses in their DIC model based predictions, see (· · ·, impulses as ×) in Figs. 6.14 and 6.16. The corresponding FR gain curves oscillate without decaying to zero, which does not reflect the observed low-pass filtering behavior of flames. Introducing a Gaussian kernel, the Dirac impulses of the DIC based

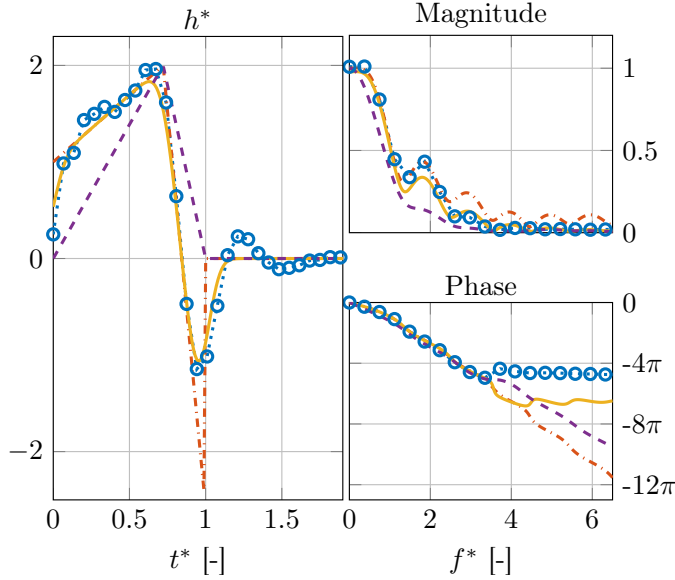


Figure 6.15: Comparison of FTF predictions for **Bunsen flames** visualized in time (left) and frequency domain (right) from CFD/SI data (⊗⊗⊗), as well as from the plain convective (---) and the incompressible-convective velocity model using a Dirac (⋯) and a Gaussian kernel with $\sigma = 1.2$ ms and $K = 1.3$ (—) for $\tau_r = 18.6$ ms.

IR become Gaussian impulses such that the gain of the associated FR shows a similar cut-off behavior as the CFD/SI data.

Generally, very good agreement between the GIC model and the CFD/SI data is found for the three investigated configurations. It shall now be analyzed if the respective flame front displacements also resemble the CFD data and how they are connected to specific features of the IR. For that purpose, it was decided to representatively analyze the Slit configuration since the relation between the global heat-release rate and flame displacements is very straight forward here. The respective data for the Bunsen and the Wedge flame are briefly discussed afterwards. Fig. 6.17 compares the IR of a Slit flame to its associated normalized flame front displacements $\xi/\hat{\xi}$, one time for the CFD data (⋯) and one time for the IC velocity model employing a Dirac (⋯, impulses as \times) and a Gaussian (—) kernel. Here, the reference displacement is defined as $\hat{\xi} = \int_0^t u_1' dt$. The displacements of the CFD data are evaluated from a simulation that is excited by an impulse forcing of $10\% \bar{u}_1$ amplitude. It was verified that the resulting global heat-release rate of this impulsively forced setup corresponds to the IR estimated from the broad-band data (not shown). Snapshots at four instants in time t_1 to t_4 of the displaced flame front are plotted in Fig. 6.17 (lower half). The corresponding temporal positions are marked in the plot of the IR (upper half) by horizontal dashed lines.

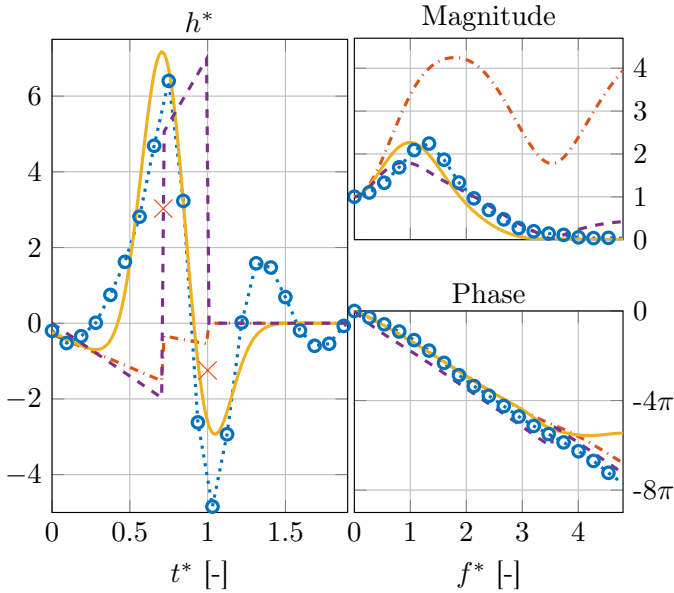


Figure 6.16: Comparison of FTF predictions for **Wedge flames** visualized in time (left) and frequency domain (right) from CFD/SI data (●●●), as well as from the plain convective (---) and the incompressible-convective velocity model using a Dirac (---, impulses as ×) and a Gaussian kernel with $\sigma = 1.9$ ms and $K = 1.3$ (—) for $\tau_r = 13.3$ ms.

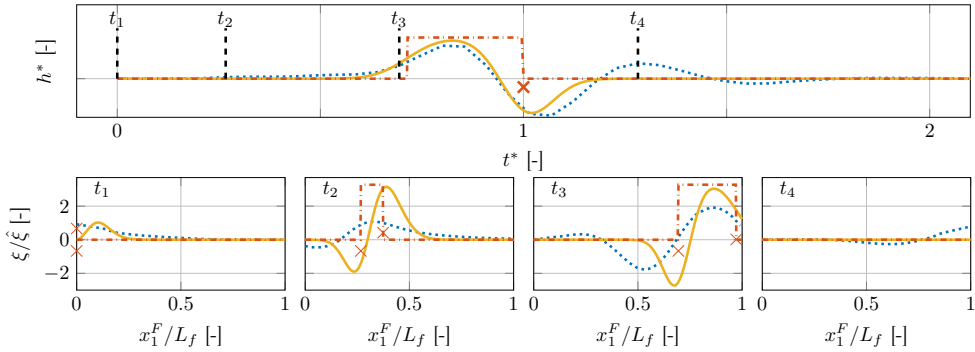


Figure 6.17: Comparison of IR (top) and the corresponding normalized flame front displacement $\xi/\hat{\xi}$ of the Slit configuration resulting from an impulse forcing at four instants in time, shown for the CFD/SI data (.....) as well as for the incompressible-convective velocity model employing a Dirac (---, impulses as ×) and a Gaussian (—) kernel, see also Fig. 6.14. Compare to Fig. 6.12a for clarification.

At time $t_1 = 0$ the impulsive velocity forcing hits the flame and both the CFD data and the GIC model show displacements in the approximate vicinity of the flame base

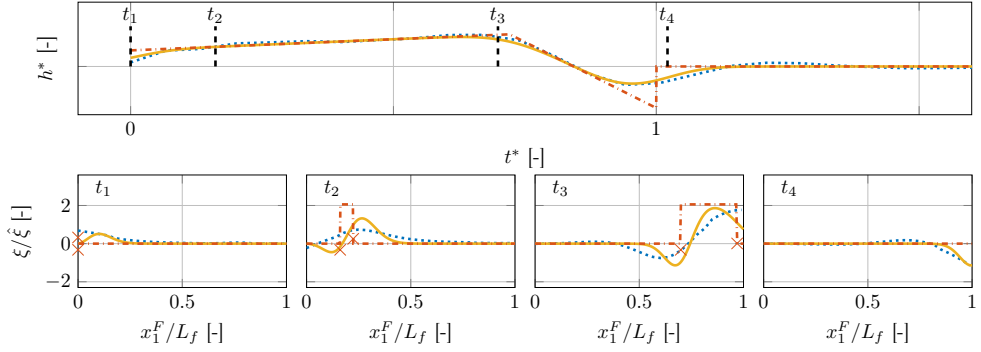


Figure 6.18: Comparison of IR (top) and the corresponding normalized flame front displacement $\xi/\hat{\xi}$ of the Bunsen configuration resulting from an impulse forcing at four instants in time, shown for the CFD/SI data (.....) as well as for the incompressible-convective velocity model employing a Dirac (---, impulses as \times) and a Gaussian (—) kernel, see also Fig. 6.15. Compare to Fig. 6.12a for clarification.

region. This is in accordance with the findings of Chap. 4 relating this to the impact of the potential part of the acoustic perturbation. The flame tip stays unaffected and thus the corresponding IR exhibits no response at t_1 . The CFD data now shows that while this initial displacement is convected downstream it grows in amplitude and smaller, secondary negative and positive displacements develop. Each time a displacement reaches the flame tip, a response of the global heat-release is provoked, see t_3 and t_4 . Having a look at the corresponding GIC and DIC data, it is apparent that displacement amplitudes are overpredicted until they reach the flame tip, where they match the CFD results reasonably well. Knowing that the global heat-release rate of Slit flames depends solely on flame tip movements, it becomes clear that the matching of amplitudes at the tip region is the crucial property that determines the quality of the associated IR prediction.

Figs. 6.18 and 6.19 show the corresponding results for a Bunsen and Wedge configuration, respectively. Again it can be seen that although flame displacements predicted by CFD and the GIC model do not perfectly match, the IRs of the global heat-release agree well. The GIC model is able to qualitatively capture the dynamics of an impulsively perturbed flame front. For harmonic forcing Baillot *et al.* [120] reported good agreement between experiment and the DIC model in terms of flame shapes. Since the GIC model improves response predictions compared to the DIC model, it can be conjectured that the GIC model should further improve that already good match.

It is interesting to note that while Slit and Bunsen configurations exhibit flame front displacements that grow in amplitude, the ones for Wedge flames show a decaying behavior (Fig. 6.19,.....). The reason for this is unclear. Further, the initial displacements at $t = 0$ are very similar for all three configurations, which means that, qual-

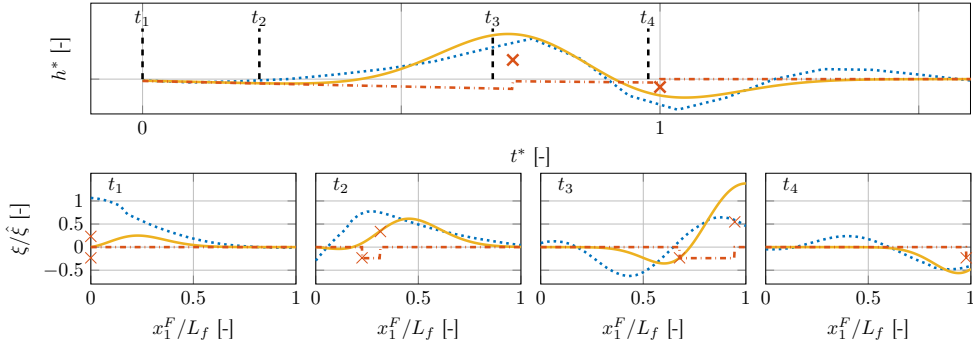


Figure 6.19: Comparison of IR (top) and the corresponding normalized flame front displacement $\xi/\hat{\xi}$ of the Wedge configuration resulting from an impulse forcing at four instants in time, shown for the CFD/SI data (.....) as well as for the incompressible-convective velocity model employing a Dirac (-----, impulses as \times) and a Gaussian (—) kernel, see also Fig. 6.16. Compare to Fig. 6.12b for clarification.

itatively, the results presented in Chap. 4 seem not to be limited to Slit flames but are rather universal. Finally, the deviation of displacements of the DIC from the GIC model for Slit and Wedge configurations illustrates the importance of the Gaussian impulses for the overall response characteristics.

Comparing predictions of the flame front displacements shown in Fig. 6.17 from the DIC (-----, impulses as \times) and the GIC (—) model, one realizes that the Gaussian kernel disperses unphysical, very localized Dirac displacements of the DIC model in space. Such a dispersion might be related to effects of flame stretch, particularly curvature, as well as to the finite width of the initial flame displacements of the CFD data at t_1 , which is an essentially inviscid effect [1].

As a consequence of the oscillatory displaced flame front, Slit flames show a decaying oscillatory IR with alternating positive and negative contributions of decreasing amplitude, see Figs. 6.14 and 6.17. The GIC model captures the first period of this signal and then immediately decays to zero. The negative part of the predicted IR is caused by the u'_2 component of the velocity model, see Eq. (6.18), which corresponds to a vortical velocity field, as described in Sec. 6.4. It is hence deduced that, in the proposed models, the first negative minimum (the second for Wedge flames) of all IRs is caused by vortical structures.

Slit flames show a very high peak gain value, which is not at all predicted by the plain convective velocity model, see Fig. 6.14 (---). For the other two geometries, this model agrees reasonably well with the CFD/SI data. It correctly predicts the cut-off behavior of Bunsen flames and only misses to capture the reoccurring maxima in the gain for $f^* > 1.5$, as depicted in Fig. 6.15. For Wedge flames, Fig. 6.16 shows that the gain exceeding unity at $f^* \approx 1.3$ is qualitatively captured, however, the maximum

gain value is underestimated. The most important feature added by the DIC model, compared to the convective one, is the occurrence of impulses in the IR (\times). Slit flames show one negative impulse at $t^* = 1$, right at the position of the first minimum of the IR. Wedge flames have two of them, a negative one at $t^* = 1$ and a positive one at $t^* = \tau_c/\tau_r$, both at positions of local extreme values of the IR.

Having a closer look at the IRs, it is found that the time scale defined by $\tau_r - \tau_c$ plays an important role. As already pointed out by Blumenthal *et al.* [116], the difference between the restorative and the convective time defines the frequency of maximum gain for (sharp) Wedge flames. The IRs of all three flame configurations show oscillations of decaying amplitude. They are most prominent for the Slit and the Wedge configuration, see Figs. 6.14 and 6.16. The width of half a period of these oscillations very well agrees with the time $\tau_r - \tau_c$. The corresponding oscillation frequency is approximated by a Strouhal number

$$f_O^* = \frac{\tau_r}{2(\tau_r - \tau_c)} = \frac{1}{2\left(1 - \frac{\cos^2(\alpha)}{K}\right)}, \quad (6.23)$$

which is $f_O^* \approx 1.7$ for all shown cases. Around this frequency the Slit and the Bunsen flame show a local maximum in the gain of their FR. The peak value of the Wedge flame is shifted to a lower Strouhal number of about 1.1.

As stated by Eq. (6.23), the frequency of maximum gain depends on K and, hence, provides a physically motivated criterion to estimate this parameter. It is therefore presumed that the width of the Gaussian kernel function, set by the standard deviation σ , determines the cut-off frequency of the FTF and the parameter K fixes the frequency of maximum gain. Physically, the value of the first might be connected to diffusive processes and the one of the latter to (baroclinic) generation of vorticity.

This finding is exploited in order to compare the proposed models to data from the literature. Since Wedge setups comparable to the ones described here could not be found (i. e. no swirl and no influence of vortex shedding), only Bunsen and Slit configurations are used. Information about the experimental data is provided in Tab. 6.2. Fig. 6.20 shows the adopted frequency responses (FR), as well as the fitted FTF predictions of the GIC models. For each data set, a frequency is identified where the gain has a local maximum and Eq. (6.23) is used to compute an associated value for K . The values of $\cos^2(\alpha)$, which is according to Eq. (6.22) required to compute τ_c , and τ_r are estimated from the cited references. The standard deviation σ is then adjusted until the cut-off frequency of the GIC model agrees sufficiently well with the experimental data. All fit parameters are provided in Tab. 6.2.

Since all Bunsen setups show a very similar trend, only one single model ($f_O^* \approx 1.85$) was fitted. On the contrary, the FR of Slit flames has a high variance and is strongly affected by τ_r : the maximum gain value and the cut-off frequency rise with increasing τ_r . Accordingly, the non-dimensional frequency f_O^* shifts from 0.9 over 2.4 to 4.4. Since the GIC model consistently overpredicts the gain for low frequencies, it is

	Source	Fit Parameter	τ_r	Fig. 6.20
Bunsen	[156] (Fig. 3.6, 2 m/s)	$K = 1.33$ $\sigma = 1.2$ ms $\cos^2(\alpha) = 0.97$	14.8 ms	 - - -
	[134] (Fig. 3.8)	-	26.1 ms	
	[134] (Fig. 6.12, 0.396 g/s)	-	31.7 ms	
Slit	[148] (Fig. 7, T50h)	$K = 2.1$ $\sigma = 1.45$ ms $\cos^2(\alpha) = 0.95$	12.50 ms	 - - -
	[149] (CBB)	$K = 1.18$ $\sigma = 1.9$ ms $\cos^2(\alpha) = 0.94$	38.3 ms	
	[149] (UBB)	$K = 1.04$ $\sigma = 1.9$ ms $\cos^2(\alpha) = 0.92$	46.6 ms	

Table 6.2: Summary of experimental data adopted from the literature, see Fig. 6.20.

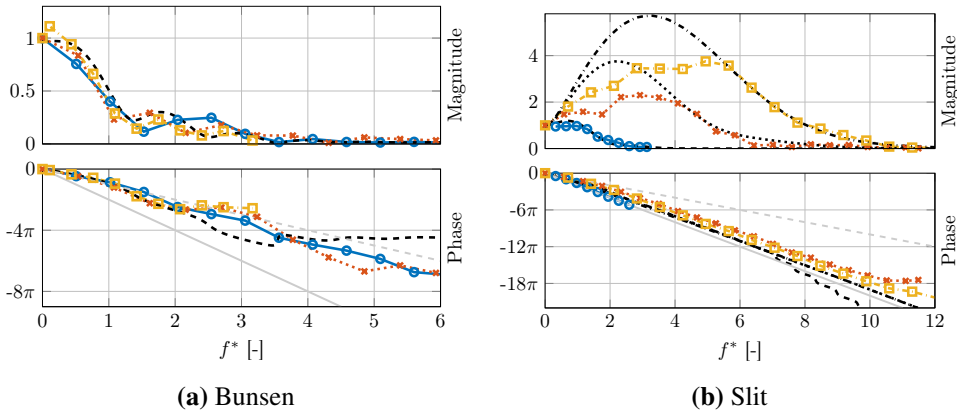


Figure 6.20: Experimental frequency response data of selected conical (a) and a slit flames (b) adopted from the literature (see Tab. 6.2). Additionally, predictions of the GIC model are shown (black lines). The phase corresponding to a fixed time delay of τ_r (—) and $\tau_r/2$ (- - -) is indicated in the phase plots.

concluded that it is lacking some damping mechanisms, which are present in experiments. Besides this, it is able to capture both gain and phase sufficiently well. This is remarkable considering the fact that in particular for Slit flames, the convective as well as the DIC model lead to very inaccurate FTF predictions, see also Fig. 6.14.

Finally, it should be pointed out that the phase of all Bunsen FTFs coincides with the one of a system with a constant time delay $\tau_r/2$, while Slit flames resemble a system of time delay τ_r , see Fig. 6.20. This result corresponds to the findings of Duchaine

et al. [146] and is captured correctly by both of the convective velocity models (DIC and GIC), see Sec. 6.5.

6.7 Summary and Conclusions

This chapter analyzed the consequences of flame geometry for the linear flame response, namely the flame transfer function (FTF). This was done by following a well established, G-equation based modeling approach and analyzing it with respect to geometry-related differences of Slit, Bunsen and Wedge type flame configurations. The process of how a wrinkled flame front leads to fluctuations in the global heat-release was identified as the key mechanism, which distinguishes the response of each flame. Therefore, the flame surface integral was analyzed in detail and analytical expressions for stiffly anchored, symmetric flames were derived. By extending the well-known incompressible-convective velocity model with a Gaussian Kernel, analytical FTF expressions were derived, which very well coincide with FTF predictions from numerical simulations for all three considered flame configurations. The derived models rely on two empirical parameters, namely the standard deviation of the Gaussian kernel and the advection velocity of the convective flow perturbation relative to the mean flow velocity. By relating the latter parameter to the frequency of maximum gain and the first to the cut-off frequency of the FTF, it was possible to provide good predictions of gain and phase of experimentally determined FTFs taken from the literature.

The main finding of the present analysis are:

1. The integral heat-release of **Bunsen** flames is proportional to the integral of the flame front displacement, the flame tip movement is negligible. Consequently, heat-release rate fluctuations induced by a displaced flame front are dispersed in time, which leads to a relatively low cut-off frequency, such that the FTFs of Bunsen flames look always quite similar when plotted over Strouhal number. The phase of the FTF is dominated by half the time of restoration $\tau_r/2$.
2. The integral heat-release of **Slit** flames is proportional to the flame tip movement. Therefore, flame front displacements directly affect the heat-release rate once they reach the tip. Compared to Bunsen flames, this leads to an increased cut-off frequency and, hence, to a higher response variance of Slit flame setups. Slit frequency responses show a high maximum gain value, which increases with the time of restoration τ_r . The heat-release of Slit flames responds time delayed to flame front perturbations, which leads to an FTF phase dominated by the characteristic flame time of restoration τ_r .
3. The integral heat-release of **Wedge** flames is proportional to the flame tip movement *and* the integral of the flame front displacement. Their impulse response shows significant positive and negative parts, which lead to gain values

exceeding unity. The phase behaves similar to the phase of a Bunsen flame and approaches the behavior of a Slit flame for long flames.

4. The impulse responses of all flame configurations, identified from CFD data, show a strongly damped oscillatory behavior, which leads to a local maximum in the FTF gain close to the oscillation frequency. In the proposed modeling framework, this frequency could be related to the difference in the time of restoration and the one of distortion, $\tau_r - \tau_c$. This dependency can be exploited in order to compute the two empirical parameters of the proposed Gaussian incompressible-convective (GIC) velocity model.
5. For surface integration, it is important to choose a coordinate system that accounts for the possible flame movements at the boundaries. Otherwise, variable integration limits are required.

Based on these results, the findings of Part II, which are based on Slit flames, can be transferred to Bunsen and Wedge geometries. Since the flame sheet dynamics essentially remains the same for all discussed configurations, differences emerge mainly from how flame shape translates to heat release. These integrals could simply be implemented into the low-order modeling framework suggested in Part II, which would allow for an approximation of the respective response characteristics.

Summary and Conclusions

This doctoral thesis analyzed the linear acoustic response of laminar premixed Bunsen-type flames primarily relying on first-principle-based, low-order modeling approaches. A literature review on the dynamics of laminar flames and interactions between acoustics and burner-stabilized flames laid the foundation for all subsequently performed investigations and provided guidance for the identification of relevant physical mechanisms determining the response characteristics. While, in the literature, the understanding of the dynamics of burner-stabilized flames whose anchoring is mechanically displaced, is based on the concepts of the Darrieus-Landau instability and thermal-diffusive mechanisms, the interpretation evolves around the notion of convected velocity perturbations in the case of acoustically perturbed flames. This is particularly surprising knowing that their dynamics should in fact be very similar, since acoustics predominately displaces the flame base region in both cases.

Motivated by this realization, a first principles-based incompressible low-order modeling framework was introduced, relying on methods adopted from aero-acoustics: the flow field is represented by a number of flow-field singularities combined with a conformal mapping technique and a Kutta condition. In a first step, flame-flow feedback was neglected and primary acoustics-flame interactions were assessed. It was found that consequences of shed vorticity for the flame response are negligible and that the irrotational part of the acoustic perturbations displaces essentially the flame base region. Hence, convective sources of flame displacement, as assumed by state-of-the-art low-order modeling approaches in the limit of negligible flame-flow feedback, could not be identified. Comparing low-order predictions to high fidelity CFD data, it could be shown that the resulting flame front displacements match only well right at the moment when the acoustic impulse hits the flame.

At later times, secondary mechanisms come into play, causing secondary displacements as well as the convective growth of displacement amplitudes. These effects could be associated with flame-flow feedback which essentially has two contributions: (i) a vortical one relying on flame-generated vorticity and (ii) an irrotational one relying on a flame-normal acceleration of the flow across a flame sheet together with a flame displacement-induced geometrical focusing. While the former mechanism causes a perturbed flame sheet to behave like a vortex sheet of varying strength, the far field of the latter resembles the one of advected dipoles. The upstream in-

fluence of each of these two mechanisms onto the unburned flow induces convected velocity perturbations. This explains observations reported by previous experimental studies. Concerning the linear response of the global heat release, it could be shown that both mechanisms of flame-flow feedback lead to the occurrence of peak FTF gain values significantly exceeding unity.

All those investigations were performed for Slit flame configurations; the literature, however, mostly reports on Bunsen flames. Therefore, in the final part of this thesis, consequences of flame geometry — namely of Slit, Bunsen and Wedge configurations — for the acoustic response were analyzed. It was found that the process of how a wrinkled flame front leads to fluctuations in the global heat-release constitutes the key mechanism that distinguishes the responses of different flame geometries. By extending the well-known incompressible-convective velocity model with a Gaussian Kernel, analytical FTF expressions were derived, which coincide very well with FTF predictions from numerical simulations for all three considered flame geometries.

The main achievements of this work can be summarized to:

- The linear thermoacoustic response (FTF) of a laminar premixed flame is essentially governed by hydrodynamic mechanisms that lead to (i) primary acoustically induced perturbations acting predominantly at the flame base and (ii) flame-flow feedback interacting with these primary flame front displacements while they are convected downstream.
- Flame-flow feedback has vortical and irrotational contributions and is responsible for FTF peak gain values significantly exceeding unity. Further it explains the observations of convected velocity perturbations upstream a wrinkled flame sheet.
- G-equation-based low-order models are usually based on the ad hoc assumption of convected velocity perturbations. They only implicitly include consequences of flame-flow feedback and, thus, do not faithfully represent the causality of the underlying flow physics.
- Flame geometry significantly impacts the dynamics of the global heat release rate, while the respective flame sheet dynamics remains essentially unchanged. Each geometry has its own unique response characteristics.

Based on the analysis performed in this thesis, some questions still remain open and, additionally, some new issues have been raised. One important point that requires further investigations concerns the quantitative analysis of flame-flow feedback: It is still unclear whether the irrotational or the vortical component is more important, although the computed data suggests the former. Furthermore, the prevailing mechanisms that impose a damping of flame front perturbations and their respective consequences for the flame response still need to be assessed. Based on these results, the introduced low-order modeling framework could then possibly be extended such

that it allows for quantitative FTF predictions. Another point of interest concerns the observed oscillatory behavior of the impulse response of the global heat release rate. It would be of high value to explain the underlying mechanism in detail and provide an estimate of the oscillation frequency. This is of particular interest knowing that this frequency is closely related to the frequency where the FTF gain exhibits its maximum. A detailed analysis of the flame anchoring dynamics might assist these efforts.

From a global point of view, the main outcome of this thesis is that modeling of the flame response in a thermoacoustic context should be driven by first-principle based analyses in future studies. It was shown in this work that one of the currently most wide-spread low-order models, the so-called convective velocity model, relies at its core on an ad hoc hypothesis that does not faithfully respect causality. While this may be acceptable for preliminary and academic studies on the global thermoacoustic behavior of a system, it prevents detailed analyses of acoustic-flame interactions. Particularly the flame-flow feedback driven high gains of the flame transfer function found for Slit flames provide strong hints that a more rigorous analysis would also be of high technical relevance. Furthermore, knowing that the flame is the main source of non-linearity in thermoacoustic systems, improved flame models would allow to compute amplitudes of non-linear self-sustained oscillations and thereby would enable more detailed stability predictions of combustors. The theoretical fundamentals required to this end have already been laid in other fields of research. A first step was conducted in this work to bring this knowledge into the field of thermoacoustics.

Appendices

A Numerical Response Analysis

Throughout this work numerical data is used for validation purposes or to provide guidance on identification of the essential underlying physical mechanisms regarding acoustics-flame interactions. This high-fidelity data is computed using numerical simulations employing a 2-step chemical reaction scheme combined with means of system identification. In order to efficiently extract information from this numerical simulations, various forcing signals and post-processing methods are applied. Details on all of these points are provided in the following.

First of all, Sec. A.1 introduces the setups of the analyzed flame configurations. Then, Sec. A.2 outlines the applied CFD/SI method using illustrative and representative examples. An excursion on the various different ways of representing and analyzing the linear flame response, with special focus on causality, will be provided in Sec. A.3. Finally, it is described in Sec. A.4 how flame front displacements are computed from CFD field data, which is specifically important for post-processing simulations of impulsively perturbed flames.

A.1 Test Case Setups

In this thesis, premixed laminar premixed flames, as sketched in Fig. 2.1, are investigated. In order to reduce complexity, only lean methane-air flames of an equivalence ratio of $\phi = 0.8$ are considered, which all have Lewis numbers of approximately unity and an expansion ratio of $e \approx 6.7$. All assessed flame configurations are anchored by a separation induced low-speed region. Considering confined flames, all setups can — based on their cross-sectional view — be idealized as backward-facing step combustors, see Fig. A.1. A length R_i defines the half-width of the inlet or feed duct and a length R_a the half-width of the combustion chamber. For axisymmetric (conical) configurations, these two lengths define the respective radii. For Wedge configurations, additionally, a central rod of radius R_r is added. A stream of fresh premixed reactants enters the domain at a bulk flow velocity \bar{u}_1 , temperature $T_{in} = 300$ K, ambient pressure and equivalence ratio ϕ .

Depending on the temperature boundary as well as the initial condition, either a Wedge or a Bunsen flame establishes. In order to reduce complexity, all walls are assumed to be adiabatic. There are two exceptions: (1) the walls of the feed duct, which are set to a temperature of $T_F = 300$ K in order to avoid a flushing back of the

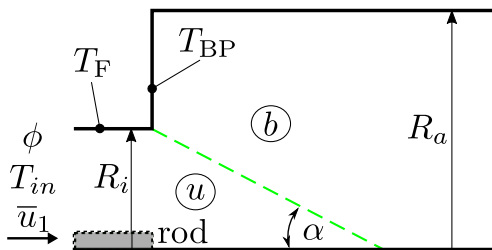


Figure A.1: Cross-sectional view of the considered idealized combustor geometry.

flame and (2) the back-plate of the combustion chamber (rod face plate for wedge flames), which is set to a temperature T_{BP} that allows to established different anchoring conditions. Details on the numerical setup as well as the identification process are specified in the following.

A.2 CFD/SI Method

CFD simulations of laminar flames of different configurations are performed and their respective linear response behavior in terms of their FTF is identified. So-called finite impulse response (FIR) models are trained from broad band input/output CFD data, which are shown to capture the dynamics very well. The applied procedure combines means of system identification (SI) with CFD simulation and is thus known in the literature as the CFD/SI approach, see e. g. Polifke [221]. It will be explained in the following.

Sec. A.2.1 introduces the numerical setup and settings used for all CFD simulations. Details on the identification process relying on transient numerical data can be found in Sec. A.2.2. Finally, Sec. A.2.3 provides an overview on methods that allow to assess the goodness of the identified models. Representative example cases are used in order to illustrate the outlined proceeding.

A.2.1 Incompressible Numerical Simulations

Numerical simulations employing well established means of computational fluid dynamics (CFD) of all flame configurations, are performed. In each case, a perfectly premixed laminar methane-air flame of fixed equivalence ratio is stabilized at a sudden expansion of a duct, which connects the feed duct to the combustion chamber. All setups are chosen to be as simple as possible, in order to serve as a clean reference. Further, the mechanisms governing the flame response to acoustic perturbations should be similar for all cases, i. e. negligible interaction with vortical structures shed

from the burner mouth for the Wedge configuration [1, 104, 201]. Here, this shedding process is suppressed by adding a straight lateral wall constraining the flame, see Fig. 6.1b.

All setups can be considered to be acoustically compact up to the respective cut-off frequency of the FTF. Since such flames hardly respond to acoustic pressure fluctuations, their acoustic response can numerically be evaluated by imposing (upstream) velocity perturbations applying an incompressible (low-Mach number) method, see e. g. [222]. In doing so, possible thermoacoustic instabilities are avoided and boundary conditions are simplified. The open source software OpenFOAM [223] is employed. Chemical reactions are respected by adopting the reduced chemical kinetic 2-step mechanism (2S-CM2) proposed by Bibrzycki *et al.* [224]. Schmidt numbers for all six considered species are set according to Duchaine *et al.* [146]. This solver setup has been used successfully in previous studies for transient and steady state simulations [1, 2, 172, 225]. A 2D uniform structured rectangular grid with a cell density of 40 cells/mm² and a slight increase of the axial cell width towards the boundaries after the flame region is adopted for all cases.

Steady state solutions for three exemplary setups are shown in Fig. 6.1. The color denotes absolute velocity and the region of maximum heat release is plotted in green. Additionally, the analytically predicted mean flame front (see Sec. 2.2.1) is included (.....). For all setups, the steady state solutions show an accelerating flow with a separating shear layer. Flow velocities of the burned gases are highest for the Wedge and lowest for the Bunsen case. Also, the shear layer is least pronounced for the Wedge case compared to the two other setups.

A.2.2 System Identification

In the following it is explained how a flame response model is fitted to transient CFD input/output data such that it represents the underlying linear dynamics. For this purpose, a black-box approach is chosen. The resulting model is then used to evaluate and analyze the respective impulse and frequency responses of the simulated flames. All means of system identification described below are explicated in much more detail in the books by Ljung [226], Keesman [227] or Tangirala [228].

In a first step, a model structure has to be chosen that adequately represents the system of interest. Hence, the investigated flame system needs to be characterized. In doing so, it can be constituted that the structure and parameters of all considered combustors usually do not vary over time and are, therefore, *time invariant*. Furthermore, since the desired flame model is used in a network model in order to assess linear stability, it has to be inherently *linear*. Conceptually, the input and output of a the flame response is constructed such that its transfer behavior reflects *causality*, i. e. that all outputs only depend on past and present inputs. The idea of a flame transfer function (FTF) representing a flame in an acoustic network model usually as-

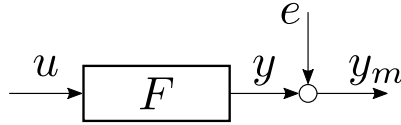


Figure A.2: Assumed model structure of the flame system: An input signal u is mapped to an output y by the system F . The measured output y_m is additionally influenced by white noise e .

sumes *bounded-input bounded-output (BIBO) stability* of the flame element, see e. g. Subramanian *et al.* [229]. Finally, the response of an impulsively perturbed flame is assumed to decay quickly, which is equivalent to the assumption of a high damping rate. For these reasons, a causal and BIBO stable linear time invariant (LTI) model structure is required.

As depicted in Fig. A.2, such systems – in the following denoted as F – are assumed to transform an input signal u to an output signal y . The measured signal y_m that constitutes the available output time series data is then the superposition of the deterministic system output y and an erratic signal e , which is in a first approximation assumed to exhibit white noise characteristics. The ratio of the power of the signals y and e is called the signal-to-noise ratio (SNR) and determines the available information in the output data: A signal $y_{m,1}$ whose SNR is higher than that of a signal $y_{m,2}$ contains more information¹ for a given signal length, which allows for identification of less ambiguous input-output models [230]. It should be mentioned that the detailed characteristics of the erratic signal e (white or colored noise) is not important for the flame setups considered here due to the obtained very high SNR for all conducted simulations, which is a consequence of the prevailing laminar conditions. That means, e can be neglected and, to good approximation, a relation $y_m \approx y$ holds.

All system properties of F described above are met by a so-called finite impulse response (FIR) model. It is discrete in time and relates the in- and output signals by convolution of the input u with an impulse response h

$$\begin{aligned} y[n] &= h_0 u[n] + h_1 u[n-1] + \dots + h_N u[n-N] \\ &= \sum_{i=0}^N h_i u[n-i]. \end{aligned} \quad (\text{A.1})$$

Here, $y[n]$ denotes the input signal at a time step $n \in \mathbb{N}$ and h_i the i -th impulse response coefficient. Such a model consists of $N+1$ finite valued coefficients h_i and is, consequently, inherently BIBO stable since $\sum_{k=0}^{\infty} |h_k| < \infty$ holds [231]. Causality is reflected by the fact that $h_i \equiv 0, \forall i < 0$, which explains why the sum in Eq. (A.1) only starts at $i = 0$. FIR models are a subset of LTI models, since their output is computed by the convolution of an impulse response with an input signal, which is a linear operation. The frequency response associated with a given FIR model is computed from

¹White noise, as one limiting case, does not contain any information

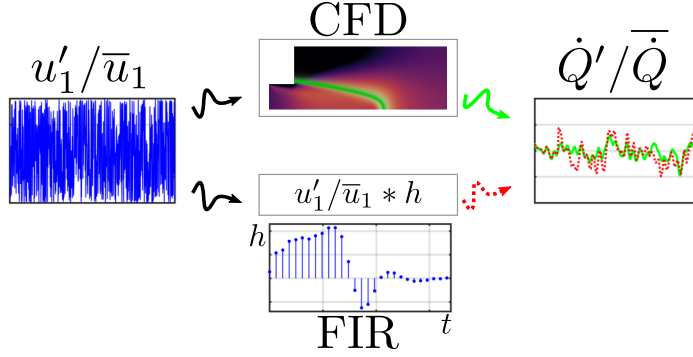


Figure A.3: Illustration of the CFD/SI approach applied to identify a FIR model using broad band input/output CFD data. The “*”-operator denotes temporal convolution.

the z -transform of the impulse response

$$F(\omega) = \sum_{i=0}^N h_i \exp(-i\omega i\Delta t) \quad (\text{A.2})$$

with the imaginary unit i (not to confuse with the summation index i), the sampling time of the FIR coefficients Δt and the real valued angular frequency ω .

One known general disadvantage of FIR models is the high number of coefficients, which have to be identified, particularly for weakly damped systems having a pole close to the unit circle [232]. However, as stated above, all flames show sufficient damping such that the available time series data allows for good estimates of all required FIR coefficients. FIR models are fairly robust against noise e , more specifically, Gaussian white noise of zero mean [232]. For systems with a rather low SNR that are exposed to non Gaussian white noise or for systems that are less damped, other model structures, such as ARX or Box-Jenkins type models, have to be applied, see for example [233, 234]. All in all, FIR models fulfill all demanded requirements of an appropriate model structure and are, thus, an appropriate choice for the type of systems encountered in this thesis.

Determining the FIR coefficients h_i based on available data is referred to as the actual process of system identification. The associated process is illustrated in Fig. A.3: In a first step, transient CFD simulations are performed, where the inlet velocity is excited around its mean, i. e. $u_1(t) = \bar{u}_1 + u'_1(t)$. The amplitude of these fluctuations is set to 2–5% of the mean velocity in order to not trigger non-linear effects but, at the same time, to achieve an adequate SNR. The input signal u (—) used for identification is the normalized velocity fluctuation at the domain inlet $u'_1(t)/\bar{u}_1$ and the output signal y_m the normalized heat release rate fluctuation \dot{Q}'/\bar{Q} integrated over the whole domain (—). Feeding the FIR model with the same input data as the CFD simulation results in a model output \tilde{y} (••••) according to Eq. (A.1). Now, those values of the FIR coefficients h_i are searched, which minimize the quadratic

error between the CFD output time series y_m (—) and the model output \tilde{y} (⋯), formally written as

$$\hat{\theta} = \arg \min_{\theta} \frac{1}{M} \sum_{j=1}^M (y_m[j] - \tilde{y}[j|\theta])^2, \quad (\text{A.3})$$

where $\hat{\theta} = h_i$ denotes the solution vector containing all FIR coefficients. Hence, computation of the optimal parameters $\hat{\theta}$ requires the solution of a linear least squares problem and, therefore, it has to be ensured that the number of sampling instants M is significantly higher than the number of FIR coefficients $N + 1$. For such linear models, the predicted model output can be written in terms of a multiplication of an input matrix Φ and the solution vector $\tilde{y} = \Phi \hat{\theta}$. Using this definition, the linear least squares problem formulated above leads to a set of linear equations whose solution is the desired optimal parameter vector $\hat{\theta}$:

$$\Phi^T \Phi \hat{\theta} = \Phi^T y_m. \quad (\text{A.4})$$

Essentially, four free parameters exist that determine the quality of the resulting fit: (1) The type of input signal u , (2) the length of the input/output time series, (3) the number of FIR coefficients $N + 1$ and (4) the sampling interval of the IR Δt . These points are discussed one after another in the following.

In order to ensure identifiability, the system input needs to excite all frequencies of interest. Otherwise, the information available in the input/output data is not sufficient for identifying a response model. For example, if the input time series data resembles a sine of only one distinct frequency, no information about the response to other frequencies is available in the input/output data set [230]. In order to obtain information on as many frequencies as possible at reasonable computational costs, it has been shown to be advantageous to use a broad band input signal that excites several frequencies at once [221, 235, 236]. The lower bound of the frequency content of such a signal is limited by the length of the signal and the upper bound by the sampling time (Nyquist frequency). Practically, the upper bound has to be set well beyond the expected cut-off frequency of the FTF. Decreasing the lower bound is expensive, since longer time series data requires longer simulations. One way of improving the low-frequency accuracy at $\omega \rightarrow 0$ is to use a step input signal: The new steady state that develops after the input velocity has been rapidly increased (step forcing) defines the zero frequency response at very high accuracy (neglecting noise). In the case of perfectly premixed flames its value is unity [157]. All models shown in this thesis are identified by use of a broad band input signal as proposed by Föllner and Polifke [235] and correctly capture this low frequency behavior.

Determining the optimal number of FIR coefficients $N + 1$ and sampling time Δt for a given setup, is an iterative and rather intuitive process. The goal is to use as few coefficients as possible by, at the same time, retaining a good representation of the system behavior. This avoids overfitting and reduces the required time series

length, since only a minimal number of parameters need to be estimated. A heuristic approach to finding these two parameters starts with a small number of coefficients and a sampling time that is related to a characteristic time of the flame, which could be the time of restoration τ_r . A reasonable initial guess would be to use $N + 1 = 15$ coefficients that are separated by a sampling time of $\Delta t = 2\tau_r/N$, since the expected IR is known to have a length of the order of τ_r . For this specific choice of parameters, the goodness of the resulting fit has to be evaluated and based on that, N and Δt have to be adjusted. This has to be repeated until a satisfactory model is retained. Although, in principle, it might be possible to develop an algorithm that manages this iterative process, two points should be kept in mind: (1) Similar flames require similar parameters and (2) finding an adequate model is a rather fast process since estimation of the fit parameters is computationally relatively cheap and only two free parameters are available. Hence, due to efficiency, the author decided to rather rely on his intuition than to develop an algorithm.

Efficiently adjusting the two FIR parameters requires some basic understanding of the physics as well as the identification process. Tools that allow to judge the goodness of a specific fit are discussed in the following.

A.2.3 Goodness of the Identified Model

While – as shown above – the process of determining the optimal set of FIR parameters N and Δt is a rather intuitive and iterative process, assessment of the goodness of the results follows well-defined processes. Several established methods exist, which are introduced in the following. Representative examples from the flame response data presented in this chapter are provided for the sake of illustration.

Generally, a good fit captures all of the deterministic part of y_m that depends (here: linearly) on the input u and filters out the noise e . Given a specific data set, it shall provide the corresponding parameter vector $\hat{\theta}$ that represents most likely the real system behavior. At the same time, overfitting the given data set, i. e. capturing features by the deterministic model that rely on probabilistic processes, shall be avoided¹. In this thesis, three points are checked:

1. Check of plausibility
2. Quantification of the uncertainties of the parameter vector $\hat{\theta}$
3. Quantification of how well the deterministic linear process is captured by the fitted model
4. Demonstration that the model does not suffer from overfitting

¹In a low-noise environment overfitting is not a severe problem, nevertheless, it should be kept in mind.

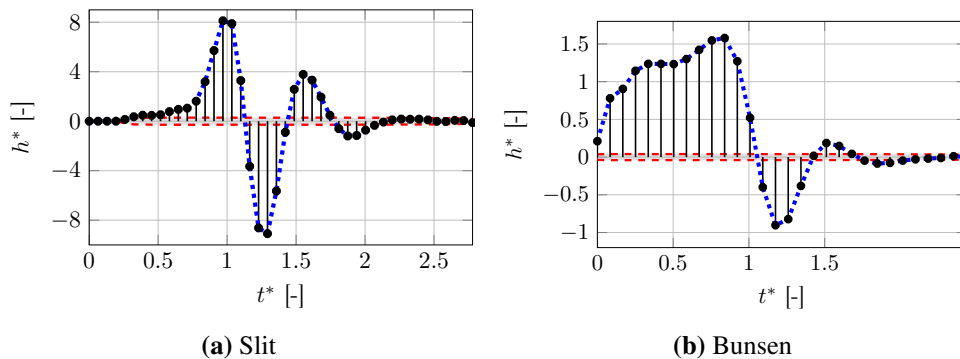


Figure A.4: Visualization of two representative FIR models, one for a Slit flame A.4a and one for a Bunsen flame A.4b configuration ($\phi = 0.8$, $\text{Re} = 650$, $T_{\text{BP}} = 700$, see Fig. 6.1). Shown are the identified FIR coefficient (\bullet) that are connected by lines (\cdots) and the associated 3σ confidence intervals (gray area, framed by $-\cdots-$).

All of them are discussed in the following.

Plausibility

First of all, prior knowledge of the expected response model should be exploited. That is, the resulting transfer function can, e. g., be compared to available low-order models in terms of cut-off frequency, low frequency limit (should be unity), excess of gain or phase decay. Furthermore, characteristics of the IR, such as the time delay or the overall shape (decay to zero, rather smooth), can be checked.

Fig. A.4 shows the FIR coefficients resulting from identification of a Slit and a Bunsen flame configuration. Both are smooth functions of time t^* and their characteristics compare well to reduced order model predictions (see Chap. 6). Evaluation of the associated frequency response would result in a low-frequency limit of unity (not shown) and the IR decays to zero after a time that is of the order of τ_r . Hence, the result shown can be considered to plausibly represent the system dynamics.

Uncertainty Quantification

Confidence intervals of the parameter vector $\hat{\theta}$ can be constructed that allow to quantify the uncertainties of the fit with respect to the length and the SNR of the underlying time series data. The shorter the available time series and the higher the SNR, the less information is contained in a given data set, which will result in a more uncertain identification of the parameter vector $\hat{\theta}$. While experimental data suffers essentially from rather low SNRs, the critical issue for CFD is the length of the available time

series data, since transient CFD simulations usually require a significant amount of computational resources. For all performed simulations of laminar flames, the SNR is very high and time series of a length of about $10\tau_r$ have been proven to be sufficient.

In order to quantify uncertainties resulting from noisy finite length time series data, the covariance matrix of the identified model parameters is employed:

$$\text{Cov}(\hat{\theta}) = \begin{bmatrix} \sigma_{00}^2 & \sigma_{01}^2 & \cdots & \sigma_{0N}^2 \\ \sigma_{10}^2 & \sigma_{11}^2 & & \vdots \\ \vdots & & \ddots & \\ \sigma_{N0}^2 & \cdots & & \sigma_{NN}^2 \end{bmatrix} \quad (\text{A.5})$$

where $\sigma_{ij}^2 = E[(\hat{\theta}_i - \theta_i)(\hat{\theta}_j - \theta_j)]$ denotes the covariance of two parameters $\hat{\theta}_i$ and $\hat{\theta}_j$ with the estimated parameter vector $\hat{\theta}$ and the expected (or ‘‘true’’) value of that parameter vector θ . Bias errors (i. e. $\lim_{M \rightarrow \infty} E[\hat{\theta}] \neq \theta$) shall be excluded here. The diagonal elements of the matrix contain the variances of each parameter and the off-diagonal elements the covariances of each pair of parameters. Assuming the covariance matrix is known and the estimated parameters follow a normal distribution, confidence intervals can be constructed:

$$E[\hat{\theta}_i] \in [\hat{\theta}_i - 3\sigma_{ii}, \hat{\theta}_i + 3\sigma_{ii}] \quad (\text{with } 99.73\% \text{ confidence}). \quad (\text{A.6})$$

Here a 3σ confidence interval is assumed, which states that, based on the provided data, there is only a 0.27% chance that $\hat{\theta}_i$ is outside of that interval.

Usually, the covariance matrix is a priori unknown and, hence, needs to be estimated from the data provided, as well. It can be shown that it is given by

$$\hat{\text{Cov}}(\hat{\theta}) = \hat{\lambda}_0 [\Phi^T \Phi]^{-1} \quad (\text{A.7})$$

where $\hat{\lambda}_0$ denotes the (estimated) variance of the residuals $\epsilon = y_m - \hat{y}[j|\hat{\theta}]$ and $\Phi^T \Phi$ the matrix of the linear regressor defined in Eq. (A.4) [237]. The former needs to be estimated from the data by

$$\hat{\lambda}_0 = \frac{1}{M - (N + 1)} \sum_{j=1}^M (y_m[j] - \hat{y}[j|\hat{\theta}])^2. \quad (\text{A.8})$$

Knowing that the SNR of a signal is computed by the quotient of the variance of the signal over the variance of the noise, it now becomes clear that the confidence intervals scale with the SNR.

Fig. A.4 depicts the 3σ confidence intervals resulting from identification of the shown FIR coefficients. They are very small in both cases and, thus, the shown coefficients $\hat{\theta}_i = h_i$ very likely represent the actual underlying dynamics of the system. All other setups discussed in this thesis exhibit similarly small confidence intervals. Therefore, visualizations of confidence intervals are omitted for all IR and FR plots. In order to further clarify the presentation by leaving out unnecessary information, throughout the thesis, impulse responses are shown as line plots (\cdots) and leave out a visualization of the FIR coefficients (\bullet).

Residual Analysis

A set of very useful tests on how well the resulting model is able to capture the deterministic part in the output signal y_m considers the residuals $\epsilon = y_m - \Phi\hat{\theta}$, i. e. the differences between model predictions $\hat{y} = \Phi\hat{\theta}$ and the actually measured output time series data y_m . Assuming that the model structure shown in Fig. A.2 describes reality and the length of the available time series data approaches infinity, the respectively estimated model parameters would asymptotically converge to those of the “real system” — assuming zero bias and a sufficient number of FIR coefficients. The model obtained would then filter out all of the deterministic content y from the measured signal y_m and, thus, the resulting residual time series data would be perfectly erratic. Based on this fact, it is possible to assess the quality of an estimated model and how reasonable the chosen model structure is. The ability of a model to capture the deterministic part of the input/output relation can be evaluated by statistically analyzing the resulting residual time series data ϵ : the more erratic and less correlated to the input signal it is, the better the estimated model performs. Consequently, the model requiring the smallest number of parameters while fulfilling the aforementioned two criteria should be chosen. This avoids overfitting, i. e. capturing erratic contents of the output signal by the deterministic model, and ensures that the underlying system dynamics is properly grasped.

Two correlations need to be evaluated: (1) The (sample) cross-correlation of the residuals with the input signal

$$\hat{\gamma}_{ue}[n] = \frac{\sum_{i=1}^M \epsilon[i]u[i+n]}{\sqrt{\sum_{i=1}^M \epsilon[i]\epsilon[i]} \sqrt{\sum_{i=1}^M u[i]u[i]}} \quad (\text{A.9})$$

and (2) the (sample) auto-correlation of the residuals

$$\hat{\gamma}_{ee}[n] = \frac{\sum_{i=1}^M \epsilon[i]\epsilon[i+n]}{\sum_{i=1}^M \epsilon[i]\epsilon[i]} \quad (\text{A.10})$$

where the lag $\tau = n\Delta t$ is an integer multiple of the sampling time Δt . Both are again estimates of the “true” correlations based on the provided data, assuming zero mean of ϵ and u .

The auto-correlation of ϵ is defined as the covariance of the time series ϵ with an instance of itself shifted by a lag τ and normalized by its variance. Plotting $\hat{\gamma}_{ee}(\tau)$ over the time lag τ provides an estimates of inherent correlations of the residuals ϵ . Assuming ϵ was purely erratic (white noise), this plot would be zero everywhere but for lag zero, where it is unity. Of course, since $\hat{\gamma}_{ee}(\tau)$ is only an estimate of the residual auto-correlation, its values at different lags are uncertain. In order to test a

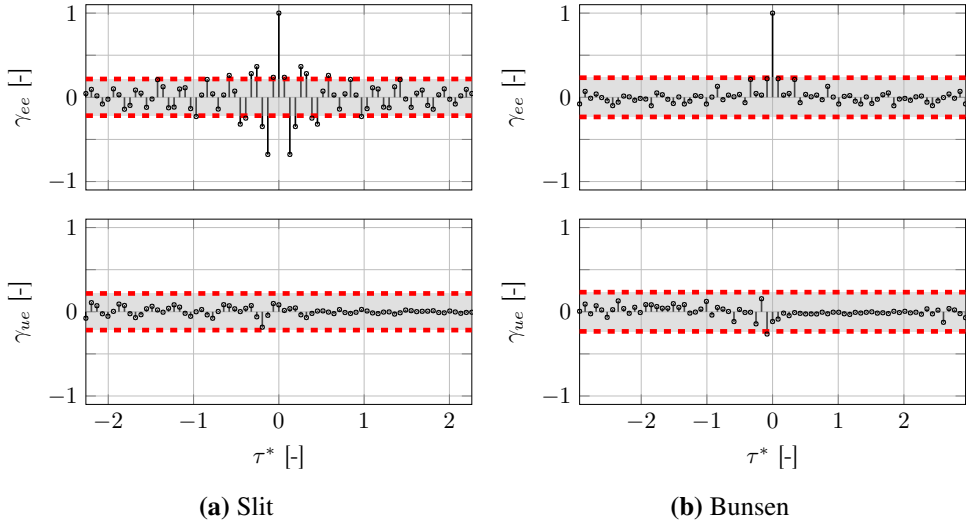


Figure A.5: Auto- and cross-correlation data of residuals $\hat{\gamma}_{ee}$ and $\hat{\gamma}_{ue}$, respectively, resulting from the identified models shown in Fig. A.4, plotted over a non-dimensionalized lag $\tau^* = \tau/\tau_r$. 3σ confidence regions are added (gray area, framed by - - -).

signal for whiteness, intervals can be provided within which $\hat{\gamma}_{ee}$ is not significant, i. e. although it might be different from zero it can to good degree be assumed to be zero. For sufficiently high M , this interval can be computed as $\pm 3/\sqrt{M}$, which corresponds to a 99.73% region of confidence.

Similarly, the cross-correlation is defined as the covariance of u and ϵ at different lags τ normalized by the standard deviations of u and ϵ at zero lag. Hence, any value of $|\hat{\gamma}_{ee}| > 3/\sqrt{M}$ would suggest a linear relation of u and ϵ at the corresponding lag τ (with a confidence of 99.73%).

Fig. A.5 shows the auto- and cross-correlations of the residuals that correspond to the identified models depicted in Fig. A.4 plotted over a non-dimensionalized lag $\tau^* = \tau/\tau_r$. All cross-correlation coefficients are within the above defined region of confidence and, hence, are not significant. Therefore, no significant hint of linear deterministic input/output relations not captured by the models can be found in the data. It can be concluded, that (1) the assumed structure of the system (see Fig. A.2) captures the real behavior very well and that (2) the identified FIR model represents the transfer behavior to a very good degree.

A similar conclusion can be drawn from the auto-correlations. However, the plot of the Slit flames shows some significant coefficients at lags $|\tau^*| < 1$. Since the cross-correlation shows no hint of input/output relations not captured by the model, they have to be a consequence of the chosen model structure. The damped oscillatory behavior of the Slit flame IR shown in Fig. A.4a requiring 44 FIR coefficients indicates

an autoregressive behavior of the system, i. e. the present output of the system does not only depend on past and present inputs but also on past outputs. Using a system structure that allows for such autoregressive interactions, such as an ARX model, could reduce the required number of model parameters. At the same time, also the erratic part e would be subjected to the autoregressive system behavior and, hence, its contribution to y_m would be colored instead of white. It has been shown by Sowards [238] (Sec. 4.2.5) that for such situations, application of an ARX model would indeed lead to a reduction of the residual auto-correlation. It was checked by the author of this thesis that this also holds for the Slit flame case discussed here. However, although the auto-correlation of e exhibits strong hints that the underlying signal is not white, its relevance for the time series data is very minor due to the fact that the amplitude of e is several orders of magnitude smaller than that of y_m . This will be illustrated in the following section where the model output is compared with the CFD data output using a test data set. For that reason, it can be concluded that the chosen FIR model performs very well for both types of flames.

Comparison with Test Data Set

It is a common practice in regression analysis to split the available time series data into a training and a test data set. The first is used in order to identify the model parameters $\hat{\theta}$, the second to evaluate the predictive quality of the model on a statistically independent data set. Usually the distance between the model predictions (.....; Fig. A.3) and the CFD output (—; Fig. A.3) is measured in terms of a norm, also known as the fit value:

$$\text{FIT} = 100 \left[1 - \frac{\sqrt{\sum_{i=1}^M (y_m[i] - \tilde{y}[i])^2}}{\sqrt{\sum_{i=1}^M (y_m[i] - y_{m,\text{mean}})^2}} \right] \% \quad (\text{A.11})$$

where \tilde{y} denotes the model output, y_m the CFD time series and $y_{m,\text{mean}}$ its mean value [239, 240].

Computing the model output for a test data set of the two identified models shown in Fig. A.4 (---) results in the time series shown in Fig. A.6. Very good agreement with the CFD data output y_m (—) is found and results in fit values of 93.87% and 95.8% for the slit and the Bunsen type configuration, respectively. Since the test data set is independent from the trainings data set, it can be concluded that both models are not overfitted to the trainings data.

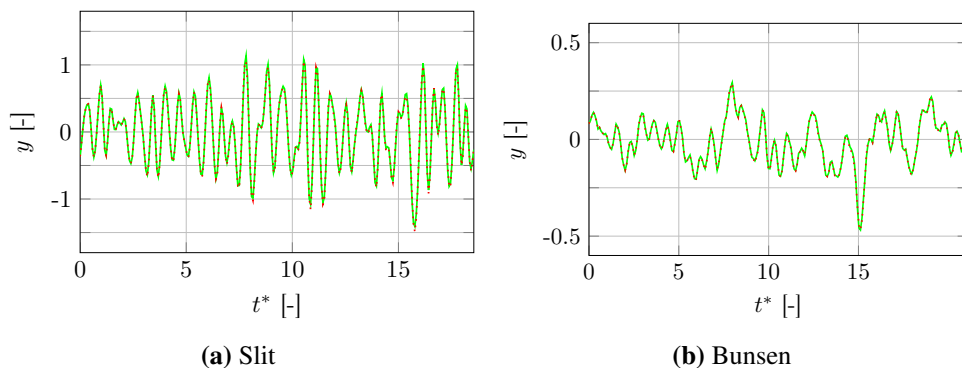


Figure A.6: Model (.....) and CFD (—) output time series for the identified models shown in Fig. A.4 for a test data set, plotted over non-dimensionalized time $t^* = \tau/\tau_r$. Fit values are 93.87% and 95.8% for the slit and the Bunsen type configuration, respectively.

A.3 Time vs. Frequency Domain Based Response Analysis

Besides CFD/SI methods relying on broad band data, there are also other methods to estimate the IR of a flame configuration. A simple direct approach relies on an impulsively excited flame using an input signal u resembling a Dirac impulse. For example, a Gaussian impulse of small variance and sufficiently low amplitude (to not trigger non-linear effects) can be used as input signal. The normalized associated response of the global heat release then provides an estimate of the IR. Such a procedure has one significant advantage: It allows for a direct and rather simple analysis of the transient CFD field data and, thus, the physical processes that determine the system behavior. Without use of further computationally expensive statistical evaluations, such a post-processing of the data is not possible for broad band excitation.

The reason behind this property is that an impulsive forcing constitutes the optimal input signal for analyzing causalities. Analyzing transient CFD data subjected to harmonic forcing, for example, might lead to identification of coherent (flow) structures that have a strong impact on the respective flame response. However, it is not easy to reveal causal relations, since in a fully established oscillatory state, as it is inherently assumed in frequency domain representations, one cannot distinguish between cause and effect. This can be improved by using broad band forcing, however, as stated above, elaborate and computational expensive computations are required in order to reveal spatially resolved causal relations. Application of an impulsive forcing allows to identify causalities by just naively inspecting the transient CFD field data: any change in a certain snapshot has to be directly related to information present in the preceding snapshots.

This advantage is paid for by, compared to broad band based methods, less robust response predictions that are caused by the reduced amount of data and, hence, in-

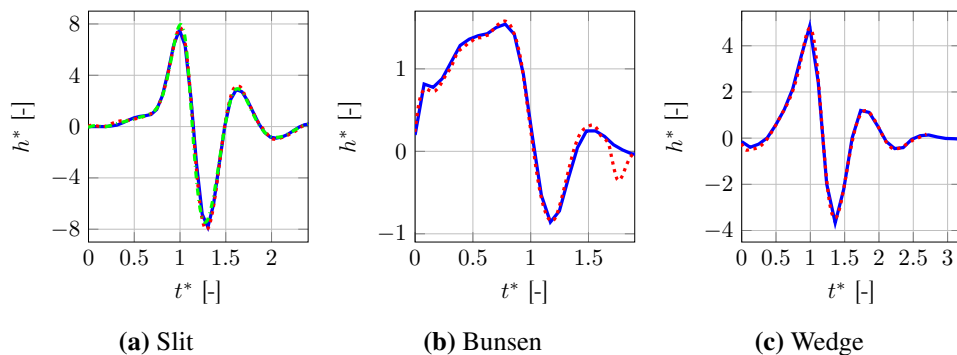


Figure A.7: Comparison of IR predictions resulting from impulsive forcing (---) as well as from the CFD/SI approach (—) for three representative setups (one for each flame geometry). All simulations were performed at a maximum perturbation velocity amplitude of $2\% \bar{u}_1$. For the slit case additionally a simulation at 10% amplitude was performed (---).

formation: the total length of usable time series data equals exactly one times the IR length. Furthermore, confidence intervals as well as quality measures quantifying the resulting model (residual analysis) cannot be specified without further considerations. Hence, in order to get both good estimates of the (linear) response behavior *and* the possibility to analyze physical causalities, one has to jointly analyze broad band and impulsively forced systems. It should be noted that the evaluation of the latter is usually only informative for systems exhibiting very low noise levels, such as laminar flames. Processing LES simulations of turbulent flames, the turbulent fluctuations will contaminate the output time series data of a step or impulse forcing and cannot be correlated out (using a single simulation).

Applying such a joint analysis, it has to be ensured that the impulsively forced systems exhibits the same linear response as the model identified from broad band data. If that is the case, non-linearities or noise related effects most probably can be ruled out to contaminate the CFD data. Fig. A.7 compares IR predictions resulting from an impulsive forcing (---) to the ones from the CFD/SI approach (—) for three representative setups. All setups were forced by a narrow Gaussian impulse with an amplitude of 2% of the bulk flow velocity \bar{u}_1 , see Appendix A.4 for more details. For the Slit setup additionally a forcing with 10% forcing amplitude is shown (---), which still exhibits the same transfer behavior as the two other cases.

Overall, very good agreement can be found for all three configurations. Only the Bunsen case in Fig. A.7b shows a minor discrepancy at $t^* \approx 1.3$ but also here the overall IR is captured very well. This result allows to safely analyze impulsively forced CFD data and draw conclusion regarding the physics that governs the linear response. This fact is exploited in Parts II and III by analyzing the transient behavior of flame normal displacements.

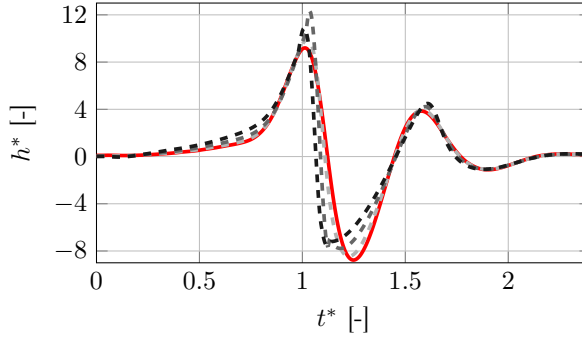


Figure A.8: IR predictions resulting from impulsive forcing of a Slit flame shown for four amplitudes: 10% (—), 20% (---), 40% (· · ·) and 60% (- · - ·) with respect to \bar{u}_1 .

Fig. A.8 analyses the amplitude dependence of a Slit flame in more detail. It shows that the linear behavior is to a good degree preserved up to amplitudes of 20%. Only at 40% amplitude non-linear effects significantly kick in and effect the response. As shown in Chap. 6, Slit flames exhibited the strongest response of all three investigated flames. Therefore, it can be expected that Bunsen and Wedge flames should stay in the linear regime for even higher forcing amplitudes.

A.4 Computation of Flame Normal Displacements

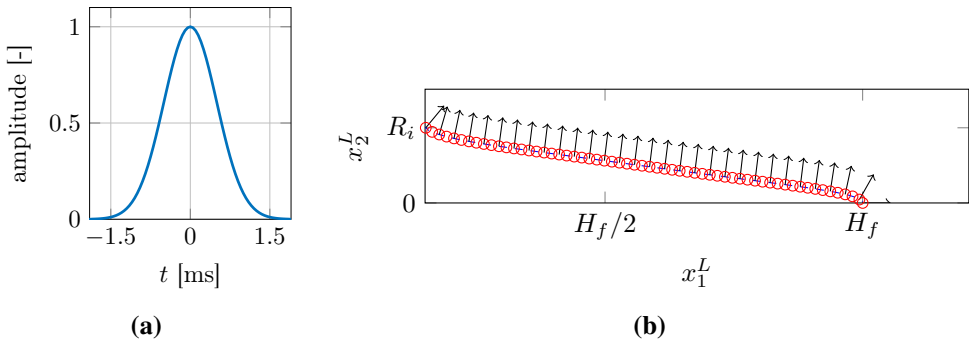


Figure A.9: (a): Signal of normalized amplitude used for impulsive forcings conducted in this thesis. (b): Flame shape computed from an CH_4 -isoline of a CFD data snapshot including its normals.

The transient behavior of flame normal displacements of impulsively excited flames is discussed in several sections of this thesis, see for example Fig. 5.1 (middle). Details on the computation and post-processing of these results are provided in the following. Background information on the motivation for such a kind of analysis is

provided in Sec. A.3.

The forcing signal employed for all impulsively forced simulations is illustrated in Fig. A.9a. It exhibits a normalized amplitude, which has yet to be scaled by the level of forcing, e. g. by $\epsilon = 2\%\bar{u}_1$. Its shape is described by

$$f(t) = \exp\left(-\frac{(t-t_0)^2}{\sigma}\right), \quad (\text{A.12})$$

where t_0 denotes the time at which the impulse forcing has to be applied and $\sigma = 5e-7$ the width of the Gaussian-like distribution. The temporal integral defines a reference displacement $\hat{\xi} = \int_0^\infty \epsilon f(t) dt$.

Having performed the impulsively forced transient numerical simulations, snapshots at several instants in time are taken and CH_4 -isolines extracted. The respective CH_4 values are chosen such that the resulting isoline adequately captures the spatial distribution of the heat release. The first snapshot corresponds to a time before the forcing is applied ($t < t_0$) and is defined to represent the unperturbed steady state solution. For this snapshot, flame normals are evaluated. An exemplary result is sketched in Fig. A.9b. Having done this, flame normal deviations from the steady state are evaluated for all subsequent snapshots. Finally, the resulting flame normal displacements from the steady state flame are normalized by the aforementioned reference displacement $\hat{\xi}$ in order to ensure comparability with other simulations or with LOM predictions.

B Impact of the Anchoring Wall Temperature

Some of the shown CFD/SI results shown in this work were conducted at different temperatures of the wall above which the flame is anchored, denoted as T_{BP} . The literature provides evidence that this temperature has a crucial impact on the associated acoustic flame response [121, 148, 149, 241, 242]. Therefore, its consequences for the FTF of the investigated flame configurations are assessed in the following. In order to specify wall temperatures, a non-dimensional quantity $T_{BP}^* = T_{BP}/T_{ad}$ is introduced relating the temperature of a wall T_{BP} to the adiabatic flame temperature T_{ad} . Adiabatic walls hence have a non-dimensional temperature of unity.

Figs. B.1 and B.2 show steady state and acoustic response data of three Slit and Bunsen flames, respectively, anchored above a back-plate exhibiting different temperature boundary conditions: (1) adiabatic walls, (2) $T_{BP} = 700$ K and (3) $T_{BP} = 373$ K. These boundaries were chosen as limiting cases of the range of possible (uncooled) wall temperatures. The study of Kornilov *et al.* [209] specified the prevailing wall temperature of a Slit flame setup to 373 – 423 K. This serves as an estimate of the lower threshold of possible temperatures and, hence, $T_{BP} = 373$ K defines a first sampling point. According to Mejia *et al.* [149], the temperature of their cylindrical bluff body could reach temperatures up to 700 K. Since around temperatures of 750 – 800 K the backplate would start to radiate light in the visible wavelengths (“incandescence”), which is not reported from experimental studies, a temperature of $T_{BP} = 700$ K was chosen to define the upper limit of temperatures of interest. The adiabatic case was added primarily because of academic interests. Such configurations define the limiting cases where the flame is anchored directly at the trailing edge.

All shown frequency and impulse response data are non-dimensionalized by use of the characteristic time of restoration τ_r . It is determined here by demanding that all IRs have to coincide at $t^* = 1$. This exploits the fact that all IRs are qualitatively very similar and that the main difference can be related to a scaling of the frequency and time scales of the FR and IR representations, respectively. In order to effectively visualize the behavior of the characteristic time of restoration, relative changes of the time of restoration

$$\Delta\tau_r^* = \frac{\tau_r - \tau_{r,ref}}{\tau_{r,ref}} \quad (\text{B.1})$$

are plotted in Figs. B.1 and B.2. Hereby, the characteristic time of the configurations exhibiting the minimal τ_r serves as the reference time $\tau_{r,ref}$.

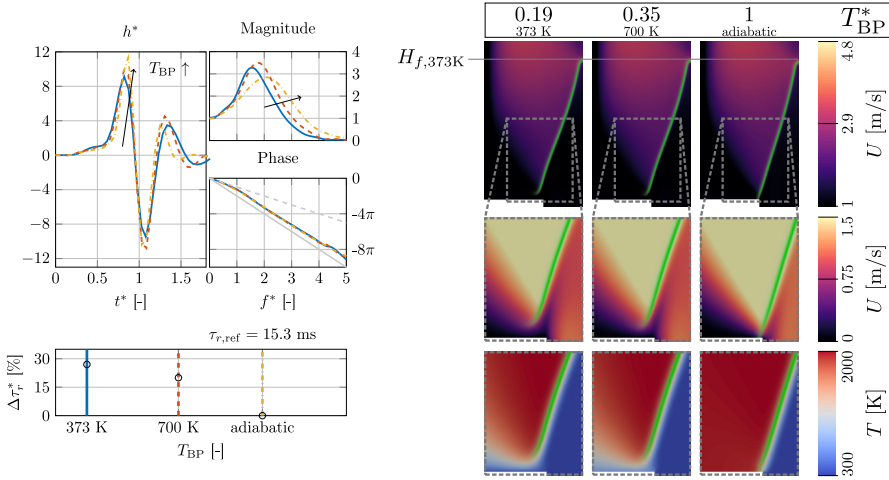


Figure B.1: Effect of temperature of the back-plate T_{BP} on on the FTF (left) and the mean flow field (right) for Slit flame configurations at $Re = 650$, $\phi = 0.8$ and $C_r = 0.4$. Close-up views of the steady state flame anchoring are provided for each setup (middle and lower row, right half).

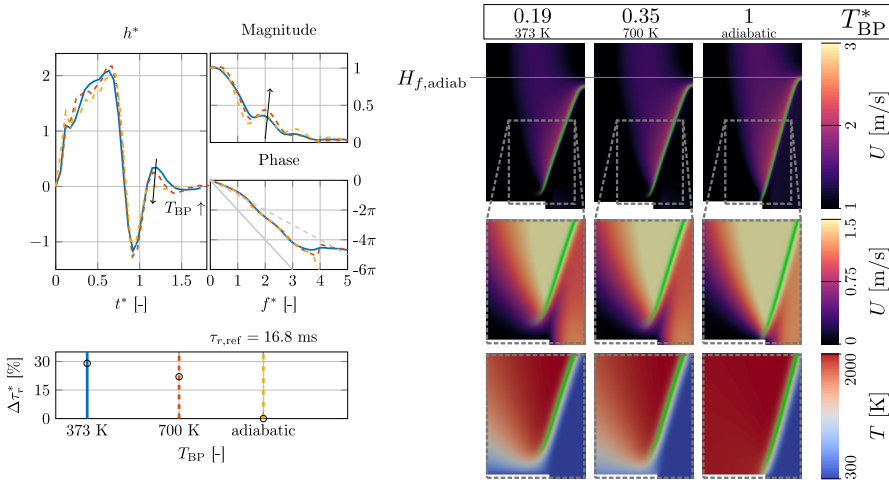


Figure B.2: Effect of temperature of the back-plate T_{BP} on on the FTF (left) and the mean flow field (right) for Bunsen flame configurations at $Re = 650$, $\phi = 0.8$ and $C_r = 0.4$. Close-up views of the steady state flame anchoring are provided for each setup (middle and lower row, right half).

From the data shown it becomes clear that variations of the wall temperature mainly lead to variations of τ_r , while the qualitative behavior of the IR/FR representations are essentially maintained. This directly translates to a significant change of the FTF phase of the three setups, when plotted over dimensional frequency. It is hence concluded that variations of the wall temperature right at the flame anchoring predomi-

nantly lead to significant changes in the phase of the corresponding FTF and only to rather weak changes of the gain. While all analyzed data provides evidence that τ_r increases with rising T_{BP} , the gain does not behave as regularly and can show both higher and lower amplitudes. On the detailed mechanisms that are responsible for this behavior can only be speculated. From the data provided, it seems that cooled walls lead to a low speed region upstream of the flame base, which might lead to an increase of τ_r . All in all, comparing FR/IR representations of different T_{BP} in non-dimensionalized form, it can in a first approximation be assumed that their overall shape remain unchanged and predominantly the respective τ_r varies.

C Flame Transfer Functions

In the following, analytical FTF expressions for two different models are provided, which were both introduced in Chap. 6.

C.1 Convective Incompressible FTFs with Gaussian Kernel

By solving Eq. (1.32) (assuming $l_M = 0$) using the velocity perturbations specified by Eqs. (6.19) and (6.20), we get for the flame front displacement of Slit and Bunsen flames

$$\begin{aligned} \xi_\Lambda(x_1^F, t) = \sin(\alpha) \frac{\tau_r}{\tau_r - \tau_c} \left\{ \right. \\ \left(1 + f_g \frac{\tau_c}{\tau_r - \tau_c} \right) \left[G \left(t - \frac{x_1^F}{L_f} \tau_c \right) - G \left(t - \frac{x_1^F}{L_f} \tau_r \right) \right] \\ + f_g \tau_c \left[1 - \frac{x_1^F}{L_f} \right] g \left(t - \frac{x_1^F}{L_f} \tau_c \right) \\ \left. - f_g \tau_c g \left(t - \frac{x_1^F}{L_f} \tau_r \right) \right\}, \end{aligned} \quad (\text{C.1})$$

and for the one for Wedge flames

$$\begin{aligned} \xi_V(x_1^F, t) = \sin(\alpha) \frac{\tau_r}{\tau_r - \tau_c} \left\{ \right. \\ \left(1 - f_g \frac{\tau_c}{\tau_r - \tau_c} \right) \left[G \left(t - \frac{x_1^F}{L_f} \tau_c \right) - G \left(t - \frac{x_1^F}{L_f} \tau_r \right) \right] \\ + f_g \tau_c \left[\frac{\tilde{r}}{1 - \tilde{r}} + \frac{x_1^F}{L_f} \right] g \left(t - \frac{x_1^F}{L_f} \tau_c \right) \\ \left. - f_g \tau_c \frac{\tilde{r}}{1 - \tilde{r}} g \left(t - \frac{x_1^F}{L_f} \tau_r \right) \right\}. \end{aligned} \quad (\text{C.2})$$

Here, $G(y)$ is defined as the antiderivative of $g(y)$: $G(y) = \int g(y) dy$. Similarly, a quantity $\Gamma(y) = \int G(y) dy$ is defined. Tab. C.1 summarizes all those expressions for a Dirac and a Gaussian kernel function. For a Dirac kernel function, the first antiderivative becomes the Heaviside step function $G(y) = \theta(y)$ and the second one the ramp function $\Gamma(y) = y\theta(y)$.

Function	Dirac Kernel	Gaussian Kernel
$g(y)$	$\delta(y)$	$\frac{1}{\sqrt{2\pi\sigma^2}} \exp\left(-\frac{y^2}{2\sigma^2}\right)$
$G(y)$	$\theta(y)$	$\frac{1}{2} \operatorname{erf}\left(\frac{y}{\sqrt{2\sigma^2}}\right)$
$\Gamma(y)$	$y\theta(y)$	$\frac{y}{2} \operatorname{erf}\left(\frac{y}{\sqrt{2\sigma^2}}\right) + \frac{\sigma}{\sqrt{2\pi}} \exp\left(-\frac{y^2}{2\sigma^2}\right)$

Table C.1: Overview of the two Dirac and the Gaussian kernel functions and their antiderivatives.

These displacements are used to evaluate the integral flame surface area fluctuation A' , according to the formulas provided in Sec. 6.2. From that, the impulse response is computed as

$$h(t) = \frac{A'}{A} \bar{u}_1, \quad (\text{C.3})$$

which yields for slit flames

$$h_{\text{slit}} = \frac{1}{\tau_r - \tau_c} \left\{ \left(1 + f_g \frac{\tau_c}{\tau_r - \tau_c} \right) \left[G(t - \tau_c) - G(t - \tau_r) \right] - f_g \tau_c g(t - \tau_r) \right\}. \quad (\text{C.4})$$

For Bunsen flames we retrieve

$$h_{\text{con},\Lambda} = \frac{2}{\tau_r - \tau_c} \left\{ \begin{aligned} & \left(1 + f_g \frac{\tau_c}{\tau_r - \tau_c} \right) \left[\frac{1}{\tau_r} \left[\Gamma(t - \tau_r) - \Gamma(t) \right] \right. \\ & \quad \left. - \frac{1}{\tau_c} \left[\Gamma(t - \tau_c) - \Gamma(t) \right] \right] \\ & + f_g \left[G(t) + \frac{1}{\tau_c} \left[\Gamma(t - \tau_c) - \Gamma(t) \right] \right] \\ & + f_g \frac{\tau_c}{\tau_r} \left[G(t - \tau_r) - G(t) \right] \end{aligned} \right\} \quad (\text{C.5})$$

Name	Time Domain	Frequency Domain
Delayed unit impulse	$\delta(t - \tau)$	$\exp(-\tau i \omega)$
Delayed unit step	$\theta(t - \tau)$	$\frac{1}{i\omega} \exp(-\tau i \omega)$
Delayed ramp	$(t - \tau)\theta(t - \tau)$	$\frac{1}{(i\omega)^2} \exp(-\tau i \omega)$

Table C.2: Fourier transform overview.

and for Wedge flames

$$\begin{aligned}
 h_{\text{con,V}} = & \frac{2}{\tau_r - \tau_c} \frac{1 - \tilde{r}}{1 + \tilde{r}} \left\{ \right. \\
 & \frac{1}{1 - \tilde{r}} \left[\left(1 - f_g \frac{\tau_c}{\tau_r - \tau_c} \right) \left[G(t - \tau_c) - G(t - \tau_r) \right] \right. \\
 & \quad \left. + f_g \tau_c \frac{1}{1 - \tilde{r}} g(t - \tau_c) - f_g \tau_c \frac{\tilde{r}}{1 - \tilde{r}} g(t - \tau_r) \right] \\
 & - \left(1 - f_g \frac{\tau_c}{\tau_r - \tau_c} \right) \left[\frac{1}{\tau_r} \left[\Gamma(t - \tau_r) - \Gamma(t) \right] \right. \\
 & \quad \left. - \frac{1}{\tau_c} \left[\Gamma(t - \tau_c) - \Gamma(t) \right] \right] \\
 & - f_g \left[\frac{\tilde{r}}{1 - \tilde{r}} G(t) - \frac{1}{1 - \tilde{r}} G(t - \tau_c) \right. \\
 & \quad \left. - \frac{1}{\tau_c} \left[\Gamma(t - \tau_c) - \Gamma(t) \right] \right] \\
 & \left. - f_g \frac{\tilde{r}}{1 - \tilde{r}} \frac{\tau_c}{\tau_r} \left[G(t - \tau_r) - G(t) \right] \right\}. \tag{C.6}
 \end{aligned}$$

For a Dirac velocity kernel $g(y) = \delta(y)$ all impulse responses are transformed to frequency domain by use of Tab. C.2. For a Gaussian kernel function, the frequency response is computed by numerically z-transforming the respective IR function.

C.2 Flame Base Velocity Forcing

For a flame base bounded velocity perturbation, as it is given by Eq. (6.13), evaluation of the expression $h_\delta(t) = A' / \bar{A} \bar{u}_1$ for an impulse forcing, yields an impulse response for each of the three considered configurations. We retrieve for Slit flames

$$h_{\delta,\text{slit}}(t) = \delta(t - \tau_r), \tag{C.7}$$

for Bunsen flames

$$h_{\delta,\text{con},\Lambda}(t) = \frac{1}{\tau_r} [\Theta(t) - \Theta(t - \tau_r)] \tag{C.8}$$

and

$$h_{\delta,\text{con},V}(t) = \frac{1}{\tilde{r}} \left[\delta(t - \tau_r) - \frac{1 - \tilde{r}}{\tau_r} \Theta(t - \tau_r) \right] \tag{C.9}$$

for Wedge flames. The corresponding frequency responses F_δ are computed by use of Tab. C.2 provided in Appendix C.1.

List of Figures

1	Sketch of a Rjike tube, photo of the Rocketdyne F-1 engines of the Saturn V rocket as well as of its injector plate.	2
2	Illustration of a modern gas turbine combustor and photo taken inside an annular combustion chamber.	4
3	Sketch of a gas turbine combustor (top) and its associated network model (bottom).	5
4	Contents of the thesis in a nutshell.	8
1.1	Internal structure of a lean methane-air flame of equivalence ratio $\phi = 0.8$	13
1.2	Cellular structure of a flat flame for n-butane-air-nitrogen mixtures at four different ambient pressures.	15
1.3	Snapshots of spherically expanding stoichiometric propane/air flames (spherical bombs) for three different ambient pressures at a Lewis number close to unity.	18
1.4	Snapshot of an aerodynamically anchored and inclined rich propane/air/oxygen flame whose base is displaced by a vibrating flame holder.	19
1.5	Temporal evolution of a randomly perturbed flame sheet according to the MS equation.	20
1.6	Illustration of Huygens's Principle, which explains the formation of cusps from an initially smooth flame front.	23
1.7	Illustration of the thermal-diffusive flame instability mechanism.	25
1.8	Dispersion relation of Eq. (1.13) for the thermal-diffusive instability mechanism.	26

1.9	Illustration of contracting (red) and expanding (blue) flow tubes due to a displaced flame front, which explain the occurrence of the Darrieus-Landau instability.	27
1.10	Darrieus-Landau parameter Ω_0 and critical Lewis number for the onset of thermal-diffusive instability $Le_{c,TD}$ plotted over non-dimensional increase of specific volume.	30
1.11	Growth rate according to Eq. (1.13) for the hydrodynamic instability mechanism plotted for several Lewis numbers and non-dimensional density increases.	30
1.13	Sketch of a perturbed flame front around its mean using laboratory and flame aligned coordinates.	36
2.1	Investigated flame geometries (taken from [2]).	42
2.2	Unconfined (left) vs. confined (right) flame.	43
2.3	TiO ₂ smoke trace flow field visualization of two Bunsen flame forced at 200 Hz, one time by transversal movements of the flame holder at which the flame is anchored (left) and one time by acoustic excitation (right).	46
2.4	Snapshots of an acoustically excited Bunsen flame at 80 Hz, taken at four equidistant phases.	47
2.5	Snapshots of a G-equation-based simulation of an acoustically excited Bunsen flame at 120 Hz relying on the convective incompressible velocity model, taken at three equidistant phases.	48
2.6	Representation of a typical linear flame response of a Bunsen flame in the frequency domain (frequency response) in terms of (a) gain, (b) phase, (c) polar plot with phase determining the angle and gain the radius and (d) real and imaginary part plotted over frequency. . .	51
2.7	Representation of a typical linear flame response of a Bunsen flame in the time domain as impulse response (left) and in the frequency domain as frequency response (right).	52
3.1	Overview of acoustics-flame-flow interactions.	61
3.2	Sketch of the investigated Slit flame setup.	63
3.3	Illustration of the baroclinic generation of vorticity for a single parcel of fluid.	64
3.4	Illustration of the Schwarz-Christoffel mapping.	66

3.5	Illustration of how impermeability boundary conditions are met by use of a mirror vortex.	69
3.6	Flow field according to source at $\xi = 0$ and a Kutta panel including close up views of this panel in the physical and the image domain. . .	71
3.7	Normalized vorticity plotted over panel coordinates in the image and the physical domain for two panel lengths, two vorticity distributions and two confinement ratios.	72
3.8	Sketch of the Kutta panel and its mirror counterpart in the image domain.	73
3.9	Summary of all computations that need to be performed during one time step when considering a Kutta condition.	75
4.1	CFD steady state snapshots of absolute velocity for a confinement ratio of $C_r = 0.4$ and $C_r = 0.66$	79
4.2	Four consecutive snapshots taken from LOM predictions of a harmonically forced flame configuration excluding flame-flow feedback, split into vortical and irrotational flow components.	81
4.3	Comparison of vorticity distribution resulting from vortex shedding due to a Kutta condition and a linear approximation for two confinement ratios.	82
4.4	Visualization of the flame normal velocity resulting from a constant mean flow and a Kutta condition evaluated for four panel lengths as well as of the associated panel shapes.	83
4.5	Four snapshots taken at equidistant instances in time of the normalized flame displacement resulting from an impulsive velocity forcing according to CFD/SI results, the proposed acoustic LOM and the FBD model at two confinement ratios.	84
4.6	IR and FR in terms of gain and phase for $C_r = 0.4$ and $C_r = 0.66$ as predicted by CFD/SI, the FBD model and the proposed acoustic LOM.	85
5.1	Impulse responses for the $C_r = 0.4$ configuration depicted in Fig. 4.1 as well as the corresponding consecutive snapshots of the normalized flame-normal flame front displacement.	92
5.2	Normalized flame displacements shown for three confinement ratios corresponding to the cases shown in Fig. 5.1 where exponential functions are fitted to the spatial traces of the primary and secondary peaks.	93

5.3	Normalized flame front displacements as predicted by the uniform (top) and the incompressible convective (middle and bottom) velocity model for a harmonic velocity forcing.	95
5.4	Illustration of the line integral of Eq. (5.17) along a path ∂S enclosing a surface S	100
5.5	Sketch of a harmonically perturbed flame sheet including an illustration of the consequences of flame-generated vorticity.	101
5.6	Three figures showing the amount of volume produced according to an increasing number of Gaussian sources.	103
5.7	Steady state flow field with the flame front being represented by a number of Gaussian sources. Additionally, the magnitude of the flow velocity is plotted along three selected stream lines.	104
5.8	Axial flow profile of a channel flow including a vertical flame sheet represented by Gaussian sources compared to results of a 1D simulation employing detailed chemical mechanism.	104
5.9	Illustration of the perturbed flow field imposed by a displaced flame sheet, which is represented by a number of Gaussian volume sources leading to a geometrical focusing of the flow, which amplifies already existent flame perturbations.	106
5.10	LOM predictions including flame-generated vorticity of a harmonically forced flame configuration (at 120 Hz and an amplitude of 10% \bar{u}_{blk}) for a confinement ratio of $C_r = 0.4$	108
5.11	LOM predictions including flame-generated vorticity of a harmonically forced flame configuration (at 120 Hz and an amplitude of 10% \bar{u}_{blk}) for a confinement ratio of $C_r = 0.66$	109
5.12	Four snapshots taken at equidistant instances in time of the normalized flame displacement resulting from an impulsive velocity forcing taken from CFD/SI results as well as from the acoustic LOM with and without flame-flow feedback resulting from flame generated vorticity at two confinement ratios.	110
5.13	IR and FR in terms of gain and phase at $C_r = 0.4$ and $C_r = 0.66$ as predicted by CFD/SI as well as by the acoustic LOM with and without consideration of flame-generated vorticity.	111
5.14	IR and FR in terms of gain and phase at $C_r = 0.4$ as predicted by CFD/SI as well as by the acoustic LOM with and without consideration of flame-generated vorticity. Shown are results for two minimum vortex kernel radii $r_{0,\omega,\text{min}}$	112

5.15	LOM predictions including irrotational flame-flow feedback of a harmonically forced flame configuration (at 120 Hz and an amplitude of 10% \bar{u}_{blk}) for a confinement ratio of $C_r = 0.4$	113
5.16	LOM predictions including irrotational flame-flow feedback of a harmonically forced flame configuration (at 120 Hz and an amplitude of 10% \bar{u}_{blk}) for a confinement ratio of $C_r = 0.66$	113
5.17	Illustration of the dipole-like flow structure in the vicinity of a perturbed duct flame as well as fluctuation of the global heat release rate for a harmonic velocity forcing at 120 Hz resulting from simulations respecting flame-generated vorticity and irrotational gas expansion. .	114
5.18	Four snapshots taken at equidistant instances in time of the normalized flame displacement resulting from an impulsive velocity forcing taken from CFD/SI results as well as from the acoustic LOM with and without flame-flow feedback resulting from irrotational gas expansion.	115
6.1	CFD steady state snapshots of absolute velocity for the three investigated flame test cases of different flame geometries.	124
6.2	Illustration of the dependency of the change of the flame line segment length $dS' = dS - \bar{dS}$ on the displacements $d\eta'_i$ and $d\eta'_{i+1}$ up to $\mathcal{O}(\epsilon)$ contributions.	126
6.3	Displaced flame segment in flame aligned and laboratory coordinates.	127
6.4	Geometric measures required for the computation of the flame surface area of Bunsen flames.	129
6.5	Geometric measures required for the computation of the flame surface area of Wedge flames.	131
6.6	Thought experiment illustrating the results of the linearized surface integrals.	133
6.7	Sketch of an advected flame pocket, which is generated by an impulsive deflection of the flame base, shown for three flame configurations.	134
6.8	Transfer function in terms of impulse response h_δ and frequency response F_δ from flame base velocity perturbations to heat release shown for three flame configurations.	136
6.9	Qualitative illustration of the velocity field resulting from unit impulse forcing and a Gaussian velocity kernel function $g(\tau)$	139
6.10	Snapshot of the velocity and vorticity field resulting from unit impulse response forcing and a Gaussian velocity kernel.	140

6.11 FTF predictions of the DIC model in terms of impulse response $h(t)$ and frequency response $F(\omega)$ shown for three flame configurations. 142

6.12 Illustration of the displaced flame front deflection $\xi(x_1^F, t)$ of the DIC model for an impulse velocity perturbation. 143

6.13 Impulse responses of the three different flame configurations. 144

6.14 Comparison of FTF predictions for Slit flames visualized in time and frequency domain from CFD/SI data, the DIC, the GCI and the plain convective velocity models. 146

6.15 Comparison of FTF predictions for Bunsen flames visualized in time and frequency domain from CFD/SI data, the DIC, the GCI and the plain convective velocity models. 147

6.16 Comparison of FTF predictions for Wedge flames visualized in time and frequency domain from CFD/SI data, the DIC, the GCI and the plain convective velocity models. 148

6.17 Comparison of IR and the corresponding normalized flame front displacement $\xi/\hat{\xi}$ of the Slit configuration resulting from an impulse forcing at four instants in time, shown for the CFD/SI data as well as the DCI/GCI models. 148

6.18 Comparison of IR and the corresponding normalized flame front displacement $\xi/\hat{\xi}$ of the Bunsen configuration resulting from an impulse forcing at four instants in time, shown for the CFD/SI data as well as the DCI/GCI models. 149

6.19 Comparison of IR and the corresponding normalized flame front displacement $\xi/\hat{\xi}$ of the Wedge configuration resulting from an impulse forcing at four instants in time, shown for the CFD/SI data as well as the DCI/GCI models. 150

6.20 Experimental frequency response data of selected conical and a slit flames adopted from the literature compared to GCI predictions. 152

A.1 Cross-sectional view of the considered idealized combustor geometry. 162

A.2 Assumed model structure of the flame system. 164

A.3 Illustration of the CFD/SI approach applied to identify a FIR model using broad band input/output CFD data. 165

A.4 Visualization of FIR coefficients and confidence intervals for two representative FIR models (Slit and Bunsen). 168

A.5	Auto- and cross-correlation data of residuals resulting from the identified models.	171
A.6	Model and CFD output time series for two identified models using a test data set.	173
A.7	Comparison of IR predictions resulting from impulsive forcing as well as from the CFD/SI approach for three representative setups. . .	174
A.8	IR predictions resulting from impulsive forcing of a Slit flame shown for four amplitudes.	175
A.9	Signal of normalized amplitude used for impulsive forcings conducted in this thesis and flame shape computed from an CH ₄ -isoline of a CFD data snapshot.	175
B.1	Effect of temperature of the back-plate T_{BP} on on the FTF and the mean flow field of a Slit flame (close-up views of the steady state flame anchoring).	178
B.2	Effect of temperature of the back-plate T_{BP} on on the FTF and the mean flow field of a Bunsen flame (close-up views of the steady state flame anchoring).	178

List of Tables

5.1	Flame parameters used for the computations of this chapter.	107
6.1	Overview of analytic expressions required to compute the linear response of stiffly anchored flames, provided for two coordinate systems.	132
6.2	Summary of experimental data adopted from the literature, see Fig. 6.20.	152
C.1	Overview of the two Dirac and the Gaussian kernel functions and their antiderivatives.	182
C.2	Fourier transform overview.	183

Bibliography

- [1] T. Steinbacher, A. Albayrak, A. Ghani, and W. Polifke. Response of Premixed Flames to Irrotational and Vortical Velocity Fields Generated by Acoustic Perturbations. *Proc. Combust. Inst.*, 37(4):5367–5375, 2019. doi: [10.1016/j.proci.2018.07.041](https://doi.org/10.1016/j.proci.2018.07.041).
- [2] T. Steinbacher, A. Albayrak, A. Ghani, and W. Polifke. Consequences of Flame Geometry for the Acoustic Response of Premixed Flames. *Combust. Flame*, 199:411–428, 2019. doi: [10.1016/j.combustflame.2018.10.039](https://doi.org/10.1016/j.combustflame.2018.10.039).
- [3] N. Rott. Thermoacoustics. *Adv. Appl. Mech.*, bf20:135–175, 1980. doi: [10.1016/S0065-2156\(08\)70233-3](https://doi.org/10.1016/S0065-2156(08)70233-3).
- [4] L. Rayleigh. *The Theory of Sound*. Macmillan, London, 1896. ISBN 0-486-60292-3.
- [5] P. L. Rijke. Notiz über eine neue Art, die in einer an beiden Enden offenen Röhre enthaltene Luft in Schwingungen zu versetzen. *Ann. Phys.*, 183(6): 339–343, 1859. doi: [10.1002/andp.18591830616](https://doi.org/10.1002/andp.18591830616).
- [6] Feldman. Review of the Literature om Rijke Thermoacoustic Phenomena. *J. Sound Vib.*, 7:83–89, 1968.
- [7] G. Bisio and G. Rubatto. Sondhauss and Rijke Oscillations – Thermodynamic Analysis, Possible Applications and Analogies. *Energy*, 24(2):117–131, 1999. doi: [10.1016/S0360-5442\(98\)00090-5](https://doi.org/10.1016/S0360-5442(98)00090-5).
- [8] J. W. S. Rayleigh. The Explanation of Certain Acoustical Phenomena. *Nature*, 18:319–321, 1878. doi: [10.1038/018319a0](https://doi.org/10.1038/018319a0).
- [9] E. M. Cortright. Apollo Expeditions to the Moon. <https://history.nasa.gov/SP-350/cover.html>, 2018.
- [10] R. Kraemer and V. Wheelock. *Rocketdyne: Powering Humans into Space*. Library of Flight. American Institute of Aeronautics and Astronautics, Inc., 2005. ISBN 978-1-56347-754-6.

- [11] J. C. Oefelein and V. Yang. Comprehensive Review of Liquid-Propellant Combustion Instabilities in F-1 Engines. *J. Propuls. Power*, 9(5):657–677, 1993. doi: [10.2514/3.23674](https://doi.org/10.2514/3.23674).
- [12] S. C. Fisher and S. A. Rahman. *Apollo Rocket Propulsion Development*. The NASA History Series. National Aeronautics and Space Administration, Washington, DC, 2009.
- [13] A. P. Dowling and Y. Mahmoudi. Combustion Noise. *Proc. Combust. Inst.*, 35(1):65–100, 2015. doi: [10.1016/j.proci.2014.08.016](https://doi.org/10.1016/j.proci.2014.08.016).
- [14] A. S. Morgans and I. Duran. Entropy Noise: A Review of Theory, Progress and Challenges. *Int. J. Spray Combust. Dyn.*, 8(4):285–298, 2016. doi: [10.1177/1756827716651791](https://doi.org/10.1177/1756827716651791).
- [15] M. Ihme. Combustion and Engine-Core Noise. *Annu. Rev. Fluid Mech.*, 49(1), 2017. doi: [10.1146/annurev-fluid-122414-034542](https://doi.org/10.1146/annurev-fluid-122414-034542).
- [16] Siemens.com. Sgt5-9000hl (567 Mw) Heavy-Duty Gas Turbine. <https://www.siemens.com/us/en/home/products/energy/power-generation/gas-turbines/sgt5-9000hl.html>, 2018.
- [17] ge.com. GT13E2 EV-Alpha Burner | GE Power. <https://www.ge.com/power/services/gas-turbines/upgrades/gt13e2-ev-alpha-burner>, 2018.
- [18] M. R. Bothien, N. Noiray, and B. Schuermans. A Novel Damping Device for Broadband Attenuation of Low-Frequency Combustion Pulsations in Gas Turbines. *J. Eng. Gas Turbines Power*, 136(4):041504, 2013. doi: [10.1115/1.4025761](https://doi.org/10.1115/1.4025761).
- [19] M. R. Bothien, D. A. Pennell, M. Zajadatz, and K. Döbbeling. On Key Features of the Aev Burner Engine Implementation for Operational Flexibility. In *Volume 1B: Combustion, Fuels and Emissions*, page V01BT04A051, San Antonio, Texas, USA, 2013. ASME. doi: [10.1115/GT2013-95693](https://doi.org/10.1115/GT2013-95693).
- [20] T. Poinso. Prediction and Control of Combustion Instabilities in Real Engines. *Proc. Combust. Inst.*, 36:1–28, 2017. doi: [10.1016/j.proci.2016.05.007](https://doi.org/10.1016/j.proci.2016.05.007).
- [21] M. Hoeijmakers, V. Kornilov, I. Lopez Arteaga, P. de Goey, and H. Nijmeijer. Intrinsic Instability of Flame-Acoustic Coupling. *Combust. Flame*, 161(11):2860–2867, 2014. doi: [10.1016/j.combustflame.2014.05.009](https://doi.org/10.1016/j.combustflame.2014.05.009).
- [22] S. Bomberg, T. Emmert, and W. Polifke. Thermal Versus Acoustic Response of Velocity Sensitive Premixed Flames. *Proc. Combust. Inst.*, 35(3):3185–3192, 2015. doi: [10.1016/j.proci.2014.07.032](https://doi.org/10.1016/j.proci.2014.07.032).

- [23] T. Emmert, S. Bomberg, S. Jaensch, and W. Polifke. Acoustic and Intrinsic Thermoacoustic Modes of a Premixed Combustor. *Proc. Combust. Inst.*, 36(3):3835–3842, 2017. doi: [10.1016/j.proci.2016.08.002](https://doi.org/10.1016/j.proci.2016.08.002).
- [24] M. J. Lighthill. The Response of Laminar Skin Friction and Heat Transfer to Fluctuations in the Stream Velocity. *Proc. R. Soc. Lond., A* 224:1–23, 1954. doi: [10.1098/rspa.1954.0137](https://doi.org/10.1098/rspa.1954.0137).
- [25] A. Witte and W. Polifke. Dynamics of Unsteady Heat Transfer in Pulsating Flow Across a Cylinder. *Int J Heat Mass Transf.*, 109(C):1111–1131, 2017. doi: [10.1016/j.ijheatmasstransfer.2017.02.072](https://doi.org/10.1016/j.ijheatmasstransfer.2017.02.072).
- [26] G. Darrieus. Propagation d'un Front de Flamme. In *La Technique Moderne and Le Congrès de Mécanique Appliquée*, Paris, France, 1938. Unpublished work; presented 1938 at La Technique Moderne (Paris) and in 1945 at Congrès de Mécanique Appliquée (Paris).
- [27] L. Landau. On the Theory of Slow Combustion. *Acta Physicochim. URSS*, 19(1):403–411, 1944. doi: [10.1016/B978-0-08-092523-3.50044-7](https://doi.org/10.1016/B978-0-08-092523-3.50044-7).
- [28] N. Peters and F. A. Williams. The Asymptotic Structure of Stoichiometric Methane-Air Flames. *Combust. Flame*, 68:185–207, 1987. doi: [10.1016/0010-2180\(87\)90057-5](https://doi.org/10.1016/0010-2180(87)90057-5).
- [29] D. G. Goodwin, H. K. Moffat, and R. L. Speth. Cantera: An Object-Oriented Software Toolkit for Chemical Kinetics, Thermodynamics, and Transport Processes. <http://www.cantera.org>, 2016. Version 2.2.1.
- [30] G. P. Smith, D. M. Golden, M. Frenklach, N. W. Moriarty, B. Eiteneer, M. Goldenberg, C. T. Bowman, R. K. Hanson, S. Song, W. C. Gardiner Jr., V. V. Lissianski, and Z. Qin. GRI-Mech 3.0. http://www.me.berkeley.edu/gri_mech, 2016.
- [31] L. de Goey, J. van Oijen, V. Kornilov, and J. ten Thijsse Boonkamp. Propagation, Dynamics and Control of Laminar Premixed Flames. *Proc. Combust. Inst.*, 33:863–886, 2011. doi: [10.1016/j.proci.2010.09.006](https://doi.org/10.1016/j.proci.2010.09.006).
- [32] B. Smith R J, M. Loganathan, and M. S. Shantha. A Review of the Water Gas Shift Reaction Kinetics. *Int. J. Chem. React. Eng.*, 8(1), 2010. doi: [10.2202/1542-6580.2238](https://doi.org/10.2202/1542-6580.2238).
- [33] G. Markstein. *Nonsteady Flame Propagation*. Pergamon Press, New York, 1 edition, 1964. ISBN 978-1-4832-2162-5.
- [34] G. I. Sivashinsky. On a Distorted Flame Front as a Hydrodynamic Discontinuity. *Acta Astronautica*, 3(11–12):889–918, 1976. doi: [10.1016/0094-5765\(76\)90001-1](https://doi.org/10.1016/0094-5765(76)90001-1).

- [35] M. Matalon and B. J. Matkowsky. Flames as Gas Dynamic Discontinuities. *J. Fluid Mech.*, 124:239–259, 1982. doi: [10.1017/S0022112082002481](https://doi.org/10.1017/S0022112082002481).
- [36] Y. B. Zeldovich, G. I. Barenblatt, V. B. Librovich, and G. M. Makhviladze. *The Mathematical Theory of Combustion and Explosions*. Plenum Publishing, Moscow, USSR, 1985.
- [37] A. G. Class, B. J. Matkowsky, and a. Y. Klimenko. A Unified Model of Flames as Gasdynamic Discontinuities. *J. Fluid Mech.*, 491:11–49, 2003. doi: [10.1017/S002211200300507X](https://doi.org/10.1017/S002211200300507X).
- [38] G. I. Sivashinsky. Nonlinear Analysis of Hydrodynamic Instability in Laminar Flames—I. Derivation of Basic Equations. *Acta Astronautica*, 4(11–12):1177–1206, 1977. doi: [10.1016/0094-5765\(77\)90096-0](https://doi.org/10.1016/0094-5765(77)90096-0).
- [39] P. Clavin and F. A. Williams. Effects of Molecular Diffusion and of Thermal Expansion on the Structure and Dynamics of Premixed Flames in Turbulent Flows of Large Scale and Low Intensity. *J. Fluid Mech.*, 116:251–282, 1982. doi: [10.1017/S0022112082000457](https://doi.org/10.1017/S0022112082000457).
- [40] P. Pelce and P. Clavin. Influence of Hydrodynamics and Diffusion Upon the Stability Limits of Laminar Premixed Flames. *J. Fluid Mech.*, 124:219–237, 1982. doi: [10.1017/S002211208200247X](https://doi.org/10.1017/S002211208200247X).
- [41] M. Matalon, C. Cui, and J. K. Bechtold. Hydrodynamic Theory of Premixed Flames: Effects of Stoichiometry, Variable Transport Coefficients and Arbitrary Reaction Orders. *J. Fluid Mech.*, 487:179–210, 2003. doi: [10.1017/S0022112003004683](https://doi.org/10.1017/S0022112003004683).
- [42] Y. B. Zeldovich, G. I. Barenblatt, V. B. Librovich, and G. M. Makhviladze. Chapter 6.3: Hydrodynamic Instability of Flames. In *The Mathematical Theory of Combustion and Explosions*, pages 487–539. Plenum Publishing, Moscow, USSR, 1985.
- [43] F. A. Williams. 9.2 Inherent Oscillations of Burning Solids. In *Combustion Theory*. Addison-Wesley Publishing Company, Menlo Park, California, 2nd edition, 1985. ISBN 0-8053-9801-5.
- [44] G. H. Markstein. Experimental and Theoretical Studies of Flame-Front Stability. *J. Aeronaut. Sci.*, 18(3):199–209, 1951. doi: [10.2514/8.1900](https://doi.org/10.2514/8.1900).
- [45] R. E. Petersen and H. W. Emmons. Stability of Laminar Flames. *Phys. Fluids*, 4(4):456–464, 1961. doi: [10.1063/1.1706349](https://doi.org/10.1063/1.1706349).
- [46] I. Miller. A High-Pressure Premixed Flat-Flame Burner for Chemical Process Studies. *NASA Tech. Pap. 1318*, 1978.
- [47] G. Searby and J. Quinard. Direct and Indirect Measurement of Markstein Numbers of Premixed Flames. *Combust Flame*, 82:298–311, 1990.

- [48] G. I. Sivashinsky. Instabilities, Pattern Formation, and Turbulence in Flames. *Annu. Rev. Fluid Mech.*, 15(1):179–199, 1983. doi: [10.1146/annurev.fl.15.010183.001143](https://doi.org/10.1146/annurev.fl.15.010183.001143).
- [49] B. Karlovitz, D. W. Denniston, D. H. Knappschaefer, and F. E. Wells. Studies on Turbulent Flames. *4th Symp. Int. Combust.*, (KARL53):613–620, 1953.
- [50] W. Eckhaus. Theory of Flame-Front Stability. *J. Fluid Mech.*, 10(1):80–100, 1961. doi: [10.1017/S0022112061000081](https://doi.org/10.1017/S0022112061000081).
- [51] P. Clavin and P. Garcia-Ybarra. The Influence of the Temperature Dependence of Diffusivities on the Dynamics of Flame Fronts. *J. Phys. Théorique Appliquée*, 2(2):245–263, 1983.
- [52] J. Bechtold and M. Matalon. The Dependence of the Markstein Length on Stoichiometry. *Combust. Flame*, 127(1-2):1906–1913, 2001. doi: [10.1016/S0010-2180\(01\)00297-8](https://doi.org/10.1016/S0010-2180(01)00297-8).
- [53] G. K. Giannakopoulos, A. Gatzoulis, C. E. Frouzakis, M. Matalon, and A. G. Tomboulides. Consistent Definitions of “flame Displacement Speed” and “markstein Length” for Premixed Flame Propagation. *Combustion and Flame*, 2014. doi: [10.1016/j.combustflame.2014.10.015](https://doi.org/10.1016/j.combustflame.2014.10.015).
- [54] G. Giannakopoulos, M. Matalon, C. Frouzakis, and A. Tomboulides. The Curvature Markstein Length and the Definition of Flame Displacement Speed for Stationary Spherical Flames. *Proc. Combust. Inst.*, 35(1):737–743, 2015. doi: [10.1016/j.proci.2014.07.049](https://doi.org/10.1016/j.proci.2014.07.049).
- [55] C. Clanet and G. Searby. First Experimental Study of the Darrieus-Landau Instability. *Phys. Rev. Lett.*, 80(17):3867–3870, 1998. doi: [10.1103/PhysRevLett.80.3867](https://doi.org/10.1103/PhysRevLett.80.3867).
- [56] G. Dixon-Lewis. Structure of laminar flames. *Symp. Int. Combust.*, 23(1):305–324, 1991. doi: [10.1016/S0082-0784\(06\)80274-2](https://doi.org/10.1016/S0082-0784(06)80274-2).
- [57] D. Bradley, P. H. Gaskell, and X. J. Gu. Burning Velocities, Markstein Lengths, and Flame Quenching for Spherical Methane-Air Flames: A Computational Study. *Combust. Flame*, 104(1–2):176–198, 1996. doi: [10.1016/0010-2180\(95\)00115-8](https://doi.org/10.1016/0010-2180(95)00115-8).
- [58] L.-K. Tseng, M. Ismail, and G. Faeth. Laminar Burning Velocities and Markstein Numbers of Hydrocarbon/Air Flames. *Combust. Flame*, 95:410–426, 1993.
- [59] D. Bradley, R. A. Hicks, M. Lawes, C. G. W. Sheppard, and R. Woolley. The Measurement of Laminar Burning Velocities and Markstein Numbers for Iso-Octane-Air and Iso-Octane-N-Heptane-Air Mixtures at Elevated Temperatures and Pressures in an Explosion Bomb. *Combust. Flame*, 115(1-2):126–144, 1998. doi: [10.1016/S0010-2180\(97\)00349-0](https://doi.org/10.1016/S0010-2180(97)00349-0).

- [60] X. J. Gu, M. Z. Haq, M. Lawes, and R. Woolley. Laminar burning velocity and Markstein lengths of methane–air mixtures. *Combustion and Flame*, 121 (1–2):41–58, 2000. doi: [10.1016/S0010-2180\(99\)00142-X](https://doi.org/10.1016/S0010-2180(99)00142-X).
- [61] G. Wang, Y. Li, W. Yuan, Y. Wang, Z. Zhou, Y. Liu, and J. Cai. Investigation on Laminar Flame Propagation of N -Butanol/Air and N -Butanol/O₂/He Mixtures at Pressures up to 20 Atm. *Combust. Flame*, 191:368–380, 2018. doi: [10.1016/j.combustflame.2018.01.025](https://doi.org/10.1016/j.combustflame.2018.01.025).
- [62] O. C. Kwon, G. Rozenchan, and C. K. Law. Cellular Instabilities and Self-Acceleration of Outwardly Propagating Spherical Flames. *Proceedings of the Combustion Institute*, 29(2):1775–1783, 2002. doi: [10.1016/S1540-7489\(02\)80215-2](https://doi.org/10.1016/S1540-7489(02)80215-2).
- [63] G. Searby, J.-M. Truffaut, and G. Joulin. Comparison of Experiments and a Nonlinear Model Equation for Spatially Developing Flame Instability. *Phys. Fluids*, 13(11):3270–3276, 2001. doi: [10.1063/1.1407815](https://doi.org/10.1063/1.1407815).
- [64] T. Sugimoto and Y. Matsui. An Experimental Study on the Dynamic Behavior of Premixed Laminar Flames. *Symposium (International) on Combustion*, 19 (1):245–250, 1982. doi: [10.1016/S0082-0784\(82\)80194-X](https://doi.org/10.1016/S0082-0784(82)80194-X).
- [65] L. Boyer and J. Quinard. On the Dynamics of Anchored Flames. *Combust. Flame*, 82(1):51–65, 1990. doi: [10.1016/0010-2180\(90\)90077-5](https://doi.org/10.1016/0010-2180(90)90077-5).
- [66] J.-M. Truffaut and G. Searby. Experimental Study of the Darrieus-Landau Instability on an Inverted-V Flame, and Measurement of the Markstein Number. *Combust. Sci. Technol.*, 149(1-6):35–52, 1999. doi: [10.1080/00102209908952098](https://doi.org/10.1080/00102209908952098).
- [67] Y. Rastigejev and M. Matalon. Nonlinear Evolution of Hydrodynamically Unstable Premixed Flames. *J. Fluid Mech.*, 554:371–392, 2006. doi: [10.1017/S0022112005008098](https://doi.org/10.1017/S0022112005008098).
- [68] Y. Rastigejev and M. Matalon. Numerical Simulation of Flames as Gas-Dynamic Discontinuities. *Combust. Theory Model.*, 10(3):459–481, 2006. doi: [10.1080/13647830500463502](https://doi.org/10.1080/13647830500463502).
- [69] F. Creta and M. Matalon. Propagation of Wrinkled Turbulent Flames in the Context of Hydrodynamic Theory. *J. Fluid Mech.*, 680:225–264, 2011. doi: [10.1017/jfm.2011.157](https://doi.org/10.1017/jfm.2011.157).
- [70] F. Creta and M. Matalon. Strain Rate Effects on the Nonlinear Development of Hydrodynamically Unstable Flames. *Proceedings of the Combustion Institute*, 33(1):1087–1094, 2011. doi: [10.1016/j.proci.2010.06.029](https://doi.org/10.1016/j.proci.2010.06.029).
- [71] D. M. Michelson and G. I. Sivashinsky. Nonlinear Analysis of Hydrodynamic Instability in Laminar Flames—II. Numerical Experiments. *Acta Astronautica*, 4(11–12):1207–1221, 1977. doi: [10.1016/0094-5765\(77\)90097-2](https://doi.org/10.1016/0094-5765(77)90097-2).

- [72] M. Matalon. Flame dynamics. *Proceedings of the Combustion Institute*, 32(1):57–82, 2009. doi: [10.1016/j.proci.2008.08.002](https://doi.org/10.1016/j.proci.2008.08.002).
- [73] S. Candel, D. Durox, T. Schuller, J. F. Bourguin, and J. P. Moeck. Dynamics of Swirling Flames. *Annu. Rev. Fluid Mech.*, 46(1):147–173, 2014. doi: [10.1146/annurev-fluid-010313-141300](https://doi.org/10.1146/annurev-fluid-010313-141300).
- [74] K. Oberleithner, M. Stöhr, S. H. Im, C. M. Arndt, and A. M. Steinberg. Formation and Flame-Induced Suppression of the Precessing Vortex Core in a Swirl Combustor: Experiments and Linear Stability Analysis. *Combustion and Flame*, 162(8):3100–3114, 2015. doi: [10.1016/j.combustflame.2015.02.015](https://doi.org/10.1016/j.combustflame.2015.02.015).
- [75] A. Ghani, T. Poinsot, L. Gicquel, and J.-D. Müller. LES Study of Transverse Acoustic Instabilities in a Swirled Kerosene/Air Combustion Chamber. *Flow Turbulence Combust*, 96(1):207–226, 2016. doi: [10.1007/s10494-015-9654-9](https://doi.org/10.1007/s10494-015-9654-9).
- [76] T. B. Benjamin. Theory of the Vortex Breakdown Phenomenon. *J. Fluid Mech.*, 14(04):593, 1962. doi: [10.1017/S0022112062001482](https://doi.org/10.1017/S0022112062001482).
- [77] K. Oberleithner, M. Sieber, C. N. Nayeri, C. O. Paschereit, C. Petz, H. C. Hege, B. R. Noack, and I. Wygnanski. Three-Dimensional Coherent Structures in a Swirling Jet Undergoing Vortex Breakdown: Stability Analysis and Empirical Mode Construction. *J. Fluid Mech.*, 679:383–414, 2011. doi: [10.1017/jfm.2011.141](https://doi.org/10.1017/jfm.2011.141).
- [78] M. C. Jones, K. Hourigan, and M. C. Thompson. A Study of the Geometry and Parameter Dependence of Vortex Breakdown. *Phys. Fluids 1994-Present*, 27(4):044102, 2015. doi: [10.1063/1.4916352](https://doi.org/10.1063/1.4916352).
- [79] K. Oberleithner, S. Schimek, and C. O. Paschereit. Shear Flow Instabilities in Swirl-Stabilized Combustors and Their Impact on the Amplitude Dependent Flame Response: A Linear Stability Analysis. *Combust. Flame*, 162(1):86 – 99, 2015. doi: [10.1016/j.combustflame.2014.07.012](https://doi.org/10.1016/j.combustflame.2014.07.012).
- [80] K. Oberleithner and C. O. Paschereit. Modeling Flame Describing Functions Based on Hydrodynamic Linear Stability Analysis. In *ASME Turbo Expo 2016: Turbomachinery Technical Conference and Exposition*, page V04BT04A009. ASME, 2016. doi: [10.1115/GT2016-57316](https://doi.org/10.1115/GT2016-57316).
- [81] C. Sun, C. Sung, L. He, and C. Law. Dynamics of Weakly Stretched Flames: Quantitative Description and Extraction of Global Flame Parameters. *Combust. Flame*, 118(1-2):108–128, 1999. doi: [10.1016/S0010-2180\(98\)00137-0](https://doi.org/10.1016/S0010-2180(98)00137-0).
- [82] G. Searby and P. Clavin. Weakly Turbulent, Wrinkled Flames in Premixed Gases. *Combust. Sci. Technol.*, 46(3-6):167–193, 1986.
- [83] M. Matalon. Intrinsic Flame Instabilities in Premixed and Nonpremixed Combustion. *Annu. Rev. Fluid Mech.*, 39(1):163–191, 2007. doi: [10.1146/annurev.fluid.38.050304.092153](https://doi.org/10.1146/annurev.fluid.38.050304.092153).

- [84] V. V. Bychkov and M. A. Liberman. Dynamics and Stability of Premixed Flames. *Phys. Rep.*, page 123, 2000. doi: [10.1016/S0370-1573\(99\)00081-2](https://doi.org/10.1016/S0370-1573(99)00081-2).
- [85] J. A. Sethian. Curvature and the Evolution of Fronts. *Commun. Math. Phys.*, 101(4):487–499, 1985. doi: [10.1007/BF01210742](https://doi.org/10.1007/BF01210742).
- [86] Y. B. Zeldovich, G. I. Barenblatt, V. B. Librovich, and G. M. Makhviladze. Chapter 1.2: Self Accelerating Chemical Reactions and Critical Phenomena - Explosions and Self-Ignition. Semenov's Theory. In *The Mathematical Theory of Combustion and Explosions*, pages 36–74. Plenum Publishing, Moscow, USSR, 1985.
- [87] N. Bouvet, F. Halter, C. Chauveau, and Y. Yoon. On the Effective Lewis Number Formulations for Lean Hydrogen/Hydrocarbon/Air Mixtures. *Int. J. Hydrog. Energy*, 38(14):5949–5960, 2013. doi: [10.1016/j.ijhydene.2013.02.098](https://doi.org/10.1016/j.ijhydene.2013.02.098).
- [88] P. Tromans and R. Furzeland. An Analysis of Lewis Number and Flow Effects on the Ignition of Premixed Gases. *Symp. Int. Combust.*, 21(1):1891–1897, 1988. doi: [10.1016/S0082-0784\(88\)80425-9](https://doi.org/10.1016/S0082-0784(88)80425-9).
- [89] F. A. Williams. Turbulent Combustion. In *The Mathematics of Combustion*, pages 97–131. edited by John D. Buckmaster, University of Illinois, Urbana, Illinois, 1985.
- [90] G. I. Sivashinsky. Diffusional-Thermal Theory of Cellular Flames. *Combust. Sci. Technol.*, 15(3-4):137–145, 1977. doi: [10.1080/00102207708946779](https://doi.org/10.1080/00102207708946779).
- [91] E. Christiansen and C. Law. Pulsating Instability and Extinction of Stretched Premixed Flames. *Proc. Combust. Inst.*, 29(1):61–68, 2002. doi: [10.1016/S1540-7489\(02\)80012-8](https://doi.org/10.1016/S1540-7489(02)80012-8).
- [92] C. Sung, A. Makino, and C. Law. On Stretch-Affected Pulsating Instability in Rich Hydrogen/Air Flames: Asymptotic Analysis and Computation. *Combust. Flame*, 128(4):422–434, 2002. doi: [10.1016/S0010-2180\(01\)00361-3](https://doi.org/10.1016/S0010-2180(01)00361-3).
- [93] I. Brailovsky, P. V. Gordon, L. Kagan, and G. Sivashinsky. Diffusive-Thermal Instabilities in Premixed Flames: Stepwise Ignition-Temperature Kinetics. *Combust. Flame*, 162(5):2077–2086, 2015. doi: [10.1016/j.combustflame.2015.01.006](https://doi.org/10.1016/j.combustflame.2015.01.006).
- [94] T. Poinso and D. Veynante. *Theoretical and Numerical Combustion*. RT Edwards, Inc., 2005.
- [95] M. L. Frankel and G. I. Sivashinsky. The Effect of Viscosity on Hydrodynamic Stability of a Plane Flame Front. *Combust. Sci. Technol.*, 29(3-6):207–224, 1982. doi: [10.1080/00102208208923598](https://doi.org/10.1080/00102208208923598).

- [96] P. Garcia-Ybarra and R. Borghi. Stability of an Oblique Flame Front Model. *Dyn. React. Syst. Part Flames Config. Part II Model. Heterog. Combust. Prog. Astronaut. Aeronaut.*, pages 296–319, 1986. doi: [10.2514/5.9781600865794.0296.0319](https://doi.org/10.2514/5.9781600865794.0296.0319).
- [97] J. A. Sethian. Numerical Methods for Propagating Fronts. In P. Concus and R. Finn, editors, *Variational Methods for Free Surface Interfaces*, pages 155–164. Springer New York, 1987. ISBN 978-1-4612-9101-5 978-1-4612-4656-5.
- [98] E. Olsson and G. Kreiss. A Conservative Level Set Method for Two Phase Flow. *Journal of Computational Physics*, 210(1):225–246, 2005. doi: [10.1016/j.jcp.2005.04.007](https://doi.org/10.1016/j.jcp.2005.04.007).
- [99] I. M. Mitchell and Y. Susuki. Level Set Methods for Computing Reachable Sets of Hybrid Systems with Differential Algebraic Equation Dynamics. In M. Egerstedt and B. Mishra, editors, *Hybrid Systems: Computation and Control*, volume 4981, pages 630–633. Springer Berlin Heidelberg, Berlin, Heidelberg, 2008. doi: [10.1007/978-3-540-78929-1_51](https://doi.org/10.1007/978-3-540-78929-1_51).
- [100] C. W. Rhee, L. Talbot, and J. A. Sethian. Dynamical Behaviour of a Premixed Turbulent Open V-Flame. *J. Fluid Mech.*, 300:87–115, 1995. doi: [10.1017/S0022112095003624](https://doi.org/10.1017/S0022112095003624).
- [101] P. Preetham. *Modeling the Response of Premixed Flames to Flow Disturbances*. PhD Thesis, Georgia Institute of Technology, 2007.
- [102] D. Hartmann, M. Meinke, and W. Schröder. A Level-Set Based Adaptive-Grid Method for Premixed Combustion. *Combustion and Flame*, 158(7):1318–1339, 2011. doi: [10.1016/j.combustflame.2010.11.007](https://doi.org/10.1016/j.combustflame.2010.11.007).
- [103] S. Hemchandra. Premixed Flame Response to Equivalence Ratio Fluctuations: Comparison Between Reduced Order Modeling and Detailed Computations. *Combust. Flame*, 159(12):3530–3543, 2012. doi: [10.1016/j.combustflame.2012.08.003](https://doi.org/10.1016/j.combustflame.2012.08.003).
- [104] S. Schlimpert, S. Hemchandra, M. Meinke, and W. Schröder. Hydrodynamic Instability and Shear Layer Effect on the Response of an Acoustically Excited Laminar Premixed Flame. *Combust. Flame*, pages 1–23, 2014. doi: [10.1016/j.combustflame.2014.08.001](https://doi.org/10.1016/j.combustflame.2014.08.001).
- [105] F. A. Williams. 5.3 The Unimolecular Decomposition Flame with Lewis Number of Unity. In *Combustion Theory*, pages 143–165. Addison-Wesley Publishing Company, Menlo Park, California, 2nd edition, 1985. ISBN 0-8053-9801-5.
- [106] P. Smereka. Semi-Implicit Level Set Methods for Curvature and Surface Diffusion Motion. *J. Sci. Comput.*, 19(1):439–456, 2003.

- [107] I. Waugh. *Methods for Analysis of Nonlinear Thermoacoustic Systems*. PhD thesis, University of Cambridge, Department of Engineering, 2013.
- [108] M. Blanchard. *Linear and Nonlinear Dynamics of Laminar Premixed Flames Submitted to Flow Oscillations*. PhD thesis, Ecole Centrale Paris, Paris, France, 2015.
- [109] S. Schlimpert, M. Meinke, and W. Schröder. Nonlinear Analysis of an Acoustically Excited Laminar Premixed Flame. *Combustion and Flame*, 163:337–357, 2016. doi: [10.1016/j.combustflame.2015.09.035](https://doi.org/10.1016/j.combustflame.2015.09.035).
- [110] A. R. Kerstein, W. T. Ashurst, and F. A. Williams. Field Equation for Interface Propagation in an Unsteady Homogeneous Flow Field. *Phys. Rev. A*, 37(7): 2728–2731, 1988. doi: [10.1103/PhysRevA.37.2728](https://doi.org/10.1103/PhysRevA.37.2728).
- [111] T. Schuller, D. Durox, and S. Candel. A Unified Model for the Prediction of Laminar Flame Transfer Functions: Comparisons Between Conical and V-Flame Dynamics. *Combust. Flame*, 134(1,2):21–34, 2003. doi: [10.1016/S0010-2180\(03\)00042-7](https://doi.org/10.1016/S0010-2180(03)00042-7).
- [112] H. Y. Wang, C. K. Law, and T. Liewen. Linear Response of Stretch-Affected Premixed Flames to Flow Oscillations. *Combust. Flame*, 156(4):889–895, 2009. doi: [10.1016/j.combustflame.2009.01.012](https://doi.org/10.1016/j.combustflame.2009.01.012).
- [113] Preetham, S. K. Thumuluru, T. Liewen, and H. Santosh. Linear Response of Laminar Premixed Flames to Flow Oscillations: Unsteady Stretch Effects. *J. Propuls. Power*, 26(3):524–532, 2010. doi: [10.2514/1.41559](https://doi.org/10.2514/1.41559).
- [114] Wolfram|Alpha. Wolfram Alpha LLC. <http://mathworld.wolfram.com/MeanCurvature.html>, 2016.
- [115] A. Fleifil, A. M. Annaswamy, Z. A. Ghoneim, and A. F. Ghoniem. Response of a Laminar Premixed Flame to Flow Oscillations: A Kinematic Model and Thermoacoustic Instability Results. *Combust. and Flame*, 106:487–510, 1996. doi: [10.1016/0010-2180\(96\)00049-1](https://doi.org/10.1016/0010-2180(96)00049-1).
- [116] R. S. Blumenthal, P. Subramanian, R. Sujith, and W. Polifke. Novel Perspectives on the Dynamics of Premixed Flames. *Combust. Flame*, 160(7):1215–1224, 2013. doi: [10.1016/j.combustflame.2013.02.005](https://doi.org/10.1016/j.combustflame.2013.02.005).
- [117] T. Liewen. Modeling Premixed Combustion - Acoustic Wave Interactions: A Review. *J. Propuls. Power*, 19(5):765–781, 2003. doi: [10.2514/2.6193](https://doi.org/10.2514/2.6193).
- [118] A. C. McIntosh. The Linearised Response of the Mass Burning Rate of a Premixed Flame to Rapid Pressure Changes. *Combust. Sci. Technol.*, 91(4): 329–346, 1993. doi: [10.1080/00102209308907652](https://doi.org/10.1080/00102209308907652).

- [119] A. C. McIntosh. Deflagration Fronts and Compressibility. *Philos. Trans. R. Soc. Lond. Math. Phys. Eng. Sci.*, 357(1764):3523–3538, 1999. doi: [10.1098/rsta.1999.0507](https://doi.org/10.1098/rsta.1999.0507).
- [120] F. Baillot, D. Durox, and R. Prud'homme. Experimental and Theoretical Study of a Premixed Vibrating Flame. *Combust. Flame*, 88(2):149–168, 1992. doi: [10.1016/0010-2180\(92\)90049-U](https://doi.org/10.1016/0010-2180(92)90049-U).
- [121] D. Michaels and A. F. Ghoniem. Leading Edge Dynamics of Lean Premixed Flames Stabilized on a Bluff Body. *Combustion and Flame*, 191:39–52, 2018. doi: [10.1016/j.combustflame.2017.12.020](https://doi.org/10.1016/j.combustflame.2017.12.020).
- [122] T. Lieuwen. Theoretical investigation of unsteady flow interactions with a premixed planar flame. *J. Fluid Mech.*, 435:289–303, 2001. doi: [10.1017/S0022112001003780](https://doi.org/10.1017/S0022112001003780).
- [123] D. W. Bechert. Sound Absorption Caused by Vorticity Shedding, Demonstrated with a Jet Flow. *J. Sound Vib.*, 70(3):389–405, 1980. doi: [10.1016/0022-460X\(80\)90307-7](https://doi.org/10.1016/0022-460X(80)90307-7).
- [124] M. C. A. M. Peters and A. Hirschberg. Acoustically Induced Periodic Vortex Shedding At Sharp Edged Open Channel Ends: Simple Vortex Models. *J. Sound Vib.*, 161(2):281–299, 1993. doi: [10.1006/jsvi.1993.1072](https://doi.org/10.1006/jsvi.1993.1072).
- [125] P. Durrieu, G. Hofmans, G. Ajello, R. Boot, Y. Auregan, A. Hirschberg, and M. C. A. M. Peters. Quasisteady Aero-Acoustic Response of Orifices. *J. Acoust. Soc. Am.*, 110(4):1859–1872, 2001.
- [126] A. Hirschberg and H. Hoeijmakers. Comments on the Low Frequency Radiation Impedance of a Duct Exhausting a Hot Gas. *J. Acoust. Soc. Am.*, 136(2):EL84–EL89, 2014. doi: [10.1121/1.4885540](https://doi.org/10.1121/1.4885540).
- [127] B. T. Chu and L. S. G. Kovasznay. Non-Linear Interactions in a Viscous Heat-Conducting Compressible Gas. *J. Fluid Mech.*, 3:495–514, 1957. doi: [10.1017/S0022112058000148](https://doi.org/10.1017/S0022112058000148).
- [128] P. G. Mehta and M. C. Soteriou. Combustion Heat Release Effects on the Dynamics of Bluff Body Stabilized Premixed Reacting Flows. In *41st Aerospace Sciences Meeting and Exhibit*, 2003.
- [129] M. Blanchard, T. Schuller, D. Sipp, and P. J. Schmid. Response Analysis of a Laminar Premixed M-Flame to Flow Perturbations Using a Linearized Compressible Navier-Stokes Solver. *Phys. Fluids*, 27(4):043602, 2015. doi: [10.1063/1.4918672](https://doi.org/10.1063/1.4918672).
- [130] D. Michaels and A. F. Ghoniem. Impact of the Bluff-Body Material on the Flame Leading Edge Structure and Flame–Flow Interaction of Premixed Ch₄/Air Flames. *Combustion and Flame*, 172:62–78, 2016. doi: [10.1016/j.combustflame.2016.07.007](https://doi.org/10.1016/j.combustflame.2016.07.007).

- [131] T. Lieuwen. Analysis of Flame-Acoustic Wave Interactions using Boundary Element Methods. Proceedings of the 2000 Meeting of the Eastern State Section of the Combustion Institute, 2000.
- [132] D. Lee and T. Lieuwen. Premixed Flame Kinematics in a Longitudinal Acoustic Field. *J. Propuls. Power*, 19(5):837–846, 2003. doi: [10.2514/2.6173](https://doi.org/10.2514/2.6173).
- [133] V. N. Kornilov, K. R. A. M. Schreel, and L. P. H. de Goey. Experimental Assessment of the Acoustic Response of Laminar Premixed Bunsen Flames. *Proc. Combust. Inst.*, 31(1):1239–1246, 2007. doi: [10.1016/j.proci.2006.07.079](https://doi.org/10.1016/j.proci.2006.07.079).
- [134] A. Cuquel. *Dynamics and Nonlinear Thermo-Acoustic Stability Analysis of Premixed Conical Flames*. PhD Thesis, Ecole Centrale Paris, Paris, France, 2013.
- [135] N. Karimi, M. J. Brear, S.-H. Jin, and J. P. Monty. Linear and Non-Linear Forced Response of a Conical, Ducted, Laminar Premixed Flame. *Combust. Flame*, 156(11):2201–2212, 2009. doi: [10.1016/j.combustflame.2009.06.027](https://doi.org/10.1016/j.combustflame.2009.06.027).
- [136] A. Birbaud, D. Durox, and S. Candel. Upstream Flow Dynamics of a Laminar Premixed Conical Flame Submitted to Acoustic Modulations. *Combust. Flame*, 146(3):541–552, 2006. doi: [10.1016/j.combustflame.2006.05.001](https://doi.org/10.1016/j.combustflame.2006.05.001).
- [137] T. Schuller, S. Ducruix, D. Durox, and S. Candel. Modeling Tools for the Prediction of Premixed Flame Transfer Functions. *Proc. Combust. Inst.*, 29(1):107–113, 2002.
- [138] Preetham, S. Hemchandra, and T. Lieuwen. Dynamics of Laminar Premixed Flames Forced by Harmonic Velocity Disturbances. *J. Propuls. Power*, 24(6):1390–1402, 2008. doi: [10.2514/1.35432](https://doi.org/10.2514/1.35432).
- [139] S. Candel, D. Durox, T. Schuller, N. Darabiha, L. Hakim, and T. Schmitt. Advances in Combustion and Propulsion Applications. *Eur. J. Mech. BFluids*, 40:87 – 106, 2013. doi: [10.1016/j.euromechflu.2013.01.002](https://doi.org/10.1016/j.euromechflu.2013.01.002).
- [140] S. Candel. Combustion Dynamics and Control: Progress and Challenges. *Proc. Combust. Inst.*, 29(1):1–28, 2002.
- [141] T. Poinso and S. M. Candel. A Nonlinear Model for Ducted Flame Combustion Instabilities. *Combust Sci Tech*, 61:121–153, 1988.
- [142] P. Mehta, M. Soteriou, and A. Banaszuk. Impact of Exothermicity on Steady and Linearized Response of a Premixed Ducted Flame. *Combust. Flame*, 141(4):392–405, 2005. doi: [10.1016/j.combustflame.2005.01.012](https://doi.org/10.1016/j.combustflame.2005.01.012).
- [143] M. J. Remie, M. F. G. Cremers, K. R. A. M. Schreel, and L. P. H. de Goey. Flame Jet Properties of Bunsen-Type Flames. *Combust. Flame*, 147(3):163–170, 2006. doi: [10.1016/j.combustflame.2006.09.003](https://doi.org/10.1016/j.combustflame.2006.09.003).

- [144] A. Cuquel, D. Durox, and T. Schuller. Scaling the Flame Transfer Function of Confined Premixed Conical Flames. *Proc. Combust. Inst.*, 34(1):1007–1014, 2013. doi: [10.1016/j.proci.2012.06.056](https://doi.org/10.1016/j.proci.2012.06.056).
- [145] H. M. Altay, S. Park, D. Wu, D. Wee, A. M. Annaswamy, and A. F. Ghoniem. Modeling the Dynamic Response of a Laminar Perforated-Plate Stabilized Flame. *Proc. Combust. Inst.*, 32(1):1359 – 1366, 2009. doi: [10.1016/j.proci.2008.06.099](https://doi.org/10.1016/j.proci.2008.06.099).
- [146] F. Duchaine, F. Boudy, D. Durox, and T. Poinsot. Sensitivity Analysis of Transfer Functions of Laminar Flames. *Combust. Flame*, 158(12):2384–2394, 2011. doi: [10.1016/j.combustflame.2011.05.013](https://doi.org/10.1016/j.combustflame.2011.05.013).
- [147] K. Kedia, H. Altay, and A. Ghoniem. Impact of Flame-Wall Interaction on Premixed Flame Dynamics and Transfer Function Characteristics. *Proc. Combust. Inst.*, 33(1):1113–1120, 2011. doi: [10.1016/j.proci.2010.06.132](https://doi.org/10.1016/j.proci.2010.06.132).
- [148] D. Mejia, L. Selle, R. Bazile, and T. Poinsot. Wall-Temperature Effects on Flame Response to Acoustic Oscillations. *Proc. Combust. Inst.*, 35(3):3201–3208, 2015. doi: [10.1016/j.proci.2014.07.015](https://doi.org/10.1016/j.proci.2014.07.015).
- [149] D. Mejia, M. M. Brebion, A. Ghani, T. Kaiser, F. Duchaine, L. Selle, and T. Poinsot. Influence of Flame-Holder Temperature on the Acoustic Flame Transfer Functions of a Laminar Flame. *Combust. Flame*, 188(2):5–12, 2018. doi: doi.org/10.1016/j.combustflame.2017.09.016.
- [150] R. Gaudron, M. Gatti, C. Mirat, and T. Schuller. Analysis of the Transfer Function of Large and Small Premixed Laminar Conical Flames. In *ASME Turbo Expo 2017: Turbomachinery Technical Conference and Exposition*, volume 4A, page V04AT04A079, Charlotte, NC, USA, 2017. ASME. doi: [10.1115/GT2017-64231](https://doi.org/10.1115/GT2017-64231).
- [151] S. Kotake and K. Takamoto. Combustion Noise: Effects of the Shape and Size of Burner Nozzle. *J. Sound Vib.*, 112(2):345–354, 1987. doi: [10.1016/S0022-460X\(87\)80201-8](https://doi.org/10.1016/S0022-460X(87)80201-8).
- [152] D. Durox, T. Schuller, N. Noiray, and S. Candel. Experimental Analysis of Nonlinear Flame Transfer Functions for Different Flame Geometries. *Proc. Combust. Inst.*, 32(1):1391 – 1398, 2009. doi: [10.1016/j.proci.2008.06.204](https://doi.org/10.1016/j.proci.2008.06.204).
- [153] K. Pausch, S. S. Herff, S. Schlimpert, M. H. Meinke, and W. Schroeder. Acoustic Flame Response of a Round and a Slot Burner. In *23rd AIAA/CEAS Aeroacoustics Conference*, AIAA AVIATION Forum. AIAA, 2017. doi: [10.2514/6.2017-3360](https://doi.org/10.2514/6.2017-3360).
- [154] B. T. Chu. On the Generation of Pressure Waves at a Plane Flame Front. In *4th Symposium (International) on Combustion*, volume 4, pages 603–612, Cam-

- bridge, Massachusetts, USA, 1953. Combustion Institute. doi: [10.1016/S0082-0784\(53\)80081-0](https://doi.org/10.1016/S0082-0784(53)80081-0).
- [155] P. Clavin. Premixed Combustion and Gas Dynamics. *Ann Rev Fluid Mech*, 26:321–352, 1994.
- [156] V. Kornilov. *Experimental Research of Acoustically Perturbed Bunsen Flames*. PhD Thesis, Technische Universiteit Eindhoven, Eindhoven, Netherlands, 2007.
- [157] W. Polifke and C. J. Lawn. On the Low-Frequency Limit of Flame Transfer Functions. *Combust. Flame*, 151(3):437–451, 2007. doi: [10.1016/j.combustflame.2007.07.005](https://doi.org/10.1016/j.combustflame.2007.07.005).
- [158] S. Ducruix, D. Durox, and S. Candel. Theoretical and Experimental Determinations of the Transfer Function of a Premixed Laminar Flame. *Proc. Combust. Inst.*, 28(1):765–773, 2000. doi: [10.1016/S0082-0784\(00\)80279-9](https://doi.org/10.1016/S0082-0784(00)80279-9).
- [159] L. Crocco. Aspects of Combustion Stability in Liquid Propellant Rocket Motors Part1: Fundamentals. Low frequency instability with monopropellants. *J. Am. Rocket Soc.*, 21(6):163–178, 1951. doi: [10.2514/8.4393](https://doi.org/10.2514/8.4393).
- [160] H. J. Merk. An Analysis of Unstable Combustion of Premixed Gases. *Symp. Int. Combust.*, 6(1):500 – 512, 1957. doi: [http://dx.doi.org/10.1016/S0082-0784\(57\)80067-8](http://dx.doi.org/10.1016/S0082-0784(57)80067-8).
- [161] A. Cuquel, D. Durox, and T. Schuller. Theoretical and Experimental Determination of the Flame Transfer Function of Confined Premixed Conical Flames. In *7th Mediterranean Combustion Symposium*, Chia Laguna, Cagliari, Sardinia, Italy, 2011.
- [162] K. Kashinath, S. Hemchandra, and M. P. Juniper. Nonlinear Phenomena in Thermoacoustic Systems With Premixed Flames. *J. Eng. Gas Turbines Power*, 135(6):061502, 2013. doi: [10.1115/1.4023305](https://doi.org/10.1115/1.4023305).
- [163] A. Orchini and M. P. Juniper. Linear Stability and Adjoint Sensitivity Analysis of Thermoacoustic Networks with Premixed Flames. *Combust. Flame*, 165: 97–108, 2016. doi: [10.1016/j.combustflame.2015.10.011](https://doi.org/10.1016/j.combustflame.2015.10.011).
- [164] S. Shanbhogue, D.-H. Shin, S. Hemchandra, D. Plaks, and T. Lieuwen. Flame Sheet Dynamics of Bluff-Body Stabilized Flames During Longitudinal Acoustic Forcing. *Proc. Combust. Inst.*, 32(2):1787–1794, 2009. doi: [10.1016/j.proci.2008.06.034](https://doi.org/10.1016/j.proci.2008.06.034).
- [165] D.-H. Shin, D. V. Plaks, T. Lieuwen, U. M. Mondragon, C. T. Brown, and V. G. McDonnell. Dynamics of a Longitudinally Forced, Bluff Body Stabilized Flame. *J. Propuls. Power*, 27(1):105–116, 2011. doi: [10.2514/1.48056](https://doi.org/10.2514/1.48056).

- [166] Preetham and T. Lieuwen. Nonlinear Flame-Flow Transfer Function Calculations: Flow Disturbance Celerity Effects. In *40 Th AIAA/ASME/SAE/ASEE Joint Propulsion Conference & Exhibit*, 40th AIAA/ASME/AE/ASEE Joint Propulsion Conference, Fort Lauderdale, Florida, 2004. AIAA.
- [167] K. Kashinath, S. Hemchandra, and M. P. Juniper. Nonlinear Thermoacoustics of Ducted Premixed Flames: The Influence of Perturbation Convection Speed. *Combust. Flame*, 160(12):2856–2865, 2013.
- [168] H. Helmholtz. Über Integrale der hydrodynamischen Gleichungen, welche den Wirbelbewegungen entsprechen. *J. Für Reine Angew. Math.*, 55:25–55, 1858. ISSN 0075-4102; 1435-5345/e.
- [169] H. Bhatia, G. Norgard, V. Pascucci, and P.-T. Bremer. The Helmholtz-Hodge Decomposition: A Survey. *IEEE Trans. Vis. Comput. Graph.*, 19(8):1386–1404, 2013. doi: [10.1109/TVCG.2012.316](https://doi.org/10.1109/TVCG.2012.316).
- [170] W. Thomson. VI.—On Vortex Motion. *Earth Environ. Sci. Trans. R. Soc. Edinb.*, 25(1):217–260, 1868/ed. doi: [10.1017/S0080456800028179](https://doi.org/10.1017/S0080456800028179).
- [171] L. Strobio Chen, S. Bomberg, and W. Polifke. Propagation and Generation of Acoustic and Entropy Waves Across a Moving Flame Front. *Combust. Flame*, 166:170–180, 2016. doi: [10.1016/j.combustflame.2016.01.015](https://doi.org/10.1016/j.combustflame.2016.01.015).
- [172] T. Steinbacher, M. Meindl, and W. Polifke. Modeling the Generation of Temperature Inhomogeneities by a Premixed Flame. *Int. J. Spray Combust. Dyn.*, 10(2):111–130, 2018. doi: [10.1177/1756827717738139](https://doi.org/10.1177/1756827717738139).
- [173] M.-Z. Pindera and L. Talbot. Some Fluid Dynamic Considerations in the Modeling of Flames. *Combustion and Flame*, 73(2):111–125, 1988. doi: [10.1016/0010-2180\(88\)90041-7](https://doi.org/10.1016/0010-2180(88)90041-7).
- [174] M. Z. Pindera and L. Talbot. Flame Induced Vorticity: Effects of Stretch. *Symposium (International) on Combustion*, 21(1):1357–1366, 1988. doi: [10.1016/S0082-0784\(88\)80367-9](https://doi.org/10.1016/S0082-0784(88)80367-9).
- [175] W. D. Hayes. The Vorticity Jump Across a Gasdynamic Discontinuity. *J. Fluid Mech.*, 2(6):595–600, 1957. doi: [10.1017/S0022112057000403](https://doi.org/10.1017/S0022112057000403).
- [176] S. B. Berndt. The Vorticity Jump Across a Flow Discontinuity. *J. Fluid Mech.*, 26(3):433–436, 1966. doi: [10.1017/S0022112066001319](https://doi.org/10.1017/S0022112066001319).
- [177] M. C. Soteriou and A. F. Ghoniem. The Vorticity Dynamics of an Exothermic, Spatially Developing, Forced, Reacting Shear Layer. In *Symposium (International) on Combustion*, volume 25, pages 1265–1272. Elsevier, 1994. doi: [10.1016/S0082-0784\(06\)80767-8](https://doi.org/10.1016/S0082-0784(06)80767-8).

- [178] R. Erickson, M. Soteriou, and P. Mehta. The Influence of Temperature Ratio on the Dynamics of Bluff Body Stabilized Flames. In *44th AIAA Aerospace Sciences Meeting and Exhibit*, Reno, Nevada, 2006. American Institute of Aeronautics and Astronautics. doi: [10.2514/6.2006-753](https://doi.org/10.2514/6.2006-753).
- [179] J. W. Brown and R. V. Churchill. *Complex Variables and Applications*. Brown and Churchill Series. McGraw-Hill Higher Education, Boston, 8th ed edition, 2009. ISBN 978-0-07-305194-9 0-07-305194-2.
- [180] M. S. Howe. *Hydrodynamics and Sound*. Cambridge University Press, Cambridge ; New York, 2007. ISBN 0-521-86862-9.
- [181] D. G. Crighton. The Kutta Condition in Unsteady Flow. *Annu. Rev. Fluid Mech.*, 17(1):411–445, 1985. doi: [10.1146/annurev.fl.17.010185.002211](https://doi.org/10.1146/annurev.fl.17.010185.002211).
- [182] J. E. F. Williams. Aeroacoustics. *Annu. Rev. Fluid Mech.*, 9(1):447–468, 1977. doi: [10.1146/annurev.fl.09.010177.002311](https://doi.org/10.1146/annurev.fl.09.010177.002311).
- [183] S. W. Rienstra. *Edge Influence on the Response of Shear Layers to Acoustic Forcing*. PhD thesis, 1979.
- [184] S. W. Rienstra and A. Hirschberg. An Introduction to Acoustics. Technical Report IWDE 92-06, Eindhoven University of Technology, 2015.
- [185] C. E. Brown and W. J. Michael. Effect of Leading-Edge Separation on the Lift of a Delta Wing. *J. Aeronaut. Sci.*, 21(10):690–706, 1954. doi: [10.2514/8.3180](https://doi.org/10.2514/8.3180).
- [186] C. E. Brown and W. H. Michael. On Slender Delta Wings with Leading-Edge Separation. Report 3430, Washington, 1955.
- [187] M. S. Howe. Contributions to the Theory of Aerodynamic Sound, with Application to Excess Jet Noise and the Theory of the Flute. *J. Fluid Mech.*, 71(04): 625–673, 1975. doi: [10.1017/S0022112075002777](https://doi.org/10.1017/S0022112075002777).
- [188] M. S. Howe. Emendation of the Brown and Michael Equation, with Application to Sound Generation by Vortex Motion Near a Half-Plane. *J. Fluid Mech.*, 329:89–101, 1996. doi: [10.1017/S002211209600883X](https://doi.org/10.1017/S002211209600883X).
- [189] D. I. Pullin. The Large-Scale Structure of Unsteady Self-Similar Rolled-up Vortex Sheets. *J. Fluid Mech.*, 88(3):401–430, 1978. doi: [10.1017/S0022112078002189](https://doi.org/10.1017/S0022112078002189).
- [190] J. H. M. Disselhorst and L. V. Wijngaarden. Flow in the Exit of Open Pipes During Acoustic Resonance. *J. Fluid Mech.*, 99(02):293–319, 1980. doi: [10.1017/S0022112080000626](https://doi.org/10.1017/S0022112080000626).
- [191] H. W. M. Hoeijmakers. *Computational Aerodynamics of Ordered Vortex Flows*. PhD thesis, 1989.

- [192] R. R. Clements. An Inviscid Model of Two-Dimensional Vortex Shedding. *J. Fluid Mech.*, 57(2):321–336, 1973. doi: [10.1017/S0022112073001187](https://doi.org/10.1017/S0022112073001187).
- [193] P. A. Nelson, N. A. Halliwell, and P. E. Doak. Fluid Dynamics of a Flow Excited Resonance, Part II: Flow Acoustic Interaction. *J. Sound Vib.*, 91(3): 375–402, 1983.
- [194] A. G. Class, B. J. Matkowsky, and A. Y. Klimenko. Stability of Planar Flames as Gasdynamic Discontinuities. *J. Fluid Mech.*, 491:51–63, 2003. doi: [10.1017/S0022112003005081](https://doi.org/10.1017/S0022112003005081).
- [195] A. Zimmermann. *Modeling the Influence of Gas Expansion on the Linear Response of Laminar Premixed Flames*. PhD thesis, Technische Universität München, München, 2018.
- [196] W. M. T. Ashurst, G. I. Sivashinsky, and V. Yakhot. Flame Front Propagation in Nonsteady Hydrodynamic Fields. *Combust. Sci. Technol.*, 62(4-6):273–284, 1988. doi: [10.1080/00102208808924013](https://doi.org/10.1080/00102208808924013).
- [197] P. G. Saffman. *Vortex Dynamics*. Cambridge Univ. Press, Cambridge, 1995.
- [198] W. T. Ashurst. Vortex Simulation of Unsteady Wrinkled Laminar Flames. *Combust. Sci. Technol.*, 52(4-6):325–351, 1987. doi: [10.1080/00102208708952582](https://doi.org/10.1080/00102208708952582).
- [199] B. I. Choi and H. D. Shin. Flame/Flow Interaction in Oscillating Flow Field. *Combust. Sci. Technol.*, 159(1):87–107, 2000. doi: [10.1080/00102200008935778](https://doi.org/10.1080/00102200008935778).
- [200] H. P. Langtangen and S. Linge. 3.1 an Explicit Method for the 1D Diffusion Equation. In *Finite Difference Computing with PDEs: A Modern Software Approach*, number 16 in Texts in Computational Science and Engineering. Springer Open, Cham, Switzerland, 2017. ISBN 978-3-319-55456-3.
- [201] D. Durox, T. Schuller, and S. Candel. Combustion Dynamics of Inverted Conical Flames. *Proc. Combust. Inst.*, 30(2):1717–1724, 2005. doi: [10.1016/j.proci.2004.08.067](https://doi.org/10.1016/j.proci.2004.08.067).
- [202] T. Schuller, D. Durox, A. Cuquel, P. Palies, J. Moeck, and S. Candel. Modeling the Response of Premixed Flame Transfer Functions – Key Elements and Experimental Proofs. In *50th AIAA Aerospace Sciences Meeting Including the New Horizons Forum and Aerospace Exposition*, Nashville, Tennessee, 2012. AIAA. doi: [10.2514/6.2012-985](https://doi.org/10.2514/6.2012-985).
- [203] L. J. Humphrey, V. S. Acharya, D.-H. Shin, and T. C. Lieuwen. Modeling the Response of Turbulent Flames to Harmonic Forcing. *Combust. Sci. Technol.*, 189(2):187–212, 2017. doi: [10.1080/00102202.2016.1202245](https://doi.org/10.1080/00102202.2016.1202245).

- [204] A. P. Dowling. A Kinematic Model of a Ducted Flame. *J. Fluid Mech.*, 394: 51–72, 1999. doi: [10.1017/S0022112099005686](https://doi.org/10.1017/S0022112099005686).
- [205] N. Karimi. Response of a Conical, Laminar Premixed Flame to Low Amplitude Acoustic Forcing – a Comparison Between Experiment and Kinematic Theories. *Energy*, 78:490–500, 2014. doi: [10.1016/j.energy.2014.10.036](https://doi.org/10.1016/j.energy.2014.10.036).
- [206] R. Gaudron, M. Gatti, C. Mirat, and T. Schuller. Impact of the Injector Size on the Transfer Functions of Premixed Laminar Conical Flames. *Combust. Flame*, 179:138–153, 2017. doi: [10.1016/j.combustflame.2017.01.022](https://doi.org/10.1016/j.combustflame.2017.01.022).
- [207] Shreekrishna and T. Lieuwen. High Frequency Premixed Flame Response to Acoustic Perturbations. In *47th AIAA Aerospace Sciences Meeting*, Orlando, Florida, 2009.
- [208] N. Noiray, D. Durox, T. Schuller, and S. Candel. Passive Control of Combustion Instabilities Involving Premixed Flames Anchored on Perforated Plates. *Proc. Combust. Inst.*, 31(1):1283–1290, 2007.
- [209] V. N. Kornilov, R. Rook, J. H. M. ten Thije Boonkkamp, and L. P. H. de Goey. Experimental and Numerical Investigation of the Acoustic Response of Multi-Slit Bunsen Burners. *Combust. Flame*, 156(10):1957 – 1970, 2009. doi: [10.1016/j.combustflame.2009.07.017](https://doi.org/10.1016/j.combustflame.2009.07.017).
- [210] N. Hosseini, V. N. Kornilov, O. J. Teerling, I. Lopez Arteaga, and P. de Goey. Evaluating Thermoacoustic Properties of Heating Appliances Considering the Burner and Heat Exchanger as Acoustically Active Elements. *Combustion and Flame*, 191:486–495, 2018. doi: [10.1016/j.combustflame.2018.01.030](https://doi.org/10.1016/j.combustflame.2018.01.030).
- [211] V. Acharya, B. Emerson, U. Mondragon, D.-H. Shin, C. Brown, V. McDonell, and T. Lieuwen. Velocity and Flame Wrinkling Characteristics of a Transversely Forced, Bluff-Body Stabilized Flame, Part II: Flame Response Modeling and Comparison with Measurements. *Combust. Sci. Technol.*, 185(7): 1077–1097, 2013. doi: [10.1080/00102202.2013.777715](https://doi.org/10.1080/00102202.2013.777715).
- [212] B. Emerson, U. Mondragon, V. Acharya, D.-H. Shin, C. Brown, V. McDonell, and T. Lieuwen. Velocity and Flame Wrinkling Characteristics of a Transversely Forced, Bluff-Body Stabilized Flame, Part I: Experiments and Data Analysis. *Combust. Sci. Technol.*, 185(7):1056–1076, 2013. doi: [10.1080/00102202.2013.777714](https://doi.org/10.1080/00102202.2013.777714).
- [213] A. L. Birbaud, D. Durox, S. Ducruix, and S. Candel. Dynamics of Confined Premixed Flames Submitted to Upstream Acoustic Modulations. *Proceedings of the Combustion Institute*, 31(1):1257–1265, 2007. doi: [10.1016/j.proci.2006.07.122](https://doi.org/10.1016/j.proci.2006.07.122).
- [214] T. Schuller. *Mécanismes de Couplage Dans Les Interactions Acoustique-Combustion*. PhD Thesis, Ecole Centrale Paris, Paris, France, 2003.

- [215] T. Komarek and W. Polifke. Impact of Swirl Fluctuations on the Flame Response of a Perfectly Premixed Swirl Burner. *J. Eng. Gas Turbines Power*, 132(6):061503, 2010. doi: [10.1115/1.4000127](https://doi.org/10.1115/1.4000127).
- [216] P. Palies, T. Schuller, D. Durox, and S. Candel. Modeling of Premixed Swirling Flames Transfer Functions. *Proc. Combust. Inst.*, 33(2):2967 – 2974, 2011. doi: <http://dx.doi.org/10.1016/j.proci.2010.06.059>.
- [217] F. Di Sabatino, T. F. Guiberti, W. R. Boyette, W. L. Roberts, J. P. Moeck, and D. A. Lacoste. Effect of Pressure on the Transfer Functions of Premixed Methane and Propane Swirl Flames. *Combustion and Flame*, 193:272–282, 2018. doi: [10.1016/j.combustflame.2018.03.011](https://doi.org/10.1016/j.combustflame.2018.03.011).
- [218] L. Humphrey, V. Acharya, D.-H. Shin, and T. Lieuwen. Coordinate Systems and Integration Limits for Global Flame Transfer Function Calculations. *Int. J. Spray Combust. Dyn.*, 6(4):411–416, 2014. doi: [10.1260/1756-8277.6.4.411](https://doi.org/10.1260/1756-8277.6.4.411).
- [219] P. L. Blackshear. Driving Standing Waves by Heat Addition. *Proc Combust Inst*, 4(1):553–566, 1953. doi: [10.1016/S0082-0784\(53\)80077-9](https://doi.org/10.1016/S0082-0784(53)80077-9).
- [220] A. Dowling and G. Bloxsidge. Reheat Buzz- an Acoustically Driven Combustion Instability. In *9th Aeroacoustics Conference*, Williamsburg, VA, 1984. American Institute of Aeronautics and Astronautics. doi: [10.2514/6.1984-2321](https://doi.org/10.2514/6.1984-2321).
- [221] W. Polifke. Black-Box System Identification for Reduced Order Model Construction. *Ann. Nucl. Energy*, 67C:109–128, 2014. doi: [10.1016/j.anucene.2013.10.037](https://doi.org/10.1016/j.anucene.2013.10.037).
- [222] A. Majda and K. G. Lamb. Simplified Equations for Low Mach Number Combustion with Strong Heat Release. In A. Friedman, W. Miller, P. C. Fife, A. Liñán, and F. Williams, editors, *Dynamical Issues in Combustion Theory*, volume 35, pages 167–211. Springer New York, New York, NY, 1991. ISBN 978-1-4612-0947-8.
- [223] The OpenFOAM Foundation. OpenFOAM 2.3.1. <https://openfoam.org/>, 2017.
- [224] J. Bibrzycki, T. Poinso, and A. Zajdel. Investigation of Laminar Flame Speed of CH₄/N₂/O₂ and CH₄/CO₂/O₂ Mixtures Using Reduced Chemical Kinetic Mechanisms. *Arch. Combust.*, 30(4):287–296, 2010.
- [225] S. Jaensch, M. Merk, E. Gopalakrishnan, S. Bomberg, T. Emmert, R. Sujith, and W. Polifke. Hybrid CFD/Low-Order Modeling of Nonlinear Thermoacoustic Oscillations. *Proc. Combust. Inst.*, 36(3):3827–3834, 2017. doi: [10.1016/j.proci.2016.08.006](https://doi.org/10.1016/j.proci.2016.08.006).
- [226] L. Ljung. *System Identification: Theory for the User*. Prentice Hall PTR, New Jersey, 2nd edition, 1999. ISBN 0-13-656695-2.

- [227] K. J. Keesman. Time-invariant System Identification. In *System Identification*, Advanced Textbooks in Control and Signal Processing, pages 59–167. Springer London, London, 2011. ISBN 978-0-85729-521-7.
- [228] A. K. Tangirala. *Principles of System Identification: Theory and Practice*. CRC Press, Boca Raton, FL, 2014. ISBN 978-1-4398-9602-0.
- [229] P. Subramanian, R. S. Blumenthal, R. Sujith, and W. Polifke. Distributed Time Lag Response Functions for the Modelling of Combustion Dynamics. *Combust. Theory Model.*, 19(2):223–237, 2015. doi: [10.1080/13647830.2014.1001438](https://doi.org/10.1080/13647830.2014.1001438).
- [230] A. K. Tangirala. Part III.13: Goodness of Estimators. In *Principles of System Identification: Theory and Practice*, pages 317–349. CRC Press, Boca Raton, FL, 2014. ISBN 978-1-4398-9602-0.
- [231] A. K. Tangirala. Part I.4: Models for Discrete-Time LTI Systems. In *Principles of System Identification: Theory and Practice*, pages 68–108. CRC Press, Boca Raton, FL, 2014. ISBN 978-1-4398-9602-0.
- [232] L. Ljung. Appendix II: Some Statistical Techniques for Linear Regressions. In *System Identification: Theory for the User*, pages 543–564. Prentice Hall PTR, New Jersey, 2nd edition, 1999. ISBN 0-13-656695-2.
- [233] C. Sovardi, S. Jaensch, and W. Polifke. Concurrent Identification of Aero-acoustic Scattering and Noise Sources at a Flow Duct Singularity in low Mach Number Flow. *J Sound Vib.*, 377:90–105, 2016. doi: [10.1016/j.jsv.2016.05.025](https://doi.org/10.1016/j.jsv.2016.05.025).
- [234] M. Merk, S. Jaensch, C. Silva, and W. Polifke. Simultaneous Identification of Transfer Functions and Combustion Noise of a Turbulent Flame. *J Sound Vib.*, 422:432–452, 2018. doi: [10.1016/j.jsv.2018.02.040](https://doi.org/10.1016/j.jsv.2018.02.040).
- [235] S. Föllner and W. Polifke. Advances in Identification Techniques for Aero-Acoustic Scattering Coefficients from Large Eddy Simulation. In *18th International Congress on Sound and Vibration (ICSV18)*, volume 4, pages 3122–3129, Rio de Janeiro, Brazil, 2011.
- [236] S. Jaensch, M. Merk, T. Emmert, and W. Polifke. Identification of Flame Transfer Functions in the Presence of Intrinsic Thermoacoustic Feedback and Noise. *Combust. Theory Model.*, 22(3):613–634, 2018. doi: [10.1080/13647830.2018.1443517](https://doi.org/10.1080/13647830.2018.1443517).
- [237] L. Ljung. Chap. 4: Models of Linear Time-Invariant Systems. In *System Identification: Theory for the User*, pages 79–139. Prentice Hall PTR, New Jersey, 2nd edition, 1999. ISBN 0-13-656695-2.

- [238] C. Sovardi. *Identification of Sound Sources in Duct Singularities*. Ph.D. Thesis, TU München, Garching, Germany, 2016.
- [239] D. Moriasi, J. G. Arnold, M. W. van Liew, R. L. Bingner, R. D. Harmel, and T. L. Veith. Model Evaluation Guidelines for Systematic Quantification of Accuracy in Watershed Simulations. *Trans. ASABE*, 50(3):885–900, 2007. doi: [10.13031/2013.23153](https://doi.org/10.13031/2013.23153).
- [240] H. Muroi and S. Adachi. Model Validation Criteria for System Identification in Time Domain. *IFAC-PapersOnLine*, 48(28):86–91, 2015. doi: [10.1016/j.ifacol.2015.12.105](https://doi.org/10.1016/j.ifacol.2015.12.105).
- [241] A. Cuquel, D. Durox, and T. Schuller. Impact of Flame Base Dynamics on the Non-Linear Frequency Response of Conical Flames. *Comptes Rendus Mécanique*, 341(1–2):171 – 180, 2013. doi: <http://dx.doi.org/10.1016/j.crme.2012.11.004>.
- [242] M. M. Brebion, D. Mejia, P. Xavier, F. Duchaine, B. Bedat, L. Selle, and T. Poinsot. Joint Experimental and Numerical Study of the Influence of Flame Holder Temperature on the Stabilization of a Laminar Methane Flame on a Cylinder. *Combust. Flame*, 172:153–161, 2016. doi: [10.1016/j.combustflame.2016.06.025](https://doi.org/10.1016/j.combustflame.2016.06.025).